MULTIWAVELENGTH LONG TERM MONITORING AND SPECTRAL ENERGY DISTRIBUTION MODELING OF BRIGHT ACTIVE GALACTIC NUCLEI MARKARIAN 421

By

Biswajit Banerjee

PHYS05201304005

ASTRO-PARTICLE PHYSICS AND COSMOLOGY DIVISION,

SAHA INSTITUTE OF NUCLEAR PHYSICS, KOLKATA

A thesis submitted to the
Board of Studies in Physical Sciences

In partial fulfillment of the requirements

For the Degree of

DOCTOR OF PHILOSOPHY

of

HOMI BHABHA NATIONAL INSTITUTE

September, 2020

Homi Bhabha National Institute

Recommendations of the Viva Voce Board

As members of the Viva Voce Board, we recommend that the dissertation prepared by **Biswajit Banerjee** entitled **"Multiwavelength long term monitoring and Spectral Energy Distribution modeling of bright active galactic nuclei Markarian 421"** may be accepted as fulfilling the dissertation requirement for the Degree of Doctor of Philosophy.

-- **Date :**
Chairman : Prof. Debades Bandyopadhyay

-- **Date :**
Guide : Prof. Pratik Majumdar

-- **Date :**
Member : Prof. Subir Sarkar

-- **Date :**
Member : Prof. Satyajit Saha

-- **Date :**
External Examiner :

Final approval and acceptance of this dissertation is contingent upon the candidate's submission of the final copies of the dissertation to HBNI.

I hereby certify that I have read this dissertation prepared under my direction and recommend that it may be accepted as fulfilling the dissertation requirement.

Pratik Majumdar -- **Date :** 23/11/2020
Guide : Prof. Pratik Majumdar

STATEMENT BY AUTHOR

This dissertation has been submitted in partial fulfilment of requirements for an advanced degree at Homi Bhabha National Institute (HBNI) and is deposited in the library to be made available to borrowers under rules of the HBNI.

Brief quotations from this dissertation are allowable without special permission, provided that accurate acknowledgement of source is made. Requests for permission for extended quotation from or reproduction of this manuscript in whole or in part may be granted by the Competent Authority of HBNI when in his or her judgement the proposed use of the material is in the interests of scholarship. In all other instances, however, permission must be obtained from the author.

Biswajit Banerjee

Biswajit Banerjee

DECLARATION

I, hereby, declare that the investigation presented in the thesis has been carried out by me. The work is original and the work has not been submitted earlier as a whole or in part for a degree/diploma at this or any other Institution or University.

Biswajit Banerjee

Biswajit Banerjee

List of Publications arising from the thesis

Journal

1. " *Time dependent spectral modeling of Markarian 421 during a violent outburst in 2010", B. Banerjee, M. Joshi, P. Majumdar, K. E. Williamson, S. G. Jorstad, A. P. Marscher,, *MNRAS*, **2019**, *487*, 1, 845–857.

2. " *Multiwavelength variability and correlation studies of Mrk 421 during historically low X-ray and γ-ray activity in 2015−2016", V. A. Acciari, S. Ansoldi, L. A. Antonelli, K. Asano, A. Babić, B. Banerjee, A. Baquero et al., Accepted for publication in MNRAS **2020**, DOI: 210.1093/mnras/staa3727.

Chapters in books and lectures notes: NIL

Conferences

1. "Time-dependent multi-zone modelling of an unprecedented flare of Mrk-421 in February 2010", B. Banerjee, M. Joshi, P. Majumdar, presented in (August-2016), 20 th Course of the International School of Cosmic Ray Astrophysics (ISCRA), Erice, Italy.

2. “Fermi-LAT analysis of the variable source Mrk 421 from 2009 till 2010”, B. Banerjee and P. Majumdar presented in (February-2015), 33rd meeting of the Astronomical Society of India, NCRA-TIFR, Pune India.

3. “A multi-wavelength study of Markarian 421 during the 2015-16 campaign”, B. Banerjee, T. Terzic, P. Majumdar, D. Paneque & MAGIC Collaboration, presented in (January-2020), Saha Institute of Nuclear Physics, Kolkata, India.

4. “A multi-wavelength long term study of Mrk 421 during 2015-16 campaign”, B. Banerjee, T. Terzic, P. Majumdar, D. Paneque & MAGIC Collaboration, presented in (June-2018), MAGIC Collaboration meeting, La Palma, Spain.

5. “Time-dependent multi-zone modeling of an unprecedented flaring episode of Mrk 421 in February 2010”, B. Banerjee, M. Joshi, P. Majumdar, presented in (October-2017), National Symposium on Particles, Detectors and Instrumentation (NSPDI), Tata Institute of Fundamental Research (TIFR), Mumbai, India.

Biswajit Banerjee.

Biswajit Banerjee

Dedicated to

My dearest grandmother (Kamma),

Late Basanti Banerjee (1943–2019)

and my parents.

ACKNOWLEDGEMENTS

First and foremost, I am grateful to my supervisor Prof. Pratik Majumdar who introduced me to the gamma-ray astronomy. This thesis would not have been possible without his guidance, patience, and critical review of my work at every step. Working for the MAGIC Collaboration as a part of the APC Division, SINP was a great experience. I thank my collaborators, especially, Manasvita, David (Paneque), Tomislav, Julian, Giovanni, Kazuma, and Jeza. I accumulated a huge fraction of my technical knowledge by interacting with them. My gratitude to my colleagues in SINP: Kamakshya, Anshu, Avik, Madhurima, Sajad, Sunita, Upala, Suraj, Satyabrata, Arindam (Com.), Ujjal, Anisur, Aminul, Arijit, Abhijit, Tapas, Ashim, Bankim, Snehal, Apurba, Saran, Sayan, Rajkamal, Anindita, Pintu and Raju (Dutta) for making this journey beautiful. I acknowledge my Ph.D. batchmates: Roopam, Mugdha, Rajarshi, Rohit, Debdutta, Saswati, Arnab-s, Mithun, Amit, Biswarup, Shramana, Sourav, Sudeshna, Maireyee, Shamik, and Sukannya, interacting with whom I found the purpose of my life. I am grateful to the SINP, MSA-I, -II, and VECC Canteen staff for their fine service. I thank my friends: Subhra, Ayon, Jalarka, Sambaran, Bijoy, Prasanta (Char), Rome, Sanjana, Somnath, Arijit, Soumya, Prasanta (Nayak) and Saptaswa, for their support and love.

During my school-days, I was fortunate enough to be guided by Bapi-Kaku and Arindam-Sir, who introduced me to the outer world, and enormously influenced my thought process. I bow down to all my primary, secondary, college (A.R.-Sir, U.N.-Sir) and university teachers, and all my mentors (Abhijit-Kaku, Gourango-Kaku, Sunil-Pisemosai) who always encouraged me and made me believe that everything is possible.

I have been blessed with my parents and my sister who supported me always without hesitation. I thank all my family members; Mama, Guddu, Mumu, Masi, Meso, Dona, Tutun, Pisi; and my in-laws (Ma, Baba, Didi, Kuntal-da, Pontu) for their support, love, and encouragement. I am immeasurably grateful to Susmita for her love, support, patience, and belief (even sometimes when I was losing faith) in me. I can not thank you enough for staying with me in my tough times and trying to bring the best out of me.

I thank DAE, GOI for funding three academic visits to MPI, Munich, and attending ISCRA-'16, Italy. These visits boosted my research activities significantly. I thank the people of the Republic of India for providing secular, rational, and scientific environments, where science & culture can thrive through discussions in a democratic way.

Contents

List of Figures

List of Tables

6

Summary and Outlook

AGNs, particularly blazars, have been studied vastly over many years, and a huge amount of simultaneous radio to VHE γ-ray data has also been accumulated. The origin of high energy emission from the AGN is still under a lot of debate. A lot of work on determining the location and the structure of the emitting region whether it is a single or multiple-zone emission are addressed by many recent works (Graff et al. 2008; Marscher 2014; Chen et al. 2011b). Because of the bias towards the high flux states estimating the average emission from these sources is a big challenge. The correlation studies are crucial for understanding the emission from the source given the fact that the technique requires a very careful study as the correlation methods may provide a high-false significance which might be driven by a flaring event or simply driven by the cadence of the data that is being used. There are two schools of thoughts for addressing the questions mentioned above: 1) Study a large number of sources and find out the different properties at different energies(Ghisellini et al. 2017; Assef et al. 2018) and 2) Study a single blazar and perform a in-depth study with all the data available. The work presented in this thesis is motivated by the second, where Mrk421 has been selected as one of the cases where despite the availability of a huge amount of data and interpretations there are still enormous amount of questions that have not been answered.

The study presented in this thesis makes an attempt to explore some of the above mentioned challenges in two ways, first, from a theoretical point of view and, second, by performing a decade long physics analysis with a huge amount of MWL data.

The study related to the time-dependent leptonic modelling aims towards the characterization of emission of Mrk421 during a flaring episode in February 2010. The modeling of the spectral energy distribution (SED) of Mrk421 is carried out with a time-dependent multi-zone radiation feedback model during a hard X-ray flare. The source behavior was unprecedented not only because of the very high flux state (around 7 Crab units in TeV energies) in X-ray and TeV energies but also because of the significant spectral slope hardening over a period of 24 hours. By selecting three days from this episode we could identify the change in the behavior on a daily basis. On 15th February the SED is similar to the steady-state observed during 2009 (Abdo et al. 2011a). The flux state changed significantly on the next day (16th February) where the X-ray spectrum was found to be hard but in GeV and TeV energies the source spectrum was similar to that of the steady-state. The outburst in the TeV energies was detected on 17th February, where the flux in the X-ray was similar to the previous day but in the TeV energies, the source was detected in a very high (and hard) state. We used the time-dependent model to explain the SED of the violent outburst that was exhibited by the source in February 2010 for the three consecutive days mentioned above. The light-curve realizations for different energies for these days highlight the main differences between the role of different model parameters in shaping the emission profiles at different energies. This is one of the very first attempts made to understand a complete flaring episode using a cylindrical shaped emission region in a multi-zone scenario. We have explored the role and variation of the key physical properties that are responsible for the flaring activity.

In future, MUZORF should be upgraded such that the injected particle population is flexible and can take other functional forms (such as log-parabola or broken power-law). The model needs to be extended in order to explain the emission of neutrino blazars. The explanation of the discovery of very high energy γ-rays in coincidence with a neutrino event from the IceCube Collaboration (Aartsen et al. 2018) have been only partially successful because of the inability of predicting time lags between neutrino flare and flares at other energies (GeV and TeV energies). In this context, in future, a theoretical framework can be developed starting from the already existing purely leptonic time-dependent model used in Joshi & Böttcher (2010). The hadronic interactions can be included into the model under the internal shock scenario, and can be used to reproduce the observed spectral states of the neutrino blazar TXS 0506+056. The model can also be used to estimate the detectability of neutrinos from different AGNs. Apart from that, this modeling work can be extended to simulate the available X-ray and HE gamma-ray lightcurves for the flaring blazars using data from Chandra, XMM-Newton, Astrosat, or Fermi-LAT.

The analysis of very high energy gamma-ray data of Mrk 421 with MAGIC telescopes along with data from other observatories (OVRO, Metsahovi, KVA and other optical R-band telescopes, *Swift*-XRT, *Swift*-BAT, and Fermi-LAT) in different wavebands is aimed for the in-depth understanding the behavior of the source. Most of the VHE and X-ray observations were planned within 2 hours which makes it one of the best data sets for probing the physics of Mrk 421. During the multiwavelength campaign of Mrk421 led by MAGIC in 2015-2016, the source was mostly found in low flux states. Interestingly, a long quiet period of the source was detected in both TeV and X-ray energies for a duration of 2 months in 2016. As mentioned earlier this campaign is one of the very few campaigns where Mrk 421 has been studied in the low flux state. We explored different aspects of fractional variability studies with the data set for different energies. The long-term correlation between several lightcurves at different energy bands observed during this period has also been extensively studied (using discrete correlation function [DCF]). We also have studied the variation of the synchrotron peak position which we estimated by performing a log-parabola fit on a daily time-scale using the optical, UV and X-ray data. From the data of this campaign along with the published data, the typical state of the source in different energy bands has been studied using three methods which has never been done before. This thesis presents one of the very first studies of the flux distribution in an unbinned manner, where the flux-uncertainties are also taken into account.

From this extensive campaign, we have found quite a few interesting results. We have detected one of the highest states in the 37 GHz radio band where clear variation of the EVPA has been observed associated with a time-scale of a few weeks. The fractional variability study indicates an energy dependent variability, where the low state (data from 2016) in the X-rays and VHE γ-rays showed higher fractional variability than the high state (data from 2015). A deviation from harder when brighter has been seen in the soft VHE gamma-ray band. Deviation of harder when brighter may also occur in the hard VHE flux but it remains inconclusive from the current data. We performed multi-band flux correlation studies from radio to VHE, where we have seen positive correlation with time lag zero in: a) VHE gamma-rays vs. X-rays, and b) Optical R-band vs. HE gamma-ray. The HE γ-ray vs. radio band(s) shows positive correlation over a wide range of time lags centered at ~45 days. The synchrotron peak of Mrk421 has been fitted with a log-parabola model using data from optical R-band, *Swift*-UVOT (three UV filters), *Swift*-XRT, and *Swift*-BAT). During the low flux state in 2016, MJD 57422–

57429, an excess (>5 sigma) at hard X-ray band has been seen. This excess may point to the existence of a new sharp spectral component and needs a more detailed look which is beyond the scope of this thesis. Using a new method, the 'flux-profile' method, we performed multi-band flux distributions which show clear preference towards the LogNormal distribution. We also have used two other methods, namely, Chi-squared minimization and unbinned likelihood method to corroborate our results. A LogNormal flux distribution hints to a multiplicative process in the jets.

Overall, the data set presented in this work, which focuses on the two observing campaigns in 2015–2016, when Mrk 421 showed very low flux at keV and TeV energies, and without any prominent flare, allowed us to derive a good number of new observational results. The continuation of these multi-instrument observations in the upcoming years, with at least the same depth in temporal and energy coverage, will be important to determine whether these novel features that we report in this work are rare, or whether they repeat over time.

The current study on the MWL properties should be extended to other blazars by performing in-depth timing analysis (correlation between different bands such as radio, UV, optical, X-rays, high energy gamma-rays, and very high energy gamma-rays), variability analysis (fractional variability and hardness ratio) and spectral analysis (determination of synchrotron peak position with quasi-simultaneous radio, optical and X-ray data). The correlation between the syncrotron peak position and the IC peak position needs to be studied. With this data set one can extend one of the very interesting studies regarding variation of the synchrotron peak position and synchrotron peak energy during 1998 flare (Tanihata et al. 2004) and non-flaring episodes. This kind of study will be very important in order to probe any emergence of an additional component during a flare in a complete model independent way.

The study on the performance of MAGIC telescopes below 100 GeV is aimed towards the improvement of the sensitivity of the telescope at lower energies (a few tens of GeV). At these energies, because of the poor gamma-hadron separation, the sensitivity is very poor. In addition, the presence of the noise produced by the Domino-Ring-Sampler (DRS4) chip makes it difficult to recover the low energy events while lowering the analysis threshold. Because of the presence of these spikes, a special type of algorithm, known as the spike-removal algorithm has been developed and applied. The performance-tests of two spike-removal algorithms has been studied. The results of the performance tests have given invaluable inputs to the dedicated group, the sum-trigger working group within MAGIC, responsible for the analysis at energies below 100 GeV for GRB observations, pulsar studies, and study of sources with soft spectra.

The main aspect of the study related to the lowering of the analysis threshold of the "standard analysis chain" is to test the performance of a special type of image-cleaning during the calibration of the data. This kind of image cleaning performs core-pixel identification around a selected time window of the DRS waveform. Through extensive studies, it has been shown that this cleaning is capable of lowering the threshold as compared to the standard cleaning methods used in MAGIC. Certainly, this image-cleaning algorithm is suitable for sources with soft-spectrum such as pulsars, GRBs, high-redshift AGNs. However, the results of this cleaning at higher energies (above 100 GeV) do not agree well with the standard analysis.

However, the sensitivity at the high energies (above 100 GeV) has been recovered by using a hybrid cleaning (a combination of the *New Cleaning* and the standard cleaning). Besides, the present set up of the analysis requires identification and removal of any bright stars in the field of view of the target source. In order to implement this cleaning as the default cleaning for the data analysis in MAGIC, this needs to be made automatic.

Summary

The studies reported in this thesis can be divided into three parts, namely, (a) the study of the performance of MAGIC telescopes below 100 GeV with the help of a New (image) Cleaning algorithm, (b) multiwavelength (MWL) study of the blazar Markarian 421 (Mrk 421), and (c) spectral modeling of Mrk 421 during a flare in 2010. The study on the performance of MAGIC telescopes below 100 GeV is important for the soft spectrum sources such as GRB, high redshift AGNs and pulsars. The sensitivity of the telescope at lower energies (a few tens of GeV) is poor primarily because of two reasons: poor gamma-hadron separation, and due to the presence of the noise produced by the Domino-Ring-Sampler (DRS4) chips. This is why it is difficult to identify the low energy events while lowering the analysis threshold. The New Cleaning algorithm showed that an improvement in the sensitivity of the MAGIC telescopes down to 40-50 GeV is possible with the standard triggered data. The work related to the analysis of very high energy gamma-ray data of Mrk 421 with MAGIC telescopes along with MWL data is aimed for the understanding of the source behavior in different wavebands. In this campaign, the VHE and X-ray observations were planned within 2 hours. During this campaign, the source was mostly found in low flux states. For a duration of 2 months in 2016, the source was found in a very low flux state in VHE gamma-rays and X-rays. The variability in the source lightcurve has been studied extensively with the help of hardness ratio and fractional variability. The long-term correlation between several lightcurves at different energy bands observed during this period has also been extensively studied (using discrete correlation function; DCF). In this study, a new spectral component at hard X-rays (15-50 keV) observed with *Swift*-BAT has been detected during the low state of the

source in 2016 which does not agree with the log-parabola fit of the synchrotron hump. This thesis reports one of the very first studies of the flux distribution in an unbinned manner with two methods: the ’flux-profile’ method (similar to Kernel Density Estimator) and unbinned likelihood method, where the flux-uncertainties are also taken into account. These studies show that the MWL flux distributions mostly follow a LogNormal flux distribution which hints to a multiplicative process responsible for the variability of the source. The study related to the time-dependent leptonic modeling aims towards the characterization of a flaring episode of Mrk 421 in February 2010. The modeling of the spectral energy distribution (SED) of Mrk 421 is carried out with a time-dependent multi-zone radiation feedback model. The source showed a very high flux state in X-ray and VHE gamma-rays. In addition, a significant spectral slope hardening over a period of 24 hours can also be seen. On 15th February the SED was similar to the steady-state observed during 2009 (Abdo et al. 2011a). In the later days, the flux state changed significantly. On 17th February, the source was detected in a very high (and hard) state. With the help of the time-dependent leptonic model, all the three states during the outburst has been explained. The light-curve realizations for different energies for these days highlight the main differences between the role of different model parameters in shaping the emission profiles at different energies. This is one of the very first attempts made to understand a complete flaring episode using a cylindrical shaped emission region in a multi-zone scenario. In this study a general trend can be established which shows that as the flare evolves from a low- to a high-flux state, higher bulk kinetic energy is injected into the system with a harder particle population and a lower magnetic field strength.

1

Introduction:

Active galactic nuclei (AGNs) are classified as compact regions at the centre of galaxies. The emission produced by the AGNs can be traced from radio to the very-high-energy (VHE; $E > 100\,\mathrm{GeV}$) gamma-rays. The emission from these astrophysical objects is believed to be powered by a central supermassive black hole (SMBH). It is believed that the central SMBH accretes mass from the host galaxy and spews out plasma in a collimated manner in the form of a jet. The class of AGNs in which the jets are pointing towards the line of sight of the observer are called *blazars*. The blazar emission can be divided into two parts: thermal emission and non-thermal emission. The broadband spectral energy distribution (SED) is fully non-thermal. In this thesis, the non-thermal emission from Markarian 421 (Mrk 421), the first blazar detected in TeV energies has been studied in detail.

1.1 AGN-classification:

AGN phenomenology is very rich and dynamic. In the 1940's Carl Seyfert described a class of active galaxies named after him (Seyfert Galaxies Seyfert 1943). Later, these type of objects at high-redshift are identified as *quasars* (Schmidt 1963).

In the mid-1970's, the AGNs were classified according to their nature of radio-band morphology (Fanaroff & Riley 1974). Later, on the basis of their optical spectra, the objects were further divided into two groups: a) broad-line and narrow-line (Grandi & Osterbrock 1978). Recent hints from the spectro-polarimetric observations in the optical-band (Antonucci & Miller 1985) triggered the idea that all the AGN subclasses can be unified depending on their viewing angle and developed the unified model of AGN (Antonucci 1993; Urry & Padovani 1995).

Despite the fact that the unified model does not accurately take into account all the phenomenological cases such as angular size, luminosity, broadband continuum, emission lines, variability, polarization, radio emission, variability (Krolik 1999) and has an observational bias (Urry 2004), the unified model is very successful because of its simplicity. All the phenomenological differences of the many-component system can be described well with only varying the angle between the observer and the direction of the object (Beckmann & Shrader 2012).

Under the basic unified model, the object consists of the following main components (see Fig. 1.1):

a) SMBH: The SMBH is the central engine which converts the gravitational energy into kinetic energy, heat, turbulence, magnetic energy, radiation, etc. in the accretion disk (Blandford et al. 2019, for a recent review). The typical range of the masses of the SMBH can be from 10^5 to 10^{10} $M_\odot$ ($M_\odot$ being the solar mass).

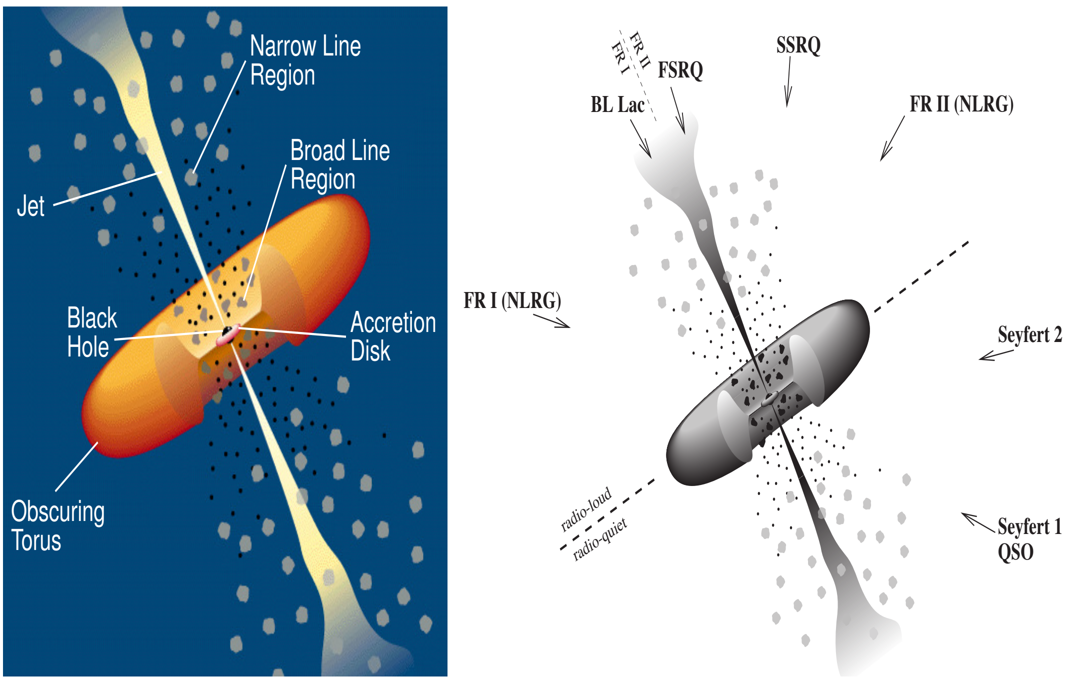

Figure 1.1: Unified schemes for radio-loud active galactic nuclei. Credit: Urry & Padovani (1995).

b) Accretion disk: An accretion disk is formed due to the accretion of mass from the host galaxy by the SMBH. During the process of accretion matter falls into the black-hole making a spiral trajectory. The matter looses its angular momentum by friction within the disk. The accretion disk serves as the primary source of radiation. Due to friction the temperature of the inner region of the accretion disk is higher than the outer region.

The accretion disks in the AGN with jets are divided based on the accretion modes: the radiatively efficient systems have more luminous accretion disks (Shakura & Sunyaev 1973, e.g.) while the radiatively inefficient disks (Narayan & Yi 1995, e.g.) are less luminous. More powerful radio sources are thought to have more luminous accretion disks, which are able to show more line emission.

c) Corona: The low density-hot plasma surrounding the SMBH is known as the *corona*. The high energy electrons inside the corona up-scatter radiations from the accretion disk to X-ray energies.

d) Dusty torus: The geometrically thick donut-like region surrounding the accretion disk hides the central engine as viewed from the outside. The typical radius of this structure ranges from 0.1 pc to more than 10 pc (1 pc= 3.1×10^{18} cm).

e) Broad-line region (BLR): The irregular structures covering the accretion disk and the central engine containing partially ionized high density gas are called the broad line regions. The broad emission lines (full width half maximum, FWHM > 1000 km s^{-1}) originating from the atomic transitions are the signatures of the BLR.

f) Narrow-line region (NLR): The structures situated at around a few kpc from the central engine containing low density ionized gas are called the narrow line regions. Both the permitted and forbidden atomic transition lines (FWHM < 1000 km s^{-1}) originate from this region.

g) Relativistic jet: Highly beamed high velocity ejecta from the central engine appears as two jets of plasma in the opposite directions perpendicular to the accretion disk. The jets can be formed through two ways: Blandford-Znajek (Blandford & Znajek 1977) process, where the spin energy of the black hole is tapped, or through the Blandford-Payne (Blandford & Payne 1982) process, where the rotational energy is extracted through the accretion disk.

Inside the jet, the particles produce non-thermal synchrotron and synchrotron self-Compton (SSC) emissions. Around 10% of the AGNs detected so far have very strong collimated jets which reach up to more than 100 kpc distances (Bagchi et al. 2014). The emission from the jet for the rest of the cases are either weak or do not show any presence of the same. In many cases, one or more brighter radio-emission can be spotted. These are called *knots* (Uchiyama et al. 2006). The *knots* sometimes show apparent

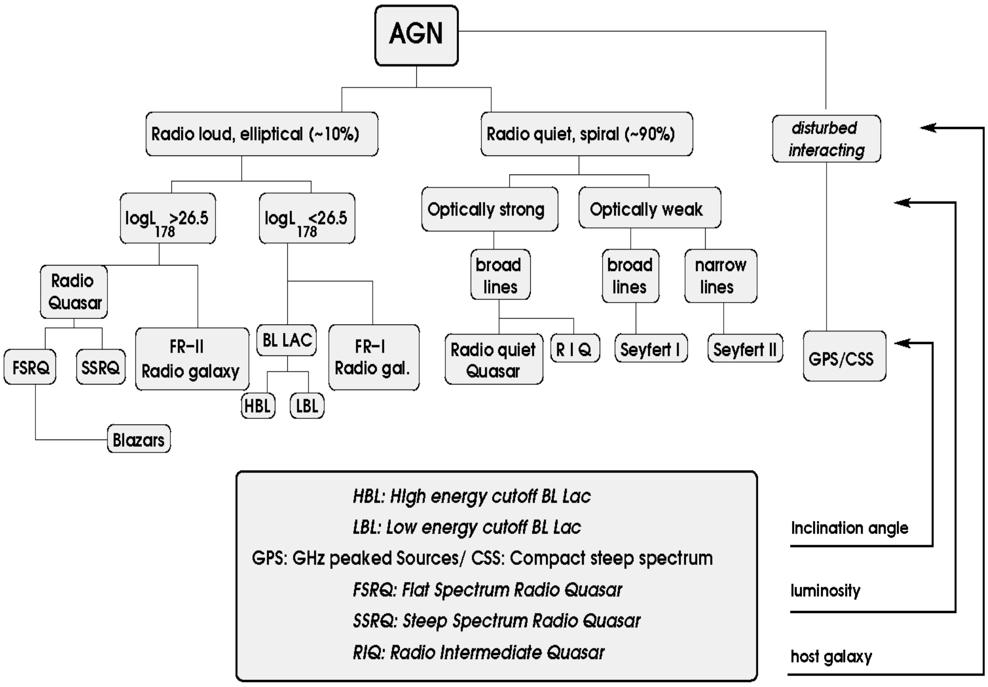

Figure 1.2: The classification of the AGNs depending on the radio loudness, optical luminosity and inclination of the jets. Credit: Becker (2008).

superluminal motion which is a situation caused by the orientation of the jet axis to the line of sight of the observer. In some cases, at the end of the jets, extended ellipsoidal structures are formed which are known as *lobes* (Owen et al. 2000). The evidence of the existence of a relativistic jet was first found in the M87 (Curtis 1918). The broad classification of the AGNs is mentioned in Fig. 1.2.

The typical SED of a blazar is characterized by a double hump structure. The low energy-hump peaks in the UV-X-ray region and the second peak appears in the high energy gamma (HE γ)-rays. In Figure 1.3, we present the double hump SED of Markarian 421 (Mrk 421; redshift=0.031) which is one of the closest TeV-blazars, where the low and high-energy peaks appear in the soft X-rays and in the HE $\gamma-$rays respectively. The blazars are further divided into sub-classes depending on the presence of emission lines in the UV-optical energy region: flat spectrum radio-quasars (FSRQs) and BL Lacertae objects (BL Lac). While FSRQs show broad and narrow emission line features in their optical-UV spectrum, BL Lacs are particularly known for the absence of emission lines or presence of very faint emission lines. BL Lacs are further divided into three categories by the energy at which the peak of the low energy hump appears (Nieppola et al. 2006) : Low-energy-peaked (LBL) - log ν_s < 14.5; Intermediate-energy-peaked (IBL) - 14.5 < log ν_s < 16.5 and high-energy-peaked (IBL) - 14.5 < log ν_s < 16.5, where ν_s stands for the peak of the low energy hump.

So far, only four non-blazar AGNs have been detected in VHE γ-rays: M87 (Aharonian et al. 2003), Centaurus A (Aharonian et al. 2009), NGC 1275 (Aleksić et al. 2012a), and 3C 264 (Rieger & Levinson 2018). These objects are known as radio-galaxies because of their high luminosity in the radio band. A huge amount of energy ($\sim 10^{60}$-10^{61} ergs) from these objects are transferred into the intergalactic medium (Kronberg et al. 2001). There are also two other radio-galaxies, namely, PKS 0625-35 (Dyrda et al. 2015) and IC 310 (Aleksić et al. 2010a) which are of unknown type (intermediate sources between BL Lac and FR I).

The simplest AGN unification scheme has been challenged by some of the recent works by Ghisellini & Tavecchio (2008); Ghisellini (2016); Foschini (2017). The updated AGN unification schemes based on theory and observations indicate that though the idea of accretion onto the SMBH is common to all AGN, the structure of the accretion flow changes depending on the bolometric luminosity (L_{bol}) and the Eddington luminosity (L_{Edd}), and their ratio defined as λ_{Edd}. The standard accretion disk (Shakura & Sunyaev 1973) is predicted to be replaced by an optically thin and radiatively inefficient one (Narayan & Yi 1994; Blandford & Begelman 1999). For different accretion rates ($\dot{M}$) of AGN with similar mass, a dichotomy can be seen based on the excitation mode into high-excitation (HERG) and low-excitation radio galaxies (LERG) based on the prominence of the spectral lines (Best & Heckman 2012). The HERGs occur in systems with radiatively efficient (luminous accretion disks) while the LERGs result from radiatively inefficient disks. Powerful radio sources associated with luminous accretion disks, generally activate more line emissions from the BLR, resulting in a higher excitation state. In the above scenario, the BL Lacs might correspond to FR I radio galaxies (Padovani & Urry 1990), while the FSRQs might correspond to FR II sources (Padovani & Urry 1992). Though the idea of the unification scheme, where BL Lacs and FR I are LERGs, and FSRQ and FR II are HERGs, has generally prevailed, a larger and deeper survey is needed to understand the classification in more detail. In order to confirm any blazar sequence, one needs to know the broad band SED, the mass of the black hole and the luminosity of the broad emission lines (Ghisellini 2016). This also requires the knowledge of the properties of high-energy Compton emission from these jets (Keenan et al. 2020) which will be possible in a large scale once the Cherenkov Telescope Array (CTA) is operational.

1.1.1 Production of radiation in Blazar Jets:

The origin of the double hump structure of the SED of blazars can be explained by leptonic and/or hadronic models. According to these models, the first hump is a result of synchrotron radiation of primary electrons accelerated to relativistic energies in the emission region. On the other hand, the production of the second hump changes, depending on the model that is being used to explain its origin. In the case of a hadronic model, if relativistic protons are present in the jet of a blazar and have energies above the interaction threshold, then the second hump is a result of interactions between accelerated protons & electron-positron pair cascades and synchrotron photons responsible for the low-energy hump (Mücke & Protheroe 2001; Mücke et al. 2003a; Boettcher

2010). However, under a leptonic scenario, the high-energy hump is a result of inverse Compton (IC) scattering of an internal and/or external photon field by primary electrons. If the internal photon field, which is the synchrotron radiation in the emission region, is involved in IC scattering, then the resultant emission is known as synchrotron self-Compton (SSC) (e.g., Bloom & Marscher 1996). On the other hand, if an external photon field is involved, then the corresponding emission is called external Compton (EC). The sources of this external photon field could be the photons from the accretion disk (Dermer et al. 1992; Dermer & Schlickeiser 1993a), or the broad line region (BLR) and/or the dusty torus (Ghisellini et al. 1998; Joshi et al. 2014; Sikora et al. 1994a).

In the following text, different physical processes that are responsible for non-thermal blazar emission are explained in detail:

Synchrotron radiation:

A moving non-relativistic charged particle inside a homogeneous magnetic field (B) produces synchrotron radiation and moves around the magnetic field lines in a helical path. The velocity of the moving charged particle has two components: parallel and perpendicular to the magnetic field. The Larmor frequency can be calculated as

$$\nu_L = \frac{1}{2\pi}\frac{eB}{m_e c} sin\phi \tag{1.1}$$

, where m_e and e are the mass and unit charge of the charged particle, B is the magnetic field strength, and ϕ is the angle between the orientation of the magnetic field and the velocity vector.

In presence of the magnetic field radiation due to the motion of the charged particle behaves like a dipole with radiation frequency of ν_L as seen from the rest frame of the moving charge (Weekes 2003). In the case of a relativistic charge particle, the output

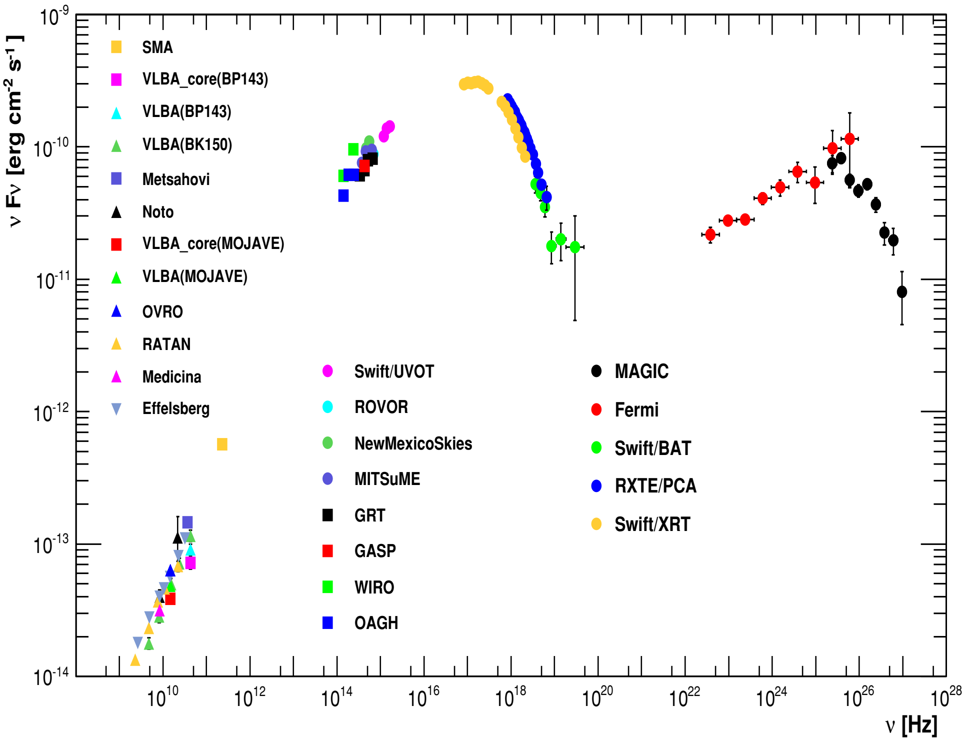

Figure 1.3: Spectral energy distribution of Mrk 421 averaged over all the observations taken during the multi-frequency campaign from 2009 January 19 (MJD 54850) to 2009 June 1 (MJD 54983). Credit: (Abdo et al. 2011a).

radiation is beamed into a cone (of angle $\theta \sim m_e c^2/E$) and forms a continuum spectrum instead of a single peak. The peak at which maximum power emitted (Weekes 2003) can be calculated as,

$$\nu_c = \frac{3}{4\pi}\frac{eB}{m_e c}\gamma^2 sin\phi \tag{1.2}$$

, where γ is the Lorentz factor of the charge particle moving at a relativistic speed.

Inverse Compton (IC) radiation:

The scattering of a static unbound electron by a photon is known as the Compton scattering. The process by which a high energy electron scatters a photon, is known as the inverse-Compton scattering (IC). The IC scattering can be thought of as the Compton scattering from the rest frame of the high energetic electron, where a stationary high energetic electron is colliding with a low energetic photon (Weekes 2003). The cross-section of IC scattering is known as the Klein-Nishina cross-section (Longair 2011).

$$\sigma_{KN} = \pi r_e^2 \frac{1}{\alpha}\Big[ln(2\alpha + 1)(1 - 2\frac{\alpha + 1}{\alpha^2}) + \frac{1}{2} + \frac{4}{\alpha} - \frac{1}{2(2\alpha + 1)^2}\Big] \tag{1.3}$$

$$\sigma_T = \frac{8}{3}\pi r_e^2 \tag{1.4}$$

$$\sigma_{KN} \sim \pi r_e^2 \frac{1}{\alpha}(ln2\alpha + \frac{1}{2}) \tag{1.5}$$

, where r_e is the classical electron radius, σ_T is the Thomson cross section, $\alpha = E_\gamma^{'}/m_e c^2 = \gamma E_\gamma\,(1 + (v/c)cos\theta)$; m_e, E'_γ, E_γ, and γ being the rest mass of an electron, energy of the photon in the rest frame of the energetic electron, energy of the photon in the observer's frame, and the Lorentz factor respectively.

Equation 1.3 reduces to the Thomson cross section (σ_T, Equation 1.4) when we choose the classical limit with $E'_\gamma << m_e c^2$. While for the ultra-relativistic case, $E'_\gamma >> m_e c^2$, Equation 1.3 can be approximated in the form of Equation 1.5. As a result of the IC process a photon gains significant energy as compared to the initial energy. For the ultra-relativistic case, $\gamma >> 1$, the boosted photon beams emerge in the direction parallel to the velocity of the electron. The maximum energy transfer happened in the head-on collision, where a photon is scattered off by the electron to its incoming direction (Longair 2011). In the Thompson regime, the maximum energy a photon can acquire is given by,

$$E^{max}_{\gamma,T} \sim 4\gamma^2 E^0_\gamma \tag{1.6}$$

, where E^0_γ, and $E^{max}_{\gamma,T}$ are the initial energy of the photon and the maximum energy of the photon after the scattering respectively. One can readily notice that in the Thomson regime, the change in the energy of the photon varies as γ^2 which can be appreciated as an effect of two successive Doppler boosts. On the other hand, in the Klein-Nishina regime, the change in the energy varies as γ, which is an indicative of the fact that the photon acquires the maximum energy in a single interaction (Krolik 1999).

Synchrotron self Compton (SSC):

Synchrotron self Compton model is the most adopted model used in order to explain the emission from the blazar jets. In this model an emission region inside the blazar jet is considered. Inside the emission region a population of relativistic electrons produce synchrotron radiation under the influence of the magnetic field. The synchrotron photons again gets up-scattered by the same population of electron that produced the synchrotron photons via IC scattering (Jones et al. 1974; Marscher & Gear 1985; Maraschi et al. 1992).

The most simple form of the SSC modeling considers the following assumptions:

1. A single spherical homogeneous emission region has been considered with a radius R.

2. For simplicity we consider only leptons (electrons and positrons) are present inside the emission region. Inside the emission region leptons are distributed isotropically.

3. The orientation of the magnetic field is fixed and the field is isotropic.

4. The electrons injected inside the emission region follow a simple power law of the form $N_e(\gamma) = N_0\gamma^{-q}$; $\gamma_{min} < \gamma < \gamma_{max}$, where N_0 is the normalization constant, q is the index, γ is the Lorentz factor, γ_{min} and γ_{max} are the minimum and maximum energy of the electrons.

5. The velocity of the emitting region is considered as $\beta = v/c$, where c is the speed of light.

The evolution of the emission from the emitting volume is associated with the following loss-terms:

1. Synchrotron energy loss with time-scale $\tau_{sync.}(\gamma)$,

2. Inverse Compton energy loss with time-scale $\tau_{IC}(\gamma)$, and

3. Loss due to escape of the charged particles (leptons) with time-scale τ_{esc} (Mastichiadis & Kirk 1997).

Considering the effects mentioned above the time-evolution of the charged particles can be summarized as:

$$\frac{\partial N_e(\gamma,t)}{\partial t} = N_e^{inj}(\gamma) - \frac{\partial}{\partial\gamma}\left[\left(\frac{d\gamma}{dt}\right)_{loss} N_e(\gamma,t)\right] - \frac{N_e(\gamma,t)}{\tau_{esc}} \tag{1.7}$$

, where the loss term $\left(\frac{d\gamma}{dt}\right)_{loss}$ includes the radiative losses. One of the specific

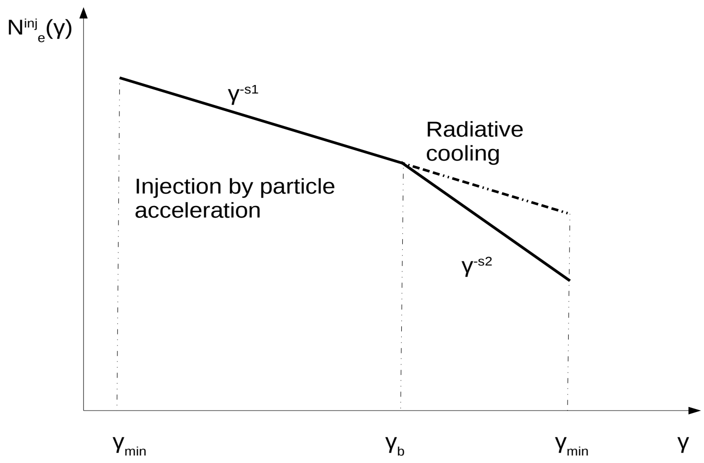

Figure 1.4: The electron injection scheme for an one zone synchrotron-self-Compton model. The injected electron spectrum, $N_e^{inj}(\gamma)$, between the maximum (minimum) energy of the electrons, denoted by γ_{min} (γ_{max}) has a break in the spectrum at energy γ_{br}, known as the break energy. The reason behind the change in the electron spectrum is due to the radiative cooling.

models has been described in details in Section 5 (equations 5.2 and 5.3). There are many variations of the model described above. One simple case is given below, where the electron spectrum is considered to follow a broken power law as mentioned in the following equation

$$N_e^{inj}(\gamma) = \begin{cases} N_0\gamma^{-s_1}, \gamma_{min} < \gamma < \gamma_b \\ N_0\gamma^{-s_2}; \gamma_b < \gamma < \gamma_{max} \end{cases} \tag{1.8}$$

, where γ_b, s_1, and s_2 are the break energy in the spectrum, the index before the break, and the index after the break respectively.

The output photon spectrum can be reproduced by using one or more breaks in the input electron spectrum (Aleksić et al. 2015c). Figure 1.4 shows one such example of a broken power law spectrum of the input electron spectrum.

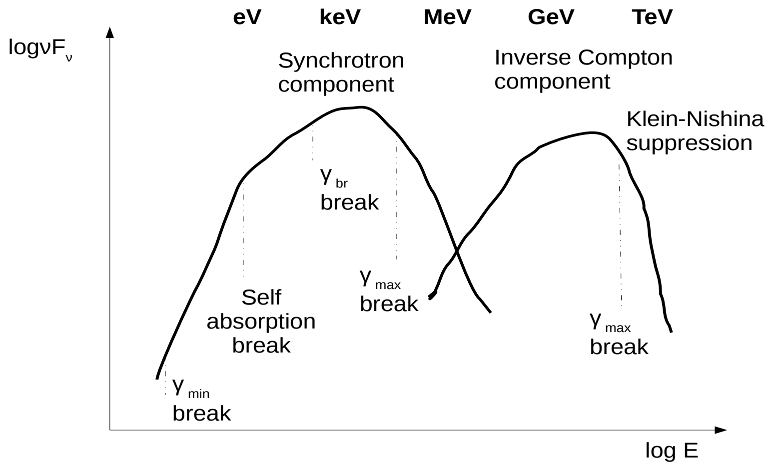

Figure 1.5: The MWL SED originating from the simulation considering an one zone spherical model with electron spectrum described in Fig. 1.4. The first bump is the result of synchrotron emission and the second bump is originated as a result of the synchrotron self Compton emission. The effect of γ_{min}, γ_{br}, and γ_{max} are pointed here. At the TeV energies the Klein-Nishina effect reduces the cross section significantly resulting in a sharp decrease in the photon spectrum.

Figure 1.5 shows the typical photon spectrum due to an electron injection following a broken power law as mentioned in Equation 1.8. In this figure, the low- and high-energy humps are due to synchrotron radiation of relativistic leptons and due to the IC scattering respectively. The effects of the breaks in the electron spectrum are also pointed in the resultant photon spectrum.

Different sources for input photon spectrum:

In the SSC scenario, the synchrotron radiation serves as the input photon spectrum which gives rise to the high energy photon spectrum. There are cases where the low energy photons external to the jet get up-scattered by the leptons. These soft photons originating from the disk and/or BLR may enter into the jet and produce the high energy photon spectrum. The radiation from the disk entering into the jet directly is called external Comptonization of direct disk radiation (Dermer & Schlickeiser 1993b, ECD). On the other hand when the radiation from the disk enters into the surrounding clouds in the BLR and gets reprocessed before entering into the jet is called external Comptonisation of radiation from the clouds (Sikora et al. 1994b; Blandford & Levinson 1995, ECC).

Hadronic models:

In the hadronic model scenario, the basic assumption is that inside the relativistic jet, hadrons (protons and heavy nuclei) are also accelerated along with the leptons (Mannheim 1993). A Doppler boosted proton can produce photons via decay of pions (π^0) and mesons (η), photo-pair production and the radiation due to synchrotron cascade. The direct synchrotron radiation of high energy protons can also be thought as the source of high energy photons. However, the efficiency of this process is relatively lower because of the high mass of protons. A proton in the energy range of $10^{11} - 10^{13}$ MeV interacting with the ambient near/mid-infrared radiation (emitted by the hot dust at a distance of 1-10 pc from the central engine), or/and the soft photons inside the jet (produced due to the synchrotron radiation of the leptons) gives rise to the photo-meson reaction as well as nuclear collisions as follows:

$$
\begin{aligned}
\eta &\rightarrow 2\gamma \\
\eta &\rightarrow 3\,\pi^0 \\
\pi^0 &\rightarrow 2\,\gamma \\
\pi^{\pm} &\rightarrow \mu^{\pm} + \nu_\mu(\overline{\nu}_\mu) \\
\mu^{\pm} &\rightarrow e^{\pm} + \nu_\mu(\overline{\nu}_\mu)
\end{aligned}
\tag{1.9}
$$

These above-mentioned processes explain the production of MeV-TeV photons from a blazar jet in the proton-induced cascade model (Mannheim 1993). The strong interactions have many channels. The charged ($\pi^{\pm}$) and neutral (π^0) pions are produced maximally as the product of the hadronic interactions in which π^0 decays further into photons. The charged pions produce muons (μ) and neutrinos (ν). Recently the discovery of the neutrino event detected by IceCube neutrino observatory associated with a flaring blazar TXS 0506+056 observed by Fermi-LAT and MAGIC in the GeV-TeV energies (Aartsen et al. 2018) has made the hadronic models more attractive over the leptonic ones. This historical discovery has also kick-started a new era of multi-messenger astronomy.

1.2 Acceleration of particles inside the jet:

The detection of non thermal emission from blazar-like objects is mostly interpreted through the acceleration of particles through magnetised plasma. The charged particles are accelerated via the interactions with the ionized plasma. The bulk motion of the plasma serves as the source of the energy of the charged particles via the interaction between the charged particles and the magnetic wave. According to these processes (Fermi 1949) the particles with velocity v are repeatedly reflected by the magnetic structures moving with velocity u inside the plasma. Thus the change in energy of the charged particle due to the magnetic scattering (Rieger et al. 2007) can be calculated as:

$$\Delta E = E_2 - E_1 = 2\Gamma^2\left(\frac{E_1 u^2}{c^2} - p_1 u\right) \tag{1.10}$$

, where $\Gamma = (1 - u^2/c^2)^{-1/2}$ is the Lorentz factor of the magnetic turbulence, $p_1 = E_1 v/c^2$ is the initial momentum of the charged particle with energy E_1 , and E_2 is the final energy of the particle after the scattering. In Fermi acceleration, collisions between the charged particles are not considered (Fermi 1949; Gaisser 1991).

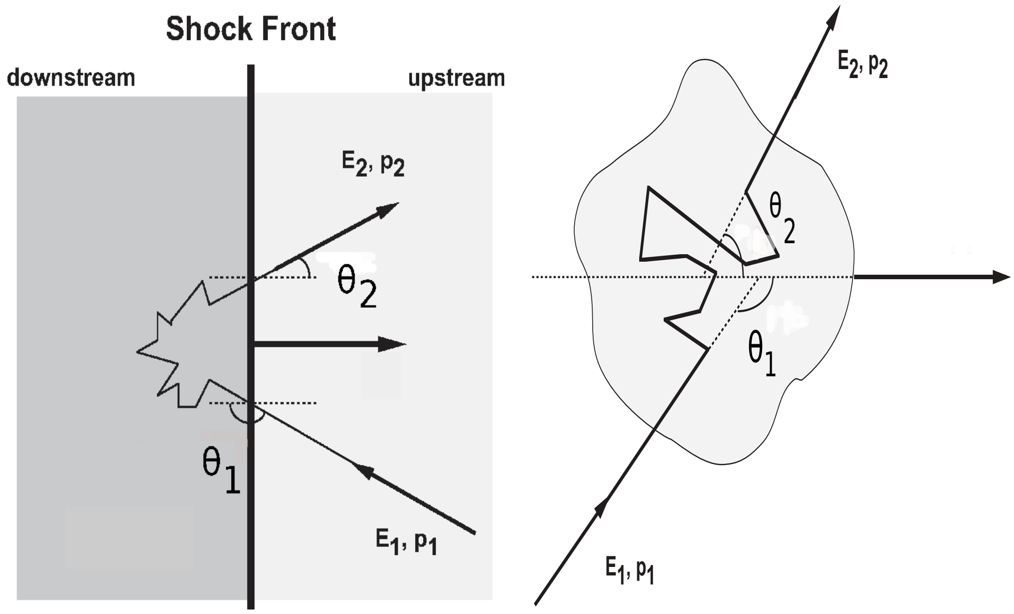

Figure 1.6: Schematic view of the first and second order Fermi acceleration shown in the left and right panel of the figure respectively. Adapted from Kataoka (1999).

Depending on the source of the magnetic scatterer two different types of acceleration processes are considered. Figure 1.6 shows schematics of the two Fermi acceleration mechanisms which are described below. In the first order Fermi acceleration the charged particles are accelerated in the astrophysical shock waves. In the second order Fermi acceleration, the magnetic molecular clouds serve as the scatterers. These two types of the acceleration processes are described in details below along with the shear acceleration, where the acceleration results from the shear flows in the magnetic structures.

1.2.1 First order Fermi acceleration (Shock acceleration):

The acceleration of particles resulting from a non-relativistic shock (Webb 1987, or relativistic shocks) front while passing through a relativistic plasma ($v \sim c$) is termed as the shock acceleration. One of the possible origins of the shock front is the internal shocks, where two shells of plasma moving with different velocities collide with each other, a shock is produced. The velocity of the charged particles ahead of the shock front (u_u), the upstream velocity is higher than the same behind the shock front known as the downstream velocity (u_d). As seen from the upstream (/downstream) plasma, the downstream (/upstream) plasma approaches with a velocity of $u = |u_u - u_d|$. Thus these two regions can be thought as two converging flows where once a particle crosses the shock front independent of the region (upstream or downstream) gains energy which takes the form,

$$\frac{\langle \Delta E \rangle}{E_1} \propto \left(\frac{u}{c}\right) \tag{1.11}$$

Since the gain in energy is in first order of u/c, the acceleration due to this process is known as the first order Fermi acceleration (Rieger et al. 2007). As the particles cross the shock front several times the directions of their momentum get randomized giving rise to an isotropic distribution of the momentum vector. The charged particles escape from the acceleration region following a stochastic process. This results in a particle spectrum of the form

$$N(E) \propto E^{-s} \tag{1.12}$$

, where $s = (\rho + 2)/(\rho - 1)$ is the index and $\rho = u_u/u_d$ is the shock compression ratio. Usually for strong shocks this can be close to 2 (Drury 1983). Several non-linear effects such as strong shock modifications can result in an index lower than 2 (Berezhko & Ellison 1999). In case of a non-uniform magnetic field with non-static field lines, an index between 2.0 to 2.5 can be produced (Kirk et al. 1996).

1.2.2 Second order Fermi acceleration:

A charged particle experiences a head-on collision while crossing the shock front in case of a strong shock which essentially leads to a first order Fermi acceleration. However, in the second order Fermi acceleration, the absence of the shock front gives rise to following or overtaking scatterings as well as head-on scattering inside the magnetised molecular cloud. As the charged particles undergo multiple scattering inside the magnetised plasma, they gain and lose energy via these stochastic processes. The resultant gain in the energy averaged over all the possible momentum directions during the escape turns out to be second order (Fermi 1949) in the initial velocity of the particles (u)

$$\frac{\langle \Delta E \rangle}{E_1} \propto \left(\frac{u}{c}\right)^2 \tag{1.13}$$

The resultant particle spectra for second order Fermi acceleration follows a power law of the form $N(E) \propto E^{-s}$ where the index s comes out to be ≤ 2 (Virtanen & Vainio 2005). The overall energy gain of this process is lower as compared to the first order acceleration.

1.2.3 Shear acceleration:

The regions inside the magnetic structures with gradual shear flow are believed to produce shear acceleration. Charged particles crossing this region with regional velocity u_z in the direction of shear flow experience multiple scattering inside the plasma. The average energy gain per crossing can be calculated as,

$$\frac{\langle \Delta E \rangle}{E_1} \propto \left(\frac{\partial u}{\partial x}\right)^2 \tau^2 = \left(\frac{\tilde{u}}{c}\right)^2 \tag{1.14}$$

, where $\tilde{u}$ and τ are the characteristic relative velocity and mean scattering time of the scattering centres respectively (Jokipii & Morfill 1990; Rieger & Duffy 2004a). The transfer in the shear acceleration is also second order in $\tilde{u}/c$. The mean free path for the protons are much larger than the electrons with the same energy. This is why the shear acceleration is mostly favoured in case of the acceleration of protons (Rieger & Duffy 2004a). The particle spectrum resulting from this type of acceleration follows a power law $N(E) \propto E^{-s}$ where the index s is typically > 1 (Berezhko & Krymskii 1981).

1.2.4 Observational constraints

First order Fermi acceleration mechanism is sufficiently effective to produce this type of a particle spectrum. This is also supported by several observational evidences where strong shock forming regions can be easily identified in the observed AGN jets. An additional feature of the first order Fermi acceleration is that it can explain the fast variability (Kirk et al. 1998). However, some features such as smooth variation of the photon spectrum from radio to UV energies along the entire jet is a direct contradiction to the result of the first order Fermi acceleration (Mikhailova et al. 2010; Stawarz 2004; Jester et al. 2001, 2005). This requires a continuous re-acceleration of the charged particles along the entire jet. This situation is suggestive of the fact that in addition to the first order Fermi acceleration, the second order Fermi and shear acceleration are needed to produce the particle spectrum which in turn will give rise to the observed photon spectrum (Rieger et al. 2007).

1.3 VHE gamma-ray astronomy:

The section of astronomy that deals with phenomena beyond 100 GeV is termed as the VHE gamma-ray astronomy. Gamma radiation is considered to be the most energetic form of electro-magnetic radiation seen in the vast class of celestial objects. One way to produce very high energy γ-radiation is via IC scattering as discussed in the previous sections. In the following sections, we note down a few classes of celestial objects and the VHE γ-ray detection technique by the ground-based detectors via imaging atmospheric Cherenkov technique (IACT).

1.3.1 Astrophysical sources of VHE gamma-rays:

The VHE γ-ray sources can be categorized into two main parts: the galactic sources and the extragalactic sources based on their location inside the Milky Way galaxy and beyond respectively. Figure 1.7 shows the distribution of point sources and extended sources in the VHE γ-ray sky. In this section, we will describe these sources.

Pulsars:

A Pulsar is associated with a high magnetic field and hosts a fast rotating neutron star. In the magnetosphere of this compact object (neutron star) charged particles are accelerated to relativistic energies. A pulsar usually serves as the powerhouse for the pulsar-wind nebula (PWN) by injecting relativistic charged particles inside Nebula around them (Gaensler & Slane 2006). So far there are only three pulsars detected in the VHE γ-rays: Crab (Aliu et al. 2008), Vela (H. E. S. S. Collaboration et al. 2018) and Geminga (MAGIC Collaboration et al. 2020b).

Pulsar wind nebula:

The special type of supernova remnants with pulsars at the centre are termed as the

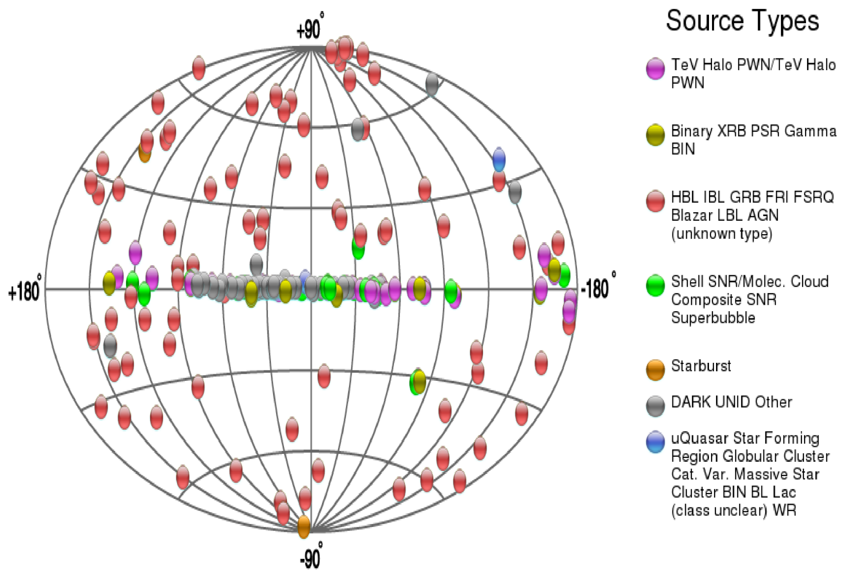

Figure 1.7: Position of the known VHE γ-ray sources. Figure taken from http://tevcat.uchicago.edu/.

pulsar wind nebula (PWNs). The PWNs are powered by the high energy radiation from the pulsars at the centre (Gaensler & Slane 2006). The most important PWN in case of the ground based VHE $\gamma-$ray astronomy is the Crab Nebula mainly because of the bright steady emission in this energy range ($Flux_{>200GeV}$ = 2.039 $\times$ 10^{-10} ph cm^{-2} s^{-1}, Aleksić et al. (2016b)). Hence, Crab Nebula is considered as the standard candle for the ground based $\gamma-$ray astronomy and usually the flux is used as the unit of the flux for most of the bright sources observed in this energy band.

Supernova remnants (SNR): At the end of the lifetime of a massive star, a supernova is formed. Depending on the mass of the stars, this might result in formation of a Neutron Star (NS) or a Black Hole (BH), surrounded by a gas nebula. In a SNR (e.g. RX J1713.7-3946, Abdalla et al. 2018), non-thermal processes are responsible for accelerating particles up to VHE gamma-rays. In SNRs, particle acceleration proceeds on the parsec distance scale in the shock formed in the interaction of the SN ejecta with the Inter Stellar Medium (ISM). Both leptonic and hadronic models successfully explain the VHE radiation from SNRs.

Gamma-ray bursts (GRB) The gamma-ray bursts are one of the most energetic phenomena in the universe. Depending on the time-scale of the bursts there exist two types GRBs- short (typical time-scale $\sim$ 2 secs) and long GRBs (time-scale longer than 2 seconds).

The long GRBs are considered to be originated from the core collapse events (Paczyński 1998), whereas the short GRBs are resulted from the merging of compact objects like black-holes or neutron-stars (Fox et al. 2005; Piro 2005). The space borne telescopes Fermi-LAT[1] and Swift-BAT [2] have been very successful in detecting countless GRBs and are still registering GRB events successfully. Very recently, the Indian satellite telescope CZTI on board Astro-SAT [3] has joined this league.

Active-galactic Nuclei (AGN): A very small fraction of the total population of the AGNs (nearly 10 %) possesses relativistic jets. The charged particles are accelerated to relativistic energies inside the jet and gamma-rays can be radiated by IC or EC scattering. The flux in case of the blazars can reach up to several C.U. (Crab units, standard Crab flux) (Acciari et al. 2020; Aharonian et al. 2007). This type of objects can show rapid flux variability over time-scales which may vary from few minutes to few days. Considering the high energy photon-production in this objects blazar spectrum have been used vastly to constrain the extragalactic background light (EBL; Acciari et al. 2019; Abdalla et al. 2017; Abeysekara et al. 2019). The first ever AGN that was established as the TeV emitter is the blazar Mrk 421, discovered by the Whipple telescope (Punch et al. 1992).

[1] https://fermi.gsfc.nasa.gov/
[2] https://swift.gsfc.nasa.gov/
[3] http://astrosat.iucaa.in/czti/?q=home

1.3.2 Detection techniques of the VHE gamma-ray sources:

The detection technique of the incoming VHE $\gamma-$rays can be divided into two branches: a) direct and b) indirect detection based on the detection of the primary $\gamma-$ radiation from the celestial objects mentioned above. Due to the fact that the Earth's atmosphere is not transparent to the high energetic photons, direct ground-based detection is not possible. The direct detection can only be carried out with the space-borne instruments. However, the biggest challenge for the space-based detectors is that the size of the detectors can not be made large (larger effective area) due to the huge cost associated with the heavy pay-load in the mission. The indirect detection of $\gamma-$radiation from the celestial objects are carried out by the ground based telescopes. In this case the Earth's atmosphere is considered as a huge calorimeter of 40 radiation lengths of material where the primary $\gamma-$ray interacts and produces a huge number of secondary particles. The detection of the secondary particle reveals the energetics and directionality of the primary $\gamma-$ray. The high energetic secondary charged particles, such as electron muons and hadrons, while moving through the atmosphere produces visible light via Cherenkov radiation. This visible light is recorded and processed to extract the information regarding the incident photon. There are several techniques developed in last 50 years in order to detect the $\gamma-$rays from celestial bodies with ground based-observatories, to name a few:

1. Via direct detection of secondary charged particles. Examples: Tibet AS-gamma Experiment[4], ARGO-YBJ[5], HEGRA[6], GRAPES[7].

2. Via indirect detection through:

[4] http://www.icrr.u-tokyo.ac.jp/em/index.html
[5] http://argo.na.infn.it/
[6] http://www.mpi-hd.mpg.de/hfm/CT/CT.html
[7] https://grapes-3.tifr.res.in/

a) Detecting Cherenkov photons produced in water: MILAGRO [8], HAWC[9].

b) Detecting Cherenkov photons produced in the atmosphere: MAGIC[10], VERITAS[11], H.E.S.S.[12], HEGRA, Whipple[13], HAGAR[14], and TACTIC[15].

1.3.3 Ground-based detection technique of an Extensive air shower (EAS):

Typically a high energy cosmic ray starts producing a bunch of secondary particles as soon as it enters into the Earth's atmosphere. This complete process of generating a shower of secondary charged particles is termed as extensive air-shower (EAS). At the height of $\sim$ 20 km, cosmic rays initiate interactions with the atmosphere and produce EAS. The incident cosmic ray can produce electrons (/positrons), $\gamma-$rays or hadrons. Depending on the nature of the primary cosmic ray particle, different kinds of secondary particles are produced. The secondary particles grow in number as they produce more particles via the interaction with the atmosphere as they propagate into the atmosphere in both of the transverse and forward (towards the ground) direction. The production of the EAS can be described by the Bhabha-Heitler model (Gaisser 1991) which is a toy model only applicable for the electro-magnetic (EM) showers. According to this model, the number of particles goes as $2^{n'}$, where n' is the number of interactions (/generations). The secondary particles produced in the shower emit Cherenkov light when the energy

[8] Smith (2005)
[9] https://www.hawc-observatory.org/
[10] http://wwwmagic.mppmu.mpg.de/
[11] http://veritas.sao.arizona.edu/
[12] http://www.mpi-hd.mpg.de/hfm/HESS/
[13] https://veritas.sao.arizona.edu/whipple-10m-topmenu-117
[14] https://www.tifr.res.in/~hagar/
[15] http://www.barc.gov.in/pg/nrl-harl/tactic.html

is higher than the energy threshold required for the Cherenkov radiation (typically 83 MeV at the sea level for an electron or positron). The speed of the secondary particles propagating through the air-medium can be considered as c/n, where c is the speed of light and n is the refractive index of the medium. The secondary particles lose their energy via ionization loss and bremsstrahlung. When the loss due to the ionization is larger than bremsstrahlung, the shower dies away and the secondary particles get absorbed by the atmosphere. An EM shower induced by a VHE photon has a more regular spread (characteristic scattering angle $\sim 5°$; Aharonian et al. (2008b)) as the secondary particles propagate through the atmosphere as compared to a hadron induced shower. In case of an electro-magnetic shower, pair production and bremsstrahlung play crucial roles while the lateral spread of the shower is mostly determined by the multiple Coulomb-scattering of the secondary electrons and positrons.

Figure 1.8 and 1.9 show the profiles of both the gamma and hadron induced showers and their projection on the ground.

The production of secondary particles (see Figure 1.8) in case of the hardon-induced shower (hadronic-shower) depends on the initial interaction of the hardon and the atmosphere. Since the strong interactions have many channels, the number of particles produced in this process is much larger than the EM shower. As shown in Eq. 1.15, the charged ($\pi^{\pm}$) and neutral (π^{0}) pions are produced maximally as the product of the hadronic shower in which π^{0} decays further into photons. These photons also induce electro-magnetic showers. This way, roughly $1/3$ energy contained into the initial hadron is given as a form of an electro-magnetic shower through π^{0}. The charged pions produce muons (μ; lifetime $\sim$ 2.2 micro-sec) which can travel directly to the detector as

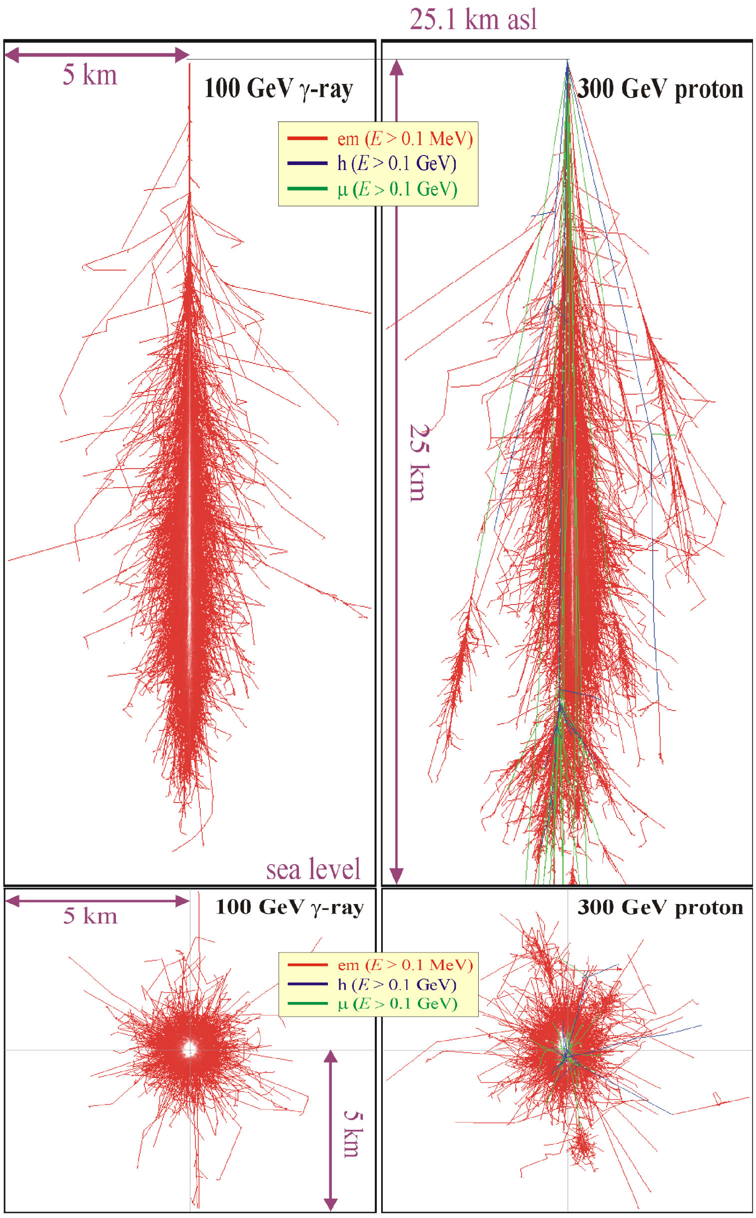

Figure 1.8: The projection of a Monte Carlo simulated 100 GeV γ ray on the left and 300 GeV proton shower on the right. The top (bottom) panel shows the vertical (horizontal) projection of the shower with an incident angle of 0° and the first interaction occurs at 25 km a.s.l. Different color tracks show different electromagnetic components: electrons, positrons and secondary γ-rays are shown in red, muons are green, and hadrons are blue. Lighter colour represents higher density of tracks. For that reason centres of showers are white. We only plot the tracks of particles above the cuts mentioned in the box. Adapted from Hrupec (2008).

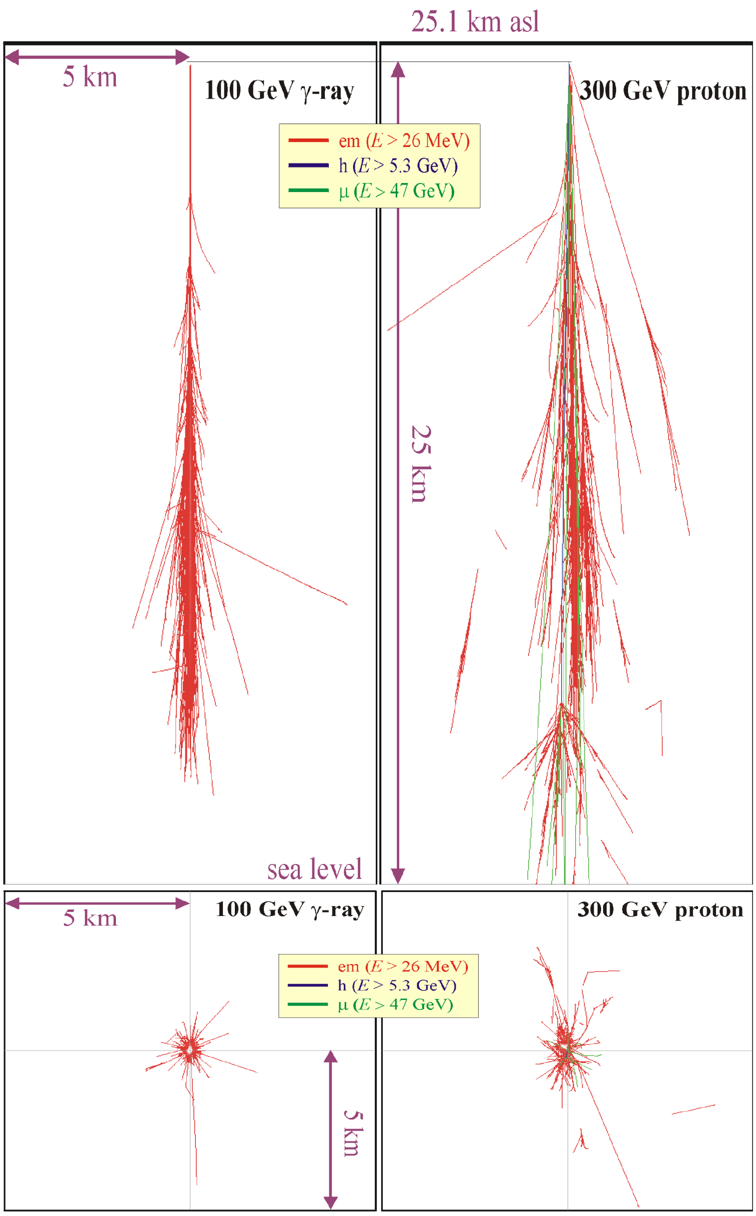

Figure 1.9: The projection of a Monte Carlo simulated 100 GeV γ-ray on the left and 300 GeV proton shower on the right with a higher energy threshold of the particles produced. Adapted from Hrupec (2008).

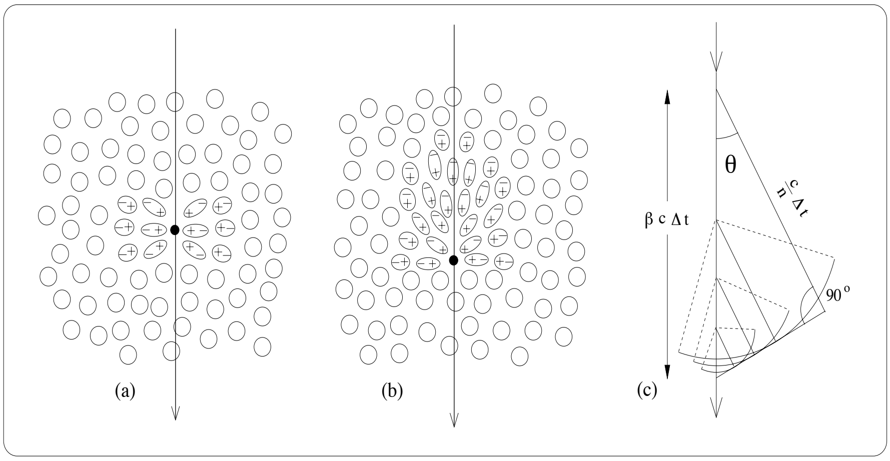

Figure 1.10: Polarization in dielectric medium produced by a charged particle with a slower moving particle shown in (a) and a faster moving particle shown in (b). The right most panel shows the construction of the Cherenkov light wave-front. Adapted from Tescaro (2010).

the energy losses for muons are less compared to the other secondary products.

$$\pi^0 \rightarrow \gamma + \gamma \quad \& \quad \pi^{\pm} \rightarrow \mu^{\pm} + \nu_{\mu}(\bar{\nu}_{\mu}) \tag{1.15}$$

The images produced by muons are primarily treated as backgrounds but also help to estimate the absolute light calibration or energy calibration (Gaug et al. 2019). Below we discuss the three most important processes that govern the development of EAS.

The Cherenkov radiation:

The radiation given away by relativistic charged particles travelling through a transparent dielectric medium with a speed greater than the speed of light in that medium is termed as the Cherenkov radiation. It was first discovered by P. A. Cherenkov in 1934 while the theoretical understanding of this effect was proposed in 1937 by Frank and Tamm. As the charged particle travels, it partially polarizes the surrounding medium. The reorientation of the dipoles as the particle passes through gives away photons in the form of Cherenkov radiation. Figure 1.10 shows the production of Cherenkov radiation by a charged particle. The Cherenkov light produced at different points of the trajectory can be summed by applying Huygen's principle as shown in this figure. The angle at which the Cherenkov radiation is produced can be written as

$$cos\theta(h) = \frac{1}{\beta n(h)} \quad \rightarrow \quad \theta(h) = cos^{-1}\left(\frac{1}{\beta n(h)}\right) \tag{1.16}$$

, where $\theta(h)$ is the angle sustained by the direction of the photon emitted via Cherenkov radiation and the direction of the velocity (β=v/c) of the charged particle, $n(h)$ is the refractive index of the medium which varies as the position of the charged particle (h) from the surface of the Earth. Thus the minimum speed of the charged particle required for the production of the Cherenkov light can be calculated from Equation 1.16 as, β_{min}=$1/n$. The energy threshold E_{th} is given by,

$$E_{th} = \frac{m_0 c^2}{\sqrt{1 - \beta_{min}^2}} = \frac{m_0 c^2}{\sqrt{1 - n^{-2}}} \tag{1.17}$$

, where m_0 is the rest mass of the charged particle. The number of Cherenkov photons produced (Yao et al. 2006) by a charged particle of charge Ze per wavelength (λ) per unit path-length (x) is given by,

$$\frac{d^2N}{dx\, d\lambda} = \frac{2\pi\alpha Z^2}{\lambda^2}\left(1 - \frac{1}{\beta^2 n^2}\right) \tag{1.18}$$

, where α (= 7.297×10^{-3}) is the fine structure constant. However, primarily due to absorption in the atmosphere, the spectrum of the Cherenkov radiation produced by the charged particles, given in Equation 1.18, becomes different from the one observed at the ground level. Figure 1.11 shows a comparison between the original and the ob-

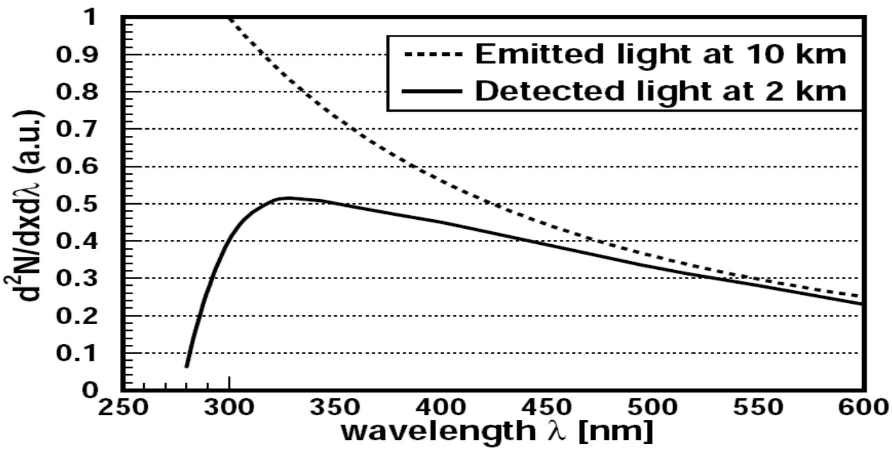

Figure 1.11: The spectrum of the Cherenkov light at shower maximum shown in dashed curve and the spectrum at 2 km altitude shown in solid line. Adapted from Tescaro (2010).

served Cherenkov radiation. The original radiation follows ($1/\lambda^2$), whereas the observed spectrum has a prominent peak at around 330 nm. This is mainly because of several attenuation effects, such as Rayleigh scattering, Mie scattering, and the absorption in the Ozone-layer.

Light pool:

The density of photons produced due to Cherenkov emission on the ground by the EAS is known as the light-pool (see Figure 1.12). This depends mainly on the type and energy of the particle that produces the EAS. The lateral extent of the shower or the propagation angles with respect to the shower axis depend on the multiple Coulomb-scattering off the secondary charged particles ($\sim 5°$, Aharonian et al. (2008a)), the Cherenkov emitting angle ($\sim 0.7°$ in air) and also on the scattering due to the dust particles present in the atmosphere. However, the Cherenkov emitting angle changes as the shower develops at different altitudes. This is mainly because at different altitudes the refractive index changes (for a recent review see Aharonian et al. 2008a). In case of the gamma-

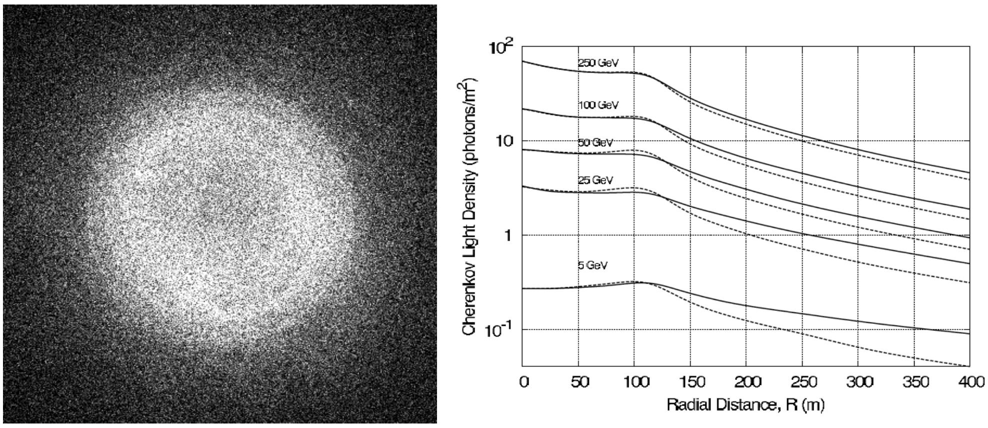

Figure 1.12: The light pool produced by a γ-induced air shower at the ground level. The density profile of the shower stays flat up to $\sim$120 m from the core region. The light pool drops afterwards which separates the core from the halo region. The left panel shows the Cherenkov photons produced by a γ-ray of 300 GeV on the ground. The right panels shows simulations of the Cherenkov light as a function of the impact distances (Aharonian et al. 2008a). The solid and dashed lines differentiate showers developing along to the earth magnetic field or 90° perpendicular to it. Adapted from Tescaro (2010).

ray induced showers, the light-pool is roughly constant up to 120m at the ground (area $\sim$ 40,000 m^2) and decreases thereafter. As the Cherenkov and the Coulomb angles are large, any sub-sample of the light-pool can be considered as a light-pool resulting from an isotropically emitted electromagnetic shower. This sub-sample of the light-pool collected by the IACTs is used to extract the information regarding the shower development. It is worth mentioning that as the energy of the primary gamma-ray increases the area projected on the ground does not become larger but the intensity of the light-pool is the quantity that increases.

1.4 The Imaging Air Cherenkov Technique (IACT):

Ground based gamma-ray astronomy via the detection of Cherenkov light is the most efficient way to detect the gamma-ray emission above 100 GeV. This technique is based on detecting the visible Cherenkov photons emitted from the interactions of the cosmic rays and VHE gamma-rays with the atmosphere via Cherenkov interactions as described above.

A Cherenkov telescope collects all the Cherenkov photons emitted by the charged cosmic rays and the gamma-ray showers by a mirror and focusing that light on to an array of light-sensors. The cluster of light-sensors, photo-multiplier tubes, are known as pixels. After the reflection on the mirror, the Cherenkov photons are focused on the pixels, where the development of the shower images are recorded pixel by pixel. Since the shower maxima of the Cherenkov emission is at around 10 km above sea level (a.s.l.), the focus of the telescope is set at 10 km unlike at infinity as used in the optical telescopes. The basic technique is to image the Cherenkov shower by registering the Cherenkov photons produced in this process in different pixels in the camera after they reflect from the mirror. The collection of the Cherenkov photons by the camera pixels mainly depends on the angle between the shower axis and the direction at which the telescope is pointed. During the process of registering a shower event the development of the shower at different altitudes is registered by the pixels of the camera. The total number of particles at different altitudes are thus related to the density of the Cherenkov photons at the ground. Once the event is registered by the camera several information of the shower event can be traced back by using **Hillas parametrization** (Hillas 1985) such as the energy, the incoming direction of the primary particle, etc. A detailed description regarding the image parametrization is given in section §1.4.1. The primary difference between the showers originating form a charged particle and a gamma-rays is in the shape of the showers on the camera plane. Since a proton (/charged particle) induced shower comprises of different hadronic interactions while entering into the atmosphere, they produce variety of particles which again induce secondary showers from π° and μ's generating from the charged π's can produce several different shapes of the shower images (Aharonian et al. 2008b). On the other hand, a shower image produced by a VHE gamma-ray is more compact than a hadron induced shower and elliptic in shape whose major axis points to the shower axis projected onto the image plane.

There are two different ways to construct a reflector plane: a) spherical, used in H.E.S.S. and b) parabolic, used in MAGIC. For larger reflector size, the difference between the arrival times of the light reflected by the different segments of the mirror become very important. Parabolic reflectors are used in MAGIC because they are isochronous. However, the parabolic shape of the telescope experiences more optical aberrations which in turn limits the field of view of the telescope. In MAGIC, several pieces of small spherical mirrors are placed together which effectively forms a giant parabolic mirror. This also requires different alignment and curvature of each mirror depending on the distance from the centre of the camera.

1.4.1 Image formation:

The main aim of a Cherenkov telescope is to trace back the information related to a VHE $\gamma-$ray by registering the shower events as the form of an image with the camera. The details of the image formation will be discussed in this section. As the showers from the charged particles or from the gamma-rays develop in the atmosphere the resulting Cherenkov photons are first reflected by the parabolic reflector (we will mainly focus on the parabolic reflectors as we use this type of reflector in MAGIC telescope system) and

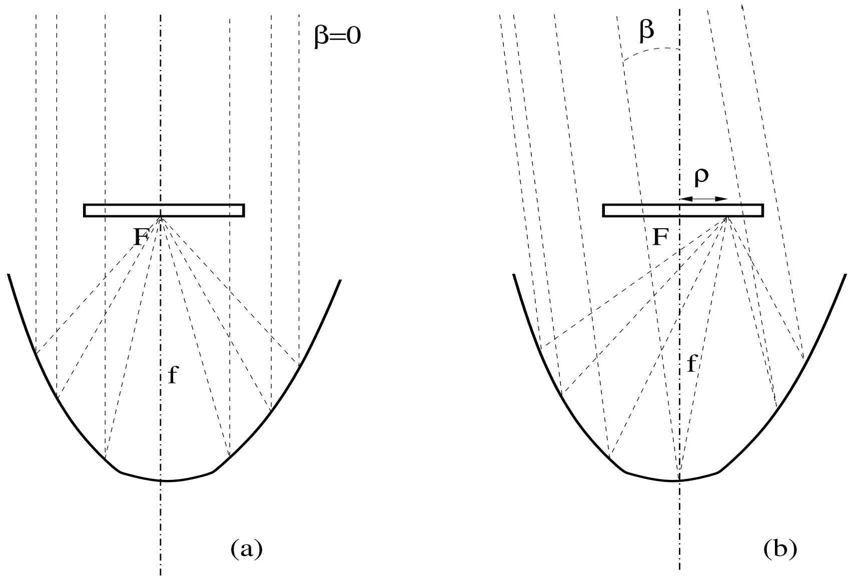

Figure 1.13: Projection of a photon beam parallel to the parabola axis of the mirror shown in panel (a), and with slightly inclined angle with respect to the axis of the mirror shown in panel (b). Adapted from Tescaro (2010).

then form an image at the focal plane where an array of PMTs, called the cameras, are kept.

Figure 1.13 shows the image formation at the camera plane by the parallel (or near parallel) Cherenkov light originating from an air-shower. The left panel of Figure 1.13 shows the formation of an image due to the parallel-rays with the telescope axis which forms an image just at the centre of the camera. However, the image formed by a parallel Cherenkov light with a certain angle θ produces an image further away from the camera centre. If we assume the coordinate of the centre of the image formed in the former case at the focal plane of the camera is (ρ, ϕ), then the incoming photon direction in the sky plane (θ, Φ) are related to the camera coordinate as:

$$\rho = sin\theta f \sim \theta f \quad \text{and} \quad \phi = \Phi, \tag{1.19}$$

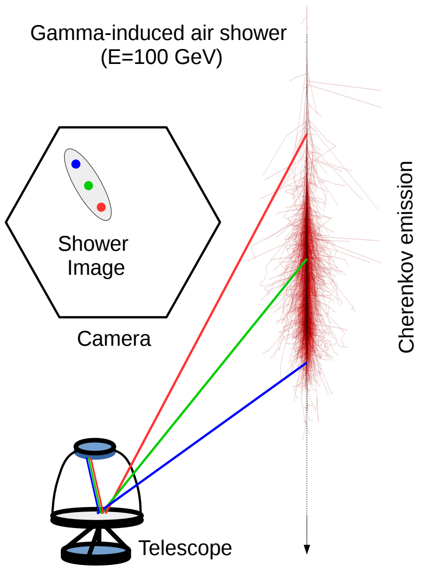

Figure 1.14: The air-shower projection scheme along with the camera of an IACT telescope. The Cherenkov light is emitted under the altitude-dependent emission angle. The image of the shower takes an elliptical shape in the camera plane. The light from the top part of the shower is projected to the head of the image (close to the camera center), while the light from the tail (close to the ground) of the shower is projected away from the center of the camera. The light from the middle of the shower is shifted towards the head of the shower (close to the camera-center). Adapted from Steinke (2012).

where f is the focal length of the telescope. The approximation $sin\theta \sim \theta$ is justified because the field of view of MAGIC telescopes is narrow, $\sim 3.5\,^{\circ}$. Thus the above equation shows that in the camera plane, the distance of the image from the focal point (ρ) varies linearly with the incident angle (θ). In addition, the shower development can be traced with the images formed in the focal plane of the camera. The illuminated pixels carry information regarding the development of the shower at different altitudes. Figure 1.14 shows the formation of an image for a single shower event. Cherenkov photons from the high altitude shower are captured by the pixels close to the centre of the camera whereas the Cherenkov photons produced at the lower altitude contribute to the parts of the image which are further away from the camera centre. The image formed at the camera plane thus takes the shape of an ellipse, where the length of the minor axis represents the lateral distribution of the air-shower. This is an important parameter which distinguishes between the hadronic and the gamma-ray induced showers as the hadron induced showers are much more distributed than the gamma-induced ones. The overall intensity of the image is directly proportional to the energy of the primary particle.

Figure 1.15 shows the schematic diagram of a gamma-ray shower in stereoscopic mode with two IACTs. The technique is based on the observation of the same shower with both of the telescopes where the event is registered by each of them as shown in Figure 1.15. The stereoscopic observation provides a better estimate of the inclination of the shower as compared to the mono-mode. With the stereoscopic observation an angular resolution of $\sim 0.1^\circ$ can be achieved. In addition, simultaneous observation with both the telescopes is very efficient to reject the hadron-induced showers and retain the gamma-induced shower by using the coincidence trigger between the two telescopes. The sensitivity of the telescope system can be improved significantly due to the precise determination of the shower maxima and the core position of the shower which in turn improves the angular resolution of the system. A detailed description of the image parametrization and analysis will be discussed in the later chapters where we present the extensive description of the MAGIC telescope system.

This thesis is structured in the following way: in the second chapter we discuss the working principles of the MAGIC telescopes. The third chapter describes the application and tests performed in order to lower the energy threshold of the MAGIC telescopes. The fourth chapter describes the analysis, results and the physics interpretation of the low flux state of Mrk 421 during 2015-2016. The fifth chapter describes the interpretation of the high flux state of Mrk 421 during the violent outburst in 2010. The last chapter summarizes the works presented in this thesis.

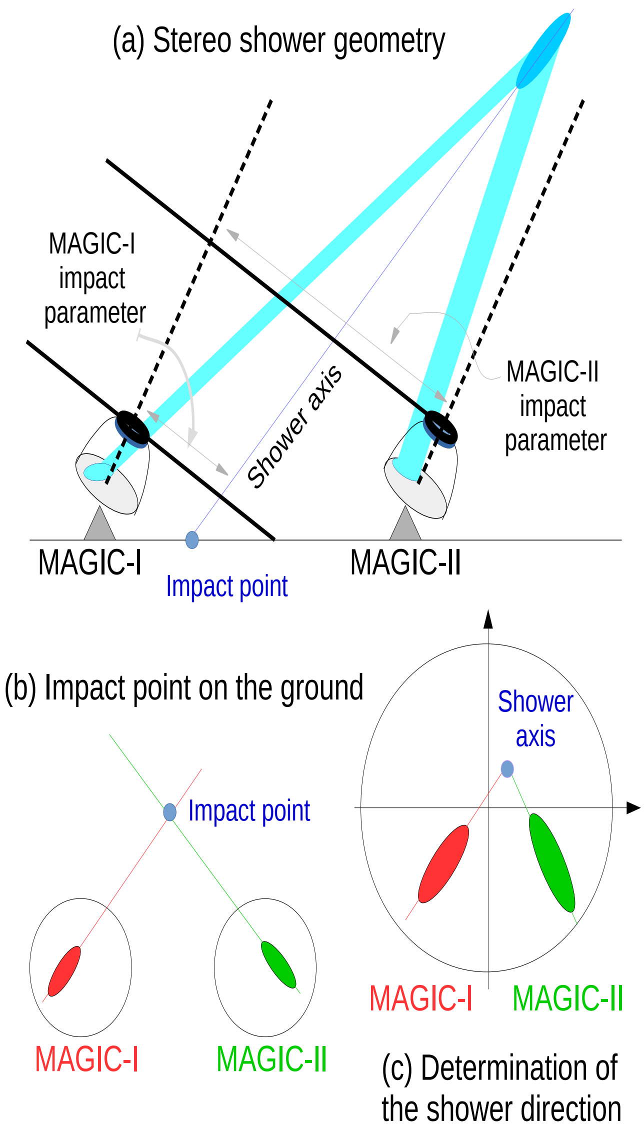

Figure 1.15: Stereo Observation scheme. Adapted from Coto (2015).

2

The MAGIC telescope system:

The MAGIC (Major Atmospheric Gamma Imaging Cherenkov) telescopes also known as Florian Goebel telescopes located at the Observatorio del Roque de los Muchachos (28° $45'$ north, 18° $54'$ west) in the Canary Island of La Palma, Spain above 2.2 km above the sea level (a.s.l.) is one of the most sensitive VHE γ-ray telescopes operational in the energy range between $\sim$ 60 GeV to several tens of TeV. Though the telescope-system usually operates in the stereoscopic mode, both the telescopes can operate in the mono mode.

2.1 Hardware

In this section, we describe the primary hardware components of the MAGIC telescope system (Aleksić et al. 2016a).

Figure 2.1: MAGIC telescopes at the Observatorio del Roque de los Muchachos. MAGIC Counting house (CH), MAGIC-I, MAGIC-II are visible in the figure. Image credit: http://wiki.magic.pic.es/index.php/Outreach_and_MWL

Figure 2.2: Side view of MAGIC-I and MAGIC-II. The carbon fibre reinforced plastic tubes are visible in white. The gray steel structures in the lower parts are also visible.

2.1.1 Construction and drive

The MAGIC reflector dishes measure 17 m in diameter and were the largest IACT operational until 2012 [1]. The MAGIC telescopes are built in such a way that the movable parts are lightweight. The total weight of the telescope is 64 tons, whereas the parts that move (mainly the structure of the reflectors, reflectors and camera) weigh only 20 tons. The lower parts of the telescopes which move only in the azimuth direction such as undercarriage and bogeys are made up of steel. The light weight upper parts such as the mirror support are made up of carbon fibre reinforced plastic tubes. This unique state-of-the-art design helps MAGIC telescopes to orient itself by 180° in the azimuth direction in about 25 seconds (Aleksić et al. 2016a). The movement of the telescope is controlled by three electrical 11 kW servomotors. The azimuth movements are maintained by two of the motors whereas the other motor is required for the elevation movements. The camera systems are placed on top of the tubular masts made up of aluminium. The cameras are held by pre-stressed steel cables. Figure 2.2 shows the overall construction and drive system of the MAGIC telescope system.

2.1.2 Reflector

The MAGIC telescope system has two parabolic reflectors of diameter of around 17 m. The reflectivity of the mirrors are very high (>70%), particularly around 350 nm, where the photo sensors in the camera are most sensitive (Will et al. 2019). The total reflective area is around 500 m^2. The spherical mirrors have specific radii between 34.5–36 m depending on their location in the dish. The mirrors are protected by quartz crystal coating. During the observations at different zenith angles the reflector surfaces deform slightly. In order to correct for this effect, each mirror panel is mounted on three points

[1]During 2012, H.E.S.S. collaboration commissioned the largest IACT of 28 m of diameter.

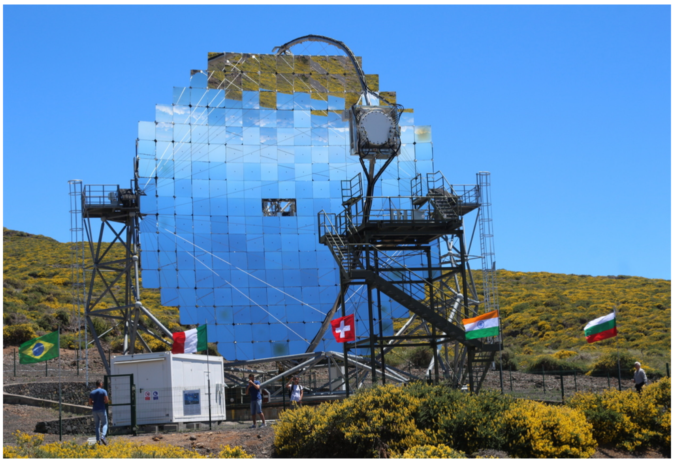

Figure 2.3: Front view of MAGIC-II reflector.

called Active Mirror Controls (AMC). The AMC, as a part of hardware, is responsible for correcting mirrors focusing at different zenith angles due to the deformation of the telescope. The system has two actuators per mirror facet which can adjust their position up to an accuracy of 20 μm. This system maximizes the focusing power to achieve a PSF of about ~0.037° (~10 mm) (Guberman 2018). The MAGIC-II reflector is shown in Fig. 2.3.

2.1.3 Camera

A single MAGIC camera consists of 1039 photomultiplier tubes (PMT) from Hamamatsu type R10408 each having 25.4 mm diameter and typical quantum efficiency of around 32%. The PMTs come with a hemispherical photocathode and 6 dynodes, with an hexagonal shape Winston cone mounted on top (see Aleksić et al. (2016a) for details). The PMTs or pixels are grouped in seven PMTs to build a modular unit for easier installation. Each modular unit is of 9 cm in width while the length is 50 cm. Two movable leads and a plexiglass plate placed in the front of each camera protect them when they are not operational. The back of the camera connects the pixels to the elec-

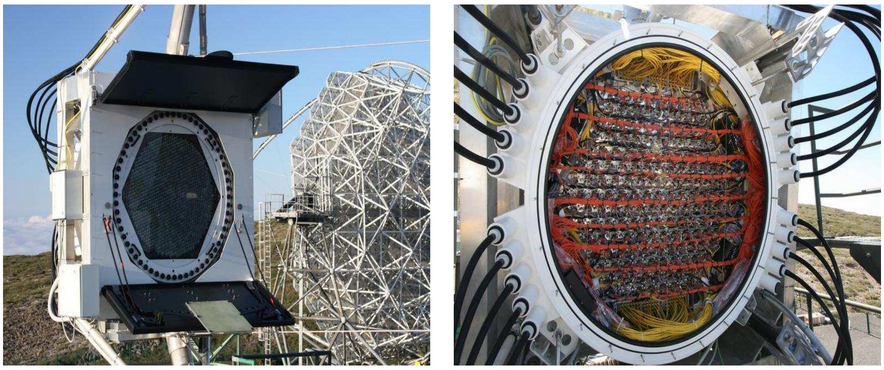

Figure 2.4: Front and back view of the MAGIC-II camera. Image credit: F. Dazzi.

tronics responsible for the power and signal transmission such as power and cooling system, cables, optical fibres, etc. Each pixel has a field of view (FoV) of 0.1°. The FoV of the MAGIC camera is 3.5°. Figure 2.4 shows the front and the back side of the MAGIC camera. A nominal HV of $\sim$ 900 V is applied to the PMTs during standard data taking. The signals from these PMTs are amplified and sent to the *counting house* situated within 100 m of the telescopes through optical fibres. The PMTs are operated with a relatively lower gain in bright sky conditions in order to prevent fast aging. The gain-differences for PMTs used in the cameras are compensated by adjusting the high voltage (HV) applied to the PMTs independently by using the $flatfielding$ procedure. The PMTs are equipped with safety limits of the anode currents (DC) of 47 μA above which the PMT is switched off. During no-moon condition (dark condition) the median current stays around 1 μA. A laser producing a beam of 355 nm placed inside the calibration box, located at the center of the reflector dish, is used in order to calibrate the cameras continuously by diffuse uniform-illumination.

2.1.4 Readout and trigger system

The counting house (CH), located at the MAGIC telescope site, is used for data acquisition, where the PMT-signals are transmitted via optical fibres. The conversion between the optical signal to the electrical signal is performed at the receiver boards. Later, the electrical signals are split into two branches: digital branch for the trigger system and the analogue branch for the readout system and sum-trigger (García et al. 2014). The receivers control the discriminator threshold (DT) by registering the trigger for the individual pixel known as the level zero trigger (LT0) and the trigger rate of the individual pixels (IPR). This IPR controls the DT for each of the pixels. A higher DT essentially lowers the accidental event rates when there are bright stars in the FoV of the camera.

Once a LT0 is triggered, the level one trigger (LT1), a topological trigger, checks for a trigger of a given number of neighbouring pixels in a temporal coincidence window. The LT1 helps in rejecting the events from the night sky background (NSB). Though in MAGIC, 2–5 next-neighbouring (NN) pixel modes can be used, the most common LT1 trigger is 3NN which is used for the stereoscopic mode of observation. On the other hand 4NN is used for the mono mode of observations.

The level three trigger (LT3) is used for the coincidence between the two telescopes where a time delay is applied to any one of the telescopes in order to adjust for the physical distance of 85 m and adjusted for various azimuth and zenith angles. The applied delay depends on the telescope pointing (zenith and azimuth orientation) and the maximum amount can be approximately around $\sim$300 ns.

The digitization of the signal is done with the help of the Domino Ring Sampler (DRS; Ritt 2004) chip, a ring buffer consisting of 1024 capacitors. The analogue signals charge those 1024 capacitors at a rate of 2 GHz in a looped manner, meaning the 1st capacitor is again charged once the charging of the capacitor 1024 is complete. After the LT3 (LT1) is triggered in the Stereo (Mono) mode of observation the voltage of 60 consecutive capacitors surrounding the event is digitised by an Analogue-to-digital converter (ADC) and subsequently stored. This corresponds to a period of 30 ns which is known as *the extraction time window*. The MAGIC-I telescope became fully operational in 2004. The MAGIC-II telescope was built and installed in 2009.

2.2 MAGIC observations

In a single MAGIC observation cycle, there are observation periods which are one lunar cycle long. The observations are usually performed up to 75% of the lunar phase, thus resulting in a 3-4 day period of moon breaks in between the lunar cycles. However, the usage of the UV moon-filters and different analysis techniques (Ahnen et al. 2017a) have significantly increased the possibility of data taking depending on the moon brightness and the position of the moon in the sky.

Standard stereoscopic observations are performed with the MAGIC telescopes with 3NN of LT1. The DTs for the individual pixel for the dark night-sky background condition are 4.25 photo-electrons (phe) which results in a stereo rate of about 280 Hz out of which 40 Hz are triggered by NSB (Ahnen et al. 2017b). This DT of 4.25 phe is considered as the operating point of the MAGIC telescopes. The DTs are modulated such that the individual pixel rates (IPR) are maintained within 0.2–1.2 MHz.

MAGIC observations are done in two observation modes, namely ON-OFF mode and wobble mode. In ON-OFF modes of observations, the source is observed during the ON mode of observations and for the background dedicated runs are performed during the OFF-mode, ideally far from the source, where the FoV does not contain any gamma-rays. However, the zenith angle and the night-sky-background (NSB) should match with the ON observations. Observations in this mode assume that the observing (telescope and atmospheric) conditions are similar so that there are no additional systematic effects.

The wobble mode (Fomin et al. 1994) is the most commonly used observation mode in MAGIC. In this mode of observation, no dedicated OFF observations are needed for background estimation and the same observing conditions for the ON and OFF source data are preserved. In this method, telescopes point slightly away from the source position and hence the background can be estimated simultaneously (Fomin et al. 1994). Instead of placing the source at the camera center, it is placed at a slight offset from the center. The choice of this offset is optimized based on the two effects: a) small offset, resulting in overlap between the ON and OFF region which degrades background estimation, and b) large offset which strongly affects the detection efficiency of the source. In MAGIC, a standard offset of 0.4° is used while each position is observed for a duration of 20 minutes. Depending on the extension of the source region, multiple OFF regions can be selected. The left panel of Fig. 2.5 shows the wobble observation scheme. For a single OFF position, the diametrically opposite position with respect to the camera center is selected. Multiple OFF positions (typically 2 or 4), also known as the wobble positions, help in the estimation of the background more precisely. These positions are selected symmetrically around the source position in such a way that the inhomogeneity in the field of view of the camera is minimized. The right panel of Fig. 2.5 shows a configuration where more than one wobble positions are considered.

During an observation, the source moves in the camera plane over a circle of radius 0.4° around the camera centre in the field of view. Thus, a standard MAGIC observation is performed with four wobble configurations. The main disadvantage of the wobble mode of observation is a small decrease in the γ-detection efficiency due to the shift of the source position towards the periphery of the trigger region ($\sim 2.7^{\circ}$). Because of this, a fraction (around 15-20%) of the EM cascades may lie outside the trigger region.

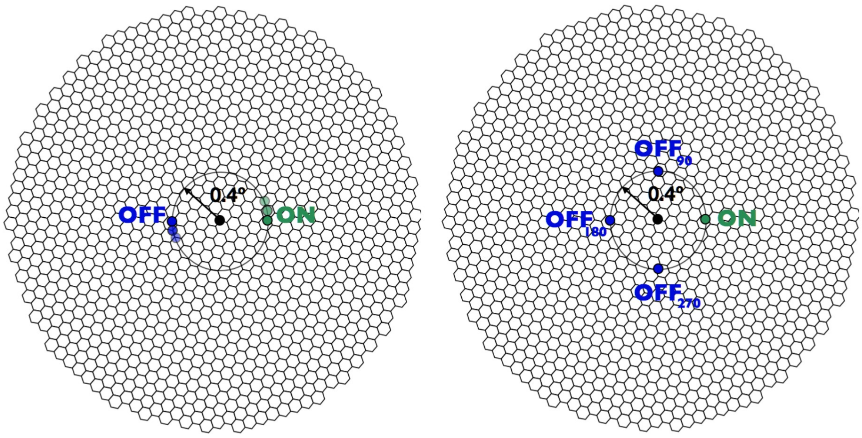

Figure 2.5: Schematic view of the wobble mode of observation. The center of the camera is marked with a black dot. The source (green dot) traces a circular track 0.4° away from the camera center. The simultaneous background (OFF, marked with blue dot) is taken on the circular track, placed diametrically opposite to the source (green dot in the left figure) in the case of one OFF region. In the case of three or more OFF regions (blue dots), as shown in the right panel, the backgrounds are selected from regions placed symmetrically in the camera plane. Figure adapted from Coto (2015).

2.3 Data analysis

In MAGIC, the data analysis is done using a software named MAGIC Analysis and Reconstruction Software (Zanin et al. 2013, MARS) written in C++ and ROOT (Brun & Rademakers 1997). The data analysis procedures can be designated by three levels: low-, intermediate- and high-level analysis. The low-level data analysis is typically done in the observatory daily after the observations end. This is known as On Site Analysis (OSA). The data are then transferred to Port d'Informació Científica (PIC)[2] located at Barcelona, where the data is stored, so that it can be re-analyzed due to major modifications in the analysis chain or bug-fixes in the software. The analyzers can access the data from PIC for intermediate- and high-level analysis. Any intermediate- and high-level analysis need to be validated by two independent analyzers. The MAGIC analysis

[2]www.pic.es/index.gsp

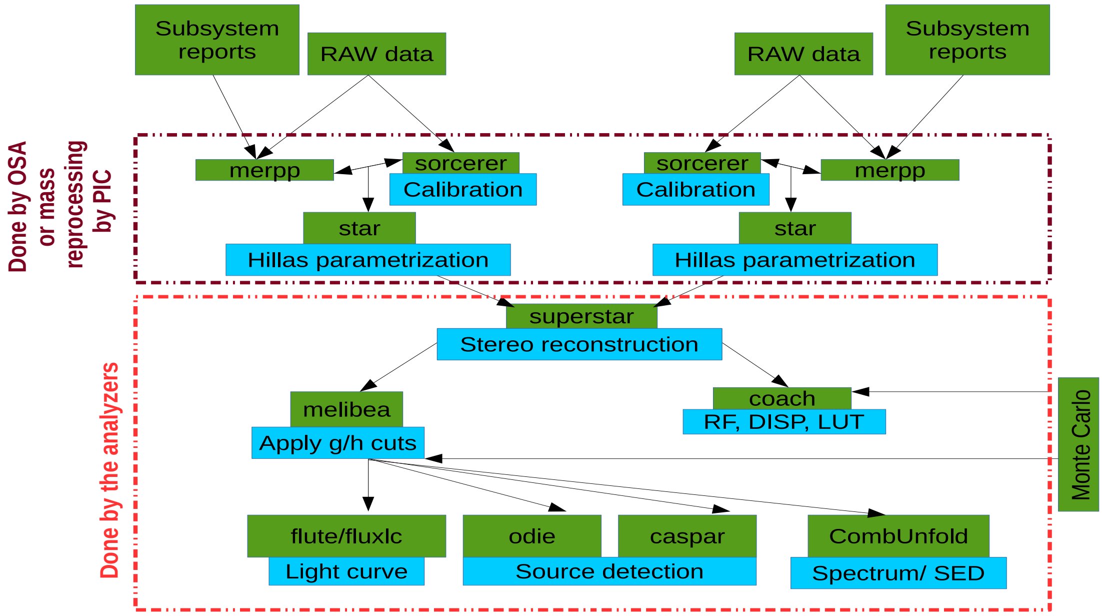

Figure 2.6: Standard MAGIC analysis chain.

chain is shown in Fig. 2.6 and will be discussed in the later sections of this chapter.

2.3.1 Low level data processing

The observed data, data from the target source (ON-data), are stored in the system in a binary format which are converted to a ROOT file format using a program called *merpp*. At the same time, the subsystem reports containing the information on the camera, pointing positions, observation conditions during the night, etc. are also merged.

Calibration

After converting in to the ROOT format and merging with the subsystem information, the data are calibrated. The analogue signal is first digitized and processed and converted into the number of phe. The program used for this purpose is called *sorcerer* (Gaug et al. 2005; Sitarek et al. 2013). The valid signals from each pixel in the window of 30 ns with a bin size of 0.5 ns are recorded. The pedestal data is recorded for the estimation of the baseline or bias for the signal and subtracted. Later, the signal is extracted using a sliding-window algorithm which seeks for the largest signal in 6 consecutive bins for each pixel. The signal arrival time is the weighted average position of the 6 selected bins, where the weight factors are the counts in each of these bins.

For converting these FADC counts to the phe, we use the F-factor method (Mirzoyan 1997). For a pulse of N phe-s which is resulted from μ-FADC counts, μ =N/C, where C phe-s give rise to 1 FADC count. Assuming Poisson-distribution of phe, the fluctuations in the signal can be written as, $\sigma_{signal}= \sqrt{N}/C$. This implies,

$$N = \left(\frac{\mu}{\sigma_{signal}}\right)^2 \quad \text{and} \quad c = \frac{N}{\mu} \tag{2.1}$$

The electron multiplication in dynodes of PMTs gives rise to non- Poissonian noise. This is taken care of by a correction factor in signal fluctuation which is known as the F-factor. The corrected formula which includes the fluctuation in the signal (σ_{signal}) and in pedestal ($\sigma_{pedestal}$) is the following:

$$C = \frac{N}{\mu} = F^2 \frac{\mu}{\sigma^2_{signal} - \sigma^2_{pedestal}} \tag{2.2}$$

Image-cleaning and image-parametrization

The Cherenkov photons produced through the extensive air shower (EAS), trigger pixels on the camera and thus an image of the shower is formed. Most of the pixels, however, are triggered by the NSB and electronic noise. This is why the image from the shower needs to be cleaned. In MAGIC, *Absolute Image Cleaning* is used which is based on the number of phe contained in the pixels. In this algorithm, two thresholds are used, namely core (Q_{core}) and boundary ($Q_{boundary}$) thresholds, where the core threshold is higher than the boundary threshold ($Q_{core} > Q_{boundary}$). In the first step, all the pixels with charge greater than Q_{core} are selected as the core pixels. The boundary pixels are considered as the pixels which have at least one triggered next neighbour with charge greater than $Q_{boundary}$. After the selection of the core pixels the arrival times are also considered. If the arrival time registered for any event in any pixel is greater than 4.5 ns with respect to the core pixel, that pixel will be discarded. A similar time bound of 1.5 ns is also applied for the selection of the boundary pixels. A higher threshold of 10 phe and 5 phe are used as Q_{core} and $Q_{boundary}$, respectively, in case of the absolute image cleaning. On the other hand, if the timing is also considered in the image cleaning, that criteria can be relaxed to 6 phe and 3.5 phe as the Q_{core} and $Q_{boundary}$, respectively.

The cleaned image is considered for the image parametrization, first introduced in Hillas (1985). The parameters mentioned in the Table 2.1 are estimated using an analysis module named *star*.

2.3.2 Standard data reconstruction

Data quality selection

After the cleaning of an image is done, the data quality selection is performed by a module named *quate*. Different parameters such as sky-brightness, zenith, rate, aerosol transmission, cloudiness, etc. per one data-slice (2 minutes of data) can be considered and the averaged values of these parameters are calculated for selecting *good* quality data. Data that do not satisfy the criteria, set by the analyzers, are discarded in the next level of the analysis chain.

Parameters	Description
Size	Total number of phes in the shower image. Size is proportional (at first approximation) to the energy of γ-ray photon that induced the shower.
CoG	Centre of gravity of the image formed at the camera. This parameter determines the position of the weighted mean signal in the camera.
Length	Semi-major axis of the elliptical fit to the image. This is related to the longitudinal development of the shower.
Width	Semi-minor axis of the elliptical fit to the image. This is related to the lateral development of the shower
Conc-n	Fraction of the phe-s contained in the n brightest pixels.
Leakage	Defined as the fraction of signal in the outer rings of the image to the total size. only a part of the showers with large impact parameters are captured in the images. This determines the ability to reconstruct the images. Low leakage means the image can be parametrized properly.
NoI	Denotes the number of islands, meaning the discrete group of pixels that survive after the image-cleaning is applied.
α	The angle between the major-axis and the line joining the CoG with the position of the source in the camera.
Dist	The distance between the CoG and the position of the source in the camera.
Time gradient	The arrival time of the events in each pixel along the major-axis is fitted with a linear function. The linear coefficient is termed as the time gradient.
Time RMS	The spread of the arrival times of the pixels in the image is termed as the time RMS.

Table 2.1: Parameters for the image-parametrization. After the image cleaning is performed, the image formed in the camera plane is parametrized and the parameters mentioned in the table are extracted and used in the later states of the analysis chain.

Stereo reconstruction

A module, named *superstar*, reconstructs the EAS in 3-D by matching the events from MAGIC-I and MAGIC-II. A sketch of the geometry of the shower is shown in Fig. 2.7. The stereoscopic reconstruction gives rise to the following parameters:

Shower direction: The shower images from both cameras (MAGIC-I and MAGIC-II) are superimposed in a single camera. The intersection between the semi-major axes in the sky-plane denotes incident direction of the γ-ray photon.

Impact point: This is the point where the shower axis intersects the ground. Here, the semi-major axis of the showers in the cameras and the physical distance between the telescopes are considered.

Impact parameters: Depending on the shower direction and the impact point, the impact parameters for each of the telescopes are determined. The impact parameters are the distance between the telescopes to the shower axis in the plane perpendicular to the shower axis.

Height of the shower maximum (h_{max}): The intersection of the shower axis and two directions from two telescopes pointing to the CoG in the sky-plane is designated as h_{max}. In reality, the intersection forms a triangle in the sky-plane. The parameter h_{max} is considered as the height with the minimum perimeter of this triangle mentioned above.

Disp: The distance between the CoG and the impact point is termed as the Disp. In practice, two impact points from each of the telescopes are determined. Disp parameter, described in the next subsection, has been shown to be an important parameter for the γ/hadron separation.

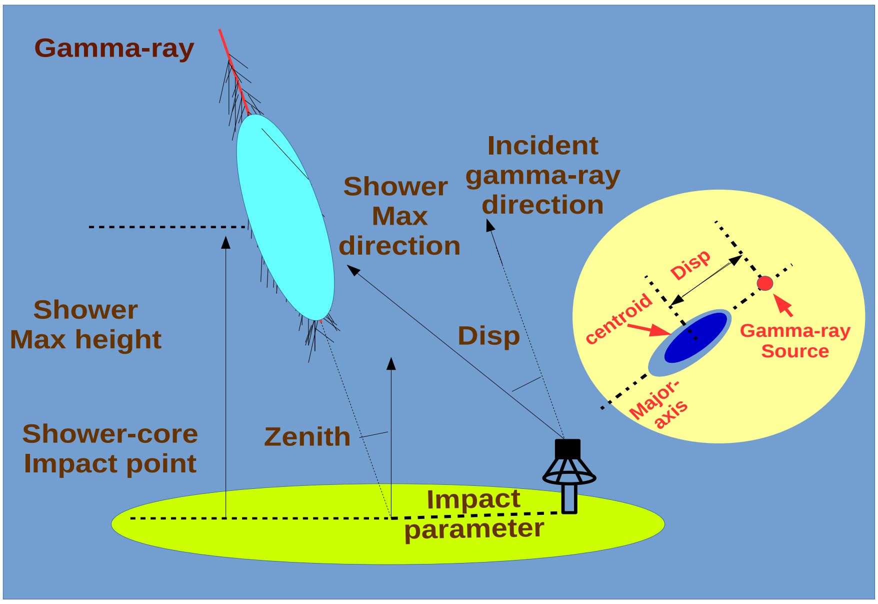

Figure 2.7: The Geometry of the EAS. Relevant parameters are described in the text.

γ-hadron separation

Hadronic events are considered as the background for the γ-events observed with the MAGIC telescopes. All the events registered by the camera are parametrized using *star* by Hillas parametrization, and later individual parameters are joined together at the higher level of analysis using *superstar*. The output of *superstar* gives stereo parameters those are used for discriminating between the gamma-events and hadron-events. This separation is done on the basis of a parameter called *hadronness*, a probability that a given event is caused by a hadron shower. The hadronness parameter is calculated from the Random Forest (RF) algorithm (for a discussion and the adaptation of RF method for the MAGIC telescopes see Albert et al. 2008). The Random Forest method is based on a collection of decision trees constructed on the basis of training samples suitable for the application. The RF is generated using the MC simulated gamma-events and the contribution from the hadrons coming from a separate set of data termed as the

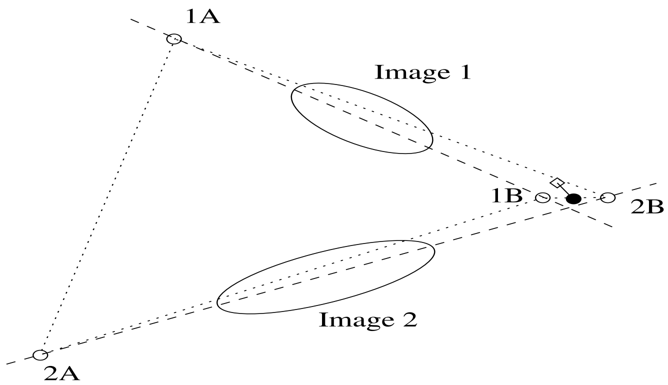

Figure 2.8: Description of stereo DISP-RF method. The dashed line represents the main axis of the image. The positions 1A, 1B, 2A, and 2B (empty circles) are the four reconstructed source positions, two per telescope. The four dotted lines, 1A-2A, 1A-2B, 1B-2A, and 1B-2B represent the angular distances. The final reconstructed position (the filled circle) is a weighted average of the two closest '1' and '2' points. The true source position is marked with a diamond. Figure adapted from Aleksić et al. (2016b).

OFF data having similar zenith azimuth distribution as the ON data (data from the target source).

Along with the hadronness cut, the direction reconstruction method also provides background subtraction. In MAGIC, the DISP-RF method is used in order to provide the event-wise direction reconstruction which is estimated based on the time gradient of the development of a shower image along the major axis (Aleksić et al. 2010b). For each of the telescopes, the source position is calculated which provides two possible solutions on either side of the telescope as shown in Fig. 2.8.

This "head-tail" discrimination can be solved by calculating the four distances between the four possible source positions as shown in the Fig. 2.8. The smallest distance between the pair of images is called the $DISP$ parameter (1B-2B, in this case). For hadronic background events this DISP parameter often gives non-consistent results when trained with simulated gamma-ray events (MC events). An event is discarded, if we do not find any similar arrival direction from the two telescopes with a criterion that the minimum distance out of the four pairs is lower than 0.22°. The reconstructed source position is the weighted average of the two positions estimated by two telescopes, where the weights are the number of pixels in each image.

The energy of the events are reconstructed using the lookup tables (LUT), a multi-dimensional table containing mean energy for each combination of the image parameters. This is a two step process. In the first step, the LUTs are created using the energy of the gamma-ray events depending on the Cherenkov photon density and Impact parameter (for a detailed explanation see Aleksić et al. (2012c)). The LUTs are based on a simple Cherenkov emission model which does not take into account the following effects: a) zenith angle, b) azimuth angle, and c) large images that are partially contained in the cameras. These corrections are made and the final estimated energies (E_{est}) are calculated by weighted averaging of the energies estimated for each telescope, where the inverse of the uncertainties are taken as the weight factors.

For this analysis chain, *coach*, we first divide the MC files (gamma-events) into train and test samples. The RF tree is grown using the train MC files and the OFF data.

The RF decision tree is grown as follows: at first a random parameter from size, length, width, etc. is chosen and the value for that parameter is estimated which separates the gamma-s from the hadrons. The estimation of the parameter continues until the whole data sample is separated between gamma-s and hadrons. In this process, typically 100 decision trees are created and the above process is repeated for each of those 100 trees. These 100 trees are then applied to the data containing the source. Each event passes through a tree and based on the values of the Hillas parameters and follows a certain path down the tree. At the end when the event exits the RF tree, a value of zero (one) is assigned if the event is identified as a gamma (hadron) event. The same is also passed through the other 99 trees and the hadronness is the sum of these zero-s and ones-s divided by 100, hence, hadroness ranges between 0 to 1.

With the help of *melibea*, the RF is applied to the data collected from the source (ON data) and test sample of the MC files. The test MC files are used for the calculation of the effective collection area and efficiency of the cuts.

2.3.3 High level analysis

With the help of the high level analysis, we extract the gamma-ray signal and calculate the source spectrum and light curves.

γ-ray signal

The squared angular distance between the nominal source position in the camera and the reconstructed source position, the shower direction, is termed as θ^2. In order to check for the excess gamma-ray events, the events as a function of θ^2 is plotted along with the cuts in the hadronness and size. The background is estimated by plotting the θ^2 distribution in the OFF-regions. For the estimation of the background using wobble-mode, more than one OFF-region can be used. The number of events will be normalised by the ratio of the number of ON- and OFF-positions (α). From the distribution of the events vs. θ^2, a cut on θ^2 is estimated which separates the ON- and OFF-region in the θ^2 axis. The number of excess events are then calculated which is the difference between the number of ON events (N_{ON}) and the number of OFF events (N_{OFF}). The θ^2 cut used for the signal extraction is optimized based on the sensitivity. The significance of the observations is calculated using the module *odie*. An example of the θ^2 plot is given in

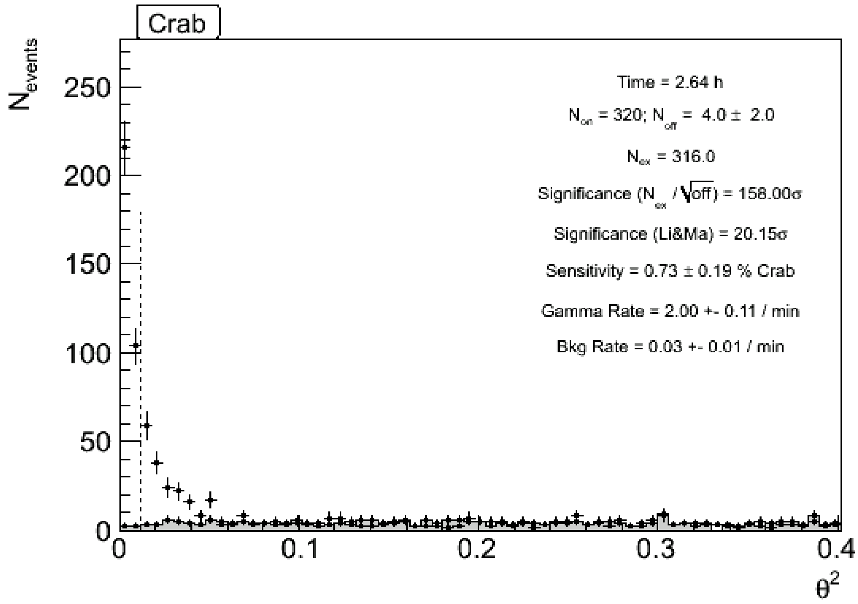

Figure 2.9: An example of the θ^2 plot with the data from Crab Nebula above a typical reconstructed energy of ~100 GeV. The ON-source events are over-plotted with the background events (OFF-source events) shown by the gray histogram. The vertical dashed-line represents the cut on θ^2.

Fig. 2.9. The significance of detection (σ) is given by (Li & Ma 1983):

$$\sigma = \sqrt{2 \times N_{ON}\ ln\left[\frac{1+\alpha}{\alpha}\left(\frac{N_{ON}}{N_{ON}+N_{OFF}}\right)\right] + N_{OFF}\ ln\left[(1+\alpha)\left(\frac{N_{ON}}{N_{ON}+N_{OFF}}\right)\right]} \quad (2.3)$$

Energy resolution and energy threshold

The energy reconstruction is estimated using the MC γ-ray simulations. The difference in the estimated (E_{est}) and the true (E_{true}) energies of the gamma-ray scaled with E_{true}, namely $(E_{est} - E_{true})/E_{true}$ is fitted in each bin. The mean and the standard deviation of the fit are termed as the bias and the energy resolution. Figure 2.10 shows the energy resolution of the MAGIC telescopes as a function of E_{true}.

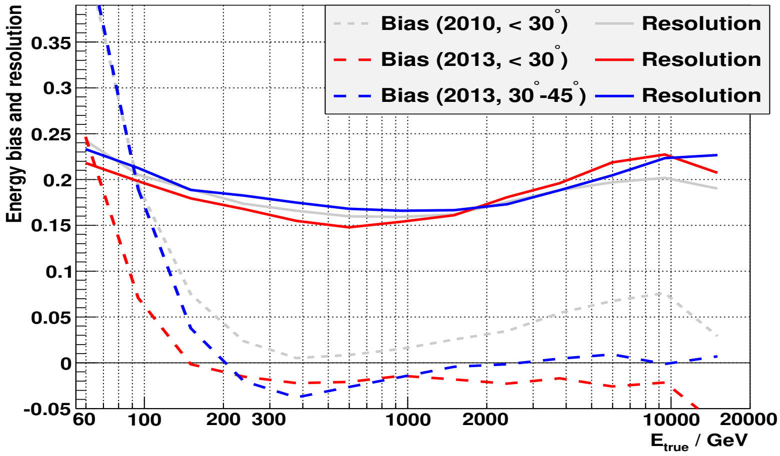

Figure 2.10: The energy resolution (solid lines) and bias (dashed lines) obtained from the MC simulations of γ-rays. The simulated events are weighted in order to represent a spectrum with a slope of -2.6. The red and blue colors represent low and medium zenith angles respectively. The gray lines are values from the pre-upgrade (before 2013). Figure adapted from Aleksić et al. (2016b).

The energy resolution for a few hundred GeV falls down to around 15%. In the higher energies it degrades due to the increased fraction of truncated events, presence of the showers of high impact parameters, and worse statistics in the training samples. At lower energies the energy resolution is poor because of the poor image reconstruction. In the multi-TeV energies, the low zenith showers are partially truncated at the edge of the camera which results in a poor energy resolution than the higher zenith.

The energy bias changes depending on the spectral slope of the source. For a source with a steep spectrum, lower energy events migrate to the higher energies resulting in an overestimation of the energy. This bias is corrected using the *unfolding* method (Albert et al. 2007b).

The analysis cuts, hadronness cuts, size cuts and signal (θ^2) cuts are applied on the events that survived image cleaning and stereo reconstruction. Figure 2.11 shows a differential rate plot for low and medium zenith ranges, where the energy threshold of the MAGIC telescope is ~70 GeV for low zenith (< 30°) observations.

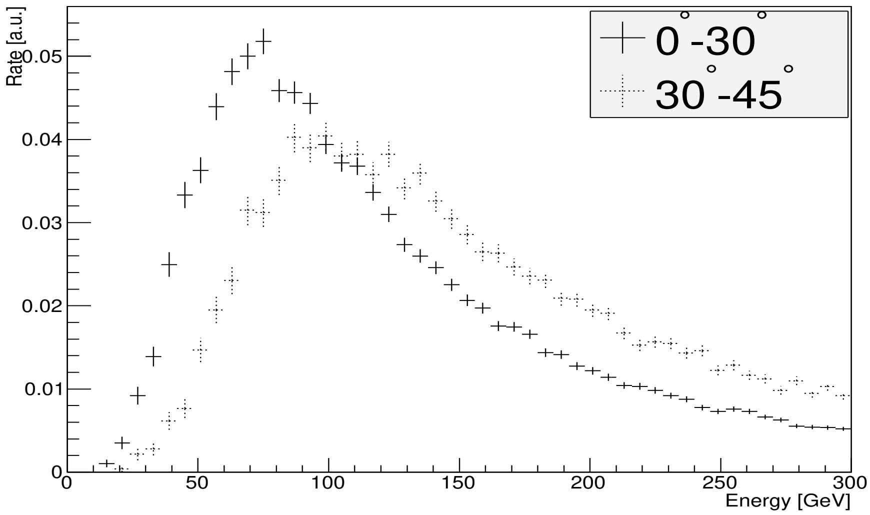

Figure 2.11: Rate of MC γ-ray events surviving the image cleaning with size >50 phe for a hypothetical source with spectral index of -2.6 for low (0°-30°; solid line) and medium zenith (30°-45°; dotted line). Figure adapted from Aleksić et al. (2016b).

Angular resolution

The angular resolution of the MAGIC telescopes can be calculated using two methods. In the first method, the angular resolution is defined as the standard deviation of the 2D Gaussian fit to the reconstructed event direction of the γ-ray excess. The 2D excess in the θ_x and θ_y space corresponds to an exponential fitting in the θ^2 distribution. A typical signal extraction window is around $\sim 0.01°$ in the θ^2 distribution, however, the fit is performed in a larger window of ~0.025 sq. degree.

The second method, an angular distance ($\Theta_{0.68}$) around the reconstructed source position is estimated which contains 68% of the excess events. This method is particularly suitable for sources with long tails in the distribution of the reconstructed direction.

Figure 2.12 shows the angular resolution of the MAGIC telescopes using both the methods with the low and medium zenith observations of the Crab Nebula data. At around 250 GeV, the angular resolution from the Gaussian fit is $\sim 0.07°$. The angular

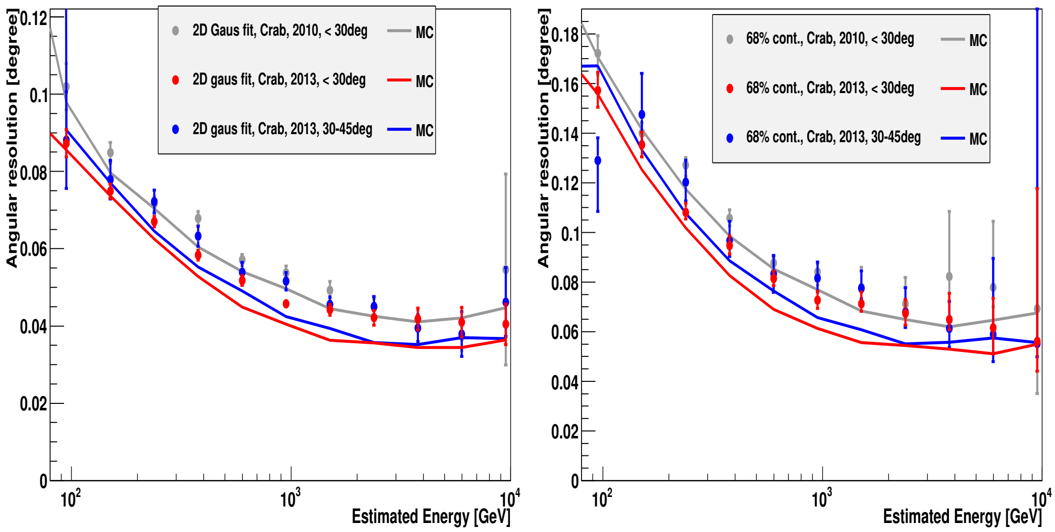

Figure 2.12: Angular resolution of the MAGIC telescopes as a function of the estimated energy obtained with the Crab Nebula data sample (points) and MC simulations (solid lines). The left and right panels show the 2D Gaussian fit and 68% containment radius respectively. The red and blue points show low and medium zenith angle samples. Figure adapted from Aleksić et al. (2016b).

resolution improves with increase in energies because the larger images are better reconstructed. The best angular resolution is achieved at around a few TeVs where the angular resolution reaches $\sim 0.04°$.

Sensitivity

The sensitivity is defined as the minimum signal that can be detected in 50 hours of observation with a detection significance of 5 σ, where significance is defined as $\sigma = N_{ex} \,/\, \sqrt{N_{off}} = (N_{on}\text{-}N_{off})/\sqrt{N_{off}}$, , where N_{ex}, N_{on}, and N_{off} are the number of excess events, number of ON (signal) events and background (OFF) events respectively. Sensitivity is generally expressed in units of the flux of Crab Nebula. The significance at time t_0 is given by

$$\sigma(t_0) = \sqrt{\frac{t_0}{t}} \frac{N_{ex}}{\sqrt{N_{off}}} \tag{2.4}$$

The sensitivity in term of minimum flux that can be detected in t_0 = 50 hours with a significance of 5σ in Crab units is given by

$$S = \frac{5\sigma}{\sigma(50h)} \times C.U. \tag{2.5}$$

The sensitivity of an instrument can be expressed in two ways: integral and differential sensitivity. A set of cuts (hadronness, size, signal cuts, etc) can be estimated that provides the best sensitivity above a given energy which is termed as the integral sensitivity. Similarly differential sensitivity is the best sensitivity in a given energy range with the best possible set of cuts. In the case of MAGIC, the best integral sensitivity 0.66 ± 0.03% C.U., is achieved above 220 GeV (Aleksić et al. 2016b).

Energy spectrum (spectral energy distribution) and light curve (LC)

The number of γ-ray photons in a given energy range divided into several smaller bins passing through a unit area in unit time is called the differential energy spectrum or spectral energy distribution (SED).

$$\frac{d\phi}{dE} = \frac{d^3 N_\gamma}{dE\, dA_{eff}\, dt_{eff}}, \tag{2.6}$$

where N_γ, A_{eff}, t_{eff} are the number of excess γ-ray events, effective area, and effective time of observation respectively. The number of excess events, N_γ is the difference between the ON (N_{on}) and OFF (N_{off}) events. As mentioned above, several bins in the entire energy range are considered to calculate the differential energy spectrum. For each of the bins, the parameters mentioned in Eq. 2.6 such as effective time, effective area, etc. are evaluated. The effective area (A_{eff}) is calculated using the Monte Carlo events for the γ-rays.

Assuming the total γ-ray events, $N_{\gamma,tot}$ simulated on the telescope area A_{sim}, the effective area takes the form:

$$A_{eff} = \frac{N(E)}{N_0(E)} \times \pi r^2_{max}, \tag{2.7}$$

where N_0(E) is the number of simulated events, r_{max} is the maximum simulated shower impact and N (E) is the number of events surviving either the trigger condition or a given set of cuts. The total effective time is slightly less than the observation time which is due to the dead-time of the readout system. The dead-time is significantly shorter, 26 μs/event, for the DSR4 chip as compared to 0.5 ms/event as achieved using the DSR2 chips. The collection area of the MAGIC telescopes is about 10^5 m^2 for 300 GeV gamma-rays at the trigger level (Aleksić et al. 2016b).

The measured spectrum depends on several factors, such as finite resolution of the instrument, the non-controllable atmospheric conditions, etc. The true spectrum is connected to the observed spectrum of the source by the following equation:

$$g_i = \sum_j M_{ij} f_j, \tag{2.8}$$

where g_i, f_j and M_{ij} are the measured spectrum in the i^{th} energy bin, the true spectrum in the corresponding bins and the migration matrix. The element of the migration matrix is determined using the simulated γ-ray events from the MC. The true spectrum is obtained using the matrix inversion which is known as *unfolding*. Since the migration matrix is not a square matrix the inversion of the same gives unstable results during

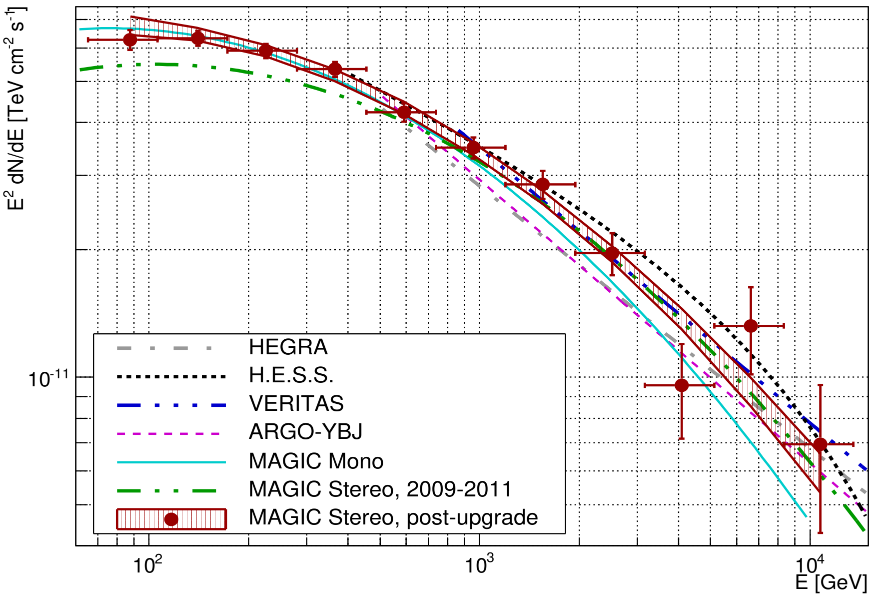

Figure 2.13: Spectral energy distribution of the Crab Nebula, ∼ 11 hours of low zenith (<30○) observations with the MAGIC telescopes in wobble mode. For comparison purposes the Crab Nebula SED observed with the other experiments are also shown. The vertical and horizontal error bars represent statistical uncertainties and the energy binning respectively. Figure adapted from Aleksić et al. (2016b).

the Chi2 minimization. In order to avoid this, a regularization is applied by adding a regularization term Reg($\vec{f}$) in the following way:

$$\chi^2 = \frac{\omega}{2}\chi_0^2 + Reg(\vec{f}), \tag{2.9}$$

where ω is the strength of the regularisation. There are different regularization methods that can be applied to the data having different regularization terms, namely Bertero (Bertero 1989), Schmelling (Schmelling 1994), Tikhonov (Tikhonov & Arsenin 1977), etc. Alternatively, one can use the *forward unfolding* method, where we assume a parametric analytic form of the true spectrum and fit the observed spectrum by Chi2-minimization numerically (Tikhonov & Arsenin 1977).

Figure 2.13 shows the spectrum of the Crab Nebula obtained from the low and medium zenith observations in the energy range between 65 GeV to 13.5 TeV. A hadronness cut of 0.9 is applied here. The SED (in red) is fitted with Eq. 1 of Aleksić et al. (2016b),

$$\frac{dN}{dE} = f_0(E/1\ TeV)^{a+blog_{10}(E/1\ TeV)}[cm^{-2}s^{-1}TeV^{-1}], \tag{2.10}$$

which resulted in the following set of fit parameters: $f_0 = (3.39 \pm 0.09_{stat}) \times 10^{-11}$, a=-2.51 ± 0.02_{stat}, and b = -0.21 ± 0.03_{stat}.

Light Curve

Light curve (LC) is the time series of measured VHE γ-ray flux. The flux is calculated from the incident signal events (gamma-ray events) in unit area within a certain time bin above a certain energy threshold, E_{min}. The time bin is the effective time that can be made as custom bins of variable time intervals (5 minutes, 10 minutes, 20 minutes, etc.) or can be made as 1-day binning which is typically the flux measured during a single night of observation. For a time bin, an upper limit in flux is calculated when the relative error on flux (flux-error/flux) is less than 0.5. Given the observing conditions, performance of the system and spectral slope, the expected signal g (gamma-ray events) can be calculated as

$$g = t_{eff} \int_0^{\infty} \mathrm{d}E \frac{\mathrm{d}\phi}{\mathrm{d}E} A_{eff}, \tag{2.11}$$

where t_{eff} is the time-bin (effective time of observation), $\frac{d\phi}{dE}$ is the source spectrum in the energy range dE, and A_{eff} is the effective area. For a particular time-bin, when the number of detected cases are below g, the spectrum of the source $\frac{d\phi}{dE}$ can be inverted in order to determine the spectrum of the source. Following this procedure mentioned above, one can calculate the upper limit of the integral flux. In order to calculate the upper limits in an energy bin of a spectrum, this procedure can also be applied if the

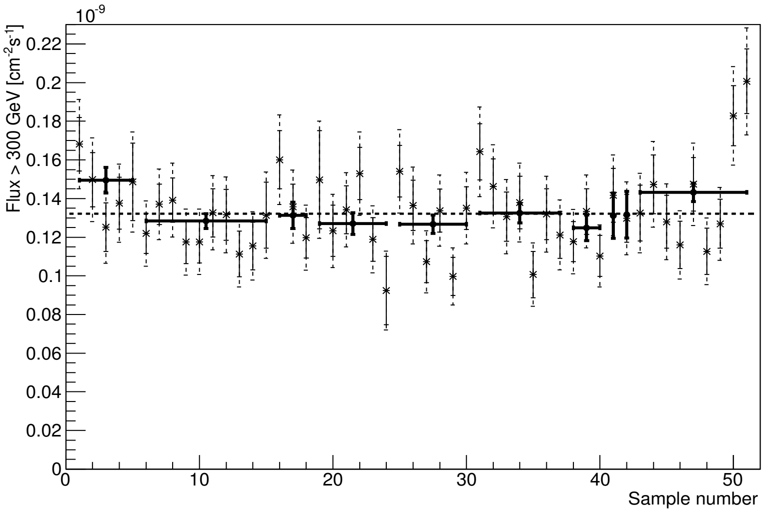

Figure 2.14: Integrated fluxes above 300 GeV of the Crab Nebula for different data runs. Each single 20 min run is represented by thin lines and asterisks. The thick lines represent night-wise fluxes . The data with dashed error bars show flux including a night-to-night systematic uncertainty of 11% (see Section 2.4) added in quadrature. The mean flux for the entire data sample is represented by the vertical line. Figure adapted from Aleksić et al. (2016b).

relative error is larger than 0.5. The calculations of the flux and spectrum is done using a module called *flute* for the stereoscopic observations.

2.4 Systematic uncertainties

The systematic uncertainties of the MAGIC telescopes (Aleksić et al. 2016b) come from individual factors known with limited precision, and mostly varies night-wise. The factors described below contribute significantly to the total systematic uncertainty.

a) Background subtraction: A prime source of the systematic uncertainty is the dispersion in the PMT response (including the effect of the 'dead' pixels) and the variation of the NSB across the field of view of the telescopes. In the camera plane, this introduces small inhomogeneity in the event distribution. Stereoscopy with just two telescopes is also a potential source of a natural inhomogeneity. The effect is minimized by wobbling mode of observation. This may produce around 1% of the systematic uncertainty.

Due to the background uncertainty, in case of weak sources (signal to background ratio of $\sim$ 5%), an additional systematic uncertainty on the flux normalization can amount up to a systematic uncertainty of $\sim$20%.

b) Pointing accuracy: Due to the load of the telescopes a slight deformation of the telescope structures leads to sagging of the camera which in turn adds systematic uncertainty. Most of the effect is corrected by the AMC and observations of the reference stars. However, the systematic uncertainty of around 0.02° on the reconstructed source position remains as the residual mispointing.

c) Energy scale: The absolute energy scale in the IACTs is very difficult to determine. The systematic effects such as lack of knowledge of the atmospheric transmission, mirror reflectivity, PMT characteristics, etc. contribute to this. The absolute energy scale of MAGIC is validated by two different methods: a) using inter-telescope calibration, and b) using the analysis of muon-rings (Vacanti et al. 1994). The uncertainty in the energy scale is around 15-17%.

d) Night to night systematic uncertainty: Apart from the systematic uncertainties which are mostly fixed and do not change night-by-night basis, one needs to consider a few effects that may change night-wise, such as atmospheric transmission, change in the optical PSF, etc. In order to correct for these effects, data from a steady source, Crab Nebula, are divided into several parts (data runs of about 20 minutes) during a night, and the flux for each temporal bin is estimated. The excess RMS of flux represents the variation of the flux. This uncertainty is estimated around $\sim$11% (see Fig. 2.14).

During data analysis of any source other than Crab Nebula, we first optimize the analysis cuts (signal cut, hadronness cut) using the data from Crab Nebula. Once the standard flux and spectrum of the Crab Nebula are reproduced, we directly apply those optimized cuts on the target source.

3

Lowering the analysis threshold of the MAGIC telescopes:

In standard operating conditions (low night-sky background, low zenith: 5°-35°, standard digital trigger), MAGIC telescope system has a trigger threshold of ~ 60 GeV. The energy range between few GeV to 50 GeV is very difficult to cover by any of the ground based or space based telescopes. However, this energy band is particularly interesting because of observing various objects such as pulsars, high redshift AGNs, and GRBs. In order to explore this energy region, a new trigger system, called the sum-trigger system was designed in 2008 for a single telescope (MAGIC-I). This resulted in a detection of the pulsed VHE $\gamma-$ray emission from the Crab pulsar above 25 GeV (Aliu et al. 2008). The system has been updated since then into sum-trigger-II (García et al. 2014; Dazzi et al. 2015). The basic concept of the sum-trigger system is based on the addition of analogue pulses from macrocells (a cluster of neighbouring PMTs, see chapter 2 for details). In case of sum-trigger, the discriminator threshold is applied only after the analogue sum. In this way, the contribution of the PMTs with a small charge located in the macrocell contributes to the final trigger decision.

Most of the data taken with MAGIC are with standard trigger (3NN data). This chapter focuses on whether the threshold can be reduced when dealing with the standard trigger data. In order to explore this, very recently, a new algorithm has been designed to reduce the energy threshold for the analysis of the standard 3NN data. This method works only during the calibration (using *sorcerer*, see Chapter 2), cleaning and image parametrization (using *star*, see Chapter 2). In this chapter, the performance of this cleaning method on the standard 3NN data will be discussed in detail.

3.1 Challenges of detecting low energy events:

Low energy primary photons develop a narrow and short cascade. Most of the cascade events are developed fully till they reach 10 – 12 km above the seal level (a.s.l.). This is why a large fraction of the Cherenkov photons produced by a low energy $\gamma-$ray photon are absorbed by the atmosphere before reaching the telescopes. In addition, the energy threshold for the production of the Cherenkov photons is higher and the refractive index is lower in the upper atmosphere. This results in a production of fewer Cherenkov photons within a very narrow angle. Because of these effects, a small number of pixels are triggered at the camera and a small projection of the shower can be sampled. Figure 3.1 shows the projection of three low-energy showers ($10 - 60$ GeV photons) in the camera from a MC simulation detected with the standard trigger. As can be seen in the Figure 3.1, the events are rather concentrated in a very narrow region for the two lower energies at 13 GeV and 21.5 GeV. The photon density in each pixel for two of these low energy events is very low, ≤ 10 photons per pixel. Also, in energies lower than 25 GeV more than one island (see Chapter 2) can be identified. As the energy of the γ-ray increases the islands combine with each other to form a single island as shown in the

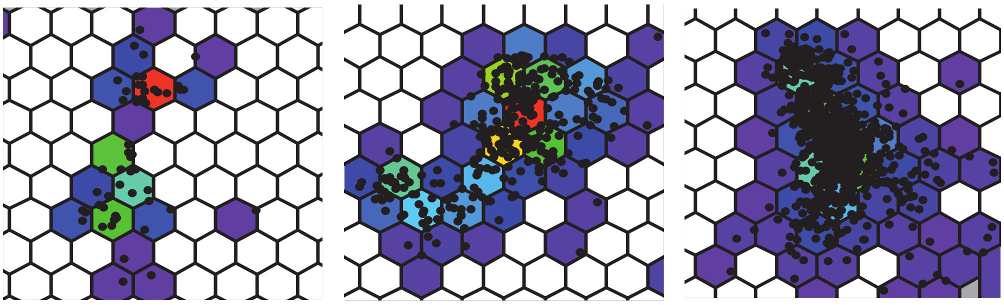

Figure 3.1: The Cherenkov photons originating from 12.9, 21.5, and 58.6 GeV γ-rays hitting the camera plane. Adapted from Dazzi (2012).

case of the 60 GeV photon in Figure 3.1.

The number of photons that triggers the camera at lower energies are very few (García et al. 2014). This results in a poor image parametrization and leads to a poor $\gamma-$hadron separation. In addition, noises from PMT and DRS4 chips also need to be taken care of in case of lower cleaning thresholds. The random noises arising due to the PMTs are called the after-pulses. These after-pulses are high rate random noise pulses which may trigger a pixel. They can be rejected by introducing clipping levels for each pixel after the time coincidence applied in stereo-mode of observation.

3.2 Spike removal algorithms:

Spikes are random features appearing in the baseline (time series of the background) of the readout system which are larger than the Gaussian-noise. Usually the readout system of the DRS4 chip has many random features which vary on a scale of the 1-2 capacitor readout and may also be of a broader form (2-3 capacitor readouts) which are called pseudo pulses. These pseudo-pulses are narrower than the signal width and appear as spikes. The left panel of Fig. 3.2 shows a waveform in which a spike is present. The right panel of the figure shows the waveform of pseudo-pulses. These spikes need to be

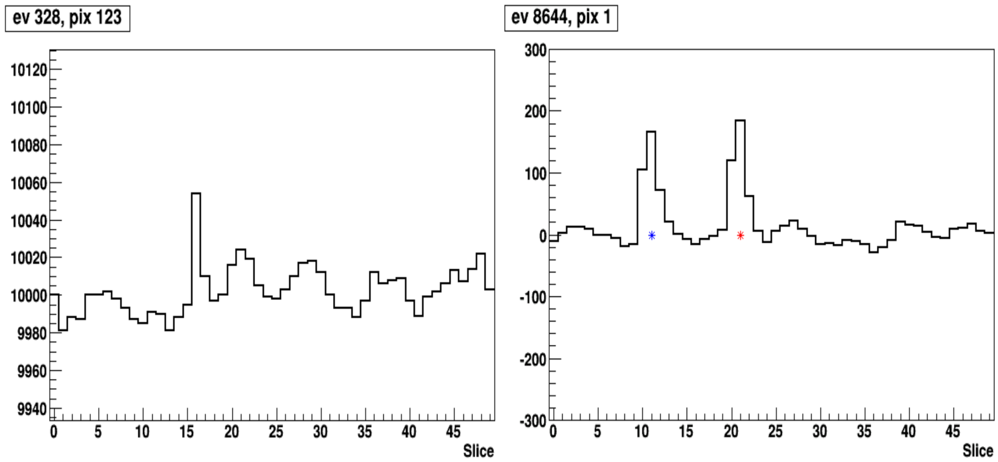

Figure 3.2: The waveform of spikes. Spikes usually appear in 1-2 time-slices as shown in the left panel. The right panel shows slightly broader features (2-3 time-slices), known as *pseudo-pulses* marked with a red dot at the center. The signal in the right panel is marked with a blue dot at the center of the pulse. Figure credit: Julian Sitarek (private communication).

removed as at lower energies they mimic the real events and/or distort the shape of an image of a real cosmic event.

There are three algorithms used in the analysis chains for removing these features:

1. First algorithm (SR1)

This algorithm deals with the pseudo-pulses. The pseudo-pulses are recognised during the calibration level with the help of the information from the first capacitor value of the previous event registered. The positions of this form of noise thus appear at fixed positions. The computational time for identifying spikes with this method is very fast and only modifies ~ 0.4% of the total waveform.

2. Second algorithm (SR2):

This algorithm scans the whole waveform and searches for the spike like pulses. The algorithm searches for pulses above the Gaussian noise rising rapidly with respect to the pulse height of the previous time-slice. Once the algorithm finds a spike-like event, it replaces the pulse height depending on the pulse height of the neighbouring slices.

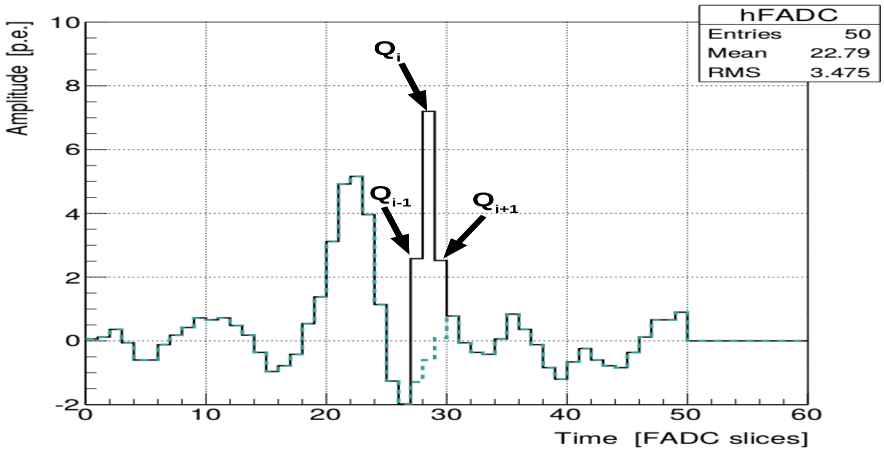

Figure 3.3: Modification of the *spiky events* wave-forms depending on the neighbouring time-slices. Based on charges (Q) in i-1, i, and i+1 slices and electronic noise value the spiky waveform is replaced following an interpolation. See text for details. Figure credit: Maxim Shayduk (private communication).

Figures 3.3 shows a typical behavior of this algorithm. The pulse shape is modified as $Q_{est} = c \times (Q_{i+1} + Q_{i-1})/2.0$, where Q_{est} is the modified pulse which is modified based on the neighbouring pulses Q_{i-1} and Q_{i+1}, and c is the normalization factor. The decision whether the pulse is indeed a spike is made depending on the parameter named as spikeness parameter calculated as S=$(Q_i - Q_{est})/Q_{est}$. Since, this type of spike-removal algorithm scans the entire waveform and is capable of modifying the same, it is considered as an aggressive method. This algorithm sometimes may treat the waveform of a real data as a spike-like pulse and modify the waveforms accordingly. However, this algorithm is computationally faster than SR1 by a factor of 2-3.

3. Third algorithm (SR3):

This third kind of algorithm uses the full waveform and searches for spike-candidates appearing in different pixels at similar times depending on specific parameters that define *spikes*. Some of the parameters are defined below:

1. Min: threshold value of the ADC counts above the baseline which points to a potential spike-candidate.

2. val: minimum amplitude that the spike-candidates can have.

3. Rel. ch.: relative change in the ADC counts in the neighbouring slices that a spike can cause for data (MC).

4. bmax: maximum bin width that a spike is supposed to posses.

This algorithm takes a Fourier transformation of the waveform and rejects the high frequency features for the total sample set. This is why it takes relatively longer time for executing spike removal than other algorithms.

A complete and very extensive check for the performance of the algorithms mentioned above has been carried out which was necessary for the optimisation of low energy analysis.

3.3 Spike removal tests on 3NN data:

Several tests have been performed to make SR3 more efficient by modifying all the relevant parameters involved in the algorithm. For this exercise, data from Crab Nebula from the night 2013/11/01 has been used. The *raw* data for both the telescopes has been downloaded from the MAGIC server and analysed in the local cluster at the Astrophysics and Cosmology division at Saha Institute of Nuclear Physics. In this analysis we ran the calibration of the data using *sorcerer* which require Pedestal-, Calibration- and Data-runs. In addition, we have done a similar check for spikes with the MC files (Pedestal-, Calibration- and Data-runs of MC files) specially generated with random spike-like features with more than 2 million events.

Str.	*Min*	*val*	*Rel. ch.*	*bmax*	Set-1 (MC)			Set-2 (data)			Set-3 (Pedestal)		
					data	ped.	cal.	data	ped.	cal.	data	ped.	cal.
s1	20	40	0.5	4	12.34	91.02	85.14	45.4	86.21	45.9	86.03	86.22	45.96
s2	30	50	0.1	4	12.52	92.11	84.85	54.34	84.68	63.14	54.24	84.68	63.14
s3	30	50	0.25	4	12.54	92.07	85.16	51.85	85.19	60.14	84.83	85.18	60.14
s4	30	50	0.25	2	9.87	70.15	63.56	15.06	68.33	11.71	68.07	68.32	11.71
s5	30	50	0.25	5	12.72	93.39	86.73	55.43	86.58	80.96	79.89	80.19	36.98
s6	30	50	0.25	3	11.86	86.43	79.08	36.25	80.19	36.99	86.22	86.59	80.97
s7	30	50	0.5	4	9.26	66.41	57.77	16.23	58.48	32.37	84.83	85.18	60.14
s8	30	50	0.75	4	1.34	5.88	6.39	3.5	14.26	7.57	14.19	14.26	7.56
s9	40	60	0.5	4	4.64	32.54	25.28	12.04	20.01	25.72	19.81	20.01	25.72
s10	50	70	0.5	4	0.61	3.23	1.97	7.40	2.08	21.05	2.18	2.08	21.05

Table 3.1: Percentage of pixels that have been identified with spikes and spike-removal applied for M1, for different strategies (different combinations of the parameters, named as s1, s2, s3, etc.) applied on the MC and data files. The numbers in the last nine columns are given in percentages (%). Columns 6-th to 8-th (Set-1) show results for the Spike removal algorithm applied on MC files. Columns 9-th to 11-th (Set-2) show the same for the Crab Nebula data. Columns 12-th to 14-th (Set-3) show the same for the Pedestal-runs (dedicated Pedestal run). For all three categories, we check the pixels identified with spikes in Data-, Pedestal-, and Calibration-runs. See text for details.

Str.	*Min*	*val*	*Rel. ch.*	*bmax*	Set-1 (MC)			Set-2 (data)			Set-3 (Pedestal)		
					data	ped.	cal.	data	ped.	cal.	data	ped.	cal.
s1	20	40	0.5	4	12.37	89.24	80.72	42.19	81.87	40.97	81.4	81.87	40.5
s2	30	50	0.1	4	12.63	90.96	80.60	55.40	80.50	60.50	79.64	80.50	60.50
s3	30	50	0.25	4	12.56	90.67	79.85	51.57	80.36	56.68	79.47	80.37	56.66
s4	30	50	0.25	2	8.91	65.39	52.94	15.39	58.07	9.42	57.10	58.07	9.42
s5	30	50	0.25	3	11.61	83.92	71.82	36.94	73.20	33.55	72.29	73.20	33.55
s6	30	50	0.25	5	12.79	92.32	81.84	57.11	82.47	76.76	81.57	82.47	76.76
s7	30	50	0.5	4	8.32	61.49	46.81	17.08	48.80	25.0	71.23	48.8	25.00
s8	30	50	0.75	4	0.19	0.98	0.13	3.44	8.05	2.52	7.27	8.05	2.47
s9	40	60	0.5	4	3.93	29.62	18.82	9.72	14.14	17.34	13.44	14.14	17.36
s10	50	70	0.5	4	0.37	1.58	0.43	6.61	1.71	13.02	1.75	1.71	13.01

Table 3.2: Percentage of pixels that have been identified with spikes and spike-removal applied for M2, for different strategies applied on MC, data, and Pedestal files. See caption of Table 3.1 and text for details.

Table 3.1 and 3.2 show the percentage of pixels identified having spiky events for M1 and M2 respectively, during the calibration of data with *sorcerer*. The identified spikes are also removed using the same algorithm. Here in the two tables the first 5 columns (columns 1-5) indicate the parameters corresponding to the spike removal strategy used to identify the spikes. The next three columns (columns 6-8) indicate the percentage of the pixels containing spikes for the MC. The next three columns (columns 9-11) point to the pixels containing the spikes in the data from Crab Nebula. As can be seen from these two tables, the maximum percentage of pixels with spikes are identified with the strategy-7 (**s5**). By this optimization, we have found the best configuration with *Min*, *val*, *Rel. ch.*, and *bmax* as 30, 50, 0.25, and 5 respectively. As a validation, we further test our configurations on a different Pedestal run of Crab Nebula data treated as a Data-run to check if a similar percentage of spikes is also identified and removed. The configuration s5 also provides the best spike identification and removal efficiency in case of the Pedestal-run treated as a Data-run.

The configurations s8, s9, and s10 identify spikes less efficiently as compared to s5. This is mainly because of a larger value of *Rel. ch.*. In case of s8, a *Rel. ch.* of 0.75 has been used which resulted in a poor identification of spikes. This is an indication of the fact the spikes can have lower relative change in amplitude in the neighbouring slices of a factor 0.25. Since, s5 is the most efficient spike removal strategy, the percentage of the surviving pedestals (reported in the next section) is the lowest.

In order to check whether the spike removal algorithm can lower the analysis threshold, we process data from Crab Nebula on 2013/11/07, 2013/11/12, and 2013/11/13 with and without the spike-removal algorithm. Figure 3.4 shows two cases where the lowest energy bin with data can be found around 60 GeV for both the cases - a) with the spike removal applied and b) without applying the spike removal. This indicates that even

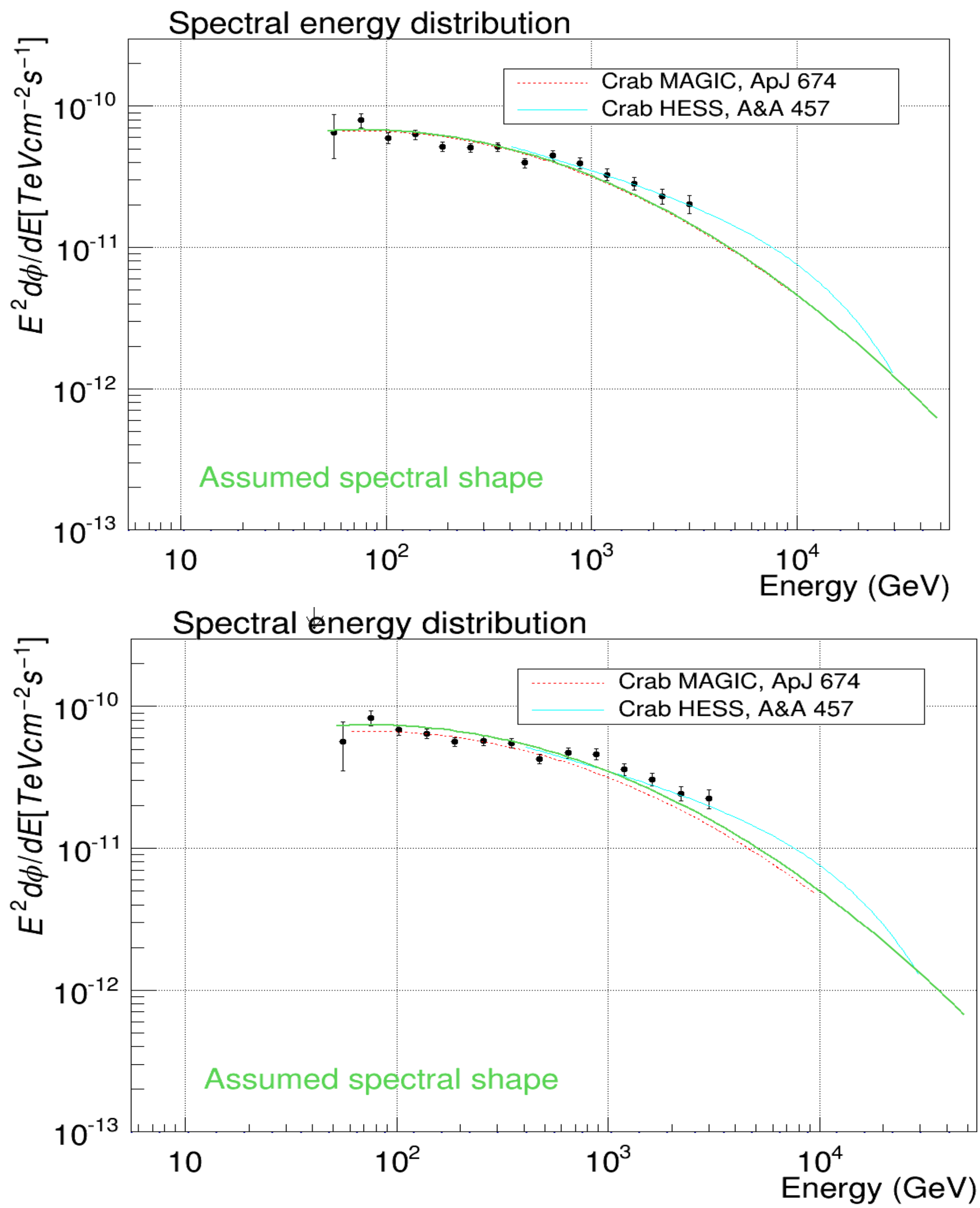

Figure 3.4: Spectral energy distribution of 3NN data from Crab Nebula analysed by: a) Without removal of the spikes (top panel) and b) With removal of the spikes (bottom panel). No significant difference can be noticed. See text for details.

after removing the spikes, the analysis threshold has not improved significantly. This is expected because of the higher level of cleaning threshold applied during *star*. In order to reduce the energy threshold, a new kind of image cleaning algorithm has been developed. In the following section, we will discuss the method that the new image-cleaning uses and the corresponding performances over the standard image cleaning method.

3.4 Tests on 3NN data: *New Cleaning* algorithm, motivation, and removal of stars from the FoV

As stated above, the standard image cleaning applied during the *star* is not suitable for the analysis below 60 GeV. The applied thresholds for image cleaning are optimized to reject the NSB and other spurious noises very efficiently, however, is high enough to exclude the low energy shower images to a great extent. Also, as the thresholds are decreased the effect of several noises in the form of spikes are highly dominant which results in distorted image formation. This is why a new image cleaning algorithm has been under consideration specifically for detecting the low energy events. Unlike the standard image cleaning algorithm, this new type of cleaning algorithm is designed to be executed at the calibration level. The algorithm works on the digitized waveform and mainly extracts two very important information: number of *calibrated* photo electrons and the corresponding time-tags. The cleaning algorithm predicts the core pixels of the image formed in the camera. The core image is identified when the signal crosses a trigger threshold for a group of 2, 3 or 4 pixels within a certain time-interval. This group of pixels is termed as 2, 3 or 4 nearest neighbour (NN) pixels. The signal threshold Q_{NN} and the time-interval T_{NN} depend on the geometry of the core pixel. Once the core pixels are selected, the boundary pixels are added as layers outside the core-pixels. For this,

M1	Q_{NN} (phe)	T_{NN} (ns)	M2	Q_{NN} (phe)	T_{NN} (ns)
2NN	7.3	1.41	2NN	8.4	1.41
3NN	4.2	1.71	3NN	4.6	1.71
4NN	3.3	1.91	4NN	3.6	1.91
Boundary	2.3	2.13	Boundary	2.5	2.13

Table 3.3: Optimized parameters for the non standard image cleaning method. The parameters have been optimised on the data.

each adjacent pixel to the core-pixels is considered as a potential candidate for boundary pixels. A slightly different time-constraint (T_B) is also applied to select the boundary pixels which cross a certain threshold Q_B. The application of this time constraint is particularly important to make sure that these boundary pixels carry information from the real shower and not the noise from the fluctuation of the baseline. In this way, many such boundary pixels around the core can be added in layers or rings which as a whole forms the shower image.

Table 3.3 shows different time constraints and threshold for core and boundary pixels. The cleaning parameters are optimized by checking the percentage of surviving pedestals in the image after cleaning. The optimisation study is carried out on the data of Crab Nebula.

Lowering the cleaning threshold introduces additional photon contribution from the stars in the field of view of the target object. This triggers the pixels and the camera registers these pixels as a part of the image from the shower. The image parametrization and image formation thus gets distorted. This requires a special treatment of the image which is known as the "star-removal" process in which bright stars in the field of view are removed based on their magnitude. In particular, there is a bright star in the field of view of Crab Nebula, named, Zeta-Tauri (R.A. 84.4083° and Dec. 21.1425°). According to the magnitude of the star Zeta-Tauri, a hole of 100 mm corresponding to 20 arcmin ($\sim 4\%$ of the total area of the camera) around the position of the star is removed from

	Cleaning Methods	Without spike removal	SR2	SR1	SR3
M1	Standard Cleaning	9.36 ± 0.78	4.00 ± 0.53	4.19 ± 0.54	3.70 ± 0.51
	New Cleaning	33.91 ± 1.27	16.56 ± 1.00	31.42 ± 1.25	N.A.
M2	Standard Cleaning	12.21 ± 0.88	6.95 ± 0.69	6.38 ± 0.66	7.45 ± 0.71
	New Cleaning	38.55 ± 1.32	31.42 ± 1.25	30.89 ± 1.24	N.A.

Table 3.4: Percentage of surviving pedestals in both the cameras (M1 and M2) after applying the spike-removal algorithms separately with the standard and *New Cleaning* without removing bright stars Zeta-Tauri from the field of view. The percentage of surviving pedestal is higher in M2 as compared to M1 because of different response in PMTs in M2. SR3 can not be applied along with the *New Cleaning* because both can not be applied at the same time during calibration. See text for details.

	Cleaning Methods	Without spike removal	SR1 + SR2	SR1 + SR3
M1	*New Cleaning*	26.14 ± 1.18	8.59 ± 0.76	6.86 ± 0.67
M2	*New Cleaning*	19.03 ± 1.07	8.54 ± 0.75	6.87 ± 0.68

Table 3.5: Percentage of surviving pedestals in both the cameras (M1 and M2) after applying the best possible combination of the spike-removal algorithms. Here, the *New Cleaning* algorithm is also used along with the removal of the bright star (Zeta-Tauri) in the field of view. See text for details.

the camera. The radius of the area to be removed depends on the brightness of the star. Since a hole in the camera is created a similar procedure is followed in MC files by identifying the pixels affected by the star, so that there is no mismatch between the data and MC.

In order to test the performance of the *New Cleaning* algorithm along with the spike removal algorithm, we select data sample from 2015/03/13, and test the percentage of surviving pedestals for both the standard and *New Cleaning* after removing the spikes.

In the following sections, the data set, the data analysis procedures, and the key-results are described. Table 3.4 shows the percentage of surviving pedestals after applying the standard and the *New Cleaning* with the three types of spike removal methods for both M1 and M2. The table shows that the introduction of the new image-cleaning results in a higher surviving pedestal, at least a factor of 4 for both M1 and M2. The fraction of surviving pedestals is similar for SR1, SR2 and SR3. The surviving pedestal is high in case of the *New Cleaning*. This is due to a direct influence of the bright stars in the field of view of Crab. Hence, we remove the Zeta-Tauri from the field of view. Table 3.5 shows the comparison between the combination of different spike removal algorithms for the *New Cleaning* method for both M1 and M2. In this study, we have combined the spike removal SR1 with both SR2 and SR3. The removal of the bright star decreases the percentage of surviving pedestals by a factor of 1.5–2 (see Tables 3.4 and 3.5). In addition, the spike removal further reduces the same by a factor of 2–3 (see Tables 3.4 and 3.5).

The time required for the execution of the spike-removal "SR1+SR3" (or SR3 alone) is around a factor of 2-3 longer than the "SR1+SR2" (or SR2 alone). The execution of SR1 takes less than 1% time required for the execution *sorcerer*. This is a crucial conclusion as the *raw* data is very heavy (2 GB for 2 minutes of observation) and thus requires a very long time to calibrate. That is why additional execution time due to spike removal will slow the process even more. Because of this the combination of SR1 and SR2 has been preferred over the combination of SR1 and SR3, though the performance of SR3 (or "SR1+SR3") is less aggressive than SR2 (or "SR1+SR2")). In the following section we will discuss the performance of SR1+SR2 and the results that have been obtained.

3.5 Description of data:

ON-data: The raw data from the Crab Nebula (ON-data) for the following days: 2017/11/19, 2017/11/20, 2017/11/23, 2017/11/24, 2018/03/09, 2018/03/11, and 2018/03/12 of around

6 hours are processed with the same set of parameters mentioned above for the spike-removal and image-cleaning during the calibration of the *raw* data.

According to the zenith angle range, 5° - 35°, the *calibrated* MC files are selected. The MC files for both the cameras (M1 and M2) are divided into two groups: "test" and "train" samples. The test and train samples are processed as we process the ON-data and OFF-data respectively.

Both the *calibrated* data from Crab and *test*-MC are processed with *star* separately, where a circular patch of radius 100 mm around the bright star Zeta-Tauri (RA: 5.627416 and DEC: 21.1425) is removed. A set of pixels in the MC image corresponding to 100 mm is also removed during the execution of *star*. In the later step, *superstar*, the data from the two camera M1 and M2 are combined to make a stereo image for both the data from Crab and the test sample of MC files.

OFF-data: The source S3 0218+35 has been used as the OFF-data because it does not contain any signal. In total, ~ 3.0 hrs of data from the nights 2016/08/10, 2016/08/14, 2016/08/31, and 2016/10/01 taken under dark background conditions (very low NSB), at low zenith angle (5°-35°), and above air transmission (Tr.) of 70%, has been selected. The *New Cleaning* algorithms along with the first and second type of spike removal algorithm have been used at the time of calibration of the data. The parameters for the cleaning and spike-removal have been used from Table 3.3.

In the next step, the $\gamma-$hadron separation is performed with the help of the RF matrices prepared with the train sample of MC files and the OFF-data sample. The *melibea* files are prepared for both the test MC files and the data from the Crab Nebula. The spectrum and light-curve are made with the help of *flute* executed on the *melibea* files of the Crab Nebula data and the *test* sample of the MC files. The results are shown in the next section.

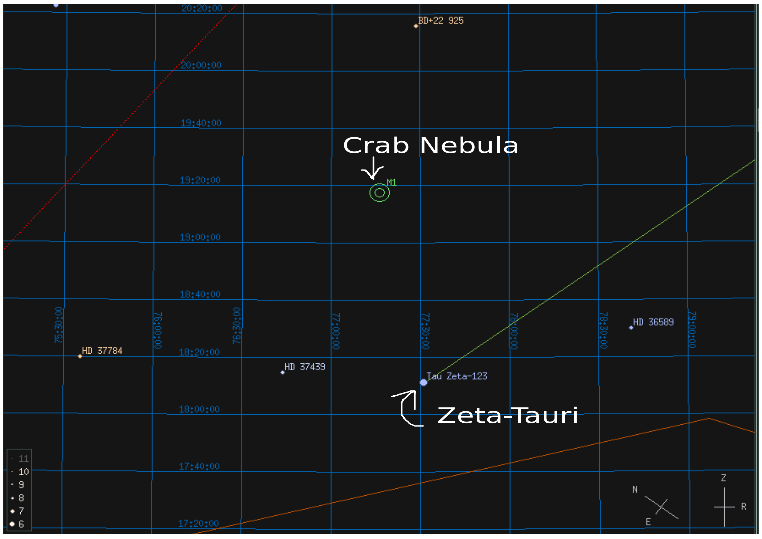

Figure 3.5: Zeta-Tauri, a bright star located in the field of view of Crab Nebula. For lower cleaning threshold (lower than the standard cleaning for MAGIC analysis) Zeta-Tauri deforms the shape of the shower image formed in the camera. Hence, this star is removed by removing the corresponding pixels of the camera.

3.6 Results of the cleaning studies:

As can be seen from Figure 3.5, there are few bright stars in the field of view of Crab. Since the standard cleaning applies a higher cut-off the contribution from the star is negligible. However, as the *New Cleaning* is applied, because of its lower cleaning levels the stars start to contribute more to the surviving pedestals which raise the baseline of the background events. In order to reduce the contribution from these stars in the background, star removal algorithm is applied which reduces the surviving pedestals. For longer exposures, the stars in the field of view of the target source move. This leaves trail(s) in the camera plane. This is why an average position of the star in the FoV is calculated and affected pixels are not considered. Similarly, the location of those pixels which are affected are removed from the MC files.

Table 3.6 shows the percentage of surviving pedestals for both the cleaning methods

Run No.	Standard Cleaning		*New Cleaning*	
	M1	M2	M1	M2
05068836	1.21± 0.07	2.42±0.11	10.09±0.21	5.91±0.16
05068837	1.29±0.07	2.34±0.11	12.65±0.22	9.13±0.19
05068838	1.11±0.07	2.27±0.11	10.01±0.21	4.96±0.15
05068839	1.24±0.07	2.49±0.11	12.21±0.22	9.29±0.19
05068840	0.95±0.11	2.39±0.16	8.21±0.28	5.55±0.24

Table 3.6: Percentage of surviving pedestals in both the cameras (M1 and M2) for the different runs of standard triggered (3NN) Crab Nebula data on 2017/11/19, after applying the best possible combination of the spike-removal algorithms. Here, the bright star (Zeta-Tauri) in the field of view has been removed. See text for details.

applied on the data of Crab Nebula on 2017/11/19 for the runs 05068836-05068840. With the help of the *New Cleaning* and the star removal the surviving pedestal has been reduced down to $\sim 10\%$. The rate vs zenith distribution has also been checked for the background. Figure 3.6 shows two rate vs zenith distributions for S3 0218+35 on 2016/08/31 (Run 05056072). The right panel shows that the rates are increased for the *New Cleaning* as compared to the standard cleaning shown in the left panel for using a lower cleaning, however, the rates are stable within 10%. As can be seen from Figure 3.7, the energy threshold by applying the *New Cleaning* algorithm has reduced the energy threshold significantly. The energy threshold for the standard cleaning turns out to be above 60 GeV whereas the *New Cleaning* has an energy threshold of $\sim$ 50 GeV.

A comparison of the excess events is shown in Fig. 3.8 (and Table 3.7), where the right panel shows the excess vs. energy for the standard analysis and the left panel shows the excess vs. energy for the new analysis method. The improvement in the significance can be clearly seen from this figure. The number of bins for the new analysis method with significance above 5 sigma is three below 100 GeV, where the same for the standard analysis is only two. However, from this plot it can be seen that the significance

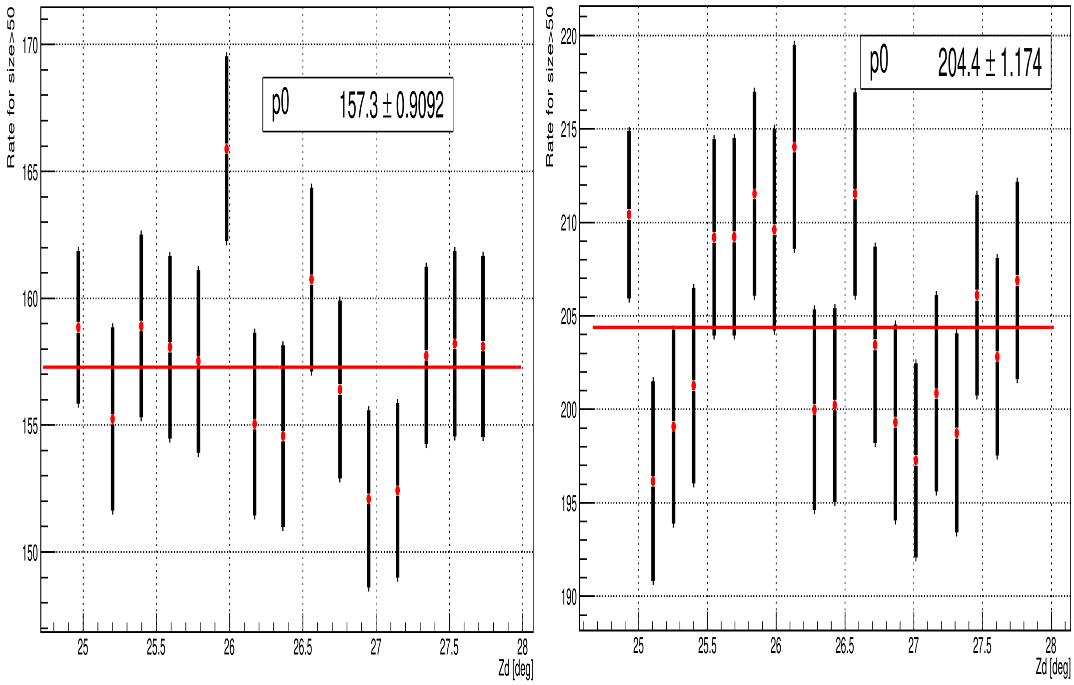

Figure 3.6: Rate of the events as a function of the zenith angle. The left and the right plots show rate vs. zenith after applying standard and the *New Cleaning* on 3NN data of S3 0218+35. See text for details.

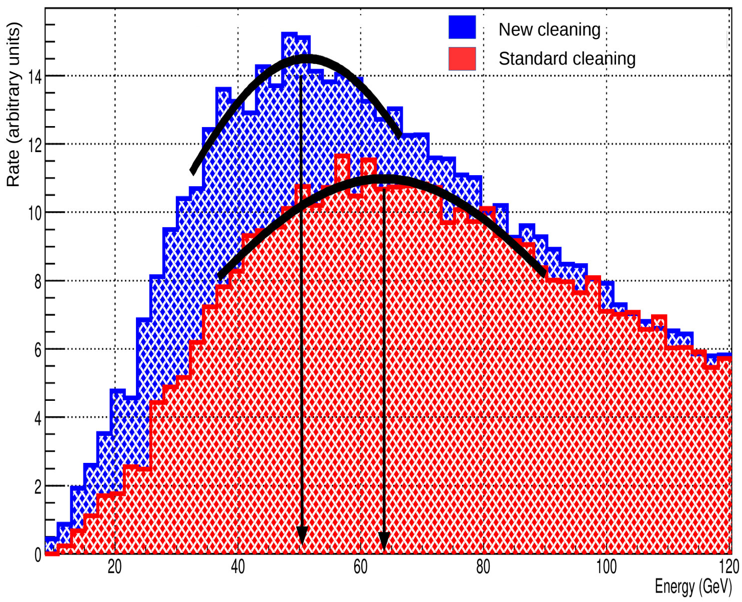

Figure 3.7: Energy threshold plot for the two cases for: a) the standard cleaning and b) *New Cleaning*. The *New Cleaning* reduces the energy threshold for the 3NN (standard data). See text for details.

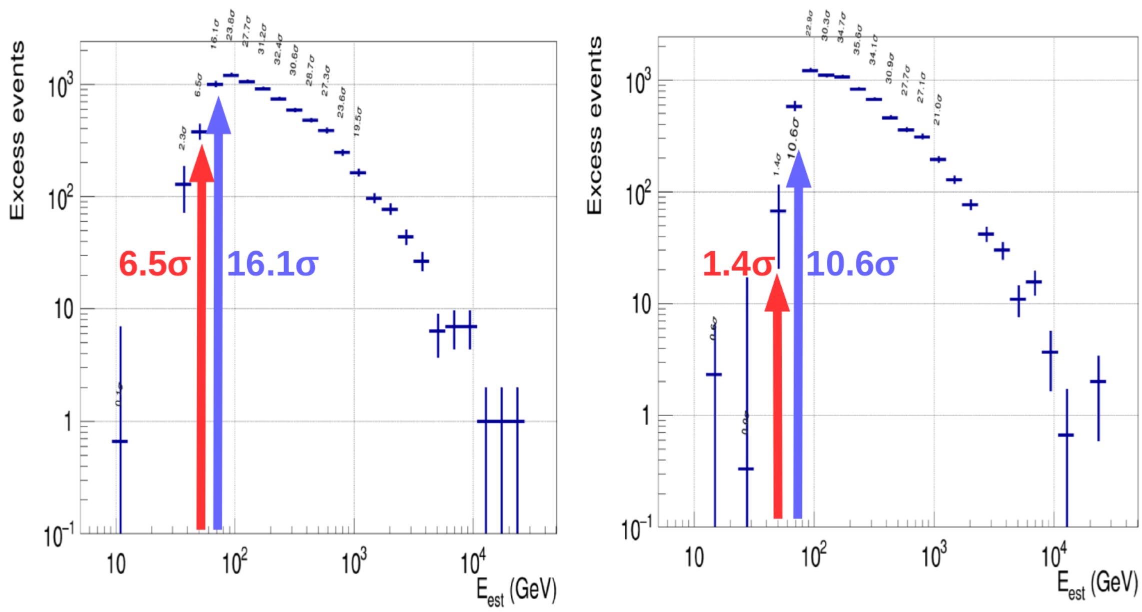

Figure 3.8: Excess events for the *New Cleaning* (left) and standard cleaning (right) with the default settings (*hadronness cuts*=0.16, *signal cuts* of 0.009, cut efficiency of 90%). In both cases, spike-removal algorithms have been applied. The excess at energies less than 100 GeV increases significantly. Table 3.7 presents the list of significance of the excess events at different energy bins. See text for details.

Energy bin (GeV)	Significance (σ)	
	New Cleaning	Standard cleaning
43.1 – 58.6	6.5	1.4
58.6 – 79.6	16.1	10.6
79.6 – 108.2	23.8	22.9
108.2 – 147.1	27.7	30.3
147.1 – 200.0	31.2	34.7
200.0 – 271.9	32.4	35.6
271.9 – 369.6	30.6	34.1
369.6 – 502.4	28.7	30.9
502.4 – 682.9	27.3	27.7
682.9 – 928.3	23.6	27.1
928.3 – 1261.9	19.5	21.0

Table 3.7: Significance of the excess events in different energy bins presented in Fig. 3.8. See text for details.

θ^2 cuts $\downarrow$	Hadronness cuts $\rightarrow$					
	0.01	0.05	0.1	**0.16**	0.3	0.5
0.005	1.38±0.12	0.93±0.09	0.85±0.06	0.91±0.05	0.98±0.05	1.08±0.05
0.009	1.47±0.11	0.87±0.07	0.80±0.04	0.86±0.05	0.91±0.04	1.02±0.04
0.02	1.62±0.11	1.02±0.05	0.93±0.06	0.93±0.04	0.97±0.03	1.08±0.03
0.04	2.43±0.29	1.28±0.07	1.10±0.05	1.09±0.04	1.15±0.04	1.3±0.04

Table 3.8: Detection sensitivity of the 3NN Crab data processed with the *New Cleaning* with different combinations of hadronness cuts and θ^2 cuts (signal cuts). For energy above 200 GeV, hadronness cut of 0.1 and θ^2 cuts of 0.009 provides the best value for the sensitivity, however, this is not significantly different from the value obtained with the default hadronness cuts and θ^2 cuts (marked in boldface).

drops significantly for the new analysis method above 100 GeV as compared to the standard analysis. The source significance above 200 GeV has been studied with different combinations of *hardronness cut* and *signal cut* (see Chapter 2 for the details of these parameters). However, significant improvement has not been noted with different cuts (see Table 3.8) and there is no room for improvement with respect to the default cuts.

Figure 3.9 shows the presence of two extra spectral points in the new analysis as compared to the standard analysis. These two additional data points are coming from using the *New Cleaning* algorithm. Figure 3.10 shows the LCs for two cleaning algorithms which are compatible with each other.

3.7 Conclusions on the *spike-removal* and *image cleaning* tests:

The work establishes that the spike removal method SR1 combined with SR3 provides lower surviving pedestals. However, SR1 & SR3 is relatively slower and is not suitable for practical applications. The tests on the cleaning studies reveal that the *New Cleaning* method along with the spike removal applied to the standard 3NN data is able to push

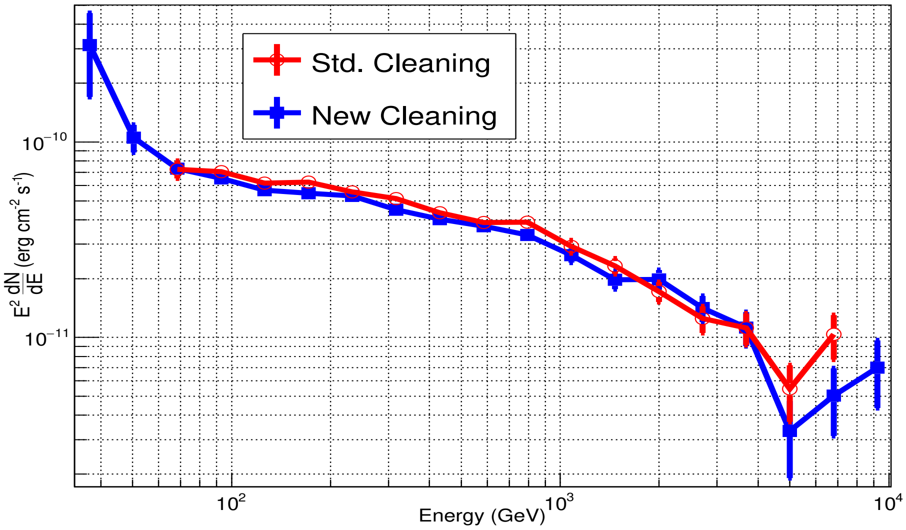

Figure 3.9: Spectrum of Crab Nebula for the *New Cleaning* and the standard cleaning. The *New Cleaning* provides two additional data point at the lower energies down to 40-50 GeV, as compared to the standard analysis. See text for details.

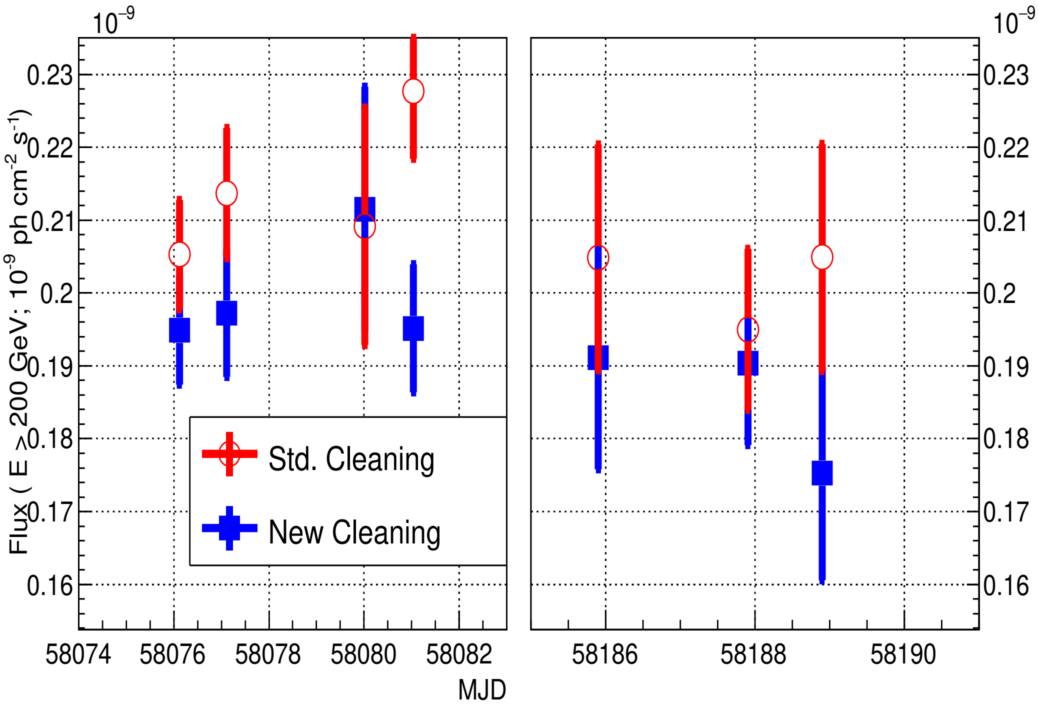

Figure 3.10: Light curve of Crab Nebula for the *New Cleaning* and the standard cleaning. The right and left panels show two different observation periods of analysis. See text for details.

the energy threshold down to 40-50 GeV. The low energy part of the spectrum below 100 GeV is consistent with the result of standard analysis. Figure 3.8 shows that the signal at higher energies, above 100 GeV, is associated with low significance. This indicates that the signal events are removed at higher energies while recovering the low energy events for the *New Cleaning* algorithms. This issue has been investigated further and a *hybrid cleaning*, a combination of the *New Cleaning* and the standard cleaning, has been developed. The *hybrid cleaning* is capable of recovering the loss of sensitivity in the higher energies (above 100 GeV). However, the description of the *hybrid cleaning* and its details are out of scope of this thesis.

4

Multiwavelength variability and correlation studies of Mrk 421 during historically low X-ray and γ-ray activity in 2015–2016

4.1 Introduction

Mrk 421, located at a redshift z = 0.031 (Ulrich et al. 1975), is an extensively studied TeV source. The light curve (LC) of Mrk 421 is highly variable, and it has gone into outburst several times in all bands (radio to TeV) in which it is observed. During an outburst, the TeV emission can vary on sub-hour timescales (Gaidos et al. 1996; Abeysekara et al. 2020). Many attempts have been made to trace the ongoing physical processes inside the jet. The majority of the simultaneous multiwavelength (MWL) observations were performed during flaring activity, when the VHE γ-ray flux of Mrk 421 exceeded the flux of the Crab Nebula[1] (there after 1 Crab) by 2–3 times, which is the standard candle for ground-based γ-ray instruments (Macomb et al. 1995a; McEnery et al. 1997; Zweerink et al. 1997; Krennrich et al. 2002; Acciari et al. 2011a; Aleksić et al. 2015c). Only a handful of attempts have been made to study the broad-band emission of Mrk 421 during non-flaring episodes. For instance, Horan et al. (2009) report a very detailed study using MWL observations of Mrk 421 that were not triggered by flaring episodes. But the VHE γ-ray activity of Mrk 421 during this observing campaign (mostly in 2006) was twice the typical VHE γ-ray activity of Mrk 421, which, according to Acciari et al. (2014), is half the flux of the Crab Nebula. Moreover, the data from Horan et al. (2009) actually contained two flaring episodes, when the flux from Mrk 421 was higher than double that of the Crab Nebula for several days. On the other hand, Aleksić et al. (2015b) performed a study with the data from a MWL campaign in 2009, when Mrk 421 was at its typical VHE γ-ray flux level, and Baloković et al. (2016a) reported an extensive study with data from 2013 January-March, when Mrk 421 showed very low-flux at X-ray and VHE.

One of the key aspects that has been investigated in several past MWL campaigns on Mrk 421 is the correlation between X-rays and VHE γ-rays. A direct correlation between these two wave-bands has been reported in several articles (e.g. Macomb et al. 1995b; Buckley et al. 1996; Albert et al. 2007a; Fossati et al. 2008; Donnarumma et al. 2009; Abdo et al. 2011a; Acciari et al. 2011b; Cao & Wang 2013; Aleksić et al. 2015c; Bartoli et al. 2016a). However, almost all of these studies were carried out during flaring activity. There are only two cases which report such a correlation during low activity without flares: Aleksić et al. (2015b) measured the VHE/X-ray correlation with a marginal significance of $3\,\sigma$, and Baloković et al. (2016a), report the VHE/X-ray corre-

[1]The flux of the Crab Nebula, used in this work for reference purposes, is retrieved from Aleksić et al. (2015a)

lation with high significance despite the low-flux in X-ray and VHE γ-rays thanks to the very high sensitivity *NuSTAR* and stereoscopic data from MAGIC and VERITAS. The emission among the other energy bands appears to be less correlated than that for the X-ray and VHE bands, and Macomb et al. (1995b), Albert et al. (2007a), Cao & Wang (2013) and Baloković et al. (2016a) reported no correlation between the optical/UV and X-rays and the optical/UV and TeV bands during low states of the source.

Using data taken in 2009, Aleksić et al. (2015b) found a negative correlation between the optical/UV and the X-ray emission. The cause of this correlation was the long-term trend in the optical/UV and in X-ray activity; while the former increased during the entire observing campaign, the latter systematically decreased. This correlation was statistically significant when considering only the 2009 dataset but, using data from 2007 to 2015, Carnerero et al. (2017) did not measure any overall correlation between the optical and the X-ray emission. On the other hand, Carnerero et al. (2017) did find a correlation between the GeV and the optical emission. This correlation study used the discrete correlation function (DCF, Edelson & Krolik 1988) and identified a peak with a DCF value of about 0.4, centered at zero time lag (τ) but extending over many tens of days to positive and negative values. However, the statistical significance of this correlation was not reported. As for the radio bands, the 5 GHz radio outburst lasting a few days in 2001 February/March, and occurring at approximately the same time as an X-ray and VHE flare, was reported by Katarzyński et al. (2003) as evidence of correlation without any time lag between the radio and X-ray/VHE emission in Mrk 421. But the statistical significance of this positive correlation was not reported. As there were many similar few-day X-ray and VHE flares throughout 2001, but only a single radio flare, the claimed correlation may simply be chance coincidence. Using the low activity data taken over almost the whole year 2011, Lico et al. (2014) reported a marginally significant ($\leq 3\sigma$) correlation between radio very long baseline interferometry (VLBI) and GeV γ-rays for a range of about $\pm$30 days centered at τ=0. Max-Moerbeck et al. (2014), however, reported a positive correlation between the GeV and radio emission at $\tau \sim 40$ days. However, the correlation reported there was only at 2.6 σ significance , and was strongly affected by the large γ-ray and radio flares from July and September 2012, respectively (Max-Moerbeck et al. 2014).

Overall, the broadband emission of Mrk 421 is complex, and a dedicated correlation analysis over many years will be necessary in order to properly characterize it. It is relevant to evaluate whether the various trends or peculiar behaviours, sometimes reported in the literature with only marginal significance, are repeated over time, and also to distinguish the typical behaviour from the sporadic events. For the latter, it is important to collect multi-instrument data that are not triggered or motivated by flaring episodes. A better understanding of the low-flux state will not only provide meaningful constraints on the model parameters related to the dynamics of the particles inside the jet, but also will provide a baseline for explaining the high-state activity of the source.

The study presented in this work focuses on the extensive MWL dataset collected during the campaigns in the years 2015 and 2016, when Mrk 421 showed low activity in both X-rays and VHE γ-rays, and no prominent flaring activity (>2 Crabs for several days) was measured. We characterize the variability using the normalized excess variance of the flux (Vaughan et al. 2003) for the X-ray and TeV bands split into two hard bands ($2 - 10$ keV and >1 TeV) and two soft bands ($0.3 - 2$ keV and $0.2 - 1$ TeV). We use these bands to compute the hardness ration, HR_{keV} and HR_{TeV}, defined as the ratio between the flux in the hard band to the flux in the soft band in order to evaluate the harder-when-brighter behaviour of the source. Using this data set, we present a detailed correlation study for different combinations of wave-bands. In order to better

	3NN			4NN
	Low-Moon	Moderate-Moon	High-Moon	Low-Moon
Low-zenith ($5° - 35°$)	~30.0 hrs	~10.0 hrs	~6.0 hrs	~7.0 hrs
Medium-zenith ($35° - 50°$)	~4.0 hrs	~1.0 hrs	~1.0 hrs	~2.0 hrs
High-zenith ($50° - 62°$)	1.0 hrs		2.0 hrs	

Table 4.1: Observation conditions at VHE γ-rays with the MAGIC telescopes during the 2015–2016 campaign. Apart from the standard data (3NN), a subset was taken without a coincidence trigger and a 4NN single-telescope trigger logic. See Section 4.2.5 for details.

evaluate the correlations among the energy bands with lower amplitude variability and longer variability timescales, we complemented the 2015–2016 dataset with data from previous years (from 2007 to 2014). A fraction of these data had already been published (Aleksić et al. 2012b, 2015c; Ahnen et al. 2016; Baloković et al. 2016a), and the rest were specifically collected and analyzed for the study presented here.

This chapter is arranged in the following way: in Section 4.2 we describe the instruments that participated in this campaign, the data analysis methods used for each energy band, and and a summary of the observed MWL data. In Section 4.3, we discuss the main characteristics of the MWL light curves from the 2015–2016 campaign. In Section 4.5, 4.6, and 4.7, we discuss the different aspects of the MWL variability and correlation studies. In Section 4.8, we discuss the estimation of the most representative time-lag for the correlation between optical/GeV vs. radio bands. In Section 4.9 and 4.10, we characterize the flux distributions in the different wave-bands, and in Section 4.11, we discuss and summarize the main observational results from our work. This chapter is based on a work submitted to MNRAS.

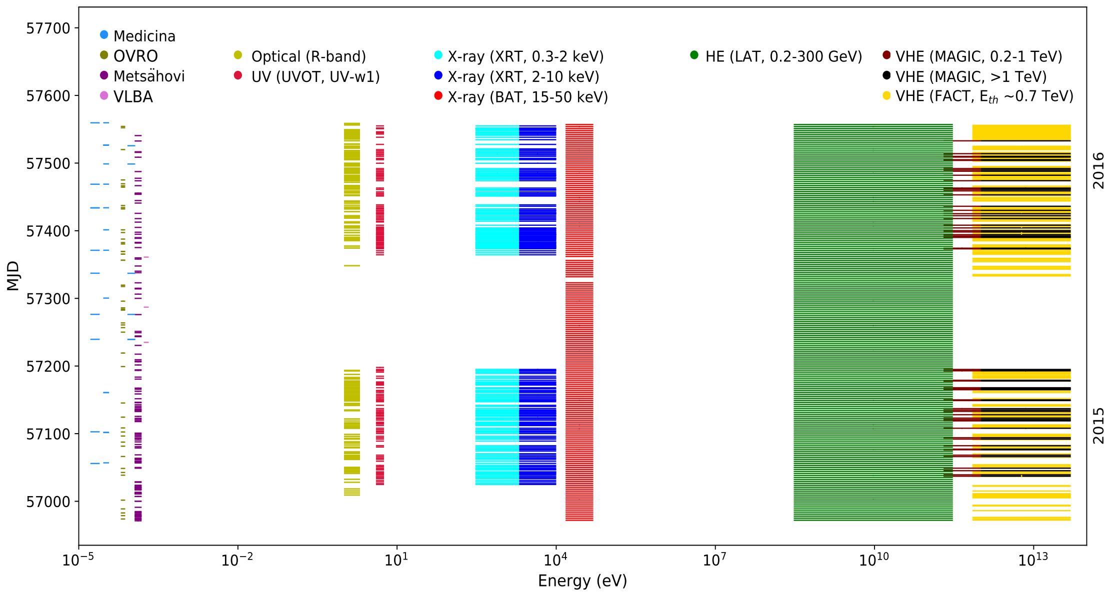

Figure 4.1: Multi-instrument temporal coverage of Mrk 421 during the 2015–2016 observation campaign.

4.2 Observations and data analysis

The temporal and energy coverage provided by the MWL observations from the two-year period reported in this work, i.e., from 2014 November to 2016 June, is depicted in Fig. 4.1. In the subsections below, we discuss the instrumentation and data analyses used to characterize the emission of Mrk 421 across the electromagnetic spectrum, from radio to VHE γ-rays.

4.2.1 Radio

The study presented here makes use of radio observations from the single-dish radio telescopes at the Metsähovi Radio Observatory, which operates at 37 GHz, at the Owens Valley Radio Observatory (OVRO, at 15 GHz), and the Medicina radio telescope, which provides multi-frequency data at 5 GHz, 8 GHz, and 24 GHz. The data from OVRO were retrieved directly from the web page of the instrument team[2], while the data from Metsähovi and Medicina were provided to us directly by the instrument team. Mrk 421 is a point source for all of these instruments, and hence the measurements represent an integration of the full source extension, which has a larger size than the emission that dominates the highly variable X-ray and γ-ray emission. Details of the observation and data analysis strategies from OVRO and Medicina are reported in Richards et al. (2011) and Giroletti & Righini (2020), respectively. As for Metsähovi, the detection limit of the telescope at 37 GHz is in the order of 0.2 Jy under optimal conditions. The flux density scale is set by observations of DR 21, and the sources NGC 7027, 3C 274, and 3C 84 are used as secondary calibrators. The error estimate on the Metsähovi flux density includes the contributions from the rms measurement and the uncertainty in the absolute calibration. A detailed description of the data reduction and analysis is given in Teraesranta et al. (1998). In this particular analysis, as is done in most analyses, the measurements that do not survive a quality control (usually due to unfavourable weather) are discarded semi-automatically. In the final data reduction, the measurements are checked manually, which includes ruling out bad weather conditions or other environmental effects such as, e.g., a rare but distinct flux density increase caused by aircraft in the telescope beam. Additionally, the Metsähovi team also checked that the general flux levels are consistent for adjacent measurements (i.e. other sources observed before and after the target source).

The study also uses the Very Long Baseline Array (VLBA) total and polarized intensity images of Mrk 421 at 43 GHz obtained within the VLBA-BU-BLAZAR program of ~monthly monitoring of a sample of γ-ray blazars[3]. The source was observed in a short-scan mode along with ~30 other blazars over 24 hrs, with ~45 min on the source.

[2] http://www.astro.caltech.edu/ovroblazars/index.php?page=home
[3] http://www.bu.edu/blazars/VLBAproject.html

A detailed description of the observations and data reduction can be found in Jorstad et al. (2017). The analysis of the polarization properties was based on Stokes Q and U parameter images obtained in the same manner as described in Jorstad et al. (2007).

4.2.2 Optical

In this work, we use only R-band photometry. These optical data were obtained with the KVA telescope (at the Roque de los Muchachos), ROVOR, West Mountain Observatory, and the iTelescopes network. The stars reported in Villata et al. (1998) were used for calibration, and the coefficients given in Schlafly & Finkbeiner (2011) were used to correct for the Galactic extinction. The contribution from the host galaxy in the R band, which is about 1/3 of the measured flux, was determined using Nilsson et al. (2007), and subtracted from the values reported in Fig. 4.2. Additionally, a point-wise fluctuation of 2 per cent on the measured flux was added in quadrature to the statistical uncertainties in order to account for potential day-to-day differences in observations with any of the instruments.

4.2.3 Neil Gehrels *Swift* Observatory

This study uses the following instruments on board the Neil Gehrels *Swift* Observatory (Gehrels et al. 2004):

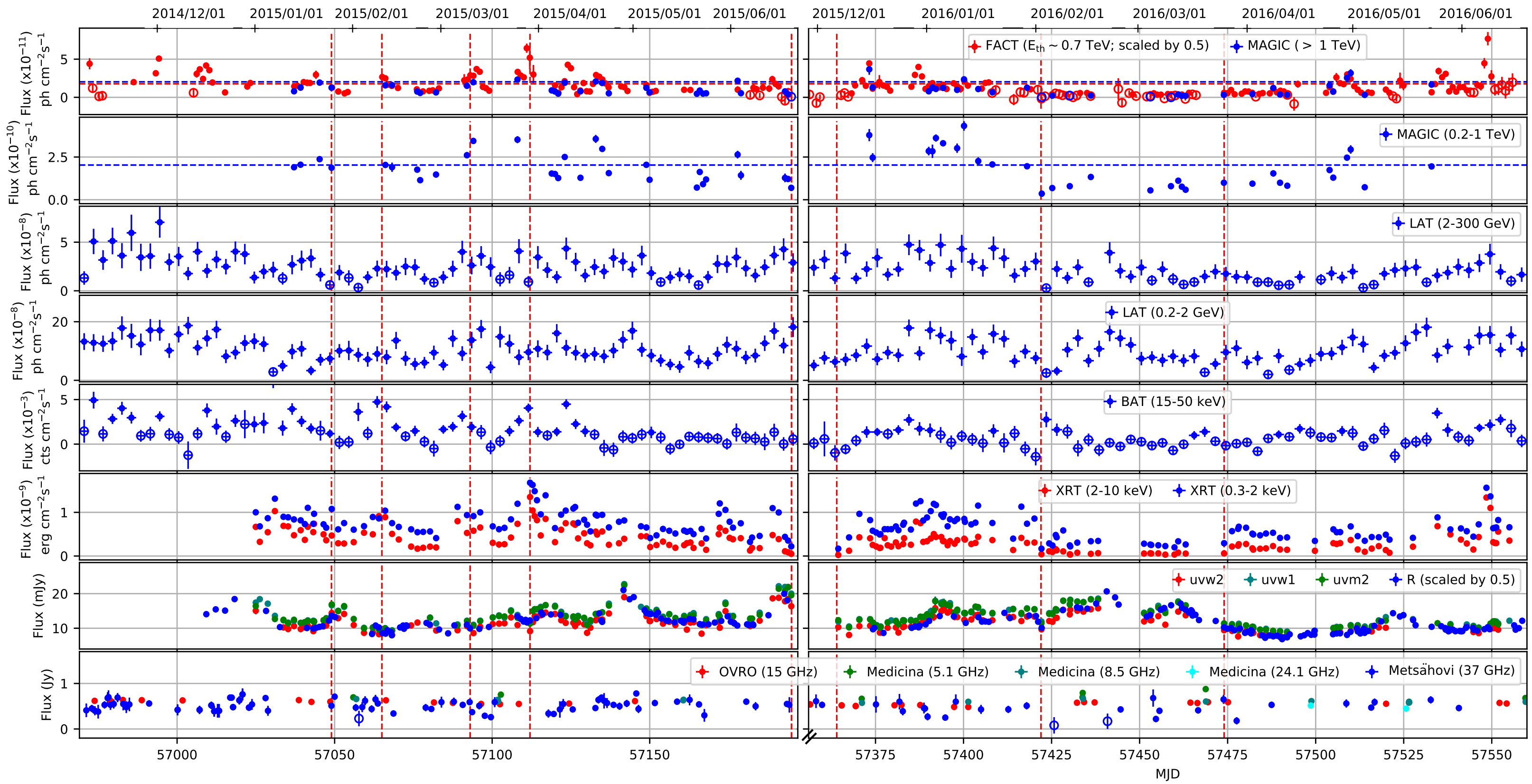

Figure 4.2: From top to bottom: light curves of MAGIC, FACT, *Fermi*-LAT, *Swift*-BAT, -XRT, and -UVOT, optical R-band telescopes (KVA telescope at the Roque de los Muchachos, ROVOR, Brigham, New Mexico Skies and the iTelescopes), Metsähovi, OVRO, and Medicina from 2014 November to 2016 June. A 3-day temporal bin has been used for the HE γ-ray fluxes from *Fermi*-LAT and hard X-ray fluxes from *Swift*-BAT. For all of the other energy bands, individual single night observations are depicted. The vertical dashed red lines represent interesting flux variations discussed in Section 4.3. The LCs from FACT and R-band are scaled by a factor of 0.5 for better visibility. In the top panel, horizontal blue and red lines represent the flux of the Crab Nebula above 1 TeV and above 0.7 TeV energy (the latter one scaled by a factor of 0.5), respectively. The horizontal line in the second panel from the top represents the the flux of the Crab Nebula in the 0.2 – 1 TeV energy band. The open markers in the MAGIC (>1 TeV), FACT, LAT, BAT, and Metsähovi light curves are used to display flux measurements with a relative error larger than 0.5.

UVOT

The *Swift* UV/Optical Telescope (UVOT; Roming et al. 2005a) was used to perform observations in the UV range (with the filters W1, M2, and W2). For all of the observations, data were analyzed using aperture photometry for all filters using the standard UVOT software distributed within the HEAsoft package (version 6.16), and the calibration files from CALDB version 20130118. The counts were extracted from an aperture of 5 arcsec radius, and converted to fluxes using the standard zero points from Breeveld et al. (2011). Afterwards, the fluxes were dereddened using $E(B-V) = 0.012$ (Schlafly & Finkbeiner 2011) with $A_\lambda/E(B-V)$ ratios calculated using the mean Galactic interstellar extinction curve reported in Fitzpatrick (1999). Mrk 421 is on the "ghost wings" (Li et al. 2006) of the nearby star 51 UMa in many of the observations, and hence the background had to be estimated from two circular apertures of 16 arcsec radius off the source, symmetrically with respect to Mrk 421, excluding stray light and shadows from the support structure.

XRT

The *Swift* X-ray Telescope (XRT; Burrows et al. 2005) was used to perform observations in the energy range from 0.3 keV to 10 keV. All of the *Swift*-XRT observations were taken in the Windowed Timing (WT) readout mode. The data were processed using the XRTDAS software package (v.3.2.0), which was developed by the ASI Space Science Data Center (SSDC) and released by HEASARC in the HEASoft package (v.6.19). The event files were calibrated and cleaned with standard filtering criteria with the `xrtpipeline` task using the calibration files available from the *Swift*/XRT CALDB (version 20160609). For each observation, the X-ray spectrum was extracted from the summed cleaned event file. Events for the spectral analysis were selected within a circle of 20-pixel ($\simeq$46 arcsec) radius, which encloses about 90 per cent of the point-spread function (PSF), centered at the source position. The background was extracted from a nearby circular region of 40-pixel radius. The ancillary response files (ARFs) were generated with the `xrtmkarf` task applying corrections for PSF losses and CCD defects using the cumulative exposure map.

Before the spectral fitting, the 0.3 – 10 keV source spectra were binned using the `grppha` task to ensure a minimum of 20 counts per bin. The spectra were modeled in XSPEC using power-law and log-parabola models that include a photoelectric absorption by a fixed column density estimated to be $N_{\rm H} = 1.92 \times 10^{20}\,{\rm cm}^{-2}$ (Kalberla et al. 2005). The log-parabola model typically fits the data better than the power-law model (though statistical improvement is marginal in many cases), and was therefore used to compute the X-ray fluxes in the energy bands 0.3 – 2 keV and 2 – 10 keV, which are reported in Fig. 4.2.

BAT

A daily average flux in the energy range 15 – 50 keV measured by the *Swift*-BAT instrument was obtained from the BAT website[4]. The detailed analysis procedure can be found in Krimm et al. (2013). The BAT fluxes related to time intervals of multiple days reported in this work were obtained by performing a standard weighted average of the BAT daily fluxes, which is exactly the same procedure used by the BAT team to obtain the daily fluxes from the orbit-wise fluxes.

[4] http://heasarc.nasa.gov/docs/swift/results/transients/

4.2.4 *Fermi*-LAT

The GeV γ-ray fluxes related to the 2015–2016 observing campaigns were obtained with the Large Area Telescope (LAT, Atwood et al. 2009a) onboard the *Fermi* Gamma-ray Space Telescope. The *Fermi*-LAT data presented in this work were analyzed using the standard *Fermi* analysis software tools (version *v11r07p00*), and the *P8R3_SOURCE_V2* response function. We used events from 0.2 − 300 GeV selected within a 10° region of interest (ROI) centered on Mrk 421 and having a zenith distance below 100° to avoid contamination from the Earth's limb. The diffuse Galactic and isotropic components were modelled with the files gll_iem_v06.fits and iso_P8R3_SOURCE_V2.txt respectively[5]. All point sources in the third *Fermi*-LAT source catalog (3FGL Acero et al. 2015a) located in the 10° ROI and an additional surrounding 5°-wide annulus were included in the model. In the unbinned likelihood fit, the spectral shape parameters were fixed to their 3FGL values, while the normalizations of the eight sources within the ROI identified as variable were allowed to vary, as were the normalisations of the diffuse components and the spectral parameters related of Mrk 421.

Owing to the moderate sensitivity of *Fermi*-LAT to detect Mrk 421 on daily timescales (especially when the source is not flaring), we performed the unbinned likelihood analysis on 3-day time intervals to determine the light curves in the two energy bands 0.2 − 2 GeV and 2 − 300 GeV reported in Fig. 4.2. The flux values were computed using a power-law function with the index fixed to 1.8, which is the spectral shape that describes Mrk 421 during the two years considered in this study, as well as the power-law index reported in the 3FGL and 4FGL (Acero et al. 2015a; Abdollahi et al. 2020). The analysis results are not expected to change when using the 4FGL (Abdollahi et al. 2020) (instead of the 3FGL) for creating the XML file. This is due to the 3-day time

[5]https://fermi.gsfc.nasa.gov/ssc/data/access/lat/BackgroundModels.html

intervals considered here, which are very short for regular LAT analyses, implying that only bright sources (i.e. already present in the 3FGL) can significantly contribute to the photon background in the Mrk 421 RoI. We repeated the same procedure fixing the photon indices to 1.5 and 2.0, and found no significant change in the flux values, indicating that the results are not sensitive to the selected photon index used in the differential energy analysis. For the multi-year (2007-2016) correlation study reported in Section 4.6, where the GeV flux is compared to the radio and optical fluxes, we applied the same analysis described above, but this time for all events above 0.3 GeV in the time interval MJD 54683–57561.

4.2.5 MAGIC

The observations with the MAGIC telescope system were performed under varying observational conditions which are shown in Table 4.1. During this MWL campaign, Mrk 421 was observed in the zenith distance range from 5° to 62°. The data were separated in the following sub-samples: a) Low zenith distance range (5° to 35°), b) Medium zenith distance range (35° to 50°), and c) High zenith distance range (50° to 62°). Depending on the influence of the night sky background light, the data were separated in the following sub-samples: i) dark condition, ii) low-moon condition and iii) high-moon condition, as defined in Ahnen et al. (2017). For analysing data in different background light conditions, the prescriptions from Ahnen et al. (2017) were followed.

Most of the data in this campaign were taken in stereoscopic mode with the standard trigger settings, including a coincidence trigger between telescopes and a 3NN single-telescope trigger logic (event registered when three next-neighbor pixels are triggered; Aleksić et al. 2016b). A minor subset was taken in the so-called mono mode (without coincidence trigger) and a 4NN single-telescope trigger logic. The data taken with the latter settings were analysed following the standard analysis procedure with a fixed size cut of 150 photo-electrons (phe) instead of 50 phe (used in standard data analysis). This size cut has been optimised by crosschecking the spectrum of the Crab Nebula observed in the same mode.

Since the analysis energy threshold increases with the background light and larger zenith distance observations, we set a uniform minimum energy of 200 GeV for the entire data sample. The data (in all observation conditions) were analysed using the MAGIC Analysis and Reconstruction Software (MARS; Zanin et al. 2013).

4.2.6 FACT

The First G-APD Cherenkov Telescope (FACT) is an imaging atmospheric Cherenkov telescope with a mirror area of 9.5 m^2. It is located next to the two MAGIC telescopes at the Observatorio del Roque de los Muchachos (Anderhub et al. 2013). Operational since 2011 October, FACT observes γ-rays in an energy range from a few hundreds of GeV up to about 10 TeV. The observations are performed in a fully remote and automatic way allowing for long-term monitoring of bright TeV sources at low cost.

Owing to a camera using silicon-based photosensors (SiPM, aka Geiger-mode Avalanche Photo Diodes or G-APDs) and a feedback system, to keep the gain of the photosensors stable, FACT achieves a good and stable performance (Biland et al. 2014). The possibility of performing observations during bright ambient light along with almost robotic operation allows for a high instrument duty cycle, minimizing the observational gaps in the light curves (Dorner et al. 2017). Complemented by an unbiased observing strategy, this renders FACT an ideal instrument for long-term monitoring.

Between 2014 November 10 and 2016 June 17 (MJD 56972 to 57556), FACT collected 884.6 hours of data on Mrk 421. The data were analysed using the Modular

Analysis and Reconstruction Software (MARS; Bretz & Dorner 2010) with the analysis as described in Beck et al. (2019).

A total data sample of 637.3 hours of Mrk 421 from 239 nights has been collected after data quality selection. We further discard nights where Mrk 421 was not significantly ($2\,\sigma$) detected, resulting in 513.6 hours of data from 180 nights.

Based on the γ-ray rate measured from the Crab Nebula, the dependence of the γ-ray rate on zenith distance and trigger threshold was determined and the data were corrected accordingly. For the conversion to flux, the energy threshold was determined using simulated data. The light curve as measured by FACT is shown in the top panel of Fig. 4.2.

4.3 Overall MWL activity

During the observation periods November 2014 to June 2015 (MJD 57037 – 57195) and December 2015 to June 2016 (MJD 57364 – 57525), Mrk 421 showed mostly low activity in the X-ray and VHE γ-ray bands. Fig. 4.2 shows the MWL LCs from radio to TeV energies observed within this period. In these two MWL campaigns, no large VHE flares (VHE flux $>$ 4 Crabs) or extended VHE flaring activities (VHE flux $>$ 2 Crabs for several consecutive days) were seen. A slower flux variation in the optical and UV emissions along with stable radio emission have also been seen. In this section, we first report on interesting features of the fluxes measured in different wave-bands during the 2015–2016 campaign, and then discuss a peculiar radio flare.

4.3.1 Identification of unusual characteristics

The multi-instrument LC from Fig. 4.2 shows several unusual characteristics, which are indicated with red vertical line and are discussed in the paragraphs below.

Intra-night variability on 2015 January 27 & March 12 (MJD 57049 & 57093):

From the 61 observations with MAGIC and 180 observations with FACT reported here, INV was observed in only two nights, 2015 January 27 (MJD 57049), found in the MAGIC data, and 2015 March 12 (MJD 57093), found in the FACT data. In the first case, the VHE flux from Mrk 421 dropped from ~1.3 Crab down to ~0.8 Crab, while in the second one, where the statistical uncertainties are larger, it decreased from ~2 Crab down to ~1 Crab. As depicted in Fig. 4.2, both nights show enhanced X-ray flux, but no particularly high flux in the GeV, optical or radio bands.

Here we report the single-night LCs at VHE γ-rays that show intra-night variability (INV), considered to occur when the fit with a constant value to the available intra-night flux measurements (time bins of 20 minute for FACT and 15 min for MAGIC) yield a p_{value} below 0.003 (i.e. more than 3σ significance). In case of FACT, the 20-minute binned light curves of all nights with a minimum observation time of 1 hour (196 nights) were checked for INV. From all the observations performed, INV was observed on only two nights, 2015 January 27 (MJD 57049) and 2015 March 12 (MJD 57093). In the first night, there were observations with both MAGIC (above 0.2 TeV) and FACT (E_{th} ~0.7 TeV). The INV is statistically significant only in the LC from MAGIC. In the case of FACT, the flux variations are not significant (less than $2\,\sigma$) because of the larger flux uncertainties and the different temporal coverage. It seems that the flux of Mrk 421 dropped by 50% sometime between MJD 57049.20 and MJD 57049.25. In the second night, there are only FACT observations. Mrk 421 shows a decrease in the VHE flux by about a factor of 3 in the 3.5 hours that the observation spans.

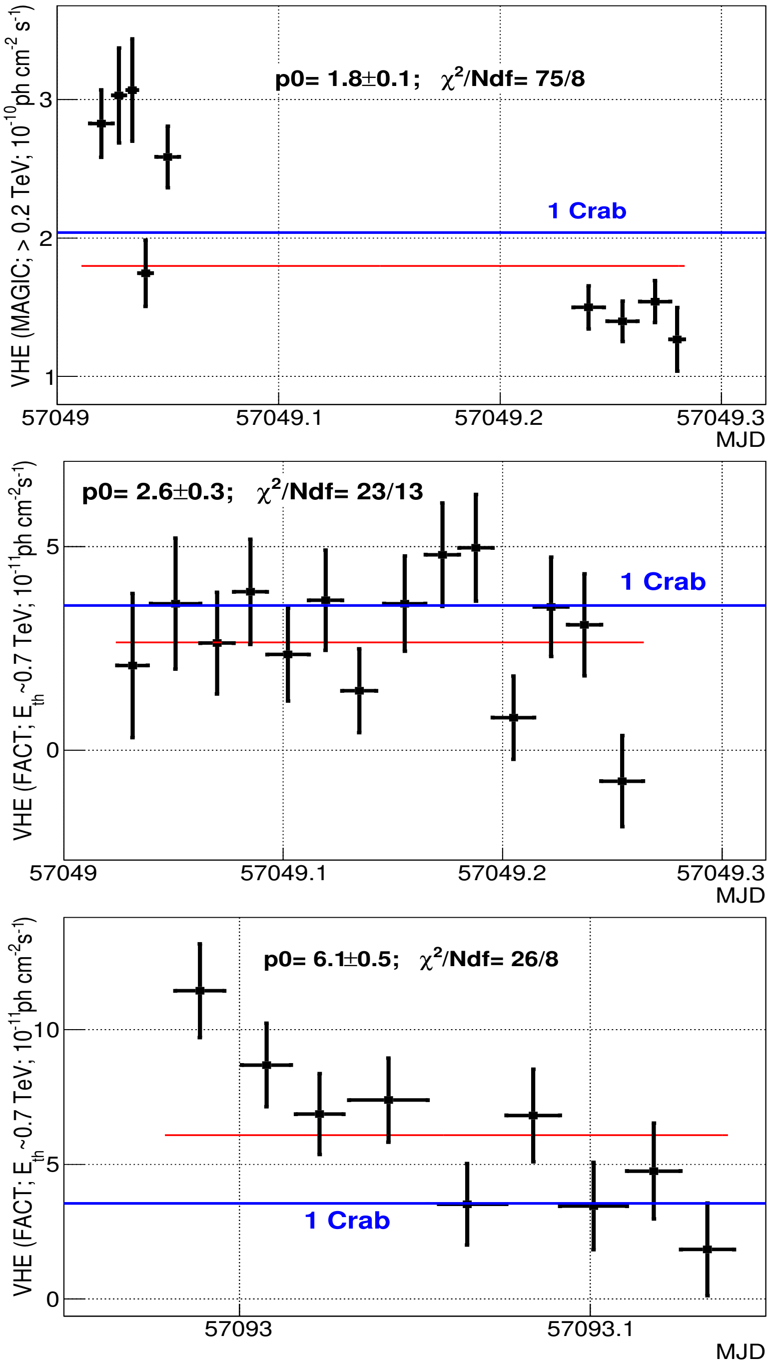

Figure 4.3: Single night VHE γ-ray LCs that show statistically significant intra-night variability. The first two panels show the MAGIC (above 0.2 TeV) and the FACT (E_{th} ~0.7 TeV) LCs for 2015 January 27 (MJD 57049). The lower panel shows the FACT (E_{th} ~0.7 TeV) LC for 2015 March 12 (MJD 57093). The blue horizontal lines depict the Crab Nebula flux in the respective energy band, and the red horizontal line represents a constant fit to the VHE γ-ray flux, with the resulting fit parameters and goodness of the fit reported in the panels.

Spectral hard state on 2015 February 12 (MJD 57065): This is the only night in the 2015-2016 campaign in which the $2-10\,\mathrm{keV}$ flux was higher than the $0.3-2\,\mathrm{keV}$ flux. The respective flux values are $F_{2-10\,\mathrm{keV}}$=$(9.12 \pm 0.12) \times 10^{-10}\,\mathrm{erg\,cm^{-2}\,s^{-1}}$ and $F_{0.3-2\,\mathrm{keV}}$=$(8.61 \pm 0.05) \times 10^{-10}\,\mathrm{erg\,cm^{-2}\,s^{-1}}$. This state is associated with a high hard X-ray flux observed with *Swift*-BAT and a low state in optical R- and UV-bands.

Highest X-ray flux during 2015–2016 on 2015 March 31 (MJD 57112): On this day, the highest flux in the X-ray band during this 2015-2016 campaign was observed. The corresponding fluxes are $F_{0.3-2\,\mathrm{keV}}$=$(1.68 \pm 0.06) \times 10^{-9}\,\mathrm{erg\,cm^{-2}\,s^{-1}}$ and $F_{2-10\,\mathrm{keV}}$=$(1.35 \pm 0.01) \times 10^{-9}\,\mathrm{erg\,cm^{-2}\,s^{-1}}$. This means that the flux increased by a factor of about five (two) compared to the average X-ray flux in the 2-10 keV (0.3-2 keV) energy band during the 2015-2016 campaign. The contemporaneous VHE γ-ray data from FACT showed a high flux state.

Low X-ray flux on 2015 June 22 & 2015 December 8 (MJD 57195 & 57364): The lowest flux in the 2015–2016 campaign in the X-ray band was observed on 2015 December 8 (MJD 57364), with the integrated flux in the $0.3-2\,\mathrm{keV}$ and $2-10\,\mathrm{keV}$ bands being $(1.67 \pm 0.03) \times 10^{-10}\,\mathrm{erg\,cm^{-2}\,s^{-1}}$ and $(2.41 \pm 0.15) \times 10^{-11}\,\mathrm{erg\,cm^{-2}\,s^{-1}}$, respectively. This is the lowest flux ever reported in the $2-10\,\mathrm{keV}$ band. Previously, to the best of our knowledge, the lowest flux in the $2-10\,\mathrm{keV}$ band was $(3.5 \pm 0.2) \times 10^{-11}\,\mathrm{erg\,cm^{-2}\,s^{-1}}$, observed on 2013 January 20 (6^{th} orbit) and reported in Baloković et al. (2016a).

On 2015 June 22 (MJD 57195), the source showed similar low-flux levels in the $2-10\,\mathrm{keV}$ and $0.2-1\,\mathrm{TeV}$ bands to MJD 57364, with measured fluxes of $(4.95 \pm 0.23) \times 10^{-11}\,\mathrm{erg\,cm^{-2}\,s^{-1}}$ and $(0.7 \pm 0.1) \times 10^{-10}\,\mathrm{ph\,cm^{-2}\,s^{-1}}$, respectively.

Low flux states during 2016 February 4–March 27 (MJD 57422–57474): On MJD 57422, the source evolved into a state where the flux remained very low in the X-

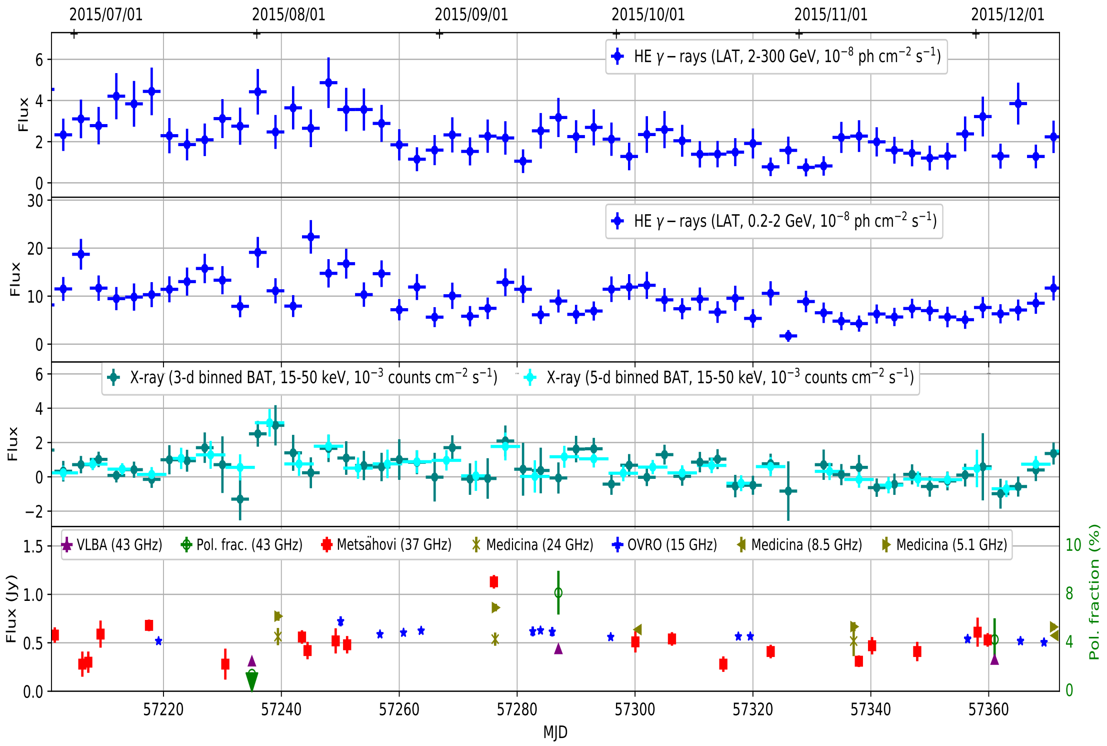

Figure 4.4: MWL light curves around 2015 September, when Metsähovi measured a large flux density increase at 37 GHz. (From the top to the bottom panels) the *Fermi*-LAT γ-ray flux in two energy bands, the *Swift*-BAT X-ray flux, the single-dish Metsähovi 37 GHz, OVRO 15 GHz and the Medicina 5 GHz, 8 GHz and 24 GHz flux densities, and the interferometric VLBI core fluxes at 43 GHz for the three measurements performed on August 1, September 22, and December 5. The linear polarization fraction for three VLBA measurements is also reported in the bottom panel with an upper limit on August 1, marked by an inverted triangle in green. See Section 4.3.2 for details.

ray and VHE γ-ray bands, as measured with *Swift*-XRT and MAGIC. MAGIC observed the lowest flux state in the 0.2 – 1 TeV energy band with a flux value of $(3.56 \pm 0.91) \times 10^{-11}\,\mathrm{ph\,cm^{-2}\,s^{-1}}$. However, there are a few days (e.g., MJD 57422–57429) with high flux at hard X-ray (15 – 50 keV), as measured with the *Swift*-BAT instrument. This will be further discussed in Section 4.3.

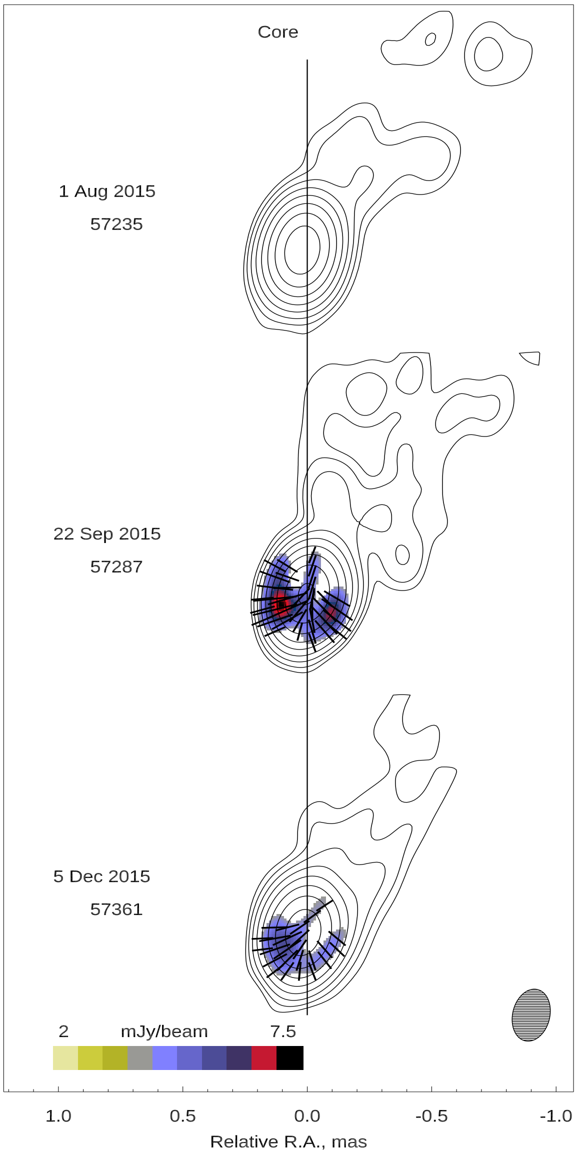

Figure 4.5: A sequence of total (contours) and polarized (color scale) intensity images of Mrk 421 at 43 GHz obtained with the VLBA. The image is convolved with a FWHM of 0.24×0.15 mas^2 along PA=-10°. The global total intensity peak is 329 mJy/beam, and the contours 0.35, 0.70, 1.4, etc. up to 89.6 per cent of the global intensity peak. The color scale is the polarized intensity, and the black line segments within each image show the direction of the polarization electric vector, with the length of the segment being proportional to the polarized intensity values. The black vertical line indicates the position of the core. See Section 4.3.2 for details.

4.3.2 Peculiar radio flaring activity in 2015 September

On 2015 September 11 (MJD 57276), the 13.7-meter diameter Metsähovi radio telescope measured a 37 GHz flux from Mrk 421 of 1.13 ± 0.07 Jy, one of the highest fluxes ever observed at this wavelength and about twice that of any other observation from this campaign, as shown in Fig. 4.4. Only during the flaring episode from September 2012 was a similar high flux state observed in the 15 GHz radio bands, along with a flare in the HE γ-rays and optical R-band about 40 days before the radio flare (Hovatta et al. 2015).

There were several 37 GHz measurement attempts of Mrk 421 in late August, late September, and early October, but all of them had to be discarded due to bad weather conditions (for details, see 4.2.1), leaving only the September 11 data point, and making it stand out as the only indication of a high state in that time period. However, a flux increase is also suggested by the OVRO 15 GHz data, in which the flux density level is slightly elevated in late August and September. There are no simultaneous data at 15 GHz and 37 GHz. There are, however, data at 5 GHz and 24 GHz from the Medicina radio telescope on the same date. The 5 GHz flux density is higher than the average value at this frequency, while the 24 GHz does not show any evidence of significant variability.

Within the regular monitoring program of the Boston University group, the VLBA performed three observations around the 2015 September 11 radio flare, namely on August 1 (MJD 57235), September 22 (MJD 57287), and December 5 (MJD 57361). The core VLBA fluxes and linear polarization fraction are displayed in Fig. 4.4, while the images yielded by these observations are reported in Fig. 4.5. Within the statistical uncertainties of the VLBA measurements, one does not see any change in the core VLBA radio flux (even though one observation happened only 11 days after the Metsähovi flare), yet there is a clear change in the polarization fraction, from less than 2 per cent for the observation from August 1, to about 8 per cent for the observation from September 22. Additionally, in the image related to the observation from September 22, there is a radial polarization pattern across the Southern half of the core region. This suggests that the magnetic field B is roughly circular and centered on the brightness peak of the core, as one might expect from a helical field when one views it down the axis. This polarization pattern remained through 2016 March. The γ-ray light curve from the *Fermi*-LAT and X-ray light curve from the *Swift*-BAT do not show any obvious flux enhancement during the time of the radio flaring activity, although they show some activity (both BAT and LAT) about 40 days before the radio flare. During this time, there were no optical or VHE observations because of the Sun.

The low polarization fraction at 43 GHz on 2015 August 1 implies that the magnetic field was very highly disordered in the core at this epoch. A radial polarization pattern, as measured at 43 GHz on 2015 September 22, can result from turbulent plasma flowing across a conical standing shock, as found in the simulations of Cawthorne et al. (2013) and Marscher (2016). However, in such a scenario the linear polarization pattern is always present, since it is created by the partial ordering of the magnetic field by the shock front. Periods of polarization $< 2\%$ across the entire core should not be observed.

An alternative picture ascribes the radial polarization pattern to the circular appearance of a magnetic field with a helical or toroidal geometry that is viewed within $\sim 0.2/\Gamma$ radians of the axis of the jet (Marscher et al. 2002), where Γ is the bulk Lorentz factor of the emitting plasma. In this case, the ratio of the observed polarization measured in the image, $\sim 8\%$, to the value for a uniform magnetic field direction, $\sim 75\%$[6], implies

[6] The linear polarization of synchrotron radiation is proportional to the value for a uniform magnetic field, $(1+\alpha)/(5/3+\alpha)$, where α is the spectral index (see classical book by Pacholczyk 1970). For typical spectral indices from 0.5 to1.5, the uniform-field linear polarization fraction ranges from 68% to 79%.

that the helical field is superposed on a highly disordered field component that is ~ 10 times stronger. If the helical field becomes disrupted by a current-driven kink instability, particle acceleration could cause a flare (Nalewajko 2017; Zhang et al. 2017; Alves et al. 2018). The polarization pattern then becomes complex, with the possibility that the polarization becomes very low at some point (Dong et al. 2020). Such a flare would be expected to start at X-ray and VHE γ-ray energies upstream of the core, then propagate downstream so that it appears later at radio frequencies (Nalewajko 2017). The disruption of the helical field by the instability could lead to the disordered component inferred from the VLBA images.

4.4 Multi-year light curves

The studies reported in this chapter are derived mostly with the extensive MWL data set collected during the campaigns in the years 2015 and 2016, when Mrk 421 showed very low flux at X-ray and VHE γ-rays. This 2-year data set is described in Section 4.2. However, for the correlation studies reported in Sections 4.6.3, 4.6.4, and 4.6.5, and the characterization of the flux distributions reported in Section 4.9, the 2015–2016 data set is complemented with data from the years 2007–2014.

The 2007–2016 data set, used for the above-mentioned correlation and flux-profile studies, is depicted in Fig. 4.6. The MAGIC VHE γ-ray and the *Swift*-XRT X-ray LCs are retrieved from various published works (Aleksić et al. 2012b, 2015c; Ahnen et al. 2016; Baloković et al. 2016a). The *Fermi*-LAT fluxes in the band $0.3 - 300$ GeV were analyzed as described in Section 4.2.4. The *Swift*-BAT fluxes were retrieved from the BAT website[7], and treated as explained in Section 4.2.3. The optical data in the R-band were retrieved from Carnerero et al. (2017). The 37 GHz radio fluxes from Metsähovi

[7] http://heasarc.nasa.gov/docs/swift/results/transients/

were provided by the instrument team, and the 15 GHz radio fluxes from OVRO were retrieved from the website of the instrument team[8]. As done in Section 4.5.1, we only consider fluxes with the relative errors (flux-error/flux) smaller than 0.5 (i.e. SNR>2). In this way, we ensure the usage of reliable flux measurements, and minimize unwanted effects related to unaccounted (systematic) errors.

There are seven MAGIC VHE fluxes from the year 2007, from the time interval MJD 54166–54438, and five VHE fluxes from the year 2009, from the time interval MJD 54800–54835, that relate to energies above 0.4 TeV (published in Ahnen et al. 2016), and all the MAGIC VHE fluxes from the 4.5-months long MWL campaign in year 2009, from the time interval MJD 54851–54977, relate to energies above 0.3 TeV. (published in Aleksić et al. 2015c). The reason for the higher minimum energy in these two publications with respect to other publications that relate to observations performed after year 2010 (where the light curves are produced with energies above 0.2 TeV) is the operation of MAGIC in mono mode (with a single-telescope). The MAGIC observations of Mrk 421 in stereo mode, which started in the MWL campaign from year 2010, provide additional sensitivity and a lower analysis energy threshold, which allows one to reliably produce light curves with a minimum energy of 0.2 TeV. During the year 2008, Mrk 421 showed high VHE flux and, despite MAGIC operating with a single-telescope, the large VHE γ-ray fluxes and the longer exposures, permitted the reliable reconstruction of the VHE fluxes above 0.2 TeV, as reported in Aleksić et al. (2012b). In order to properly compare the published VHE fluxes from the years 2007 and 2009 with those from 2008 and from 2010 onwards, we scaled VHE fluxes above 0.4 TeV and 0.3 TeV (and their related errors) by a factor of 2.83 and 1.84, respectively.

[8] http://www.astro.caltech.edu/ovroblazars/index.php?page=home

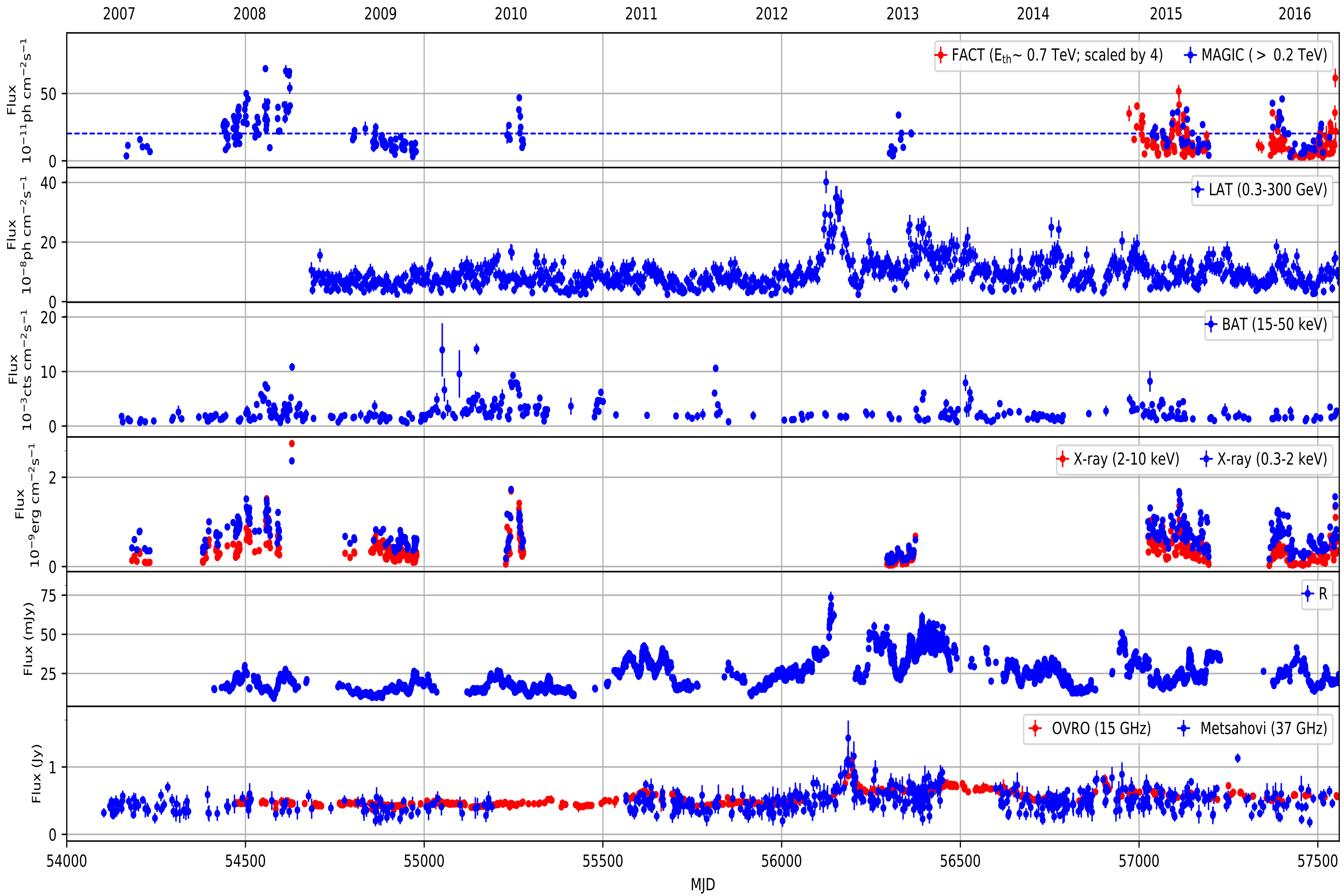

Figure 4.6: Multi-year data set used in the study reported in Sections 4.6.3, 4.6.4, 4.6.5, and 4.9. In the top panel, the horizontal blue line represents 1 Crab flux in above 0.2 TeV.

These scaling factors were calculated by considering that the VHE spectral shape of Mrk 421 around the energy of 0.3 TeV can be well described with a power-law function with index 2.5, when Mrk 421 is in its typical (non-flaring) state (Abdo et al. 2011a). They can then be used to convert the VHE fluxes above 0.4 TeV and 0.3 TeV to that above 0.2 TeV. The spectral shape of the VHE emission of Mrk 421 does vary over time, and it is known to be related to the flux (e.g. harder-when-brighter behaviour). However, owing to the relatively small energy range over which one needs to extrapolate, and the relatively low VHE flux and low variability from years 2007 and 2009, including these spectral variations would vary the reported VHE fluxes by less than ±10% in most cases. These additional flux variations are typically smaller than the statistical uncertainties of the flux measurements during these low-flux periods, and hence they do not affect the reported study in any significant manner.

4.5 Variability study

Mrk 421 is known to exhibit significant flux variations from radio to VHE γ-rays. In this work, we quantify different aspects of variability by computing the fractional variability (F_{var}) and the hardness ratio (HR).

4.5.1 Fractional variability

We use fractional variability (F_{var}) as a tool to characterize the variability of the source in different wave-bands. It is defined as the normalized excess variance of the flux (Vaughan et al. 2003):

$$F_{\mathrm{var}} = \sqrt{\frac{S^2 - < \sigma_{\mathrm{err}}^2 >}{< F_\gamma >^2}}, \tag{4.1}$$

where

S is the standard deviation of N flux measurements, $< \sigma^2_{\rm err} >$ is the mean squared error, $< F_\gamma >$ is the average photon flux. The uncertainty in the fractional variability ($F_{\rm var}$) has been estimated using the formalism described in Poutanen et al. (2008):

$$\Delta F_{\rm var} = \sqrt{F^2_{\rm var} + err(\sigma^2_{\rm NXS})} - F_{\rm var}, \tag{4.2}$$

where

$$err\left(\sigma^2_{\rm NXS}\right) = \sqrt{\left(\sqrt{\frac{2}{N}} \cdot \frac{\langle\sigma^2_{\rm err}\rangle}{\langle F_\gamma\rangle^2}\right)^2 + \left(\sqrt{\frac{\langle\sigma^2_{\rm err}\rangle}{N}} \cdot \frac{2F_{\rm var}}{\langle F_\gamma\rangle}\right)^2}. \tag{4.3}$$

The $F_{\rm var}$ computed from the multi-band light curves of Fig. 4.2 are shown in Fig. 4.7. In order to ensure the use of reliable flux measurements, we only consider fluxes with relative errors (flux-error/flux) smaller than 0.5, i.e. Signal-to-Noise-Ratio (SNR) larger than 2. This is done to avoid dealing with systematic uncertainties that could arise in very-low-significance measurements, when we mostly deal with background that may not be well modelled. This cut discards only a small fraction of the full data set (see open markers in Fig. 4.2). The only instrument that is substantially affected is *Swift*-BAT, whose data are not used for the variability studies reported here.

The highest variability was measured with FACT and MAGIC at energies above 1 TeV, with $F_{\rm var}$ close to 0.7. The MAGIC data in the energy range 0.2 – 1 TeV show variability at the level of 0.5. These values are about a factor of two higher than that reported during the 2009 campaign (Aleksić et al. 2015b).

In order to quantify the variability for different levels of emission, we further divide the X-ray and VHE γ-ray data (the two energy bands with the highest variability) into two data subsets, the 2015 campaign (MJD range 56970–57200) and the 2016 campaign (MJD range 57350–57560). For this study, we only use simultaneous X-ray and VHE

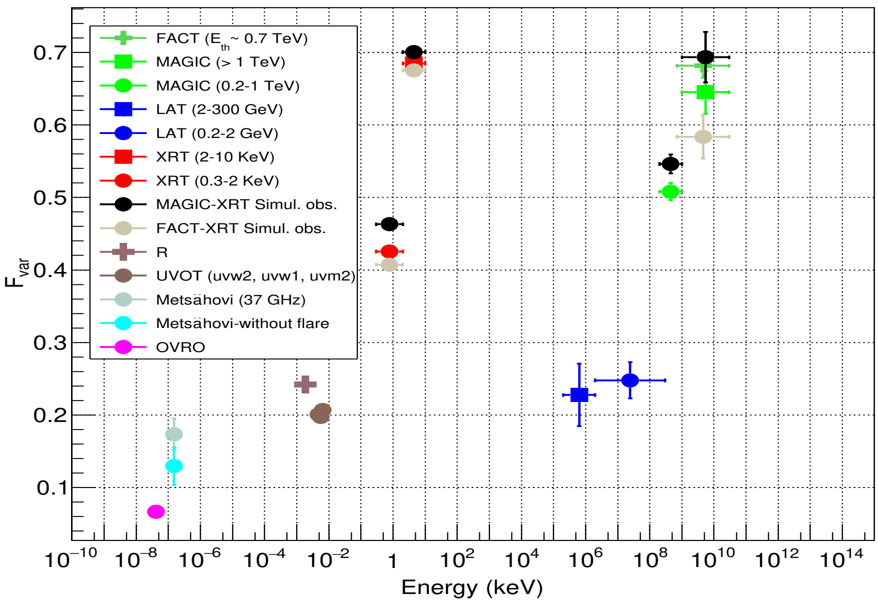

Figure 4.7: Fractional variability as a function of energy for the MWL LCs presented in Fig. 4.2. The horizontal error bars represent the energy bin and the vertical error bars denote the 1 σ uncertainties on the calculated fractional variability (not visible for some of the datasets). For the X-ray and VHE data, we show the results derived with all data from 2015–2016 campaigns, and also the results obtained with simultaneous X-ray (*Swift*) and VHE data (MAGIC or FACT). See Section 4.5.1 for details.

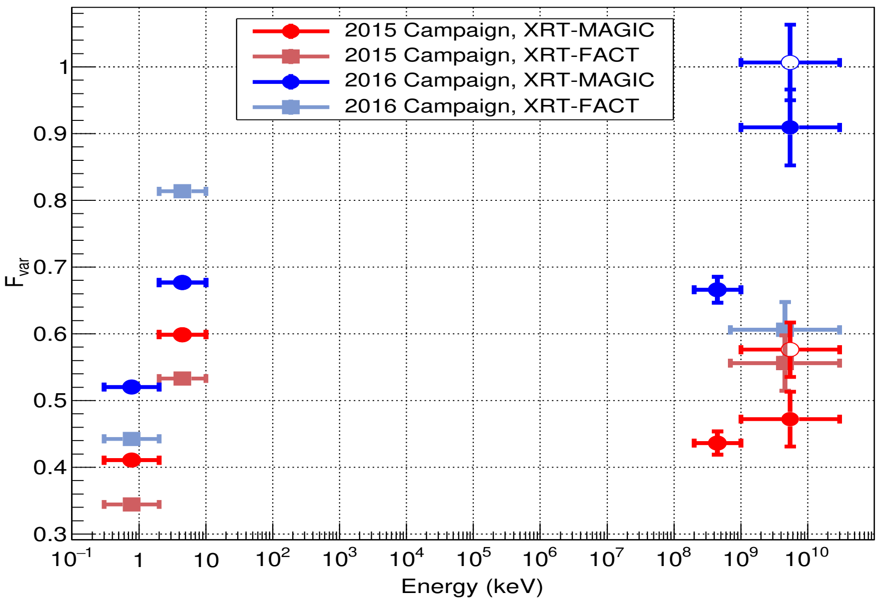

Figure 4.8: Fractional variability for X-rays and VHE γ-rays for two subsets of data, the 2015 campaign (MJD range 56970–57200) and the 2016 campaign (MJD range 57350–57560). The open markers display the F_{var} above 1 TeV for the two subsets when adding four flux measurements with SNR below 2 (see text for details).

γ-ray observations. Most of the MAGIC and *Swift*-XRT observations occurred within 2 hours, but owing to the lack of intra-night variability for most of the nights, for this study we consider simultaneous observations those taken within the same night (within 0.3 day). This results in 21 pairs of XRT/MAGIC observations for the 2015 campaign subset and 24 for the 2016 campaign subset. The average X-ray flux in the 2 – 10 keV energy range for the first data set is 4.1×10^{-10} erg cm^{-2} s^{-1}, while it is 2.1×10^{-10} erg cm^{-2} s^{-1}, for the second one, while the 2-year average flux is 3.1×10^{-10} erg cm^{-2} s^{-1}. Therefore, the 2016 data tell us about the activity of Mrk 421 during the lowest fluxes, while the 2015 campaign tells us about predominantly higher fluxes within the 2-year dataset considered here. For each X-ray/VHE pair, we have four flux measurements, two at X-rays (0.3 – 2 keV and 2 – 10 keV) and two at VHE (0.2-1 TeV and >1 TeV). The F_{var} for these two subsets is reported in Fig. 4.8. All flux measurements have a SNR>2.0, apart from four VHE flux measurements above 1 TeV: MJD 57195, MJD 57422, MJD 57430 and MJD 57453. These four flux values were excluded from the calculation of F_{var} above 1 TeV. The first day belongs to the 2015 campaign subset, while the other three belong to the 2016 campaign subset. All of them are related to time intervals with very low X-ray and VHE γ-ray flux (see Fig. 4.2). Because of the low number of XRT/MAGIC pairs, for completeness, Fig. 4.8 also reports the F_{var} when the four excluded measurements above 1 TeV with SNR<2 are included in the calculations. Because of the addition of 1+3 flux points with very low-flux, the F_{var} increases slightly, compared to the F_{var} computed using only the measurements with SNR>2. We repeated the same exercise using *Swift*-XRT and FACT observations taken within 0.3 days, which yielded 37 and 34 XRT/FACT pairs of observations (with flux measurements with SNR>2) for the 2015 and 2016 campaigns, respectively. The calculated F_{var} values for these data subsets are also shown in Fig. 4.8. The F_{var} calculated with the simultaneous XRT/FACT data is, in general, somewhat lower than that calculated with the XRT/MAGIC simultaneous data. The reason behind this lower variability is the requirement for SNR> 2 in the VHE flux measurements by FACT, which removes simultaneous XRT/FACT pairs with X-ray fluxes that are well below the average flux for each of the two campaigns (see Fig. 4.2), and hence decreases the overall F_{var}. On the other hand, the F_{var} for the simultaneous XRT/FACT in the $2-10$ keV band is higher than that computed with the simultaneous XRT/MAGIC data in the same energy band. This is due to the XRT/FACT data covering time intervals in 2015 December and 2016 June, which are not covered by the XRT/MAGIC data, where the $2-10$ keV flux in the X-rays was several times higher (up to factor of ~5) than the average 2-10 keV flux in the 2016 campaign. Two conclusions can be derived from this exercise with this data set. First, the F_{var} is higher during the 2016 campaign (lower X-ray and VHE fluxes) than during the 2015 campaign. Second, for the 2015 campaign, the variability is similar in keV and in TeV energies, while for the 2016 campaign, the variability in TeV is somewhat higher than in keV energies.

4.5.2 Hardness ratio

In X-rays and VHE γ-rays, we define the hardness ratio as the ratio of the integral flux in the high-energy (hard) band to the integral flux in the high-energy (soft) band:

$$\mathrm{HR_{TeV}} = \frac{\mathrm{F_{>1\,TeV}}}{\mathrm{F_{0.2-1\,TeV}}}; \quad \mathrm{HR_{keV}} = \frac{\mathrm{F_{2-10\,keV}}}{\mathrm{F_{0.3-2\,keV}}},$$

where $\mathrm{F_E}$ is the integrated flux in the energy band E.

The upper panel of Fig. 4.9 shows the variation of $\mathrm{HR_{TeV}}$ calculated from the 2015–2016 data. During the low-flux state (MJD 57422 to 57474), the $\mathrm{HR_{TeV}}$ is $\leq$0.03. The bottom two panels show the variation of $\mathrm{HR_{TeV}}$ with the integral flux in two energy bands namely 0.2 − 1 TeV and above 1 TeV observed with MAGIC. Additionally, the bottom panel of Fig. 4.9 also depicts the average and the standard deviation of data subsets of 10 observations[9], binned according to their flux. This is done for a better visualization of the overall trend in the $\mathrm{HR_{TeV}}$-flux plot, as well as the dispersion of the data points. In both plots, one can see a bending in the *HR* vs. flux trend. This distortion is particularly important for the $\mathrm{HR_{TeV}}$ vs. soft-band VHE flux (left panel), where one can see a flattening in the *HR* beyond 20×10^{-11} ph cm^{-2} s^{-1}.

Figure 4.10 shows the variation of $\mathrm{HR_{keV}}$ with time and flux. The $\mathrm{HR_{keV}}$ ranges from 0.15 to 1.05 ($\Delta\ HR$ = 0.9). The $\mathrm{HR_{keV}}$ observed on 2016 March 10 (MJD 57457) is the lowest reported $\mathrm{HR_{keV}}$ so far, which is 0.14±0.01. The low-flux state mentioned in Fig. 4.2 from MJD 57422 to 57474 can be identified in Fig. 4.10 with a sustained $\mathrm{HR_{keV}}$< 0.3, smaller than the lowest $\mathrm{HR_{keV}}$ previously reported (HR=0.47, Kapanadze

[9]The exact number of measurements for grouping the data is not relevant. For the MAGIC data we used 10 measurements, which provides sufficient event statistics, and allows one to visualize different segments of the HR vs Flux relation.

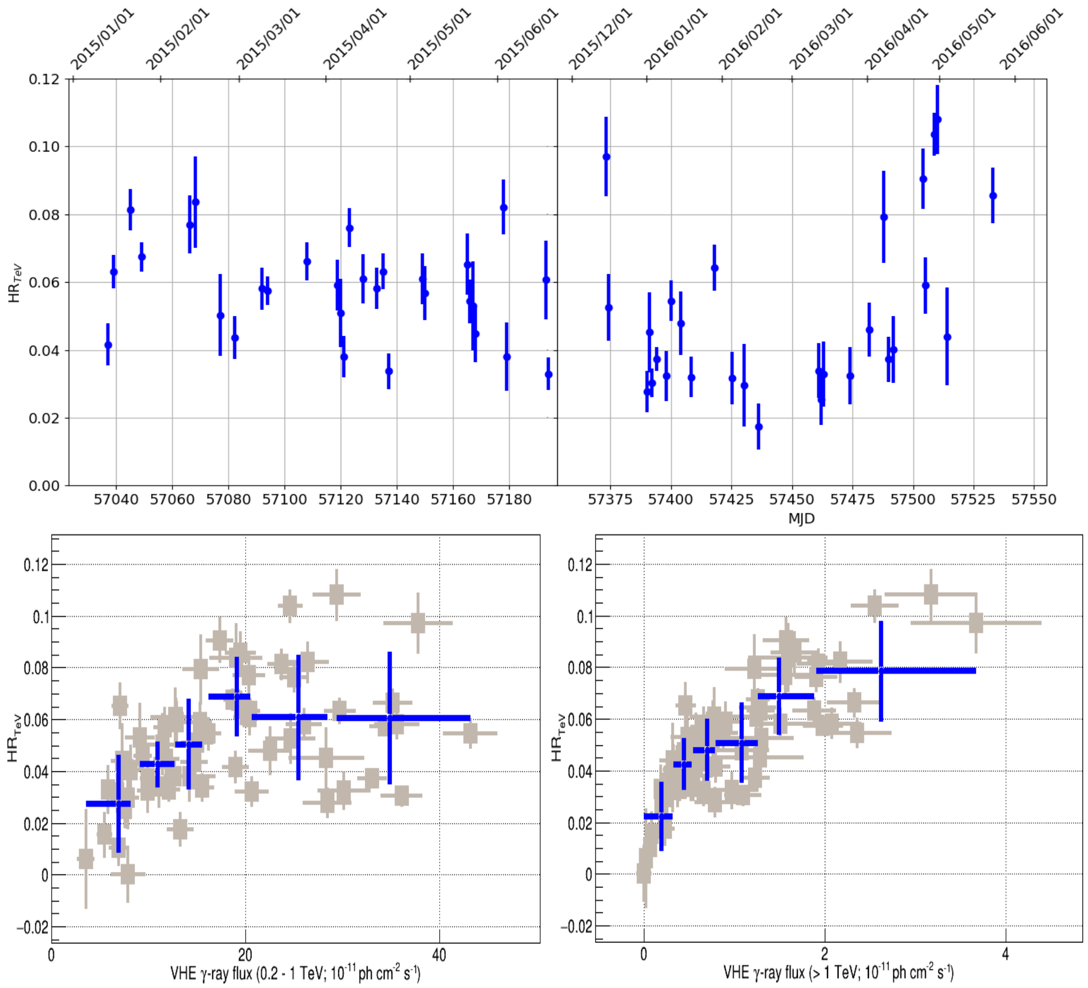

Figure 4.9: HR as a function of time (top panel) and flux (bottom panels) during 2015–2016 for two TeV energy bands, namely 0.2 – 1 TeV and above 1 TeV. The blue markers report the average and standard deviation of the HR_{TeV} data binned with 10 entries. See Section 4.5.2 for details.

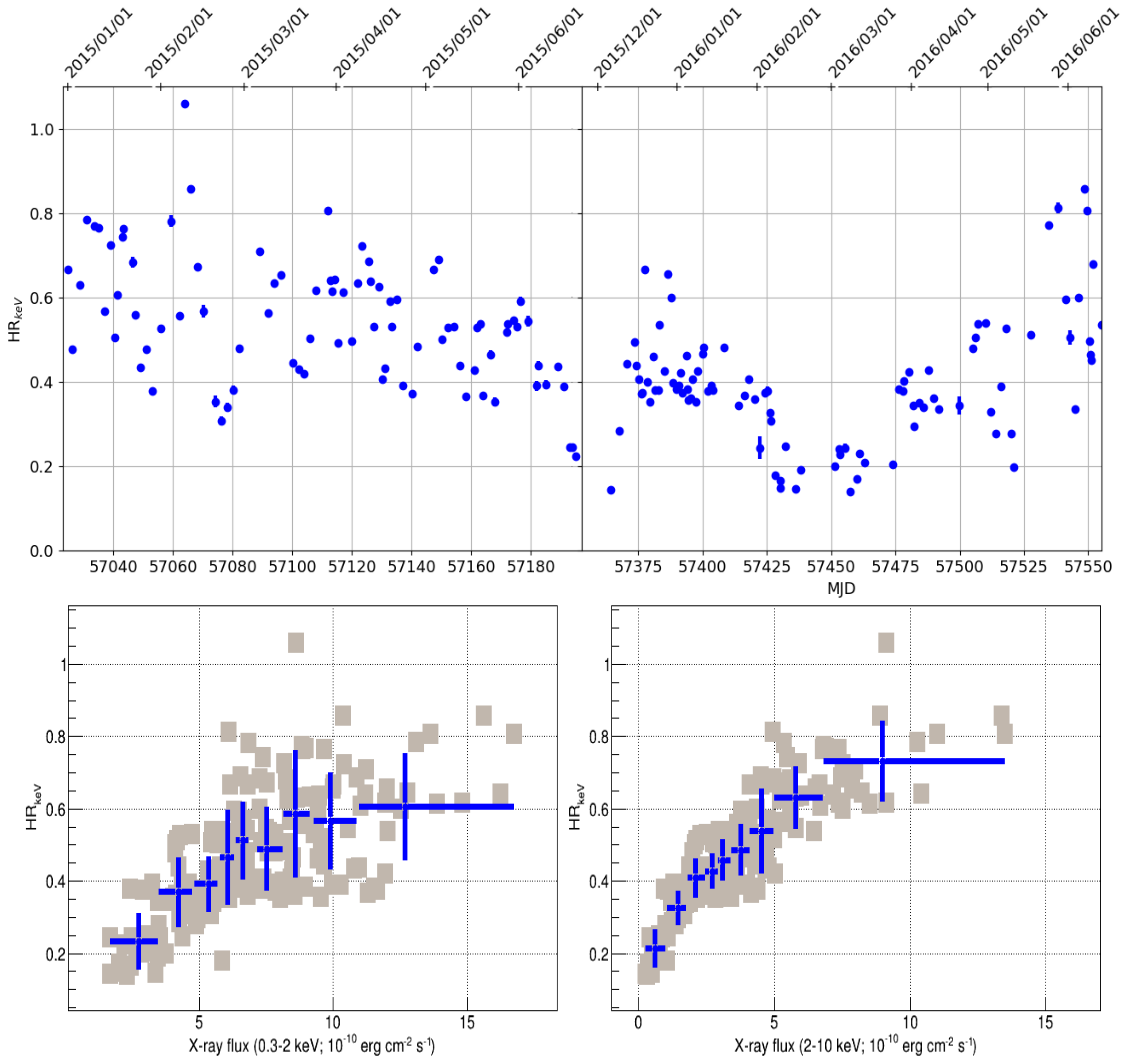

Figure 4.10: HR as a function of time (top panel) and flux (bottom panels) in the X-rays in two energy bands, namely 0.3 – 2 keV and 2 – 10 keV observed with *Swift*-XRT. The blue markers depict the the average and standard deviation of the HR_{keV} data binned with 20 entries. See Section 4.5.2 for details.

et al. 2017) where the source was claimed to be in a historical low-flux state observed by *NuSTAR* (Baloković et al. 2016a). The lower panels of Fig. 4.10 show the variation of the $\mathrm{HR_{keV}}$ with $\mathrm{F_{0.3-2\,keV}}$ and $\mathrm{F_{2-10\,keV}}$. The hardest X-ray state can be identified on MJD 57065 with $\mathrm{HR_{keV}}$=1.05, which is the only occasion of $HR_{keV} > 1$, and consistent with the X-ray spectrum peaking around 10 keV, previously reported in Kapanadze et al. (2017). Apart from the high flux observed at hard X-rays by *Swift*-BAT, no exceptionally high flux is observed in any of the other energy bands. As in the bottom panel of Fig. 4.9, we also depict here the average and the standard deviation of the data binned in 20 observations[10] according to their flux, which also show the flattening in the *HR* vs flux relation.

Overall, the *HR* vs flux plots in Fig. 4.9 and Fig. 4.10 show a clear hardening-when-brightening trend in both the X-ray and VHE γ-ray energy ranges. However, for the highest activities, one can observe that the spectral hardening trend flattens, which is more evident when reporting the HR as a function of the flux in the lower band from each of the two energy ranges, namely 0.3 – 2 keV and 0.2 – 1 TeV. Baloković et al. (2016a) had already reported a saturation in the X-ray spectral shape variations of Mrk 421 for very-low and very-high flux. The saturation at high fluxes appears to be consistent with what is reported here, i.e., a flattening in the X-ray spectral shape starting for 2 – 10 keV fluxes above $8{\times}10^{-10}\,\mathrm{erg\,cm^{-2}\,s^{-1}}$. On the other hand, the flattening in the *HR* vs flux relation at VHE γ-rays has not been reported previously.

4.5.3 Appearance of a new component at hard X-ray energies

In this section we report a characterization of the shape of the low-energy SED bump (presumably the synchrotron bump) for the time interval MJD 57422–57429 (2016 Febru-

[10]Owing to the larger number of XRT observations, in comparison with that of MAGIC observations, we decided to bin the XRT data in groups of 20, instead of the 10 used for the MAGIC data.

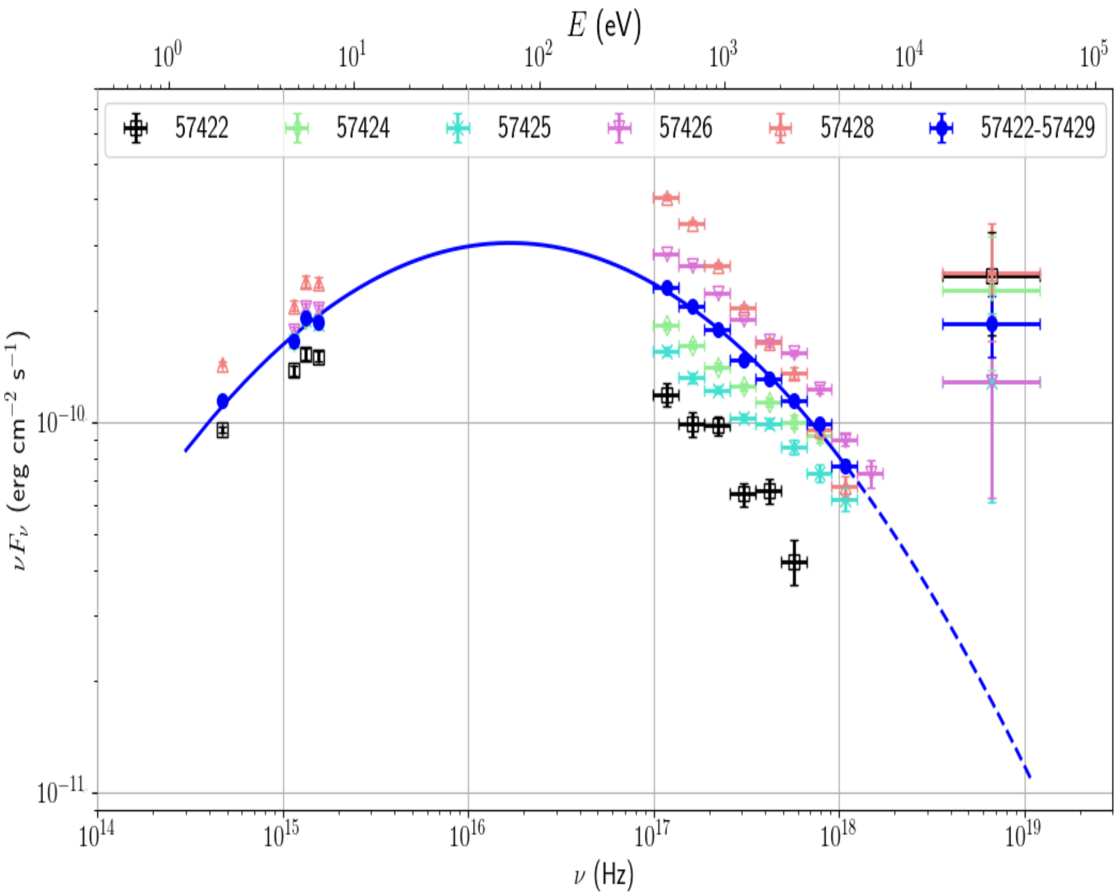

Figure 4.11: Characterization of the low-energy SED bump of Mrk 421 during the time interval MJD 57422–57429 (2016 February 4–11). The five available daily observations (from optical to hard X-rays) during this 7-day time interval are reported with open markers, while the 5-day weighted-averaged fluxes are reported with blue-filled markers. The blue solid line depicts the resulting fit with a log-parabola function in the energy range from 1 eV to 10 keV, and the dashed line shows the extrapolation of this log-parabola function to the hard X-ray energy range. See Section 4.5.3 for details.

ary 4–11), which is a time interval with a very low X-ray flux and a very low HR (see Fig. 4.2 and Fig. 4.10). Fig. 4.11 shows the fluxes in the optical (R-band), UV (W1,M2,W2), soft X-rays ($0.3 - 10\,\mathrm{keV}$) and hard X-rays ($15 - 50\,\mathrm{keV}$) for five days (out of 7-day interval) and the related 5-day combined fluxes obtained with a standard weighted average procedure. The daily fluxes were obtained as described in Section 4.2. The weighted-averaged BAT fluxes (daily and combined) are converted into energy fluxes (in units of $\mathrm{erg\,cm^{-2}\,s^{-1}}$) using the prescription in Krimm et al. (2013). The hard X-ray BAT fluxes (both the daily fluxes and the 5-day combined flux) appear to be inconsistent with the simple extrapolation from the soft X-ray XRT fluxes. In order to evaluate this, we fit the 5-day combined optical to soft X-ray spectra (solid blue markers in Fig. 4.11) with a log-parabola function $\mathrm{F}(\nu)=\mathrm{N}_0(\nu/\nu_0)^{-\alpha-\beta log_{10}(\nu/\nu_0)}$, where ν_0 has been fixed to 3.0×10^{16} Hz and N_0, α, and β are the free parameters of the fit. Because of the very small uncertainties in the 5-day weighted average of the flux values (typically in the order of $\sim$1%), a regular fit to the data would be affected by the small spectral distortions (wiggles) caused by small systematics in merging data sets from different instruments and with somewhat different spectral shapes. We find that we can smooth out these small spectral distortions by adding a relative flux error of 3% in quadrature to the actual flux error resulting from the weighted average procedure. The resulting spectral fit, performed in the νF_ν vs. ν representation, yields a χ^2 of 11.6 for 9 degrees of freedom, with the following parameter values: N_0, α, and β as $(2.91\pm0.07)\times10^{-10}\mathrm{erg\,cm^{-2}\,s^{-1}}$, $(9.11\pm0.39)\times10^{-2}$, and $(1.77\pm0.06)\times10^{-1}$ respectively. Therefore, the log-parabola function provides a good representation of the synchrotron emission averaged over 5-day, from eV to 10 keV energies. The weighted average of the 1-day BAT fluxes over these 5 days with XRT/UVOT observations is (1.84±0.34)

$\times\ 10^{-10}\,\mathrm{erg\,cm^{-2}\,s^{-1}}$ [11]. As shown in Fig. 4.11, the extrapolation of this log-parabola function to the $15-50\,\mathrm{keV}$ band goes well below the BAT 5-day weighted-averaged flux point (5 times the error bar). If instead of using the prescription of Krimm et al. (2013) to convert the BAT count rate to energy flux, which employs the spectral shape of the Crab Nebula in the energy range 15-50 keV (i.e., a power-law shape with index 2.15), we employ the spectral shape given by the above-mentioned log-parabola function (which in the 15-50 keV band could be approximated with power-law function with index ~2.5), the BAT energy flux would be only 10% lower than the one reported above (and displayed in Fig. 4.11), and hence it would not change the overall picture in any significant way. This observation suggests the presence of an additional component, beyond that of the synchrotron emission of the main emitting region. See Section 4.11 for further discussion about it.

4.6 Correlation study

In this section, we discuss the potential correlations between the different LCs presented in Fig. 4.2. The correlation between two energy bands (two LCs) is quantified using two methods: the Pearson correlation coefficient with its related $1\,\sigma$ error and correlation significance (calculated from Press et al. 2002), and the discrete correlation function (DCF, Edelson & Krolik 1988). The Pearson correlation is widely used in the community, but the DCF has the advantage over the Pearson correlation that it also uses the uncertainties in the individual flux measurements, which also contribute to the dispersion of the flux values, and hence affect the actual correlation between the two LCs. The DCF and Pearson correlation between two energy bands is computed with one LC and

[11]This number is derived from the 5-day weighted average of the BAT count rate, $(3.21\pm0.59)\times\ 10^{-3}$ $\mathrm{cts\,cm^{-2}\,s^{-1}}$, and the counts-to-energy conversion stated in Krimm et al. (2013).

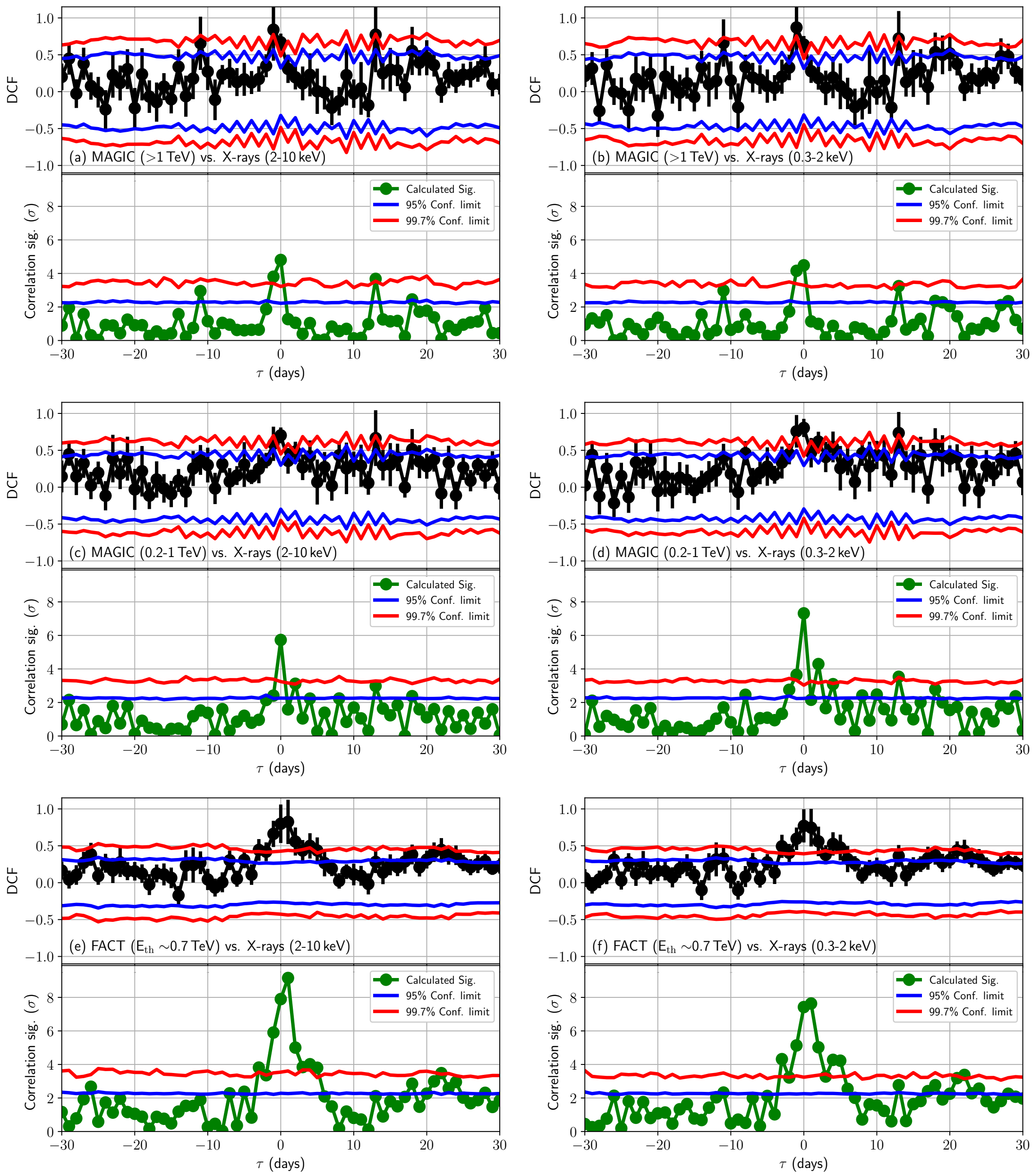

Figure 4.12: Correlation between VHE γ-rays and X-rays during 2015–2016 from Mrk 421 using the DCF and the Pearson correlation functions. The top and bottom blocks of each panel show the DCF and related errors, and the significance of the Pearson correlation, respectively. A positive time lag indicates a lag in the emission of the second (lower) energy band with respect to the first (higher) energy band. The blue- and red-lines indicate the 95 and 99.7 per cent confidence intervals estimated from the Monte Carlo simulations described in Section Section 4.6.

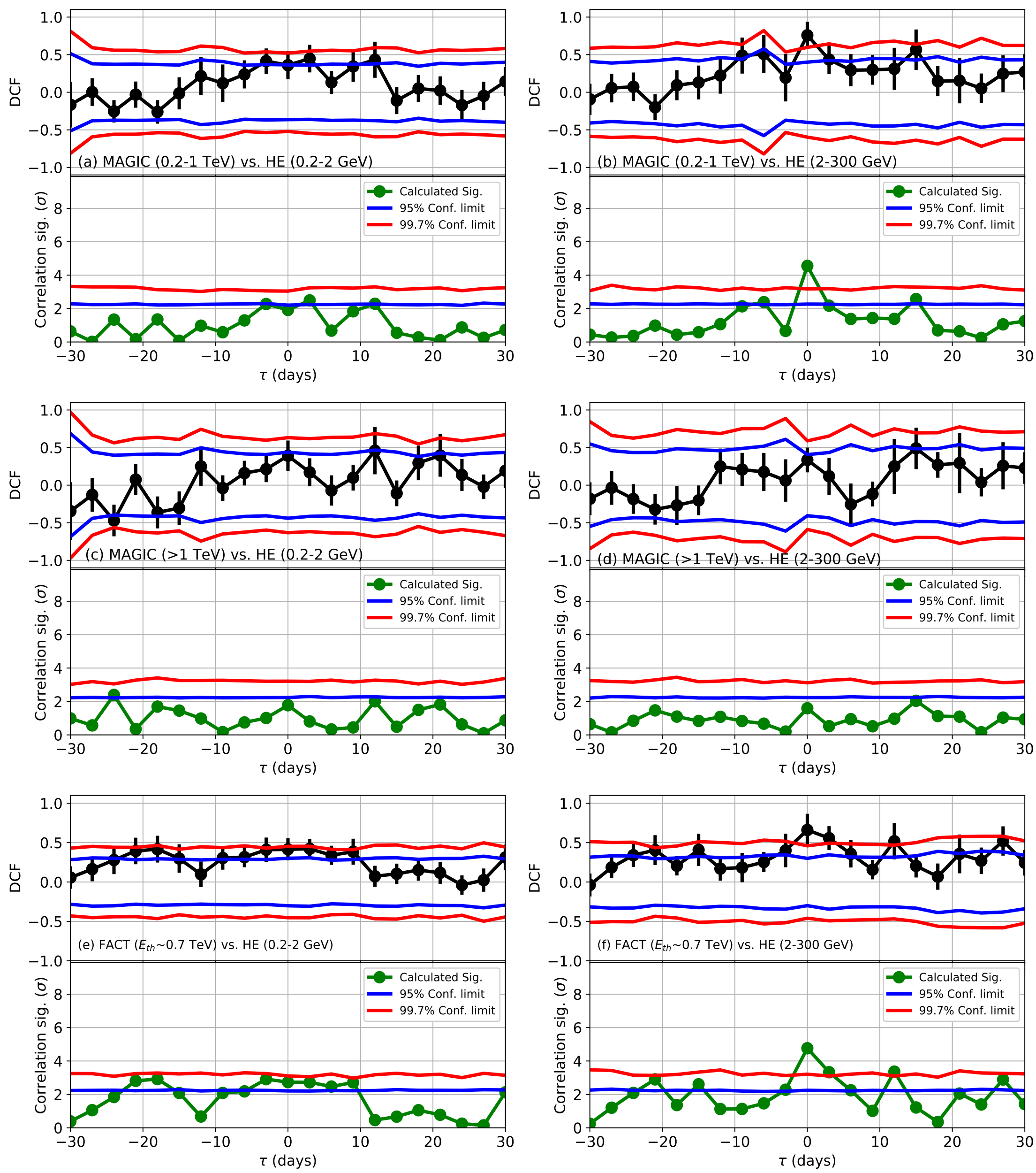

Figure 4.13: Correlation between different MWL emissions during 2015–2016 from Mrk 421 using the DCF and the Pearson correlation functions for VHE γ-rays and HE γ-rays. See caption of Fig. 4.12 for further explanations about the panel contents.

with a second shifted in time by zero or more time lags. We only consider the time lags where we have more than 10 simultaneous observations. As in Section 4.5.1, we only consider fluxes with SNR>2 (i.e. filled markers in Fig. 4.2) for the characterization of the correlations. This ensures the usage of reliable flux measurements, and minimizes unwanted effects related to non-accounted (systematic) errors.

The calculated significance of the Pearson correlation and the uncertainties of the DCF do not necessarily relate to the actual significance of the correlation, because the correlation can be affected by the way the emission in the two bands has been sampled. A LC may have many data points in some time interval with some specific features (either real or due to fluctuations), and this may artificially boost the significance of the correlation. In order to better assess the reliability of the significance of the correlated behaviour computed with the measured LCs, we performed the same calculations using Monte Carlo simulated LCs. Each simulated LC is produced from the actual measured LC by randomly shuffling the temporal information of the flux data points, which ensures the resemblance to the actual measured LC in terms of flux values and flux uncertainties. For each correlation we want to study, we generate 10000 Monte Carlo simulated LCs, compute the DCF and Pearson correlations, and derive the 95 per cent ($2\,\sigma$) and 99.7 per cent ($3\,\sigma$) confidence intervals by searching for the correlation values within which 9500 and 9970 cases are confined, respectively. The simulated LCs are not correlated, by construction, and hence the DCF and Pearson correlation values that lie outside the $3\,\sigma$ contours can be considered as statistically significant (i.e. not produced by random fluctuations).

Despite the low flux in the X-ray and VHE γ-ray bands in the 2015–2016 campaign, the related flux measurement uncertainties are relatively small, and the variability amplitudes in these bands are large, which allows relatively good accuracy in quantifying the correlation. These correlations are computed using simultaneous observations[12] (performed within 0.3 days), and can be quantified on time lags of 1 day. We note that, as shown in the VHE and X-ray LCs from Fig 4.2, there are substantial flux variations on timescales of 1–2 days, and hence it is important to be able to perform the correlation study for time lags of 1 day so that the study takes into account these relatively fast flux variations. However, when quantifying the correlation between the VHE emission measured with MAGIC and FACT and the HE emission measured with *Fermi*-LAT, the study is limited by the 3-day time bins from the *Fermi*-LAT LC shown in Fig. 4.2. The LAT analysis could be performed using time intervals of 1 day (instead of 3 days), but the limited sensitivity of LAT to measure Mrk 421 during non-flaring activity would lead to large flux uncertainties, as well as many time intervals without significant measurements (we used SNR>2 for this study), which would affect the correlation study.

The radio, optical and the GeV emission of Mrk 421 show a substantially lower amplitude variability (see Fig. 4.7) and longer timescales for the flux variations (see Fig. 4.2), in comparison to the keV and TeV bands. Because of that, the 2015–2016 data set is not large enough to evaluate reliably the possible correlations among these energy bands. In order to better quantify the correlations among these bands, we complemented the 2015–2016 dataset with data from previous years (from 2007 to 2014). Some of these data have already been reported in previous papers (Aleksić et al. 2012b, 2015c; Ahnen et al. 2016; Baloković et al. 2016a), while other data were specifically analyzed (or collected) for this study.

[12] In a few cases, there were more than one *Swift*-XRT short observations within the 0.3 days of the MAGIC or FACT observation. In these situations, we selected the X-ray observation that is closest in time to the VHE observation.

Light curve 1	Light curve 2	DCF	Pearson Corr. Coeff. (σ)	Normalized slope of fit	
				unbinned	binned
VHE γ-ray (MAGIC; 0.2 – 1 TeV)	X-ray (XRT; 0.3 – 2 keV)	0.80±0.12	$0.81^{+0.05}_{-0.06}$ (7.3)	0.86±0.02	0.96±0.30
VHE γ-ray (MAGIC; 0.2 – 1 TeV)	X-ray (XRT; 2 – 10 keV)	0.70±0.1	$0.71^{+0.07}_{-0.08}$ (5.7)	0.56±0.02	0.60±0.21
VHE γ-ray (MAGIC; > 1.0 TeV)	X-ray (XRT; 0.3 – 2 keV)	0.64±0.12	$0.62^{+0.1}_{-0.11}$ (4.5)	0.96±0.05	1.15±0.38
VHE γ-ray (MAGIC; > 1.0 TeV)	X-ray (XRT; 2 – 10 keV)	0.67±0.12	$0.65^{+0.08}_{-0.10}$ (4.8)	0.73±0.04	0.82±0.25
VHE γ-ray (FACT; E_{th} ~ 0.7 TeV)	X-ray (XRT; 0.3 – 2 keV)	0.76±0.22	$0.72^{+0.05}_{-0.06}$ (7.4)	1.00±0.05	1.20±0.53
VHE γ-ray (FACT; E_{th} ~ 0.7 TeV)	X-ray (XRT; 2 – 10 keV)	0.80±0.26	$0.74^{+0.05}_{-0.06}$ (7.9)	0.72±0.04	0.80±0.30
VHE γ-ray (MAGIC; 0.2 – 1 TeV)	HE γ-ray (LAT; 0.2 – 2 GeV)	0.30±0.21	$0.20^{+0.17}_{-0.18}$ (1.1)	4.72±1.46	0.57±0.82
VHE γ-ray (MAGIC; 0.2 – 1 TeV)	HE γ-ray (LAT; 2 – 300 GeV)	0.75±0.21	$0.61^{+0.10}_{-0.13}$ (3.8)	2.05±0.47	0.90±0.69
VHE γ-ray (MAGIC; > 1 TeV)	HE γ-ray (LAT; 0.2 – 2 GeV)	0.39±0.20	$0.27^{+0.14}_{-0.15}$ (1.8)	5.76±2.10	0.75±1.18
VHE γ-ray (MAGIC; > 1 TeV)	HE γ-ray (LAT; 2 – 300 GeV)	0.34±0.16	$0.24^{+0.14}_{-0.15}$ (1.6)	4.79±1.89	0.34±0.79
VHE γ-ray (FACT; E_{th} ~ 0.7 TeV)	HE γ-ray (LAT; 0.2 – 2 GeV)	0.41±0.14	$0.29^{+0.09}_{-0.10}$ (2.7)	4.47±0.88	0.62±0.49
VHE γ-ray (FACT; E_{th} ~ 0.7 TeV)	HE γ-ray (LAT; 2 – 300 GeV)	0.66±0.20	$0.47^{+0.08}_{-0.09}$ (4.8)	2.53±0.44	0.58±0.44

Table 4.2: Correlation results for the X-rays, HE and VHE γ-rays during 2015–2016 campaign. This table reports the correlation results for τ=0 (simultaneous emission). The discrete correlation function (DCF) and the corresponding errors are calculated following Edelson & Krolik (1988). The 1 σ Pearson correlation errors are calculated following Press et al. (2002). The slopes of fit for the unbinned (grey markers) and binned data (blue markers), presented in Fig. 4.15, are normalized with the average flux of the bands under consideration. 1-day binning of the data has been used for VHE γ-rays (MAGIC and FACT) and X-rays (0.3 – 2 keV and 2 – 10 keV) while a 3-day binning has been used for HE and VHE γ-ray (FACT; E_{th} ~ 0.7 TeV) LCs. See Section 4.6 for details.

Differently to what occurs for the X-ray and VHE fluxes, the lower variability and longer variability timescales in the radio/optical/GeV emissions allow us to use the observations that are not strictly simultaneous, but only contemporaneous within a few days. For this study, we quantified the observations in temporal bins of 15 days, as done in Carnerero et al. (2017). The study is performed in the same fashion as for the simultaneous X-ray/VHE fluxes, but with time-bins of 15 days instead of 1 day.

The following subsections report the results obtained from this correlation study, and in Section 4.11, we provide some discussion and interpretation of these results.

4.6.1 VHE γ-rays and X-rays

The quantification of the correlations between the VHE γ-rays and X-rays for a range of ±30 days, examined in steps of 1 day, is reported in the panels (a)–(f) of Fig. 4.12. All of the panels report the DCF vs. the time lag and the significance of the Pearson correlation vs. the time lag. The panels (a)–(d) show the correlation for the two energy bands ($0.2-1$ TeV and >1 TeV) measured with MAGIC and the two energy bands ($0.3-2$ keV and $2-10$ keV) observed with *Swift*-XRT, and the panels (e) and (f) show the correlations obtained using the VHE flux with E_{th} ~0.7 TeV measured with FACT, and the two energy bands from the *Swift*-XRT.

All the panels (all the energy bands probed) show a positive correlation above $3\,\sigma$ for τ=0, which drops quickly for negative and positive lags. While the shape of the DCF peak is similar for all the bands, the peak in the significance of the Pearson correlation is narrower when using MAGIC than when using FACT. This is produced by the rapid drop in the number of available flux-flux pairs when examining time lags different from zero (simultaneous observations), which critically affects the significance with which a correlation is measured. In the case of MAGIC , the number of flux-flux pairs for τ=0 is 45, while the number drops to 14 for $\tau = -1$ day (X-ray LC shifted 1 day earlier) and 20 for $\tau = +1$ day (X-ray LC shifted 1 day later). On the other hand, when using FACT, the number of flux-flux pairs for $\tau = 0$ is 71, and the number is 71 (72) for $\tau =$ -1 (+1) day, which ensures the same resolution to evaluate the correlation for these different time lags. Table 4.2 reports the DCF and the Pearson correlation, with their related $1\,\sigma$ uncertainties, and the significance of the Pearson correlation for $\tau = 0$ (simultaneous observations). This table also reports the normalized slopes that relates the VHE γ-ray and the X-ray fluxes in the various energy bands (see Fig. 4.15.

4.6.2 VHE γ-rays and HE γ-rays

In this study, the daily LCs from MAGIC and FACT were re-binned to match the three-day cadence of the HE γ-ray LC from *Fermi*-LAT. The panels of Fig. 4.13 show the correlation between the VHE fluxes and the HE fluxes for a range of ± 30 days in three-day steps. We do not find a significant correlation between the VHE fluxes and the 0.2-2 GeV fluxes, but we do see a marginally significant correlation between the VHE fluxes from MAGIC (in the range $0.2 - 1$ TeV) and FACT ($E_{th} \sim 0.7$ TeV) and the HE fluxes above 2 GeV. This correlation occurs for $\tau = 0$, indicating that the emission in these two energy bands is simultaneous (within the ± 3 days resolution of this study). The DCF and Pearson correlation values, $\tau = 0$, are reported in Table 4.2. The DCF analysis, which takes into account the flux measurement errors from MAGIC, FACT and *Fermi*-LAT for the 3-day time intervals, yields 0.75 ± 0.21 for MAGIC and 0.66 ± 0.20 for FACT. The Pearson correlation is 0.6 and 0.5, with a significance of $4\,\sigma$ and $5\,\sigma$ respectively. As shown in Fig. 4.13, for both MAGIC and FACT, the DCF and the Pearson significance is above the $3\,\sigma$ contour from our Monte Carlo simulations.

The evaluation of whether a correlation exists between the MAGIC VHE fluxes above 1 TeV and the HE flux above 2 GeV is hampered by the relatively large flux uncertainties. No evidence for a correlation was found (Pearson correlation of 0.24±0.15, with a significance of 1.6 σ). The flux-flux correlation plots for these energy bands are shown in Fig. 4.16.

Despite the smaller flux uncertainties from MAGIC (in the range 0.2 − 1 TeV), in comparison with those from FACT, the significance of the Pearson correlation is the highest when using FACT. This is very likely due to the substantially lower temporal sampling of MAGIC (61 measurements used in the correlation study) with respect to that from FACT (180 measurements). This includes the additional temporal coverage provided by FACT in 2014 November-December and 2016 June, when Mrk 421 showed enhanced VHE flux, which appears to have a counterpart in the GeV range (see Fig. 4.2). Because of the low fractional variability in the GeV range, the additional temporal coverage provided by FACT proved very beneficial for the understanding of this correlated behaviour.

A similar correlation had been previously reported in Bartoli et al. (2016a) for VHE γ-rays measured with the ARGO-YBJ at TeV energies and the HE γ-rays measured with *Fermi*-LAT above 0.3 GeV. They quantified the correlation with the DCF analysis, obtaining a correlation for $\tau = 0$ with DCF=0.61 ± 0.22. The main differences with respect to the result presented here are the somewhat different energy bands involved, and the very different temporal scales used for these two correlation studies. While Bartoli et al. (2016a) used 4.5 years (from mid 2008 to 2013) 30-day bins, we performed the study over 1.5 years in time bins of 3 days. Additionally, in this work, we also quantify the correlation using the Pearson correlation function and Monte Carlo simulations to better evaluate the reliability of the significance of the correlation.

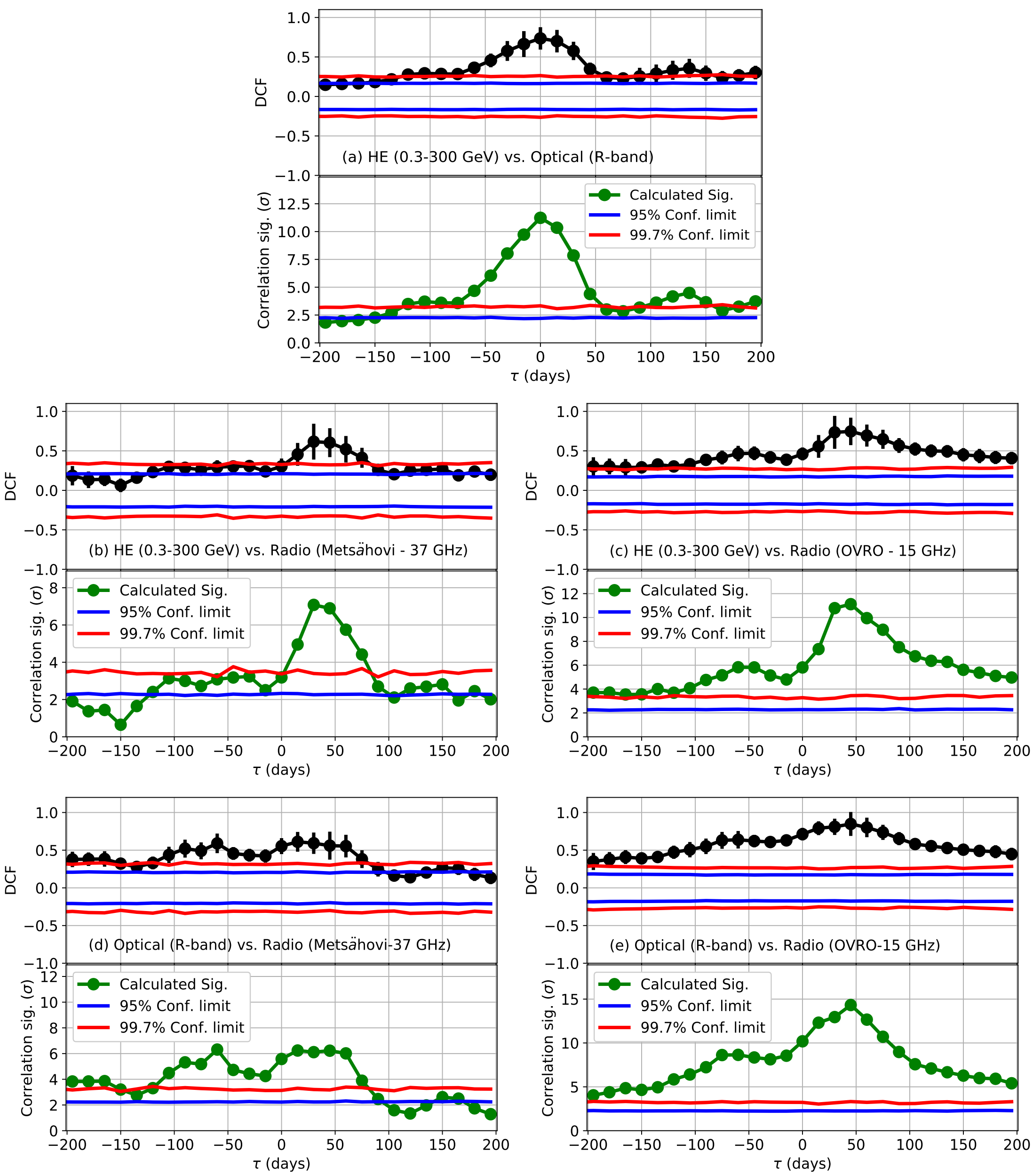

Figure 4.14: Correlation between the HE γ-rays, optical (R-band) and two radio bands using fluxes for 15-day time intervals from 2007 to 2016. See caption of Fig. 4.12 for further explanations about the panel contents.

4.6.3 HE γ-rays and optical band

The panel (a) of Fig. 4.14 shows the quantification of the correlation between the HE fluxes in the $0.3-300$ GeV energy band measured with *Fermi*-LAT and the optical fluxes in the R-band, as measured by a large number of instruments over a time range spanning from 2007 to 2016 . The correlation is computed for a time lag range of ± 200 days in steps of 15 days, with the HE and R-band fluxes computed in 15-day temporal bins. The plot shows a correlation peak of about 60 days FWHM, and centered at $\tau = 0$. As reported in Table 4.3, the Pearson correlation is 0.72 ± 0.04, with a correlation significance of about 11 σ, and the DCF is 0.74 ± 0.17. Because of the 15-day fluxes and 15-day time steps, the resolution with which we can estimate the time lag with the highest correlation is somewhat limited. Following the prescription from Peterson et al. (1998), we estimate the time lag with the highest correlation is 3^{+5}_{-9} days, which is perfectly consistent with no time lag, suggesting that the emission in these two energy bands is simultaneous. Panel (a) of Fig. 4.17 shows that the relation between the GeV and R-band fluxes can be approximated by a linear function with a normalized slope of 0.6–0.7 (see Table 4.3).

A positive correlation between the multi-year *Fermi*-LAT γ-ray flux and the optical R-band flux had been first reported in Fig. 25 of Carnerero et al. (2017). The DCF from that study, also performed in steps of 15 days, shows a broad peak of many tens of days around $\tau = 0$, with the highest DCF value being around 0.4, for the multi-year data set. However, the significance of the correlation was not quantified in Carnerero et al. (2017). In this work, we show that a DCF of 0.4 is not necessarily related to a significant ($>3\,\sigma$) correlation. We also show that the *Fermi*-LAT γ-ray flux and optical R-band emissions are positively correlated with a DCF of about 0.8, and with a very high significance ($>12\,\sigma$), hence confirming and further strengthening the claims made in Carnerero et al. (2017).

Light curve 1	Light curve 2	Time-shift	DCF	Pearson Corr. Coeff. (σ)	Normalized slope of fit	
					unbinned	binned
HE γ-ray (LAT; 0.3 – 300 GeV)	Optical (R-band)	0	0.74±0.14	$0.72^{+0.04}_{-0.04}$ (11.2)	0.66 ± 0.03	0.63 ± 0.21
HE γ-ray (LAT; 0.3 – 300 GeV)	Radio (Metsähovi; 37 GHz)	45	0.60±0.18	$0.53^{+0.06}_{-0.06}$ (6.9)	2.63±0.17	0.79±0.33
HE γ-ray (LAT; 0.3 – 300 GeV)	Radio (OVRO; 15 GHz)	45	0.75±0.17	$0.72^{+0.04}_{-0.04}$ (11.1)	1.53±0.06	1.32±0.41
Optical (R-band)	Radio (Metsähovi; 37 GHz)	45	0.56±0.18	$0.50^{+0.06}_{-0.07}$ (6.2)	2.93 ± 0.17	0.83 ± 0.33
Optical (R-band)	Radio (OVRO; 15 GHz)	45	0.85±0.16	$0.84^{+0.02}_{-0.03}$ (14.3)	2.82 ± 0.02	2.0 ± 0.35

Table 4.3: Correlation results between the low-variability radiation components of Mrk 421. The long-term (2007–2016) data have been used for the correlation results of the radio, optical, and HE γ-rays. The column time-shift reports the temporal shift applied to the second light curve with respect to the first one. This time shift corresponds to the time lag with the highest DCF in Fig. 4.14. The various columns report the same quantities as in Table 4.2. The slopes of fit for the unbinned (grey markers) and binned data (blue markers), presented in Fig. 4.17, are normalized with the average flux in the corresponding bands. See Section 4.6 for details.

4.6.4 HE γ-rays and radio band

Panels (b) and (c) of Fig. 4.14 show the correlation between the HE γ-rays in the 0.3 – 300 GeV energy band, measured with *Fermi*-LAT, and the 37 GHz and 15 GHz radio flux densities, as measured with Metsähovi and OVRO. In both cases one finds a positive correlation characterized by a wide peak, of about 60 days, centered at $\tau \sim 45$ days. Section 4.8 reports an estimation of the time lag between these energy bands, obtained with the prescriptions from Peterson et al. (1998). We estimate that the time lag between the HE γ-rays and the 37 GHz radio flux is 41^{+10}_{-11} days, while for the 15 GHz radio flux it is 47^{+5}_{-9} days. The panels (b) and (c) of Fig. 4.17 show that, for a time shift of 45 days, the relation between the GeV and the radio fluxes can be approximated by a linear function. As reported in Table 4.3, for a time shift of 45 days, the Pearson correlation is about 0.5–0.7, with a correlation significance of 7 σ for Metsähovi and 11 σ for OVRO, and the DCF is 0.6 ± 0.2 and 0.7 ± 0.2, respectively for Metsähovi and OVRO. Therefore, the correlation between these bands is robustly measured.

The radio emission of blazars has been found to be correlated to the γ-ray emission using EGRET data (e.g. Jorstad et al. 2001; Lähteenmäki & Valtaoja 2003) and *Fermi*-LAT data (e.g. León-Tavares et al. 2011; Ackermann et al. 2011), very often with the radio emission delayed with respect to the γ-ray emission by tens and hundreds of days (e.g. Ramakrishnan et al. 2015). As for the specific case of Mrk 421, Max-Moerbeck et al. (2014) had first reported a positive correlation between γ-rays from *Fermi*-LAT and radio from OVRO for a time lag that, using the recipe from Peterson et al. (1998), was estimated to be 40±9 days. However, the correlation reported in that paper was only at the level of 2.6 σ (p-value of 0.0104), quantified with a dedicated MC simulation, and strongly affected by the large γ-ray and radio flares from July and September 2012, respectively (Max-Moerbeck et al. 2014). Hovatta et al. (2015), which considered also data from another (smaller) radio flare in 2013, reported a positive correlation for a range of τ of about 40–70 days, but did not assign any significance to this measurement. In the study reported upon here our dedicated MC simulations show that the significance of the correlation between *Fermi*-LAT and OVRO is well above the 3σ contour, and, when using the prescription from Press et al. (2002) to quantify it, we obtained $11\,\sigma$. Moreover, because of the twice larger data set, it is not dominated by the large γ-ray and radio flares in 2012. In order to better understand this correlation, we removed this large γ-ray and radio flare from 2012 by generously excluding the time interval MJD 56138–56273 from both the γ-ray and radio LCs, and repeated the test. We obtained a positive correlation with a significance of $9\,\sigma$, with a peak that extends over a range of about 60 days, centered at $\tau \sim 45$ days. Therefore, we confirm and further strengthen the correlation reported in Max-Moerbeck et al. (2014), stating with reliability that this is an intrinsic characteristic in the multi-year emission of Mrk 421, and not a particularity of a rare flaring activity.

4.6.5 Optical band and radio band

Panels (d) and (e) of Fig. 4.14 show the correlation between the flux in the optical R-band from GASP-WEBT and the 37 GHz and 15 GHz radio flux densities measured with Metsähovi and OVRO, respectively. In the case of OVRO, one finds that the highest correlation occurs for $\tau \sim 45$ days, and it is characterized by a wide peak that resembles the one obtained for the GeV vs 15 GHz band, as depicted in the panel (c) of Fig. 4.14. In the case of Metsähovi, the DCF shows much wider structure, without any clear peak, but with high DCF values also around $\tau \sim 45$ days. As done above, we followed the prescriptions of Peterson et al. (1998) to estimate the time lag between these bands (see Section 4.8). We obtained $\tau = 33^{+19}_{-11}$ days for the R-band and the 37 GHz radio flux, and $\tau = 39^{+6}_{-2}$ days for the R-band and the 15 GHz radio flux. The panels (d) and (e) of Fig. 4.17 show that, for a time shift of 45 days, the relation between the R-band and the radio fluxes can be approximated by a linear function. As reported in Table 4.3, for a time shift of 45 days, the Pearson correlation is 0.5 and 0.8, with a correlation significance of 6 σ and 14 σ for Metsähovi and for OVRO, respectively. The DCF is about 0.6 and 0.9 for them, hence indicating a very clear and significant correlated behaviour for these two bands.

4.7 Multi-band flux-flux relations

This section reports the multi-band flux-flux plots related to the correlations discussed in Section 4.6.

Panels (a)–(d) in Fig. 4.15 show the integral VHE γ-ray flux from the two energy bands measured with MAGIC (reported in Fig 4.2, namely 0.2−1 TeV and above 1 TeV), plotted against the X-ray flux in the two energy bands from *Swift*-XRT (reported in Fig 4.2). The panels (e)-(f) of Fig. 4.15 show the VHE vs X-ray flux relations when using the VHE fluxes with E_{th} ~0.7 TeV measured with FACT. Only simultaneous observations are used in these figures. Besides the display of all the flux measurements (roughly equivalent to unbinned data), the panels also show the average and the standard deviation computed with data subsets of 10 observations, binned according to their flux (binned data). The binned data allow us to better visualize the main trend, as well as the dispersion in the single-day flux measurements. Both the unbinned and binned data are fitted with a linear function to quantify the slope in the VHE vs X-ray flux relation. These slopes are reported in Table 4.2. Despite the large dispersion in the VHE vs X-ray flux values, there is a roughly linear trend for all the bands, with the slope of the trend increasing for increasing VHE energy band, or for decreasing X-ray energy band.

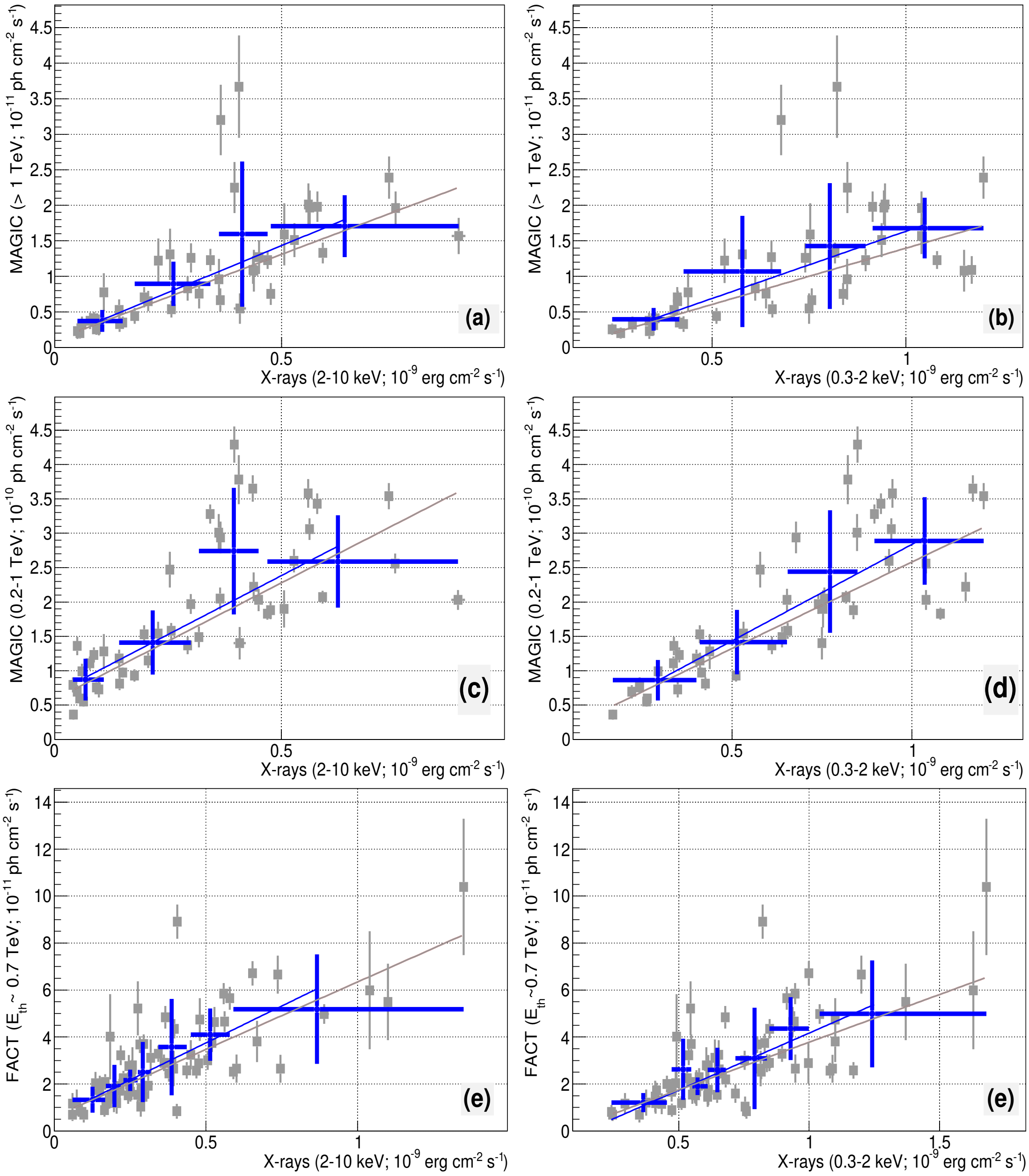

Figure 4.15: VHE vs X-ray flux correlation plots during 2015–2016 campaign. The grey markers denote the individual flux measurements and related errors (unbinned data), while the blue markers show the average and the standard deviation computed with data subsets of 10 observations, binned according to their flux (binned data). The grey and blue lines depict the best linear fit to the unbinned and binned data, with the slopes reported in Table 4.2. Only simultaneous VHE-X-ray data (taken within 0.3 days) were used. See Section 4.6.1 for details.

The panels in Fig. 4.16 show the integral VHE γ-ray flux from MAGIC and FACT in various energy bands, plotted against the HE flux from *Fermi*-LAT in two energy bands. The energy bands used are those employed in Fig 4.2, and the flux values relate to 3-day time intervals (see Section 4.6.2). As with the panels in Fig. 4.15, besides showing of all the 3-day flux measurements (unbinned data), the panels also show the average and the standard deviation computed with data subsets of 10 observations, binned according to their flux (binned data). Both the unbinned and binned data are fitted with a linear function to quantify the slope in the VHE vs HE flux relation. These slopes are reported in Table 4.2. In contrast to what happens in the panels of Fig. 4.15, there is a large difference between the slopes in the linear functions fitted to the unbinned and binned data. The difference is ascribed to VHE vs HE flux pairs which are well outside the main trend (outliers), which have a large impact on the fit to the unbinned data, but not to the binned data. The difference is also partly due to the weak (if not absent) correlation between these energy bands (see Section 4.6.2 for further details).

Figure 4.17 shows the HE vs optical flux correlation plots for the HE γ-rays vs optical for τ=0, the HE γ-rays vs radio for a time shift of 45 days, and the optical vs radio for a time shift of 45 days. The time shift of 45 days is the time for which the correlation between these two bands is the highest (see Section 4.6.4 and 4.6.5). The panels (b) and (c) of Fig. 4.17 show that, for a time shift of 45 days, the relation between the GeV and the radio fluxes can be approximated by a linear function. As with Fig. 4.15, the panels also show the average and the standard deviation computed with data subsets of 10 observations, binned according to their flux (binned data). In the case of LAT vs Metsähovi, there is a large difference between the slopes from the linear functions fitted to the unbinned and binned data. This is produced by a few HE vs optical flux pairs which are well outside the main trend; they have a substantial impact on the fit to the unbinned data, while they do not affect the binned data.

4.8 Estimation of the most representative time lag

In this section, we report an estimate of the most representative time lag and its related uncertainty for the multi-band fluxes used in the correlation studies reported in Sections 4.6.3, 4.6.4, and 4.6.5. We use the model-independent Monte Carlo flux randomization (FR) and random subset selection (RSS) method described in Peterson et al. (1998) and Peterson et al. (2004), which is the methodology used by Max-Moerbeck et al. (2014) to estimate the time lag of 40±9 days between the *Fermi*-LAT and OVRO fluxes. Briefly, the method employed in this study is as follows: we perform RSS of the first LC and select the simultaneous observations between the first and second LC. Then, we perform FR according to the flux uncertainties of both LCs. In this way, through this process of RSS and FR, we generate a set of 1000 Monte Carlo simulated LC pairs. Then we perform the DCF study for these 1000 simulated pairs. As in Peterson et al. (1998), a cross-correlation is considered successful if the maximum correlation coefficient is large enough such that the correlation between the LC pairs is significant above 95% confidence level. Instead of using the peak of the DCF (DCF_{max}), following the prescriptions from Peterson et al. (2004), we used the centroid of the DCF (DCF_{cen}), computed with the DCF values above $0.8\times DCF_{max}$, which is expected to provide better results when the DCF has a broad peak. The distributions of DCF_{cen} are then obtained. The most representative value of the time lag is estimated by considering the mean of the distribution, and the uncertainties are computed using the 68% containment, that would correspond to 1 σ error for a normal distribution.

Figure 4.18 shows the distribution of DCF_{cen} for the 1000 simulated LCs for the HE and optical R-band. The average and the 68% containment (depicted with the black and

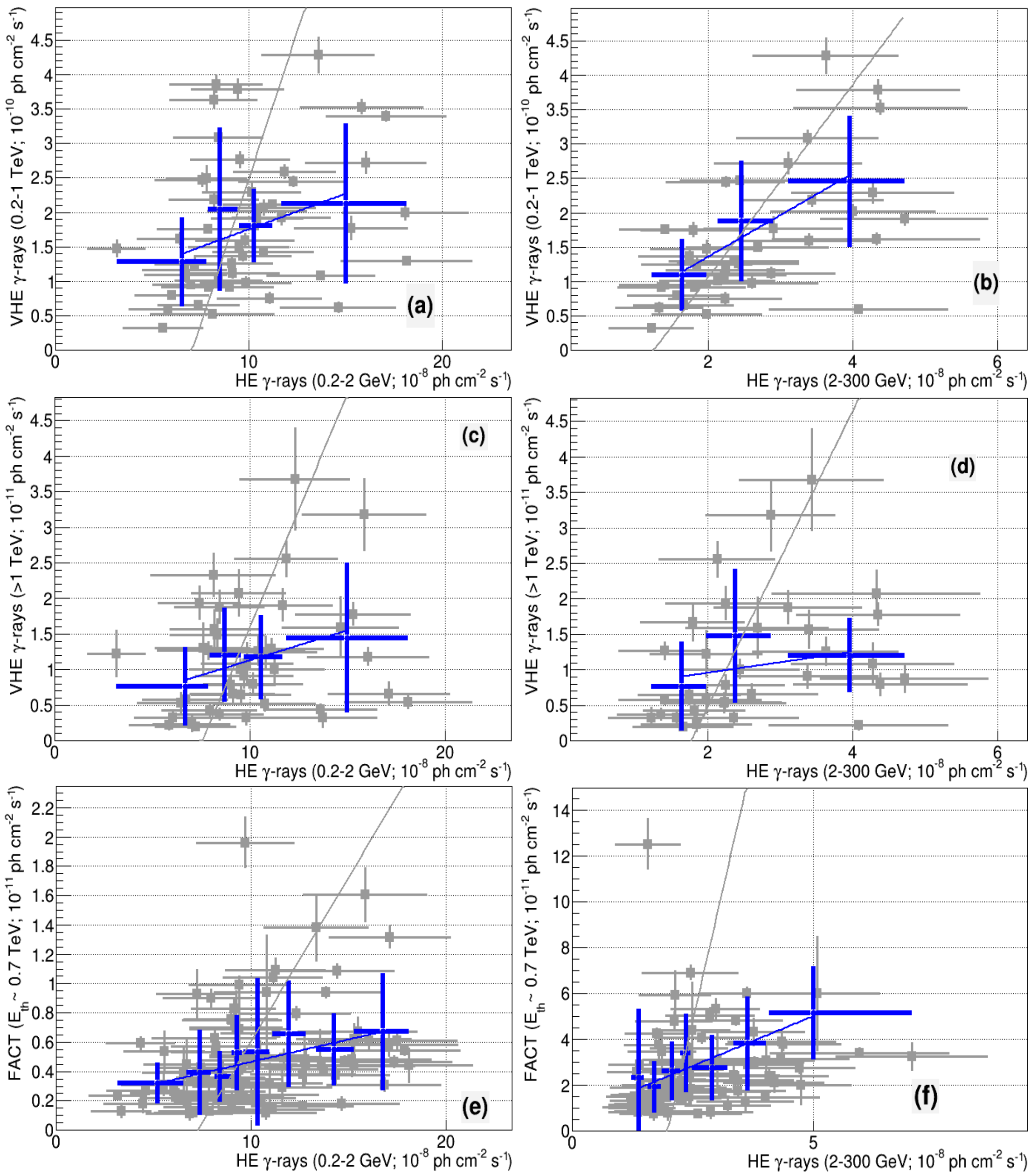

Figure 4.16: VHE vs HE flux correlation plots during the 2015–2016 campaign. The grey and blue markers as in Fig.4.15. The grey and blue lines depict the best linear fit to the unbinned (grey) and binned (blue) data, with the slopes reported in Table 4.2. The flux values relate to 3-day time intervals. See Section 4.6.2 for details.

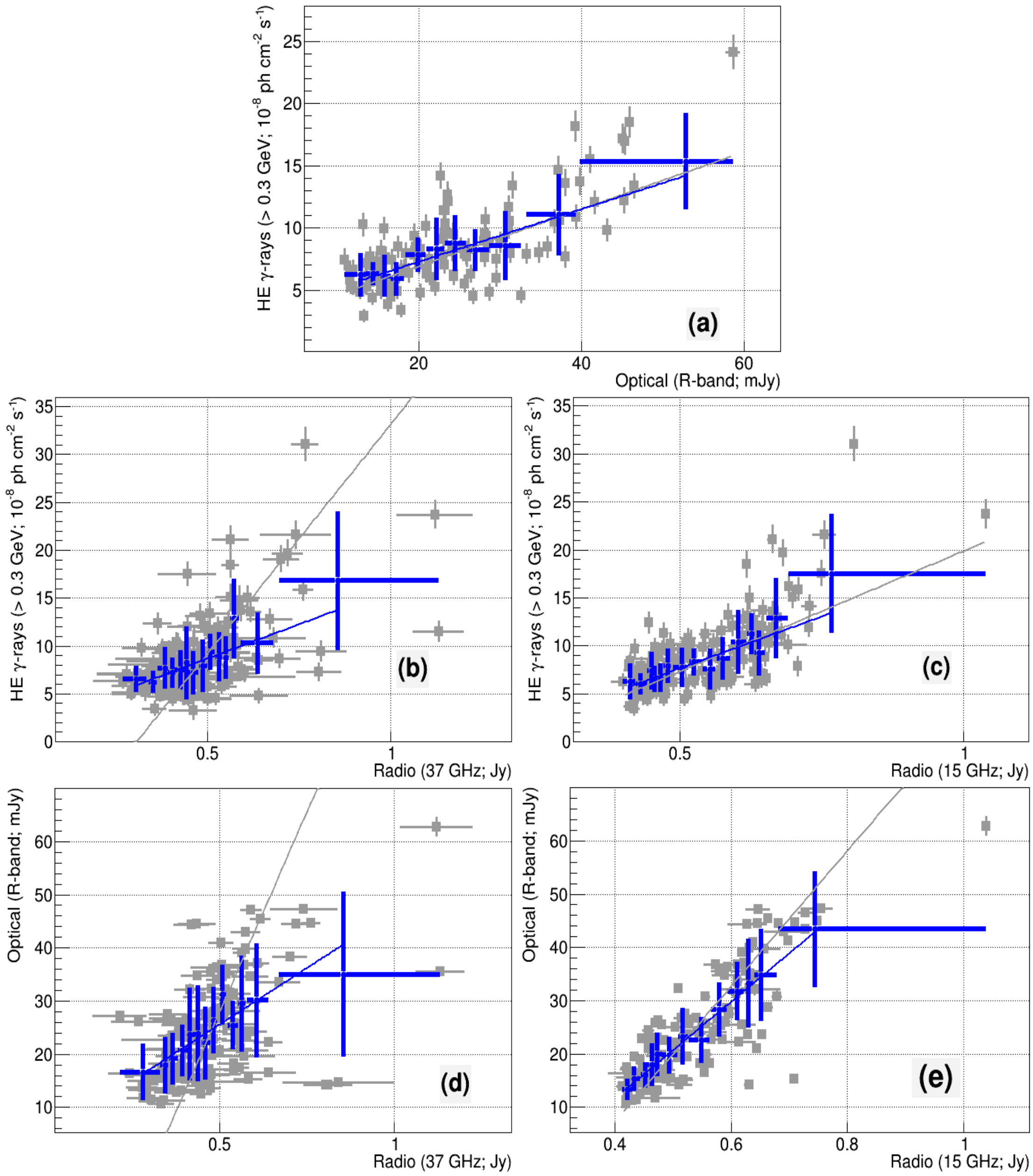

Figure 4.17: Flux-flux plots for several energy bands. The grey and blue markers as in Fig.4.15. The grey and blue lines depict the best linear fit to the unbinned (grey) and binned (blue) data, with the slopes reported in Table 4.3. Panel (a) shows the flux-flux cross-correlation between the HE γ-rays (LAT; >0.3 GeV) and optical (R-band) fluxes, computed for 15-day time intervals at a zero timelag. The panels (b)-(e) report fluxes computed for 15-day time intervals, where the radio (15 GHz and 37 GHz) have been shifted 45 days earlier in order to match the time lag observed in the correlation plots from Fig. 4.14. See Section 4.6.3, 4.6.4, and 4.6.5, for details.

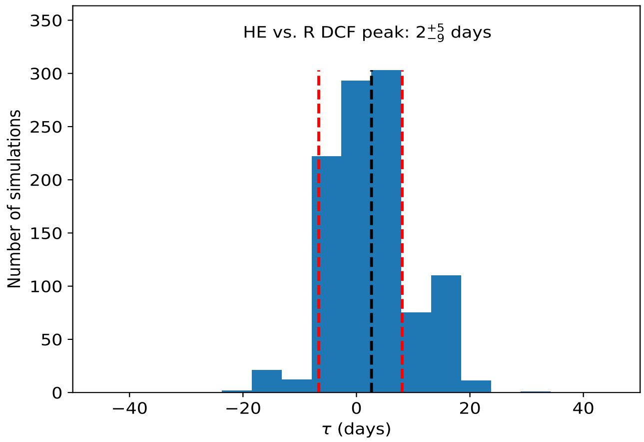

Figure 4.18: Distribution of DCF$_{cen}$ derived with 1000 Monte Carlo FR/RSS simulations to estimate the time lag between the HE γ-ray and optical R-band LCs that were used to compute the DCF reported in panel *a* of Fig. 4.14. The average and the 68% containment are depicted with the black and red lines, respectively, and are used as the estimate of the time lag between these two bands. See text in Section 4.8 for further details.

red lines in Fig. 4.18) is 2^{+5}_{-9}, which can be considered as good estimate of the time lag and related uncertainty between the fluxes for these two energy bands. This is perfectly consistent with no time lag, and hence simultaneous emission in these two energy bands.

The panels in Fig. 4.19 show the distributions of DCF$_{cen}$ for the 1000 simulated LCs for the HE and R band vs. the two radio bands observed with Metsähovi and OVRO. Since the time lags shown in Fig 4.19 are statistically compatible, we decided to combine the GeV and R-band with the 37 GHz and with the 15 GHz cases, in order to estimate combined time lags for the GeV/optical and 37 GHz, and the GeV/optical and 15 GHz. The combined distributions of DCF$_{cen}$, derived with the 2000 simulated LCs, are shown in Fig. 4.20, leading to the estimation of combined time lags of 37^{+15}_{-11} days and 43^{+8}_{-5} days, respectively.

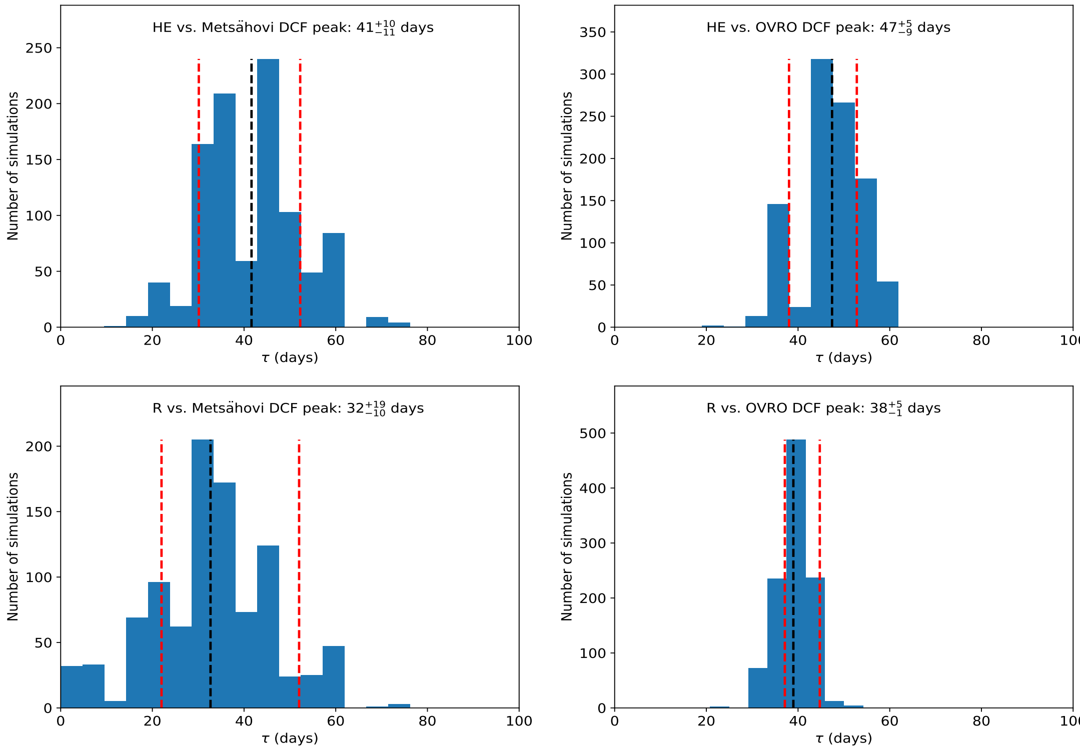

Figure 4.19: Distributions of DCF_{cen} derived with 1000 Monte Carlo FR/RSS simulations to estimate the time lag between the various multi-band LCs that were used to compute the DCFs reported in panels *b, c, d,* and *e* of Fig. 4.14: a) HE vs. Metsähovi (top-left), b) HE vs. OVRO (top-right), c) R vs. Metsähovi (bottom-left) and d) R vs. OVRO (bottom-right). The average and the 68% containment are depicted with the black and red lines, respectively, and are used as the estimate of the time lag between the bands. See text in Section 4.8 for further details.

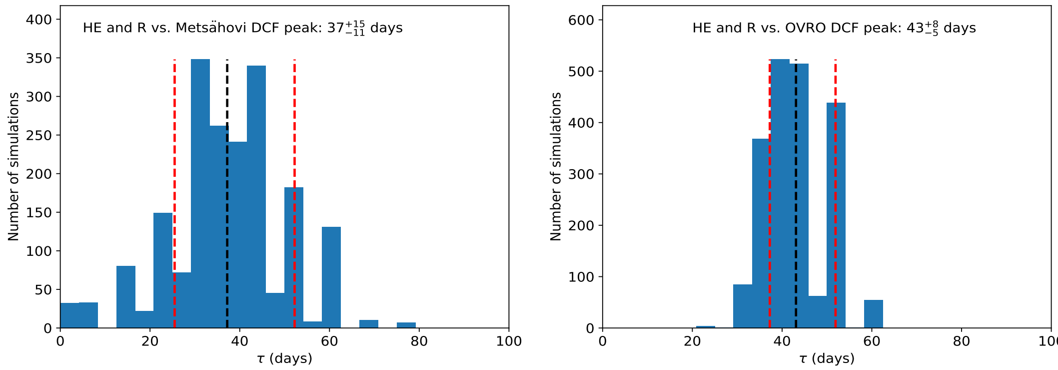

Figure 4.20: Distribution of DCF_{cen} from the combinations of the two panels with 37 GHz Metsähovi data (left) and the two panels with 15 GHz OVRO data (right) from Fig. 4.19. See text in Section 4.8 for further details.

4.9 Determination of the MWL flux distributions

The emission mechanisms in accreting sources like active galactic nuclei and X-ray binaries have been found to be consistent with stochastic processes (McHardy et al. 2006; Chatterjee et al. 2012; Nakagawa & Mori 2013; Sobolewska et al. 2014). For a linear stochastic process, one expects a Gaussian distribution of fluxes. However, a LogNormal distribution was found to be preferred (over a Gaussian one) in the long-term X-ray light curve of the blazar BL Lac where the average amplitude variability was found to be proportional to the flux (Giebels & Degrange 2009). The Galactic X-ray binary Cygnus X-1 also showed such features in X-rays (Uttley & McHardy 2001). Since then, LogNormal behaviour has been observed in several blazars primarily in optical/near IR, X-ray and γ-ray wavelengths (Sinha et al. 2016, 2017; Romoli et al. 2018; Valverde et al. 2020). The presence of LogNormality indicates an underlying multiplicative process in blazars contrary to the additive physical process. It has been suggested that such multiplicative processes originate in the accretion disk (Lyubarskii 1997; Uttley et al. 2005; McHardy 2010), however, Narayan & Piran (2012) strongly argue the variability to originate within the jet. In case of Mrk 421, using data from 1991 to 2008, mostly from the old generation of VHE ground-based γ-ray instruments, the flux distribution above 1 TeV was found to be consistent with a combination of a Gaussian and a LogNormal distribution (Tluczykont et al. 2010). The improvement of the sensitivity of the present day telescopes over last few years now provides us with the opportunity to study the flux states with a much better accuracy, and a minimum energy as low as 0.2 TeV, where the minimum energy is always above the analysis energy threshold.

Here, we report on a detailed study of the flux distributions observed in different wave-bands, from radio to VHE γ-rays, using the data from the 2015–2016 campaigns, together with previously published MWL data from the 2007, 2008, 2009, 2010 and 2013 campaigns (Aleksić et al. 2012b; Ahnen et al. 2016; Aleksić et al. 2015c; Baloković et al. 2016a), published multi-year optical R-band data (Carnerero et al. 2017), and unpublished data at radio (OVRO, Metasahovi), hard X-ray (*Swift*-BAT) and GeV γ-rays (*Fermi*-LAT). The multi-year light curves used for this study are reported in Section 4.4. The two large VHE γ-ray flaring episodes of Mrk 421 in 2010 February (Abeysekara et al. 2020) and 2013 April (Acciari et al. 2020) have been excluded to avoid large biases in the distributions. During these two time intervals of about 1 week, Mrk 421 showed a VHE activity larger than 20 times its typical flux and, because of the exceptional activity, the number of X-ray and VHE observations were also increased by more than one order of magnitude with respect to the typical temporal coverage during the regular MWL campaigns. The inclusion of these two periods would create a large structure in the X-ray and VHE γ-ray distributions at fluxes of about ten times the typical ones, and would hamper any fit with a smooth function, like Gaussian or Log-Normal. The data used here relate to time intervals when Mrk 421 showed typical or low activity (e.g. during years 2007, 2009, 2015, 2016) or somewhat enhanced activity, as it happened during year 2008 and 2 weeks in 2010 March. Because of the high activity in 2008, some of the X-ray and VHE observations came from dedicated ToOs, which increased somewhat the number of observations that would not have been performed in the absence of high activity. The accurate identification of the "extra observations" is complicated because the dynamic scheduling that was being used at the time, and the fact that these observations occurred 12 years ago. We note that the inclusion of the 2008 data introduces a bias towards high fluxes in the X-ray and VHE flux distributions (because of the additional observations during a period of high activity).

In order to determine the preferred shape, we fit the flux distributions staring from the minimum flux with the following functions:

1) Gaussian: G(x; μ_G, σ_G) = $\frac{N_G}{\sigma_G \sqrt{2\pi}} e^{-\frac{(x-\mu_G)^2}{2\sigma_G^2}}$, and

2) LogNormal: LN(x; $\mu_{\mathrm{LN}}, \sigma_{\mathrm{LN}}$) = $\frac{N_{\mathrm{LN}}}{x\sigma_{\mathrm{LN}} \sqrt{2\pi}} e^{-\frac{(log(x)-\mu_{\mathrm{LN}})^2}{2\sigma_{\mathrm{LN}}^2}}$,

where N_G and N_{LN} are the normalization constants for the Gaussian and LogNormal profiles, respectively, and μ_i and σ_i are the mean and standard deviation of the fitted profiles (i=G and LN for Gaussian and LogNormal, respectively).

4.10 Characterization of the MWL flux distributions using a (binned) Chi-square fit and a (unbinned) log-likelihood fit

This section reports the characterization of the flux distributions using a binned Chi-square fit and an unbinned log-likelihood fit. These are the conventional ways of quantifying the shape of a distribution, and complement the results obtained with the flux profile method reported in Section 4.9 and Section 4.10.1. In both exercises, we use fluxes and their errors scaled by the average flux for each of the energy bands, and present them as F and ΔF.

In order to perform the Chi-square fit, we first bin the scaled flux F. For each of the energy bands, the number of histogram bins employed permits to show the overall shape of the distribution, while keeping sufficient statistics (more than 10 entries) in most of the bins. Afterwards, we performed a regular fit with a Gaussian and LogNormal functions, starting from the minimum flux F_{min}, and obtaining the function parameters mean (μ) and standard deviation (σ) for which the Chi-square is minimum. It must be noted that the outcome of the Chi-square fit can depend on the histogram binning, and does not consider the flux uncertainties. Figure 4.21 shows the results of the Chi-square fit for all the bands.

In the log-likelihood fit, the log-likelihood function used for the Gaussian PDF, as a function of the parameters μ and σ, is given as:

$$L_g(f(F_i, \Delta F_i)|\sigma, \mu) = -\frac{1}{2} \sum \left[log(2\pi(\Delta F_i^2 + \sigma^2)) + \frac{(F_i - \mu)^2}{\Delta F_i^2 + \sigma^2} \right] \tag{4.4}$$

In order to calculate the log-likelihood of the LogNormal distribution, we consider a grid with 3000 points (x_i), using a dynamic grid resolution, ranging from log(F_{min})-5 to log(F_{max})+5, where F_{min} and F_{max} are the minimum and maximum scaled fluxes in the corresponding energy bands. The exponential of the grid points (e^{x_i}) are then used for the defining the LogNormal PDF as a function of the parameters μ and σ, in the form given below:

$$L^i_{\mathrm{LN}}(f(x_i|\sigma, \mu) = -\frac{1}{\sqrt{2\pi}} \frac{1}{e^{x_i}\sigma} exp\left[-\frac{(x_i - \mu)^2}{2\sigma^2} \right] \tag{4.5}$$

Next, we calculate the Gaussian probability $G^j_i(F_j, \Delta F_j)$ for each of the flux measurements with measured flux (F_j) and flux-error (ΔF_j) using the following equation (Eq. 4.103) at different grid-points (x_i).

$$G^j_i(F_j, \Delta F_j) = -\frac{1}{\sqrt{2\pi}} \frac{1}{\Delta F_j} exp\left[-\frac{(e^{x_i} - F_j)^2}{2\Delta F_j^2} \right] \tag{4.6}$$

We obtain the log-likelihood by the convolution of these two terms and integrating over the grid-range. Finally, we minimize the log-likelihood and obtain the optimal parameters for μ and σ. The results are presented in Fig. 4.22 where, for completeness, the flux histograms used in Fig. 4.21 are also shown. By construction, the log-likelihood fit considers the flux uncertainties, and does not require to bin the data, both representing

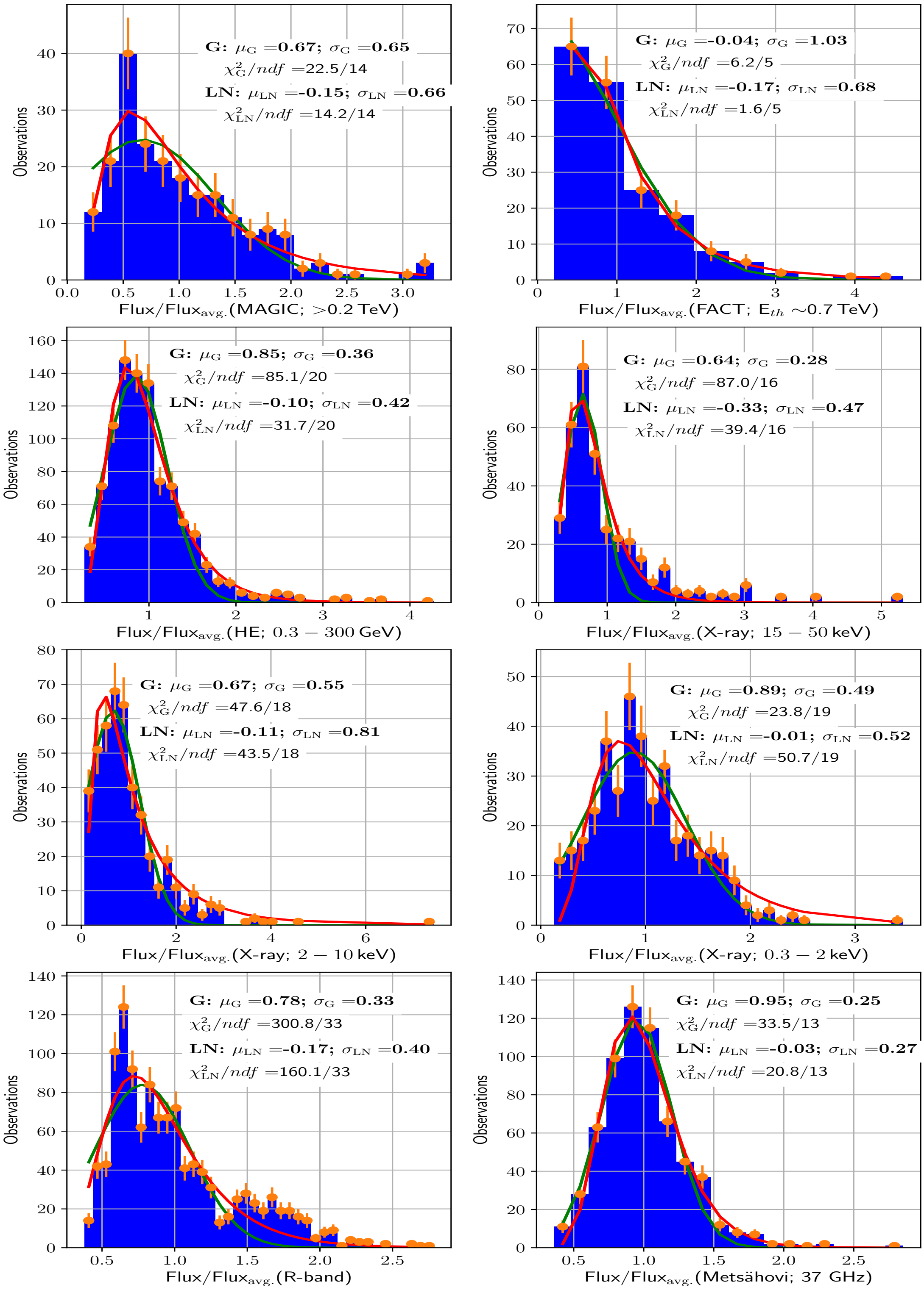

Figure 4.21: Characterization of the MWL flux distributions with a Chi-square fit. The X-axis shows the scaled flux and the Y-axis presents the number of observations. The green and red lines represent the best fit with the Gaussian and LogNormal functions for flux histograms (presented in blue). See text in Section 4.10 for details.

big advantages over the Chi-square fit. However, we note that log-likelihood fit applied here is very simple and generic because we are using the same PDF functions for all the energy bands. One could exploit the full potential of the log-likelihood method by using dedicated PDFs for each energy band, which would allow one to address the problem in a more efficient manner. However, that would require introducing instrument response functions and physical models of emission into the PDFs, which is out of the scope of this work.

4.10.1 Flux profile

Almost all the studies done so far in this respect involve construction of Chi-square fit to the flux histograms (Tluczykont et al. 2010; Abeysekara et al. 2017; Sinha et al. 2016; Dorner et al. 2019). However, generating flux distributions from histograms has certain inaccuracies and biases related to the selection of the bin-width and the flux measurement errors, which are not considered when making a simple flux distribution. In order to address this issue, we have developed a new method, in which, we construct "flux profiles" instead of histograms. This method is largely inspired by the kernel density estimation (KDE), dubbed "flux profile construction". We treat each flux measurement, in a given energy band, as a Gaussian with the flux values as the mean and the flux uncertainty as the standard deviation. The amplitude is inversely proportional to the standard deviation, so that the area under each individual Gaussian is unity. A “flux profile” for a certain energy band is constructed by adding all individual flux measurements in that band. In order to determine the preferred shape of a flux profile, we used the LMFIT[13] method. Here, the goodness of fit is given by the parameter `redchi`, which is calculated from the ratio of the sum of the residuals to the degrees of freedom. A better fit is chosen

[13] https://lmfit.github.io/lmfit-py/fitting.html

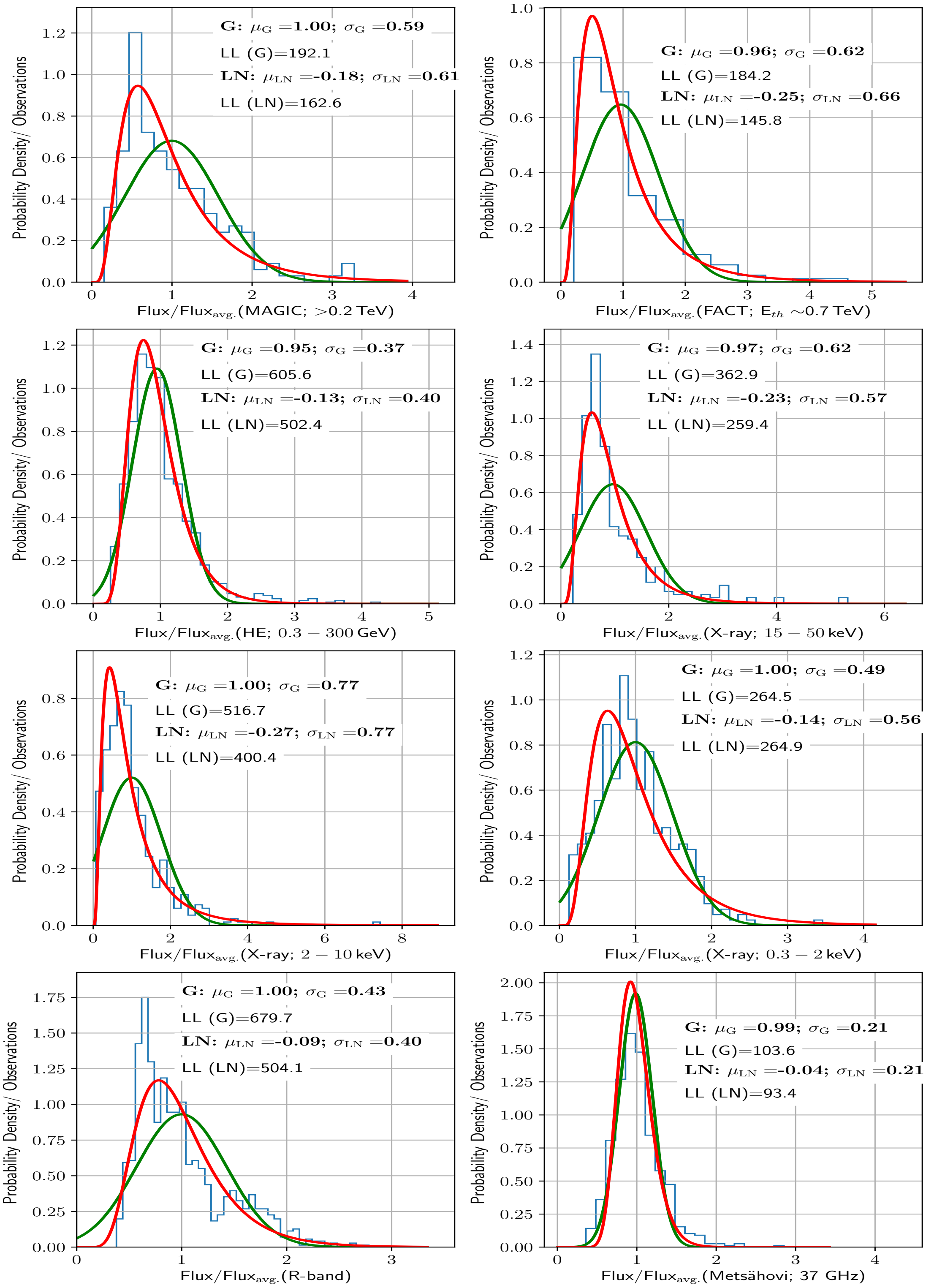

Figure 4.22: Characterization of the MWL flux distributions with a log-likelihood fit. The X-axis shows the scaled flux and the Y-axis the probability density. The green and red lines represent the Gaussian and LogNormal functions for which the log-likelihood is minimum. For completeness, the flux histograms used in Fig. 4.21 are also shown in blue. See text in Section 4.10 for details.

based on the ratio of the corresponding `redchi` parameters named R^{G}_{LN}. A LogNormal profile for the flux distribution is preferred if $R^{G}_{LN} > 1$. The chance probability (p), based on toy Monte Carlo, indicates the probability of wrongly reconstructing a LogNormal (Gaussian) distribution as a Gaussian (LogNormal).

Flux profile from a light curve:

We create the flux profile by adding contributions from individual flux measurements. We assume that for individual observations, flux errors are normally distributed around the mean. At VHE γ-rays (> 0.2 TeV) during 2015–2016, the lowest number of excess events was found to be around 40, supporting this assumption. Therefore, for each individual measurement we create a Gaussian profile $G(x : \mu, \sigma)$, where μ and σ are the flux and flux error, respectively. The amplitude of the profile is normalised to $1/(\sigma\sqrt{2\pi})$, so that the area under each individual flux profile is unity. Therefore, a high uncertainty measurement will result in a smaller amplitude, but will contribute to a wider range of flux values. Finally, the overall flux profile for the whole observation period is obtained by adding contributions from individual flux profiles. A few examples of such individual flux profiles are presented in Fig. 4.23. In order to create the flux profile in the VHE band for the 2007–2016 period, we have selected only flux points for which the detection significance (flux-error/flux) is less than 0.5. The highest flux in this data set, $(86.1\pm3.2)\times10^{-11}$ ph cm^{-2} s^{-1}, was observed on MJD 54555.9, while the lowest flux state of $(3.2\pm0.6)\times10^{-11}$ ph cm^{-2} s^{-1} was observed on MJD 57422. The corresponding flux profiles are presented in Fig. 4.23. Also, the flux profile for MJD 54562 is also shown which has a rather large flux uncertainty $(78.4\pm8.1)\times10^{-11}$ ph cm^{-2} s^{-1}. In addition, we construct the flux profiles using the individual fluxes and flux errors scaled with the average flux of the entire observation period reported in Fig. 4.6 (e.g. at VHE the

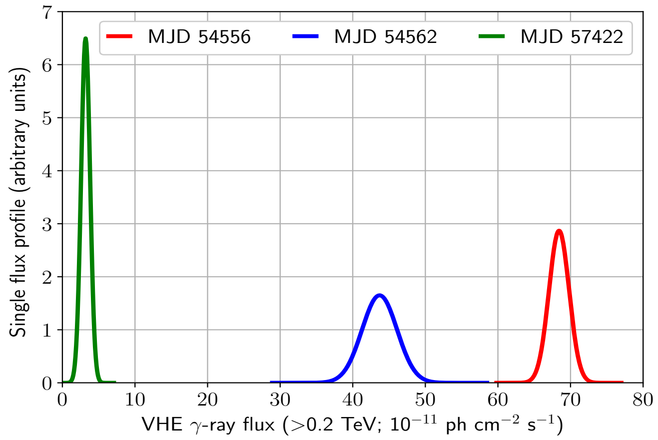

Figure 4.23: Examples of contributions to the VHE γ-ray flux profiles from three selected flux measurements with the MAGIC telescopes.

fluxes and errors are scaled with $2.09{\times}10^{-10}$ ph cm^{-2} s^{-1} which is the long-term average flux). From the overall flux profile, we determine the most probable state to be around 60 per cent of the average flux.

Validation of the flux profile method using VHE γ-ray data:

In this section, we present the validation of the flux profile method by assuming the flux distribution of the source as i) Gaussian and ii) LogNormal. We explain the procedure for this exercise for the Gaussian case and for the VHE γ-ray data set, but the same procedure also applies to LogNormal case, as well as for all the energy bands. The steps are as follows:

Step 1: We create a histogram of the fluxes in the VHE band using the long-term (2007–2016) data set, as shown in Fig. 4.21 (top left panel), and fit it with a Gaussian using Chi-square minimization.

Step 2: We assume that the fluxes from our source are distributed according to the fitted distribution from Step 1. We simulate 226 flux values as present in the real VHE LC.

Step 3: We then use real measurements to create a 2-D histogram of the flux vs. SNR, with 10 bins in flux and 5 bins in SNR (top panel of Fig. 4.24). The SNR bins are not the same for each flux bin, rather, in each flux bin, we take the range between minimum and maximum values of the SNR and divide it in 5 bins. Finally, we take the number of points in each SNR bin and divide it with the total number of points in the whole flux bin to estimate the distribution of SNR in each flux bin.

Step 4: Using fractions of SNR in each flux bin (obtained in Step 3), we generate flux errors for each of the 226 fluxes produced in Step 2. Some high flux bins in the real data histogram are empty (see top panel of Fig. 4.24). In such cases, we take the SNR to be the average SNR of the first lower flux bin.

Step 5: The 226 generated flux and flux-error pairs are now used to create a simulated flux profile.

Step 6: Steps 2–5 are repeated 1000 times in order to create 1000 generated flux profiles.

Step 7: Every generated flux profile is fitted with both the Gaussian and LogNormal functions. The fit parameters are μ_G^i and σ_G^i (μ_{LN}^i and σ_{LN}^i) for fitting with Gaussian (LogNormal), where i is the flux profile index. In addition, a parameter `redchi` is calculated (see Section 4.9 for details) for each flux profile and both the functions, as well as a ratio of `redchi` parameters $\mathrm{R}_{\mathrm{LN}}^{G}$ (`redchi`(G)/ `redchi`(LN)).

Step 8: Using the fit parameters for individual flux profiles, we calculate the average values of the fit parameters (μ_G and σ_G) and their standard deviations ($\Delta\mu_G$ and $\Delta\sigma_G$). A Gaussian function with μ_G and σ_G as mean and standard deviation is plotted in Fig. 4.24 as the reconstructed Gaussian distribution (green lines in middle left and bottom left panels). The errors on mean and standard deviation of the Gaussian are quoted as $\Delta\mu_G$ and $\Delta\sigma_G$ in the same panels. The same procedure is followed for LogNormal distribution (shown as blue lines in Fig. 4.24).

Step 9: We make a distribution of the R^{G}_{LN} which quantifies the goodness of fit.

First, we perform the described analysis by fitting the real data fluxes with a Gaussian function (Step 1). The resulting fit parameters are (μ_G= 0.67, σ_G= 0.65), and the corresponding function is shown in the top left plot of Fig. 4.21 with the red line. These parameters are used to generate 213 flux values (Step 2), and later to generate 1000 flux profiles (Step 6). Fitting each flux profile with Gaussian and LogNormal (Step 7) and averaging over all flux profiles (Step 8) results in the average fit parameters (μ_G= 0.68 $\pm$ 0.09, σ_G= 0.65 $\pm$ 0.08) and (μ_{LN}= -0.08 ± 0.06, σ_{LN}= 0.81 $\pm$ 0.14), for Gaussian and LogNormal distributions, respectively. The results are shown in the middle left plot of Fig. 4.24. The red line indicates the fit of the real data set with the Gaussian distribution, while the green and blue lines indicate the Gaussian and LogNormal functions, respectively. The average fit parameters for the Gaussian are consistent with the fit parameters of the initial real data distribution (the red and green lines overlapping). In addition, the ratio of the parameters `redchi` for Gaussian to the LogNormal for this case is R^{G}_{LN} = $0.40^{+0.14}_{-0.07}$, indicating that the Gaussian distribution is the preferred one, and thus proving that we correctly recovered the initial distribution. The chance probability (p), based on toy Monte Carlo, indicates the probability of wrongly reconstructing a LogNormal (Gaussian) distribution as a Gaussian (LogNormal). We calculate this by the distribution of the parameter R^{G}_{LN}. For an initial true LogNormal (Gaussian) distribution, we calculate the survival function (sf [14]) of R^{G}_{LN} below (above) 1 assuming the distribution to be a *skew-normal*[11]. This survival fraction indicates the chance probability of obtaining a Gaussian (LogNormal) flux distribution from a true LogNormal (Gaussian) distribution. The chance probability for the flux distribution in VHE γ-rays is $1.1{\times}10^{-4}$. The distri-

[14] https://docs.scipy.org/doc/scipy/reference/generated/scipy.stats.skewnorm.html

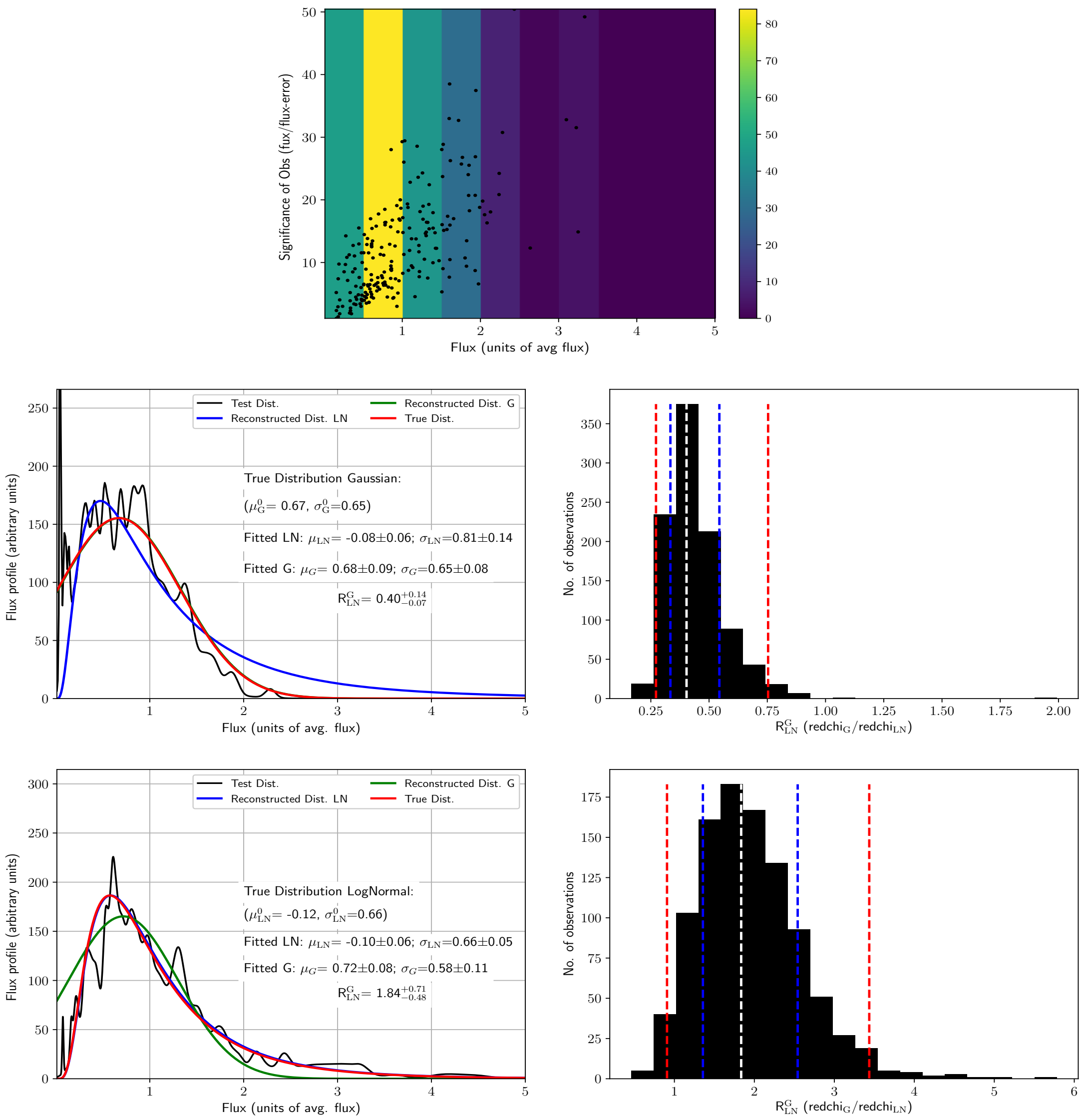

Figure 4.24: Validation of flux profile-method using long-term VHE observed flux. The parameters from the histogram of real data (fluxes) along with fits with the Gaussian (red line) and LogNormal (green line) are taken from Fig. 4.21. These functions are shown in red in the middle left (Gaussian) and bottom left (LogNormal) plots. The top plot shows the distribution of the flux/flux-error ratio (SNR) vs. flux. The colour scale indicates the number of flux measurements in each flux bin. In the middle left and bottom left plots, the red lines represent fits to the true flux distribution with a Gaussian (middle) and LogNormal (bottom), while the green and blue lines show fits to simulated flux profiles with Gaussian and LogNormal, respectively. In each of these two plots, one example of the 1000 simulated Gaussian (LogNormal) flux profiles is presented with black line. The middle right and bottom right plots the distributions of the parameter R^G_{LN} for Gaussian and LogNormal distributions, respectively. The white, blue, and red vertical dashed lines represent the weighted average of the histograms bins , the 1 σ and 2 σ confidence intervals.

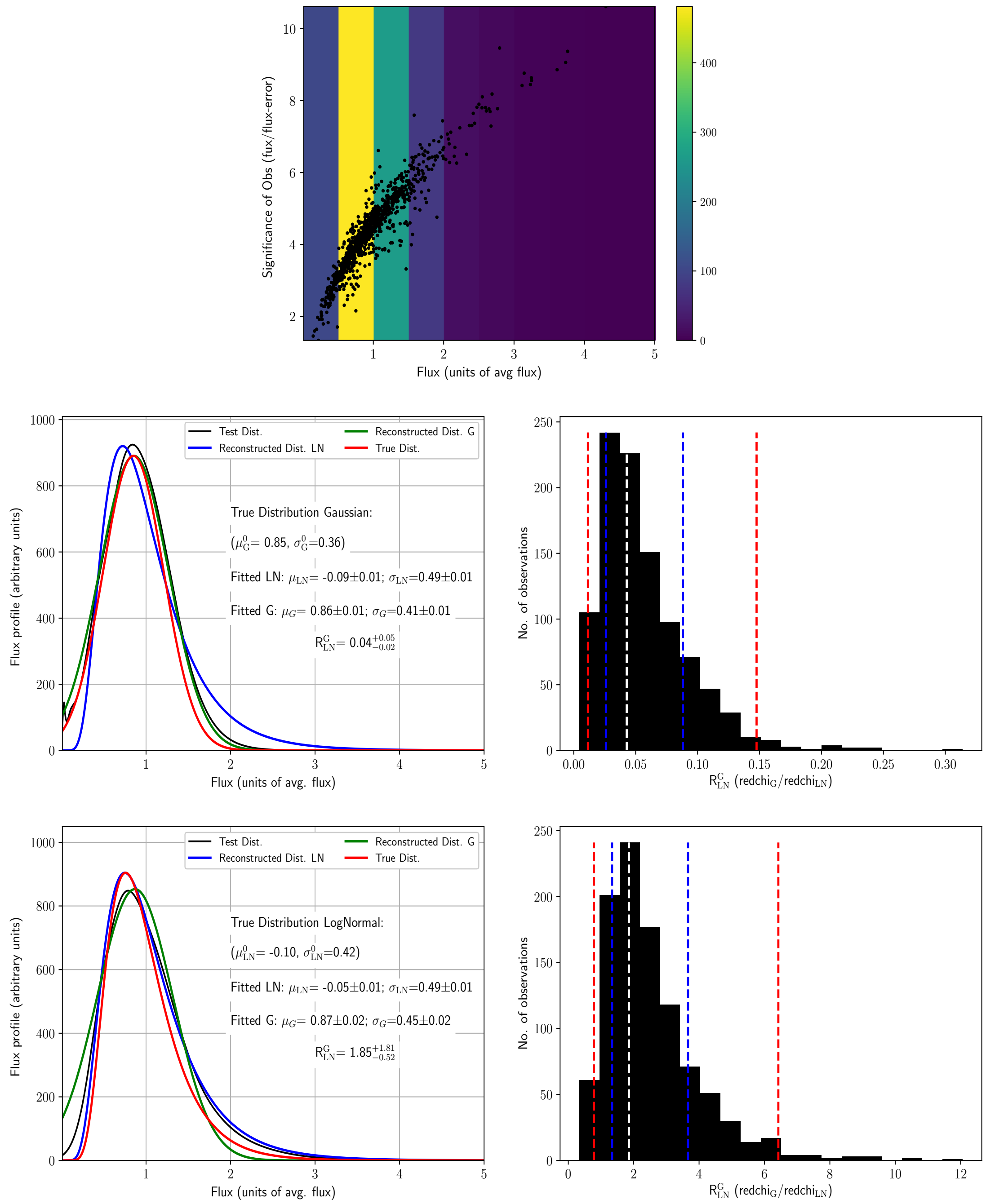

Figure 4.25: Validation of flux profile-method using long-term HE γ-ray (0.3-300 GeV) data

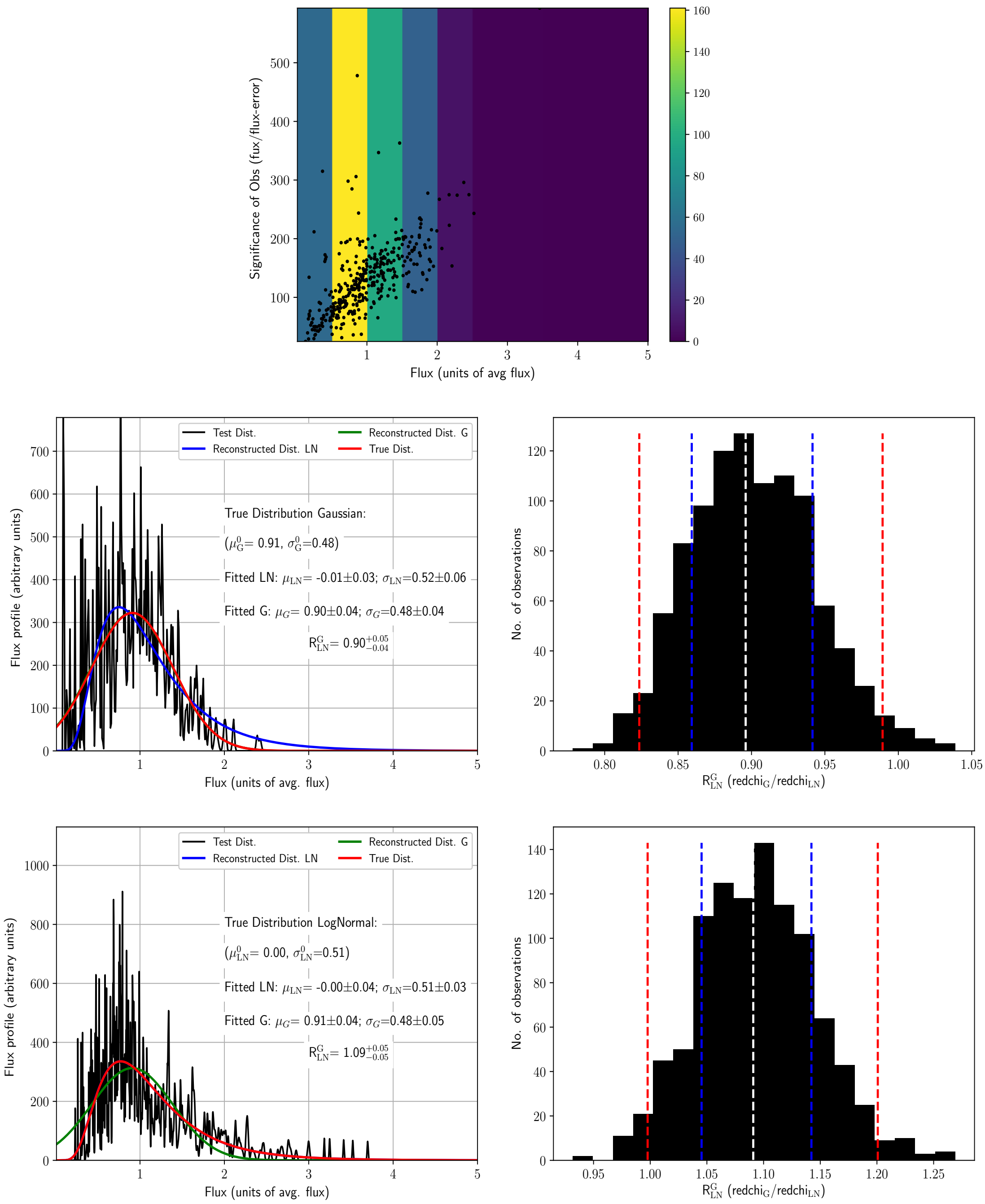

Figure 4.26: Validation of flux profile-method using long-term X-ray (0.3 – 2 keV) data

bution of the R^{G}_{LN} for individual simulated flux profiles is shown in the middle right plot. Next, we repeat the analysis, this time fitting the real data fluxes with the LogNormal function (Step 1), resulting in parameters ($\mu_{\rm LN}$= -0.12, $\sigma_{\rm LN}$= 0.66). The corresponding function is shown in the top left plot of Fig. 4.21 with the green line. The final results of the analysis are shown in the bottom plots of Fig. 4.24. In the left plot, the red line indicates the fit of the real data set with the LogNormal distribution, while the green and blue lines again indicate the Gaussian and LogNormal functions, respectively. This time, the simulated flux profiles were generated using parameters of the initial LogNormal distribution. The average fit parameters in this case are (μ_G= 0.72 ± 0.08, σ_G= 0.58 ± 0.11) and ($\mu_{\rm LN}$= −0.10 ± 0.06, $\sigma_{\rm LN}$= 0.66 ± 0.05), while $R^{G}_{LN} = 1.84^{+0.71}_{-0.48}$ (chance probability of having a Gaussian distribution is 4.4×10^{-2}). We can see that the average fit parameters for the LogNormal are consistent with the fit parameters of the initial real data distribution (the red and blue lines overlapping), and that the LogNormal distribution is the preferred one. Therefore, we again correctly recovered the initial distribution. The distribution of the R^{G}_{LN} for individual simulated flux profiles is shown in the bottom right plot.

We inspected our method on flux profiles in HE and X-ray bands. HE was chosen as an example of a band with larger relative flux uncertainties and lower variability, while the X-ray band is an example of the opposite (smaller relative flux uncertainties and higher variability). The procedure used in HE (X-ray) is exactly the same as that of the VHE band, with the exception of using 955 (374) flux points in Step 2 and 15 (10) flux bins in the 2-D histogram in Step 3. The results are shown in Fig. 4.25 and 4.26 for the HE and X-ray bands, respectively. In the HE band, the parameters of the initial flux distributions are not recovered. This is mainly because of the relatively large flux uncertainties. However, the chance probability of having LogNormal (Gaussian) from a true Gaussian (LogNormal) is 0.0 (8.1×10^{-2}) which indicates that we do correctly reconstruct and distinguish between Gaussian and LogNormal shapes of the initial distribution. In the X-ray band, the chance probability of having LogNormal (Gaussian) from a true Gaussian (LogNormal) is 1.7×10^{-2} (3.3×10^{-2}). Therefore, in the VHE and X-ray bands, we were able to recover the initial flux distributions (including the parameters), thus validating our method for measurements with higher sensitivity.

We recognize the following types of biases that can affect our results:

a) A cut on the relative error: In this study, we only use flux measurements with a SNR > 2.0. This will bias towards slightly higher values of flux for some of the distributions (those with the largest errors), e.g., FACT, *Fermi* and BAT. It affects only the rising part of the flux distribution. For FACT, there will be some distortion in the distribution because we remove 25% of the data. In any case, it is the high fluxes what dominates the distinction between G and LN, and those remained unaffected. For the flux distribution of data from the *Fermi*-LAT, the impact is negligible (only 3% of data removed).

b) The bias for including the observations during alert (ToO) for the high flux states: The MAGIC and *Swift*-XRT observations triggered by the target of opportunity (ToO) programs during the high flux of the source may bias the flux distribution. Ideally, the unbiased observations should only be considered. The data set under consideration includes the following campaigns, 2008 (Aleksić et al. 2012b) and 2010 (Aleksić et al. 2015c; Abeysekara et al. 2020) where the source showed high flux states. While the 2008 flaring episode had many ToOs involved, the 2010 March flaring activity observed consisted on observations that had been coordinated with *Swift* and *RXTE* several weeks in advanced. We have performed a study by removing all the high flux states observed during 2008 (Aleksić et al. 2012b) to check for LogNormality. We have found that even with this extreme condition, a LogNormal is preferred over a Gaussian flux profile. This

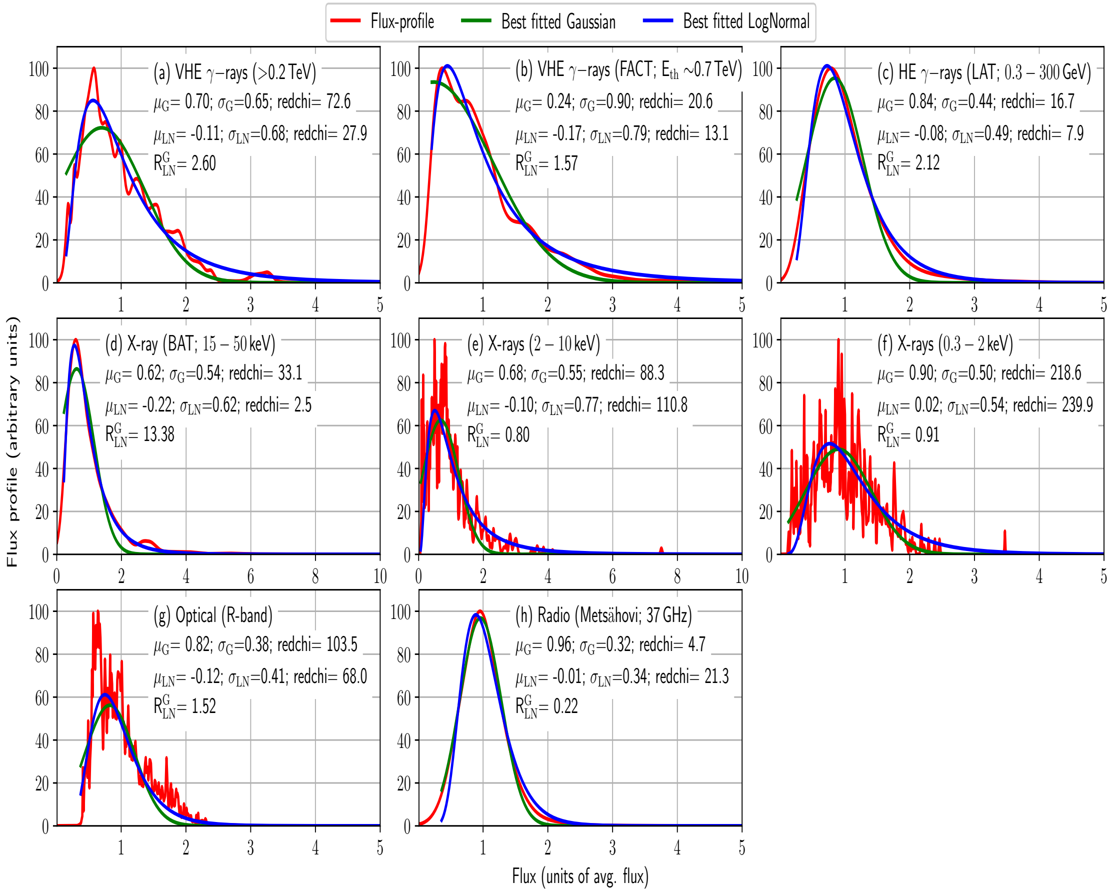

Figure 4.27: Flux distributions of Mrk 421 in the 2007–2016 period in different energy bands, except for FACT where only data from 2015–2016 period were used (see Section 4.4), and using the flux profile method (see Section 4.10.1).

proves that the LogNormal distribution of the flux at VHE is a feature of the source and does not depend on the ToOs. We also note that this bias is negligible for MAGIC and *Swift*-XRT and has no effect on the observations with the FACT, *Fermi*-LAT and *Swift*-BAT.

The flux profiles from radio to VHE γ-rays, along with the fits with the Gaussian and LogNormal functions, are shown in Figure 4.27.

The fluxes were scaled with the average flux in the respective energy bands. The fit parameters are presented in Table 4.4.

Energy-bands	G		LN		MPS (Avg. flux)	redchi		R^{G}_{LN} (p)
	μ_g	σ_g	μ_{LN}	σ_{LN}		G	LN	
VHE γ-rays (MAGIC; > 0.2 TeV)	0.70	0.65	-0.11	0.68	0.56 (2.09×10^{-10} ph cm^{-2}s^{-1})	72.6	28.0	2.6 (4.4×10^{-2})
VHE γ-rays (FACT; $E_{th} \sim 0.7$ TeV)	0.24	0.90	-0.17	0.80	0.45 (3.33×10^{-11} ph cm^{-2}s^{-1})	20.6	13.1	1.57 (2.1×10^{-2})
HE γ-rays (LAT; 0.3 – 300 GeV)	0.84	0.44	-0.08	0.50	0.72 (9.45×10^{-8} ph cm^{-2}s^{-1})	16.7	8.0	2.1 (8.1×10^{-2})
X-ray (BAT; 15 – 50 keV)	0.62	0.54	-0.22	0.62	0.54 (0.27×10^{-2}counts cm^{-2}s^{-1})	33.1	2.5	13.4 (1.6×10^{-1})
X-ray (2 – 10 keV)	0.68	0.55	-0.10	0.77	0.68 (3.67×10^{-10}erg cm^{-2} s^{-1})	88.3	111.0	0.80 (2.4×10^{-2})
X-ray (0.3 – 2 keV)	0.90	0.50	0.02	0.54	0.90 (6.82×10^{-10} erg cm^{-2} s^{-1})	218.6	240.0	0.91 (1.7×10^{-2})
Optical (R-band)	0.82	0.38	-0.12	0.41	0.75 (24.37 mJy)	103.5	68.0	1.52 (1.0×10^{-3})
Radio (Metsähovi; 37 GHz)	0.96	0.32	-0.01	0.34	0.90 (0.50 Jy)	4.7	21.3	0.22 ($<1.0\times10^{-4}$)

Table 4.4: The model parameters for the flux profiles in different energy bands fitted with Gaussian (G) and LogNormal (LN) distributions. The most probable states (MPS) are retrieved from the function preferred by the flux profile, and presented as fractions of the mean flux (given in the parentheses). The parameter R^{G}_{LN} is the ratio of `redchi` for LN to the `redchi` for G (see main text) and is used to estimate the goodness of fit. $R^{G}_{LN} > 1$ means the profile is likely to be fitted better with a LN. The chance probability (p), given in the parentheses in the last column indicates the probability of wrongly reconstructing a LogNormal (Gaussian) distribution as a Gaussian (LogNormal). See Section 4.9 and 4.10.1 for details. The results for the 15 GHz band have not been included here as the distribution is bimodal. See Section 4.10.1 for details.

The flux profiles for X-ray observations in the 0.3 – 2 keV and 2 – 10 keV energy bands show spikes. This is due to the very high SNR (average SNR above 60), which makes the available number of flux measurements insufficient to produce a smooth convolved distribution. Despite this caveat, our simulations show that the number of measurements is sufficient to characterize the shape of the distribution, as well as to marginally distinguish between a Gaussian and LogNormal function. Our findings suggest that the LogNormal is preferred over Gaussian for emissions in the VHE and HE γ-rays, hard X-rays in the 15 – 50 keV and optical band. The hard X-rays in the 15 – 50 keV shows a preference for a LogNormal profile, but with a chance probability (p) of only 0.16 (due to the large flux uncertainties), these results are not conclusive. The 37 GHz radio band shows a clear preference for the Gaussian, while the flux profile for the X-rays in the 0.3 – 2 keV and 2 – 10 keV show a marginal preference for the Gaussian. The peak-position of the function (Gaussian/LogNormal) with which a flux profile is better fitted (depending on the value of the $\mathrm{R}_{\mathrm{LN}}^{G}$) is considered as the most probable state (MPS). The MPS for the energy bands above the synchrotron and IC peaks (such as X-rays, 2 – 10 keV and 15 – 50 keV, and VHE γ-rays) are found to be in the range of 0.4 – 0.7 times the average flux. On the other hand, the energy bands below the synchrotron and IC peaks (such as HE γ-rays, soft X-rays 0.3 – 2 keV, UV, optical, and radio emissions) lie in the range of 0.7 – 1.0 times the average flux.

Year-wise variation of flux profiles in 15 GHz radio band

The flux distribution of the 15 GHz radio band is shown in Fig. 4.28, where the flux histogram and the flux profile are presented. This suggests that the flux distribution for this band is a bimodal distribution, hence, the Gaussian and LogNormal functions are not suitable. The year-wise variation of the flux profiles for the 15 GHz radio band, observed by OVRO, has been reported in Fig. 4.29. We have divided the multiyear radio LC into four different periods:

a) 2006 September 22 to 2010 October 31 (MJD 54000–55500),

b) 2010 November 01 to 2012 March 14 (MJD 55501–56000),

c) 2012 March 15 to 2013 July 27 (MJD 56001–56500), and

d) 2013 July 28 to 2016 June 11 (MJD 56501–57550).

For each of the periods stated above, we shuffled the uncertainties on the flux and added to the flux in order to construct a simulated flux profile. We repeated this exercise for 1000 times for a single period in order to estimate the standard deviation on the flux profiles. The bands in Fig. 4.29 represent the standard deviation on the flux profile (68% confidence limit) estimated from the simulations mentioned above. This study indicates that the most probable states of the source in different years are not unique. The flux profile also changes according to the flux states in different years. For example, the flux profile for the period (c) shows an isolated peak at higher flux. This is due to the huge radio flaring event in 2012. The variation in flux profiles in Fig. 4.29 indicates a shift form the low-flux state in period (a) to a high flux state (c) via an intermediate state (b). During period (c) the low/ typical state can also be identified.

Table 4.5 lists the preferred flux-distributions (Gaussian or LogNormal) from the Chi-square fit, log-likelihood fit and the flux profile methods. The flux distribution for the OVRO (15 GHz) is not included in the table and in the figures because it has a bimodal shape due to the strong flare in 2012 (see Section 4.10.1). The entries marked with "*" denote cases where the preference is not clear, either because both options are roughly equally probable, or because the methods suffer from some caveats. In the case of the Chi-square fit, this happens for FACT (E_{th} ~0.7 TeV), where the resulting Chi-square values show equally probable fits. In the case of the log-likelihood fit, this occurs

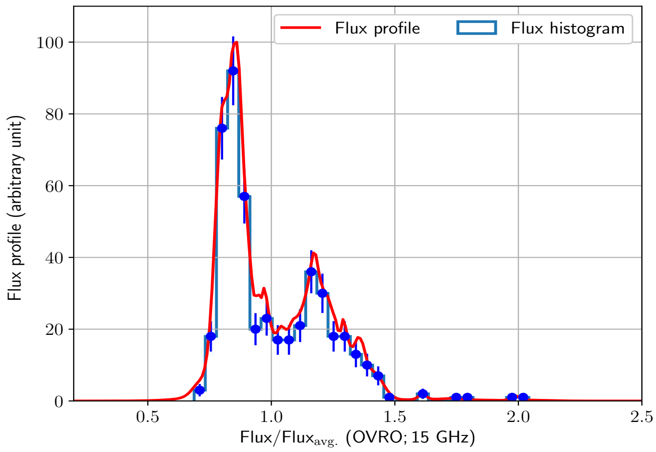

Figure 4.28: The flux profile and flux histogram of Mrk 421 in radio (15 GHz) band. See text for details.

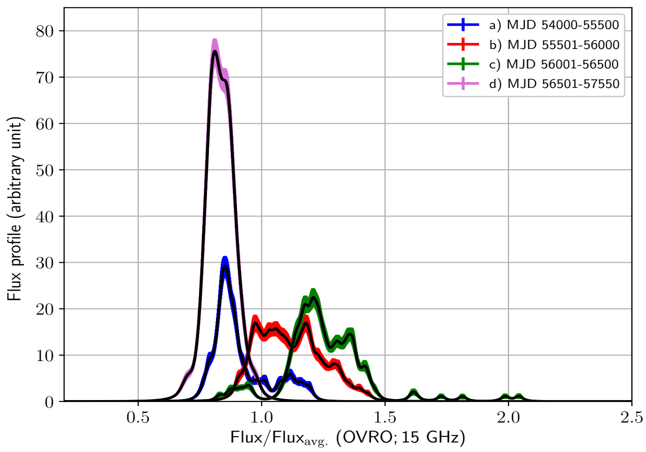

Figure 4.29: Year-wise variation of flux profiles of Mrk 421 in radio (15 GHz) band. The bands for different colors indicate 1 σ confidence intervals for different years. We have divided the multiyear radio LC into four different periods of observations. See Section 4.10.1 for details.

Energy-bands	Chi-square fit	Log-likelihood fit	Flux profile
VHE γ-rays (> 0.2 TeV)	LogNormal	LogNormal	LogNormal
VHE γ-rays (FACT; $E_{th} \sim 0.7$ TeV)	LogNormal*	LogNormal*	LogNormal
HE γ-rays (LAT; > 0.3 GeV)	LogNormal	LogNormal	LogNormal
X-ray (BAT; $15 - 50$ keV)	LogNormal	LogNormal*	LogNormal*
X-ray ($2 - 10$ keV)	LogNormal	LogNormal	Gaussian
X-ray ($0.3 - 2$ keV)	Gaussian	Gaussian*	Gaussian
Optical (R-band)	LogNormal	LogNormal	LogNormal
Radio (Metsähovi; 37 GHz)	LogNormal	LogNormal	Gaussian

Table 4.5: The preferred flux-distributions based on the three methods namely Chi-square fit, log-likelihood fit and the flux profile method. Entries in the table that are marked with "*" do not have a clear preference for Gaussian or LogNormal and are discussed in Section 4.10 . The flux distribution for OVRO (15 GHz) has a bimodal shape, hence, it is not included in this comparison table. See Section 4.9 and text in Section 4.10 for details.

for FACT (E_{th} ~0.7 TeV), *Swift*-BAT (15 – 50 keV) and X-ray in the 0.3 – 2 keV band. In the first two cases, the applicability of the PDF (Gaussian or LogNormal) suffers from the truncation of these two distributions at low flux values (given the limited sensitivity to measure low fluxes)[15], and in the latter case, the resulting log-likelihood values are equal (within one unit) for both the functions. In the case of the flux profile method, the preference is not clear for *Swift*-BAT (15 – 50 keV) because the chance probability (p; see Section 4.9 and Section 4.10.1 for details) for a Gaussian distribution when the true distribution is a LogNormal is only 0.16. The table shows preference for the LogNormal distribution shape in all of the energy bands, apart from the X-rays in the 0.3 – 2 keV, 2 – 10 keV and the 37 GHz radio band. The three methods prefer the Gaussian shape for the 0.3 – 2 keV (although the preference is not clear in the case of the log-likelihood method), while for the other two bands, the Chi-square and log-likelihood fits prefer a LogNormal shape, while the flux profile method prefers a Gaussian shape.

[15]The Chi-square fit and the flux profile method are less sensitive to this effect because the fits are performed above the minimum flux F_{min}, and hence do not need to apply the entire distribution shape to the available data.

4.11 Discussion and conclusions

This chapter presents a detailed study of the broadband emission of Mrk 421 during two observing campaigns, 2014 November to 2015 June, and 2015 December to 2016 June. For simplicity, we dubbed them as the 2015 and 2016 observing campaigns. The MWL data set used for this study was collected with 15 instruments, covering the emission of Mrk 421 from radio (with OVRO, Metsähovi, Medicina, and VLBA) to VHE γ-rays (with FACT and MAGIC), and including various instruments covering the optical and UV bands (KVA, ROVOR, West Mountain Observatory, iTelescopes network, and *Swift*-UVOT), X-ray bands (*Swift*-XRT and *Swift*-BAT) and GeV γ-rays (with *Fermi*-LAT). The sensitivity of the instruments used, and the large number of observations performed, enabled the detailed characterisation of the MWL variability and correlations during this period. A distinctive characteristic of this multi-year campaign is the large degree of simultaneity in the X-ray and VHE γ-ray observations, which are two energy ranges where the variability is typically the highest and can occur on the shortest timescales. We consider that the X-ray and VHE observations are simultaneous if taken within 0.3 days (i.e., the same night), although most of the observations were performed within 2 hours. The large degree of simultaneity in the observations ensure reliability in the results reported, in contrast to other published works that use multiwavelengh data that are contemporaneous (taken within one or a few days), but not simultaneous. This simultaneity is particularly important for the X-ray and VHE γ-ray observations which, as we report in 4.5 and Section 4.6 of this chapter, show large variability and a large degree of correlated behaviour on timescales shorter than a day.

4.11.1 Multi-band flux variability and correlations

During the 2015 and 2016 observing campaigns, Mrk 421 showed a very low activity in the X-ray and VHE γ-rays (see Section 4.3 and Fig. 4.2), which are the energy bands where the emitted power is the largest. The spectral shape, quantified here with the HR_{keV} and HR_{TeV}, also showed periods of extreme softness (very low HR_{keV} (/HR_{TeV}) values), like the one during the time interval of about MJD 57422 to MJD 57474, where the HR_{TeV} is $\leq$0.03, and the HR_{keV} is $\leq$0.25 (see Fig. 4.9 and Fig. 4.10). We found the typical harder-when-brighter trend in the X-ray and VHE γ-ray emission; although we also found a deviation in the *HR* vs flux trend for the largest X-ray and VHE γ-ray activity. The flattening in the *HR* vs flux trend for high (and low) X-ray fluxes had already been reported in Baloković et al. (2016a), but here we report, for the first time, a similar behaviour in the VHE γ-ray band.

The fractional variability showed the typical double-bump structure reported in previous studies of the broadband (radio to VHE) emission of Mrk 421 during low (non-flaring) activity (e.g. Aleksić et al. 2015b; Baloković et al. 2016a), and high (flaring) activity (e.g. Aleksić et al. 2015c; Abeysekara et al. 2020; Acciari et al. 2020). The highest variability is always observed in the highest X-ray and VHE γ-ray energies at a similar level (see Fig. 4.7).

We also searched for correlated behaviour among the emission from the various energy bands probed with these observations. We quantified these correlations (using Pearson and DCF) and evaluated the significance with Monte Carlo simulations. We detected a significant correlation between the emissions in the X-ray and VHE γ-ray bands. The positive correlation between these bands has been reported with a high confidence level whenever the source showed a flaring activity (e.g. Aleksić et al. 2015c; Acciari et al. 2020), but it is more elusive during typical or low flux (e.g. Aleksić et al.

2015b; Baloković et al. 2016a). Despite the strength of the correlation being similar for the various combinations of X-ray and VHE γ-ray energies probed, we report that the slope in the VHE vs X-ray flux plots changes with the specific energy band being used. In all cases, we found a slope lower than 1, with the largest slope obtained for the highest energies (VHE γ-ray band; >1 TeV) versus the lowest X-ray band (0.3-2 keV). These results (see Fig. 4.15 and Table 4.2) are somewhat similar to those reported in Acciari et al. (2020) during an extreme high activity in 2013 April. The results reported in this work further support that the X-ray and VHE emissions are closely related without any time delay, for all the energy bands probed, during high and during low activity. This indicates the presence of somewhat similar processes governing the emission of the source during a large range of activity, but showing also complexity in these processes, as is deduced from the diversity in the VHE vs X-ray flux slopes when moving across nearby energy bands.

The strongly correlated zero-lag behaviour between the VHE and X-ray emissions, persistent during the 2015–2016 observing campaigns, indicates that the X-ray and VHE γ-ray emissions are dominated by leptonic scenarios (presumably SSC), where the same population of high-energy electrons radiate simultaneously at X-ray and VHE. The higher variability for the highest energies and the harder-when-brighter behaviour may be interpreted as an indication of injection of high-energy particles dominating the flux variations over a large range of activity. But above a given flux, the spectral shape no longer changes substantially with the flux, which suggests that the flux variations may be dominated by a different process yielding a variability that does not have a strong dependence with energy. One possibility could be a small change in the viewing angle, that would increase the Doppler factor and, in first order approximation, produce a flux change that is similar in all energies[16]. In order to produce flux changes of about a factor of two, one would need to change δ by about 20%, which, for Γ=10 and a viewing angle of 5°, could be achieved by a change in the viewing angle of about 1°. Such change in δ would also produce an energy-dependent flux change through the displacement of the broadband SED, but it would be a relatively small effect (e.g., 2.0 keV would become 2.4 keV).

We did not find a correlated behaviour between the optical and the X-ray bands, and did not find a correlation between the γ-ray emission below 2 GeV and the one above 200 GeV, hence indicating that the rising and falling segments of the two SED bumps may actually be produced by different particle populations, and even located at different regions. However, as reported in Section 4.6.2, we did observe, for the first time, a significant ($> 3\,\sigma$) correlated behaviour, between the >2GeV emission measured with *Fermi*-LAT and the VHE fluxes measured with MAGIC (0.2 − 1 TeV) and with FACT (E_{th} ~0.7 TeV). The correlation, quantified in time steps of ±3 days, occurs only for τ=0, indicating that the emission in these two energy bands is simultaneous within the resolution of the study. This observation suggests that the multi-GeV emission is produced (at least partially) by the same particle population that dominates the VHE emission, but such relation does not exist for the sub-GeV emission. A correlation between GeV and TeV energies for Mrk 421 had also been claimed by Bartoli et al. (2016a), using *Fermi*-LAT and ARGO-YBJ. Apart from technical details in the quantification of the correlation, and the somewhat different energy bands considered in that study (median energy of 1.1 TeV for ARGO-YBJ and energies above 0.3 GeV for *Fermi* LAT), the main practical difference is the temporal scale involved in these two studies, with Bartoli et al. (2016a) reporting a positive correlation with τ=0 within ±30 days, while we can ensure

[16]The flux change would depend approximately on $\delta^{3.5}$ while the dependence in energy would relate to the energy shift that is proportional to δ.

simultaneous emission within ±3 days.

Owing to the substantially lower fractional variability and the longer variability timescales observed for the emission from the rising segments of the two SED bumps (namely radio, optical and GeV emission), the 2015–2016 data set was complemented with data from years 2007–2014 (see Section 4.4) to enlarge the data set and better evaluate the correlations among these bands (see Section 4.6). This correlation study, performed in the same fashion as done for the simultaneous X-ray/VHE fluxes, but with time-bins of 15 days instead of 1 day, yielded a number of interesting results, as reported in Section 4.6.3, 4.6.4, and 4.6.5.

We found a positive correlation between the >0.3 GeV emission (from *Fermi*-LAT) and optical (R-band) emission for a range of about 60 days centered at τ=0 (see Section 4.6.3), which confirms and further strengthens the claim made by Carnerero et al. (2017). Overall, this observation indicates that these two bands, belonging to the rising segments of the two SED bumps (and located somewhat close to the peak of the bumps) may indeed be produced (at least partially) by the same particle population and in the same region (or regions). The wide time interval with positive correlation may be due to a large size R of the region dominating the optical and γ-ray emission. For instance, a variability timescale of about 30 days can be use to set an upper limit to the size R of about 8×10^{17} cm for a Doppler factor of 10. And, if the optical/GeV emitting region could be related to the radio emitting region, whose Doppler factor has often been estimated to be lower than 2 (see e.g. Piner et al. 2010), the upper limit to the size R would be 2×10^{17} cm.

Additionally, we found a positive correlation between the >0.3 GeV emission (from *Fermi*-LAT) and the radio emission at 15 GHz and 37 GHz (from OVRO and Metsähovi) for a range of about 60 days centered at $\tau \sim 45$ days (see Section 4.6.4), meaning that the radio emission occurs about 45 days after the GeV emission. The same correlation with the same time lag occurs also for the optical and the radio emissions (see Section 4.6.5), which is expected given the correlation between γ-rays and optical emission mentioned above. Combining the time lags for the correlations among the GeV, R-band and the 15 GHz fluxes, one obtains an overall time lag between optical/GeV and radio of 43^{+9}_{-6} days. If instead one uses the 37 GHz from Metsähovi, where the DCF plots have less pronounced peak, the overall time lag between optical/GeV and radio is 37^{+15}_{-12} days (see Section 4.8 for details).

A positive correlation between the *Fermi*-LAT and OVRO fluxes for a time lag of about 40 days had been first claimed by Max-Moerbeck et al. (2014). The claim was only at $2.6\,\sigma$ (p-value of 0.0104), and strongly affected by the large γ-ray and radio flares from July and September 2012, respectively. In this work, we report a correlation with a significance at the level of $11\,\sigma$ when considering the entire data set, and, if we exclude the large flares, the significance is $9\,\sigma$. Therefore, we can confirm and further strengthen the correlation reported in Max-Moerbeck et al. (2014), stating with reliability that this is an intrinsic characteristic in the multi-year emission of Mrk 421, and not a particularity of a rare flaring activity.

Within the scenario of the emission being produced by plasma moving along the jet of Mrk 421, the delay of the radio emission with respect to the γ-ray emission can be considered as an indication that the plasma (or jet disturbance) first crosses the surface of unit γ-ray opacity making the γ-ray emission visible, and then, about 0.2 pc down the jet (assuming a common δ of 4 and Γ of 2, see Max-Moerbeck et al. 2014, for details of the calculation), the radio emission is produced when the plasma (or disturbance) crosses the surface of unit radio opacity.

There are three distinct natures of correlation emerging from this study, a) correlation between X-ray and VHE γ-ray LCs at τ=0, b) correlation between optical and HE γ-rays at τ=0, and c) correlation between radio and HE (and optical) LCs at $\tau \sim$ 45 days. The correlation in cases (b) and (c) have broader peaks compared to the case (a). The broader peaks for the radio, optical and GeV emission may be due to the lower variability and longer variability timescales related to the energy bands in consideration (because the emission involves lower energy particles), or it may related to the existence of two (or more) different radiation zones responsible for the production of the corresponding radiation components (see Aleksić et al. 2015c, for description of the broadband SED variability of Mrk 421 with these two theoretical scenarios).

4.11.2 Multi-band flux distributions

Using the historical MWL data (from 2007 to 2016), we also quantified the flux variations with a methodology that allows us to estimate the flux distributions even for flux measurements with relatively large errors (see Section 4.10.1 for details). Using this methodology, we determined the most probable flux values and the dispersion in the flux values for all the bands probed (see Fig. 4.27 and Table 4.4). Among other things, we found that the most probable flux is close to the average flux for the energy bands below the synchrotron and inverse-Compton SED peaks (i.e. radio, optical and soft X-rays), while it substantially differs from it for the energy bands above the two SED peaks (i.e., hard X-rays and VHE γ-rays). The flux distributions in radio and soft X-rays are better described with a Gaussian function, while the flux distributions in the optical, hard X-rays, HE and VHE γ-rays are preferably described with a LogNormal function. A LogNormal distribution of flux implies that the emission is being powered by a multiplicative process rather than an additive one. Suggestions have been put forward by several authors that LogNormality is a result of fluctuations in the accretion disk (Uttley et al. 2005; McHardy 2010). If the same behaviour is found in blazars, this may lead to the conclusion that the source of variations in blazars lie outside the jet, i.e., in the accretion disks which then modulate the jet emission.

4.11.3 Radio flare at 37 GHz

On 2015 September 11, the Metsähovi telescope observed an increase by a factor of two in the 37 GHz radio flux, from about 0.5 Jy to about 1.1 Jy (see Fig. 4.4 and Section 4.3.2). It is the first time that such a large flux change, with a temporal timescale shorter than 3 weeks, is observed in the 37 GHz radio emission of Mrk 421. The VLBA observations show an increase in the polarization fraction on September 22, while it returns to normal values on December 5 (see Fig. 4.4). The flare could be explained via a kink instability that momentarily disrupts the ordering of the field and accelerates particles to cause an increase in flux and a decrease in polarization. The disturbance propagates down the jet, causing first a high-energy flare, followed by a millimeter-wave flare, as observed. After the flare, the polarization returns to its normal radial pattern. Other simultaneous observations are those from *Fermi*-LAT, and *Swift*-BAT where there is no substantial enhancement in the γ-ray or X-ray flux activity around the time of the radio flare.

4.11.4 Hard X-ray component

During the 7-day time interval MJD 57422–57429 (2016 February 4–11) where Mrk 421 showed a very low X-ray flux and low HR_{keV} (i.e. soft X-ray spectra), we noted a $15 - 50$ keV flux (from *Swift*-BAT) that is well above the emission that one would expect if the optical to X-ray emission (from 1 eV to 10 keV), characterized with a log-parabola function, is extrapolated to the hard X-ray range above 15 keV (see Fig. 4.11). This is the first time that BAT measures a flux significantly above the one expected from the simple extrapolation of the XRT spectral data. But an excess in the hard X-ray with respect to the expected flux from the synchrotron component has already been reported by Kataoka & Stawarz (2016) for Mrk 421, using *NuSTAR* data during a period of very low X-ray and VHE activity in 2013, and considered to be the onset of the SSC component. Such hard X-ray excesses, considered to be the beginning of the SSC component, have also been observed in another blazar, PKS 2155–304, also using *NuSTAR* observations during a period of very low X-ray flux (Madejski et al. 2016; H. E. S. S. et al. 2019). On the other hand, the hard X-ray *NuSTAR* excess in the Mrk 421 data from 2013 was also interpreted within the scenario of the spine/layer jet structure, and considered to be an indication of inverse-Compton emission produced by high-energy electrons from the spine region up-scattering the synchrotron photons from the layer, as was proposed by Chen (2017). Another possible origin of the hard X-ray excess could be a Bethe-Heitler cascade, which is expected to occur in many of the hadronic scenarios, such as the ones that were used to explain the broadband emission of TXS 0506+056 contemporaneous to a high-energy astrophysical neutrino detected by IceCube in 2017 September (e.g. Ansoldi et al. 2018). Moreover, the BAT excess reported here may also be related to the presence of an additional (and narrow) spectral component that appears occasionally, as has been recently reported for Mrk 501 at multi-TeV energies (MAGIC Collaboration et al. 2020a), and interpreted as a indication for pile-up in the electron energy distribution, or an indication for electrons accelerated in the vacuum gaps close to the super-massive black hole that is powering the source.

5

Time dependent spectral modeling of Markarian 421 during a violent outburst in 2010

5.1 Introduction

Blazars are considered as among the most violently variable objects in the entire electromagnetic spectrum in the universe, explained by emission beamed along the line of sight by relativistic jets of high-energy plasma (Blandford & Königl 1979). Variability, on time scales of months to hours (and in some cases down to minutes), is a common phenomenon for these objects, and is pervasive throughout the electromagnetic spectrum. As explained earlier in Chapter 1, the non thermal spectral energy distribution (SED) of a blazar shows a double hump structure. Based on the position of the peak of the first hump, these objects are characterized into four different classes: LBL (low-frequency peaked BL Lacertae (BL Lac) object) peaking in the infrared to optical regime, IBL (intermediate-frequency peaked BL Lac objects) peaking at optical-near-UV frequencies, HBL (high-frequency peaked BL Lac objects) peaking at X-ray energies, and FSRQs (flat-spectrum radio quasars) peaking in the infrared regime and exhibiting strong emission lines in their optical spectrum (Padovani & Giommi 1995; Sambruna et al. 1996; Marscher 1980; Konigl 1981; Ghisellini et al. 1985; Boettcher 2012).

The origin of the double hump structure of the SED of blazars can be explained by leptonic and/or hadronic models. According to these models, the first hump is a result of synchrotron radiation of primary electrons accelerated to relativistic energies in the emission region. On the other hand, the production of the second hump changes, depending on the model that is being used to explain its origin. In the case of a hadronic model, if relativistic protons are present in the jet of a blazar and have energies above the interaction threshold, then the second hump is a result of interactions between accelerated protons & electron-positron pair cascades and synchrotron photons responsible for the low-energy hump (Mücke & Protheroe 2001; Mücke et al. 2003a; Boettcher 2010). However, under a leptonic scenario, the high-energy hump is a result of inverse Compton (IC) scattering of an internal and/or external photon field by primary electrons. If the internal photon field, which is the synchrotron radiation in the emission region, is involved in IC scattering, then the resultant emission is known as synchrotron self-Compton (SSC) (e.g., Bloom & Marscher 1996). On the other hand, if an external photon field is involved, then the corresponding emission is called external Compton (EC). The sources of this external photon field could be the photons from the accretion disk (Dermer et al. 1992; Dermer & Schlickeiser 1993a), or the broad line region (BLR) and/or the dusty torus (Ghisellini et al. 1998; Joshi et al. 2014; Sikora et al. 1994a).

Markarian 421 (Mrk 421; redshift=0.031) is among the best studied BL Lac objects at all wavelengths. Rapid flux variations (~ minutes to hours) have been detected from the source by a number of instruments (see Gaidos et al. 1996). The broad-band SED of the source has been measured in great detail by most of the current generation instruments at a number of epochs. At TeV energies, the source has displayed many high-flux states (Acciari et al. 2014). It was detected in a flaring state by the Whipple telescope in 1995 (Macomb et al. 1995a). These authors reported the first ever quasi-simultaneous multi-waveband observations of this source. The event was characterized by a quiescent or a steady flux in the optical and 100 MeV-GeV regimes while the source varied strongly at X-ray and TeV energies. In 1997, another flaring event was observed, where the highest flux state was detected by Whipple telescope to be around ten times that of the Crab Nebula above 500 GeV (McEnery et al. 1997; Zweerink et al. 1997). An outburst with a flux level of 13 Crab units (above 380 GeV) and high variability of the source was reported in 2001 by Whipple (Krennrich et al. 2002), where the flux state remained high from January to May 2001. Another big flaring event was reported by Whipple (> 400 GeV) (Swordy 2008) and VERITAS (> 300 GeV) (Acciari et al. 2011a) in a 2003-2004 campaign, where the flux reached 10 Crab units. Similarly, in X-rays the source has displayed many outbursts. An orphan flaring event (X-ray flares with no VHE counterpart) was reported in 2003-2004 campaign by Fraija et al. 2015. The source showed another violent outburst in 2006 in X-rays, where the measured flux reached ~ 85 milli-Crab (mCrab) in the energy range of 2-10 keV (Tramacere 2010; Ushio et al. 2009). The peak of the synchrotron hump appeared beyond 10 keV for this flaring event. Super-AGILE, operational in the hard X-rays, reported a flare on 2008 June 10 (Pittori et al. 2008). However, the strongest hard X-ray flare reported by MAXI (Monitor of ALL-sky X-ray Image) was in February 2010, where the flux went up to ~ 164 ± 17 mCrab (Isobe et al. 2010; Isobe et al. 2015). This is the largest X-ray flare ever reported for this source (Niinuma et al. 2012). In addition, it was followed by very bright VHE γ-ray emission ($\sim$ 10 Crab) (Ong, R. A. 2010, ATel, 2443, 1).

In this work, we focus on analyzing the spectral states of Mrk 421 that were observed in February 2010, during which the blazar was found to be in one of the brightest states in both X-ray and TeV energies (Galante & for the VERITAS Collaboration 2011; Shukla et al. 2012; Singh et al. 2015; Bartoli et al. 2016b; Tluczykont 2011). Such flaring events offer a unique possibility of understanding the role of particle acceleration along with the temporal evolution of the source from a low- to a high-flux state. A similar but low magnitude ($\sim$ 2 Crab flux above 200 GeV) flare was detected with unprecedented multi-wavelength (MWL) data coverage during March 2010 (Aleksić et al. 2015d). Through this study, we aim to constrain the role of intrinsic parameters and understand the physical processes in Mrk 421 responsible for producing different flux states during the giant outburst of February 2010. We reproduce a total of three spectral states observed over a period of five consecutive days, from 13-17 February 2010, using a multi-zone time-dependent leptonic jet model with radiation feedback (Joshi & Böttcher 2011). These days include a representative (a) low-flux state (from 2010 February 13-15), (b) intermediate-flux state (2010 February 16), and (c) high-flux state (2010 February 17). In order to establish a baseline for the nature of relevant physical parameters for the source and facilitate the comparison of parameters between the three spectral states, we also reproduce an averaged emission state of Mrk 421. This emission, which we term as the steady state (SS), is reported in Abdo et al. 2011b and has been obtained by averaging the flux of Mrk 421 over a period of 4.5 months when the source was found in a relatively quiescent state.

We have used a cosmology with $\Omega_m = 0.3$, $\Omega_\Lambda = 0.7$, and $H_0 = 70\ km\ s^{-1}\ Mpc^{-1}$. In this cosmology, for a redshift of $z = 0.031$, the luminosity distance of Mrk 421 is dL

= 136 Mpc. The work described in this chapter is based on the paper Banerjee et al. (2019).

5.2 Data collection:

Several collaborations like VERITAS (Galante & for the VERITAS Collaboration 2011), TACTIC (Singh et al. 2015; Chandra et al. 2012), HAGAR (Shukla et al. 2012, ARGO-YBJ (Bartoli et al. 2016b), and H.E.S.S. (Tluczykont 2011) reported that Mrk 421 underwent a huge flare in TeV and X-ray energies in February 2010, exhibiting rapid changes in flux and spectral index from 2010 February 13 (MJD 55240) to 17 (MJD 55244). Figure 5.1 shows the SEDs for the three spectral states under consideration, along with the SS data of Mrk 421 (Abdo et al. 2011b). As discussed below, the low-flux state uses X-ray data from Shukla et al. 2012, which is 3-day averaged data from 2010 February 13-15. Since Mrk 421 did not show any significant variation in X-rays over this time period, we consider this averaged emission to be representative of a low-flux state over a 24-hour period. As can be seen from Figure 5.1, the low-flux state is different from SS in its flux and spectral hardness for both X-ray and γ-ray bands. This implies that the low-flux state represents the beginning of the flare in Mrk 421 that culminated in a high-flux state on 2010 February 17 in those bands. In addition, the source exhibited significant spectral variability in both X-ray and TeV regimes during intermediate- and high-flux states. However, the same level of variability was not observed at optical and GeV energies during that time. The source was reported to be found in the highest flux and hardest spectral state on 2010 February 17 by both VERITAS and HAGAR in the VHE band (Galante & for the VERITAS Collaboration 2011; Shukla et al. 2012), and the flaring activity was also prominent in soft and hard X-rays (Shukla et al. 2012). In this section, we summarize our multi-wavelength data collection.

5.2.1 Optical and Ultraviolet data:

We have used the optical data for Mrk 421 from Steward observatory. The data was collected in V band using 2.3 m Bok telescope on Kitt Peak, Arizona. The data was reduced based on the procedure described in Smith et al. 2009. In addition, we have collected the optical and ultraviolet (UV) data for Mrk 421 from the UVOT telescope (Roming et al. 2005b) on board *Swift* observatory. Details on data reduction procedure are provided in Williamson et al. 2014. The UVOT data used for 2010 February 15 and 16 are from V-band, *Swift*-UVW1, -UVW2, and -UVM2 filters. Data used for SED construction on 2010 February 17 are from V-band, UVW2, and UVM2 filters. As described in Williamson et al. 2014, all our data has been corrected for dereddening and host galaxy contribution. The dereddened magnitudes for Swift and ground-based observations have been converted to fluxes based on the details given in the paper.

5.2.2 X-ray Data:

MAXI (operational in 2 to 20 KeV), *Swift*-XRT (operational in 0.3 to 10 KeV) and *Swift*-BAT (operational in 20 to 60 KeV) observed this giant flaring activity in the soft and hard X-rays (Shukla et al. 2012; Singh et al. 2015). Both papers reported that the flux measured by the four instruments (*RXTE*-ASM [1.5-12 keV], -PCA [2-20 keV]; & *Swift*-XRT [0.5-2 KeV], -BAT [15-50 keV]) showed an increase by at least a factor of 4 within a period of two days as the source evolved from a low-flux to a high-flux state. The activity in the hard X-ray band can be seen in light curves (LCs) presented in Shukla et al. 2012 from MAXI and *Swift*-BAT, which makes this event exceptional. The corresponding evolution of the synchrotron peak position in the observed SEDs can be seen in the inset of Figure 5.1. As the peak position of the synchrotron component evolves from the low to the high-flux state, the slope of the line joining the optical to X-ray data changes, indicating spectral hardening in the X-ray regime during that time period. The inset of Figure 5.1 shows the change in slope of the line joining the optical and X-ray data for different flux states.

5.2.3 High Energy γ-ray data from *Fermi*-LAT:

Fermi-LAT (Atwood et al. 2009b) is a pair conversion telescope, with a field of view (FoV) of above 2 sr, operating in the energy range from 20 MeV to 300 GeV. It is the most sensitive instrument available in this energy range (Ackermann et al. 2012). A few months after the launch in June 2008, *Fermi*-LAT started to operate in all sky survey mode. The telescope scans the whole sky in 3 hours (Atwood et al. 2009b). For this work, we have analyzed the Pass8[1] data from 2010 February 13 to 17. We analyzed the data for Mrk 421 using the latest Fermi Science Tool[2] software package version v10r0p5. The detailed list of parameters we used for this work is listed in Table 5.1. We have used the *likelihood analysis with python* following the instructions on the *Fermi*-LAT analysis webpage[3]. In order to determine the flux and the spectrum of the source, maximum likelihood optimization has been used (Abdo et al. 2009). The data selection and quality checks have been made using the gtselect tool[4]. Since the telescope is sensitive to γ-rays from the interactions of cosmic rays with the ambient matter, we set our maximum zenith angle at 105 degrees to remove the background γ-ray events from Earth's limb. The analysis included all photons from a circular region of 10 degrees around Mrk

[1] https://fermi.gsfc.nasa.gov/ssc/data/analysis/documentation /Pass8_usage.html

[2] https://fermi.gsfc.nasa.gov/ssc/data/analysis/software/

[3] https://fermi.gsfc.nasa.gov/ssc/data/analysis/scitools/python_tutorial.html

[4] https://fermi.gsfc.nasa.gov/ssc/data/analysis/scitools /likelihood_tutorial.html

421, which we call the region of interest (ROI). Only photons of energy above 100 MeV were considered for further analysis. The latest LAT instrument response function (IRF) "P8R2_SOURCE_V6" has been used. The third *Fermi*-LAT catalog (3FGL catalog: Acero et al. 2015b) has been used to include the contributions of sources inside the ROI. The spectral model of the source has been considered as a simple power law of the form $dN(E)/dE = N_0(E/E_0)^{-\Gamma_{ph}}$, where N_0 is called the prefactor, Γ_{ph} is the index, and E_0 is the scale in energy. The spectral parameters of the sources including Mrk 421 inside the ROI are kept free, whereas the spectral parameters of the sources beyond 10 degrees from Mrk 421 are kept fixed to the values according to the 3FGL catalog. The unbinned likelihood[5] method has been used in order to estimate the detection significance of the sources. The test statistics parameter determined from the aforementioned method is given by $TS = 2\Delta log(L)$, where L denotes the likelihood function between the model with the source and without the source. According to the definition TS=9 corresponds to a detection significance of $\sim 3\sigma$ (Mattox et al. 1996). All the sources with TS < 9 are excluded from the likelihood analysis. In order to model the spectrum of sources we used the latest Galactic diffuse emission model "gll_iem_v06" and the isotropic background model "iso_P8R2_SOURCE_V6_v06". We estimated the corresponding butterfly plots for the source using the methods mentioned in the *Fermi*-LAT webpage[6]. VERITAS observed the high-flux state of Mrk 421 for ~ 6 hours. In order to obtain quasi-simultaneous data with VERITAS, we also analyzed the Fermi-LAT data for this state by taking 12 hours around the VERITAS observation period. In Figure 5.2(d), we show the butterfly plots for both 24 & 12 hours by closed butterfly (gray) and open butterfly with cross at the edges (blue), respectively, for the high-flux state.

[5]https://fermi.gsfc.nasa.gov/ssc/data/analysis/scitools /likelihood_tutorial.html

[6]https://fermi.gsfc.nasa.gov/ssc/data/analysis/scitools /python_tutorial.html

Parameters	Values
Radius of interest (ROI)	10
Energy Range	100 MeV–300 GeV
Fermi-LAT Science Tool version	v10r0p5
filter for event selection	
Event class Source type	128
Event type Front+Back	3
Maximum zenith angle cut	105
gtmktime for time selection	
Filter applied	(DATA QUAL > 0)&&(LAT CONFIG == 1)
ROI-based zenith angle cut	No
expCube for Livetime Cube	
Maximum zenith angle cut (zcut)	90
Step size in cos(θ)	0.025
Pixel size (degrees)	1
expMap for Exposure map	
Instrument Response Function (IRF)	CALDB
Size of the X & Y axis (pixels)	140
Image scale (degrees/pixel)	0.1
Source radius	20
Number of logarithmically uniform energy bins	37
diffuse models and Source model XML file	
Galactic diffuse emission model	gll iem v06.fits
Extragalactic isotropic diffuse emission model	iso P8R2 SOURCE V6 v06.txt
Source catalog	3FGL
Spectral model of Mrk 421	Power law
gtlike for likelihood analysis	
Response functions	CALDB
Optimizer	NEWMINUIT

Table 5.1: Parameters for the analysis of the data from *Fermi*-LAT. See Section 5.2.3 for the details of the analysis procedures.

5.2.4 Very-high-energy (VHE) gamma-ray data:

Mrk 421 was detected during the flare, exhibiting different flux states above 250 GeV from 2010 February 13-17 by the HAGAR telescope array located at Hanle, India (Shukla et al. 2012). Activity of the source for these days was also reported by the TACTIC telescope (in operation at Mount Abu in Western India) above 1 TeV (Singh et al. 2015; Chandra et al. 2012). Both HAGAR and TACTIC observed Mrk 421 on 2010 February 16 and reported an enhancement in flux compared to previous days. The flux above 1 TeV observed by TACTIC on 2010 February 16 (MJD 55243.77758-55243.98686) (Singh et al. 2015) was (2.5±0.4) $\times 10^{-11}$ $ph\ cm^{-2}\ s^{-1}$. The brightest flux state of Mrk 421 was observed by VERITAS on 2010 February 17 (55244.3-55244.5) above 100 GeV (see Figure 5.1 for details). The observed flux was 8 times that of the Crab. On the same night HAGAR also reported the detection of Mrk 421 in the brightest state, showing a flux of 6-7 times that of the Crab above 250 GeV. However, TACTIC (Chandra et al. 2012) reported a lower flux on 2010 February 17 as compared to VERITAS (Galante & for the VERITAS Collaboration 2011) . From the MJDs quoted above it is clear that the observations were not strictly simultaneous, and hence it is highly probable that on 2010 February 17, TACTIC caught only the decaying part of the flare. For our analysis, we have corrected for attenuation of the VHE spectrum by the extra-galactic background light (EBL) using the model of Domínguez et al. 2011.

5.2.5 Summary of MWL data:

It can be seen from the above discussion that Mrk 421 had undergone a change in flux and spectral hardness from a low-soft state to a high-hard state in a matter of 5 days

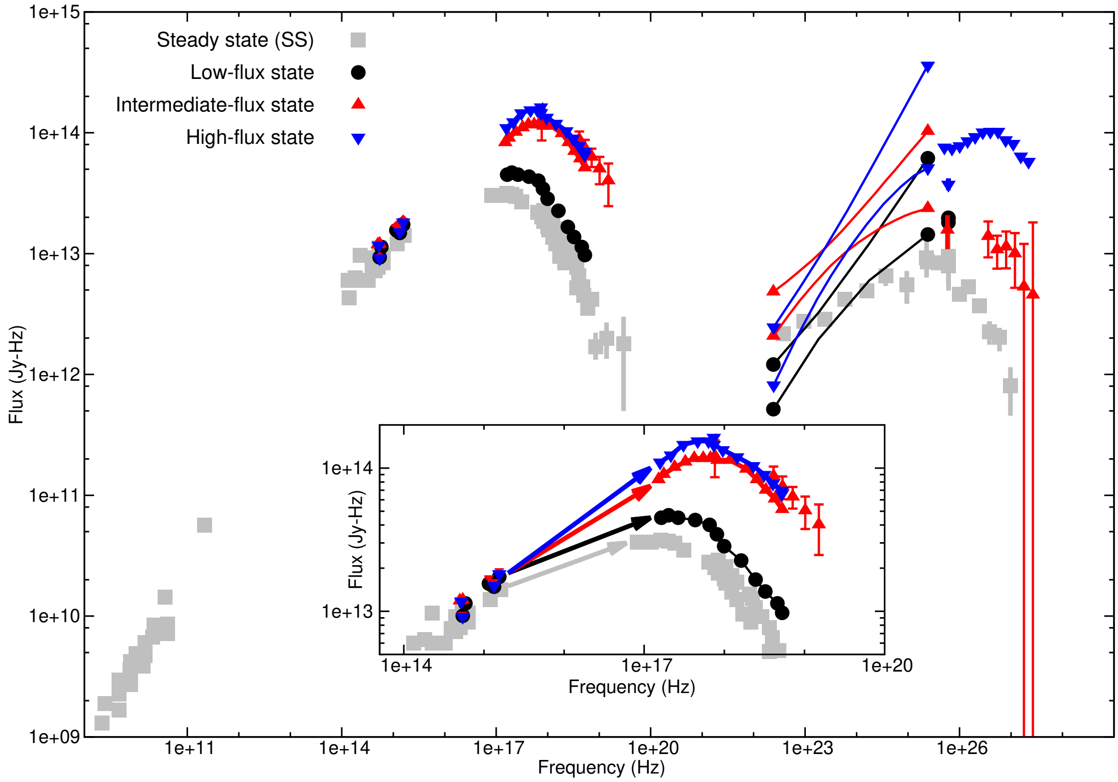

Figure 5.1: Multi-wavelength data of Mrk 421 from optical to TeV energies from February 13-17, 2010. Different markers denote the following dates: Square (gray)- SS data, Circle (black)- average of 2010 February 13-15 (low-flux state), Regular triangles (red)-2010 February 16 (intermediate-flux state), Inverted triangles (blue)- 2010 February 17 (high-flux state). The spectral hardening can be seen in X-ray and TeV bands as the source became brighter. The VERITAS data in high-flux state shows the highest flux state in TeV energies during this giant outburst (see text for details). The EBL correction has been carried out according to the model presented in Domínguez et al. 2011. The change in the slopes of lines joining optical and UV (see the inset plot) shows that the spectrum became harder as the source brightened. The optical-UV data used in this work has been corrected for dereddening and host galaxy contribution. Figure adapted from Banerjee et al. (2019).

Day (MJD)	Optical/UV	X-ray	γ-ray	VHE γ-ray
2010 February 13–15 (55240 to 55242)	Steward-Observatory, *Swift*-UVOT	*Swift*-XRT, -BAT	*Fermi*-LAT	HAGAR
2010 February 16 (55243)	Steward-Observatory, *Swift*-UVOT	*Swift*-XRT, -BAT	*Fermi*-LAT	HAGAR, TACTIC
2010 February 17 (55244)	Steward-Observatory, *Swift*-UVOT	*Swift*-XRT, -BAT	*Fermi*-LAT	HAGAR, VERITAS

Table 5.2: Data collected from different instruments. The optical V-band data from Steward observatory and UV data from *Swift*-UVOT (using three filters UVW2, UVM2, UVW1) have been used. The *Fermi*-LAT data has been analyzed using latest Fermi tools (see texts for details). The X-ray data for different days has been used from Shukla et al. 2012. For intermediate- and high-flux states the TeV data from TACTIC (Singh et al. 2015) and VERITAS (Galante & for the VERITAS Collaboration 2011) have been used, respectively. In addition, we have used the available VHE data from HAGAR (Shukla et al. 2012) for different states to approximate the flux level at those energies and not for performing SED data-fitting.

from 2010 February 13-17 in X-rays, GeV and TeV γ-rays. However, in the optical band there was no significant change in flux during that time. The inset plot of Figure 5.1 shows that the slopes of the lines joining the optical and the X-ray spectrum in the SEDs became steeper as the flare set in during the low-flux state. This implies that the X-ray spectrum, in the 2-10 keV energy range, became harder and the synchrotron peak shifted to higher energies in the hard X-rays as the flare progressed to the high-flux state. During this progression, a quasi-linearity was also observed between 1-10 keV X-rays and γ-rays above 100 GeV (Shukla et al. 2012; Singh et al. 2015). Such strong variations in both X-ray and γ-rays and the quasi-linear correlation between the two suggests that the flare has a leptonic origin rather than a hadronic one, as no correlation between X-ray and TeV variabilities is expected under a hadronic scenario (Aharonian 2000; Mücke et al. 2003b). The details of the data used for this work are listed in Table

5.2. As can be seen from the inset plot in Figure 5.1, the synchrotron curvature decreased as the flux increased and the synchrotron peak shifted to higher energies. This variation in the shape of the synchrotron peak could be associated with statistical or stochastic acceleration mechanisms (Donnarumma & AGILE Team 2012). The prevalence of these acceleration mechanisms during the flare is further supported by the value of electron energy indices that were obtained as best fit values for reproducing the three spectral states.

5.3 Model description:

We have used the MUlti-ZOne with Radiation Feedback (MUZORF) model of Joshi & Böttcher 2011 to individually reproduce the three flux states and the SS of Mrk 421 in a time-dependent manner. The model assumes a background thermal plasma of non-relativistic electrons, positrons, and protons in the jet. Two shells of plasma with different mass and velocity are assumed to be injected into the jet from the central engine that consists of a super-massive black hole (SMBH) and an accretion disk. A merged shell is formed when a faster moving inner shell ejected at a later time catches up with a slower moving outer shell ejected at an earlier time. This merged shell serves as an emission region inside which two internal shocks, a reverse shock (RS) and a forward shock (FS), are produced. In the frame of the shocked fluids, the shocks (FS/RS) travel in opposite directions from each other and the corresponding emission regions are called the forward and reverse emission regions (Joshi & Böttcher 2011). As the shocks propagate through their respective emission regions, a fraction of the internal kinetic energy of the shocked fluid that is stored in the baryons, is transferred to electrons and positrons. The particles in these regions subsequently get accelerated to relativistic and non-thermal energies due to this transfer. The fraction of the bulk kinetic energy density of the shocked fluid that gets converted into magnetic and particle energy density is quantified by their respective partition parameters, ε'_B and ε'_e. The ratio of these parameters provides a first-order estimate of the equipartition parameter, e'_B, of the model. We consider this as first-order because the time-dependence of our model makes the particle energy density evolve with time. Consequently, the equipartition parameter of our model is time-dependent. Hence, the above-mentioned ratio provides only an initial value of the equipartition parameter resulting from the model. The observed emission from the jet is a result of the energy lost by highly accelerated particles in the shocked medium. As the shocks move into their first radiating zone, they accelerate a fraction of its particle population, which subsequently loses energy via the synchrotron and SSC mechanisms and produce the observed radiation. The model takes into account Klein-Nishina effects for calculating inverse Compton emission. Throughout the chapter, we consider primed quantities representing co-moving or shocked plasma frame values, starred quantities stand for the observer's frame, and unprimed variables denote the rest frame of the host galaxy (lab frame). The cylindrical emission region is considered to have a co-moving radius R'_{cyl} with a width Δ'_{cyl}. The radiation mechanism inside the entire cylindrical emission region is mainly governed by a randomly oriented magnetic field (B') and the injected electron energy distribution (EED). The injected EED follows a simple power law ($N(E) = N_0 E^{-q'}$) with a single index q' and minimum and maximum electron energy distribution cutoffs represented by their corresponding Lorentz factors γ'_{min} & γ'_{max}, respectively. The fraction of electrons, ζ'_e, that get accelerated behind the shock fronts into a power-law distribution along with ε'_e govern the initial value of γ'_{min} of the injected electron distribution. Once the shocks exit their respective zones, γ'_{min} & γ'_{max} of those zones are made to evolve with time according to the formalism:

$$\gamma^{new}_{min(/max)} = \gamma^{old}_{min(/max)} - \dot{\gamma}\Big|_{min(/max)} dt \tag{5.1}$$

, where

dt is the time step of the simulation.

The following two equations govern the dynamics of particle and photon populations inside the emission regions in a time-dependent manner (Joshi & Böttcher 2011).

$$\frac{\partial n_e(\gamma, t)}{\partial t} = -\frac{\partial}{\partial t}\left[\left(Qt\right)_{loss} n_e(\gamma, t)\right] + Q_e(\gamma, t) - \frac{n_e(\gamma, t)}{t_{e,esc}} \tag{5.2}$$

&

$$\frac{\partial n_{ph}(\epsilon, t)}{\partial t} = \dot{n}_{ph,em}(\epsilon, t) - \dot{n}_{ph,abs}(\epsilon, t) - \frac{n_{ph}(\epsilon, t)}{t_{ph,esc}} \tag{5.3}$$

, where

$n_e(\gamma, t)$ is the lepton density inside the system,

$(Qt)_{loss}$ is the loss rate of particles,

$Q_e(\gamma, t)$ is the sum of injection of leptons and $\gamma - \gamma$ electron-positron pair production rate,

$t_{e,esc}$ is the electron escape time scale,

$\dot{n}_{ph,em}(\epsilon, t), \dot{n}_{ph,abs}(\epsilon, t)$ are the photon emission and absorption rates, respectively,

$\epsilon = h\nu/m_ec^2$ is the dimensionless photon energy,

$t_{ph,esc}$ is the angle and volume averaged photon escape time scale for a cylindrical emission region.

The model addresses inhomogeneity in photon and electron density inside the emission region by dividing the emission regions into multiple zones and considering radiative transfer within each zone and in between the zones. The emission region has been split into multiple zones only along the width of the cylinder. A fraction of the resulting volume and angle averaged photon density from a zone is fed subsequently to the zones on its adjacent sides. The feedback is essentially the angle and volume averaged photon density escaping (in forward, backward and sideways directions) from a cylindrical emission region. The total photon output from a zone consists of three components: synchrotron, SSC, and forward (feed-up) & backward (feed-down) feedback received from adjacent zones. The radiation feedback scheme also lets us calculate the SSC emission accurately as compared to models with homogeneous one-zone emission regions. This is especially important for appropriately reproducing the high-energy component of TeV blazars (such as Mrk 421), in which SSC is likely an important, or even dominant, process for producing high-energy photons (Joshi & Böttcher 2011).

The cylindrical emission region is divided into 100 zones, with 50 in the forward and 50 in the reverse emission region. The steps to solve the above two equations in order to get the time averaged photon spectrum are discussed in detail in the paper mentioned above. The frequency range of 7.5×10^{6} Hz to 7.5×10^{29} Hz has been selected for carrying out the simulations. The chosen range of the EED is from 1.01 to 10^{7} for each simulation. Both ranges are divided into 150 grid points.

5.4 Results and Discussion:

The SEDs presented in Figure 5.1 represent the temporal evolution of Mrk 421 over a period of 5 days from a low- to high-flux state in February 2010. In addition, a typical state of the source has been presented in the form of SS for carrying out a comparison of key physical parameters between flaring and non-flaring states and how they contribute toward the evolution of a flare in a source like Mrk 421. As can be seen from the figure, the low-flux state is different in its spectral hardness and flux level in X-rays and γ-rays as compared to that of the SS. Hence, it can be identified with an initial phase, where the flare is beginning to build up. During the course of the flaring event the source underwent significant changes in flux and spectral hardness across X-ray and γ-ray wavebands. Such a behavior allows us to study the daily evolution of the source at different energies. In order to explore the physical phenomena occurring inside the jet, we have used MUZORF to constrain the role of key physical parameters, such as the bulk kinetic luminosity, nature of the particle population, and magnetic field strength present in the system. We reproduced the SED of each of the four spectral states individually, in a time-dependent manner. The model reproduces observational signatures of blazars: instantaneous SEDs that are used to understand the dynamical evolution of radiation components and LCs that are used for deriving the time-averaged SED based on a selected time window from these variability profiles (Joshi & Böttcher 2011). It is the time-averaged SED that is used for carrying out data-fitting for each spectral state by varying key physical parameter values for that state through an iterative process. For our analysis, the parameters of the successful fit for a particular spectral state served as guiding points for carrying out fitting efforts for the next state. The model, however, is not designed to carry forward the information of physical parameters from the previous state to the next in a self-consistent manner.

In order to execute our data-fitting method, we first estimated some model-independent parameters for each spectral state using the data from their respective SEDs (Böttcher et al. 2003; Tavecchio et al. 1998). We have considered a minimum variability timescale (t^{*}_{var}) of the order of 1 day. This is justified because a flux doubling time scale of $\sim$ 1 day can be seen at GeV, X-ray, and TeV energies from the multi-wavelength LCs for this time period (Shukla et al. 2012). The variability timescale of the blazar allows us to put a constraint on the length of the cylindrical emission region. This gives us, $\Delta'_{cyl} = c\ D\ t^{*}_{var}/(1 + z)$. We can estimate the radius of the cylindrical emission region by assuming it to have the same volume as a spherical emission region of radius Δ'_{cyl}. In that case, $(4/3)\ \pi\ \Delta'^{3}_{cyl} = \pi\ R'^{2}\ \Delta'_{cyl}$. The value of R' can be estimated as, $(2/\sqrt{3})\ \Delta'_{cyl}$. Considering t_{var} as 1-day and Doppler factor as 40, the values for the width of the emission region and radius of the emission region turns out to be $\sim 1.4 \times 10^{17} cm$ & $\sim 1.0 \times 10^{17} cm$, respectively. We note that our chosen value of Doppler factor is higher than the typical value of $\sim$ 21 that is used for Mrk 421 (Abdo et al. 2011b) but is not uncommon for what has been previously used for this source to satisfactorily reproduce its TeV data (Chen et al. 2011a). A lower value of Doppler factor results in a SSC peak at lower energies and a softer TeV spectrum that is not in accordance with our observed data for the three states. Hence, we initialize the Doppler factor to a slightly higher value of 40. The derived set of model-independent parameters is presented in Table 5.3. These parameters served as initial input parameters for simulating the spectral states and were modified to obtain the successful fits for each of the states. These parameters were estimated based on the identification of the peak flux and frequencies of the two SED bumps, spectral indices below and above the synchrotron peak, variability timescale of the observations, and the Doppler factor of the source (Tavecchio et al. 1998). Since the observed data may not always allow a precise determination of these observables, the subsequent model-independent parameter estimates may not be that accurate and may not necessarily provide a good spectral fit. Nevertheless, for modeling efforts they can still be used as reasonable starting points and the values of key physical parameters can be adjusted in subsequent runs to obtain a satisfactory spectral fit of a given spectral state.

Close to one-thousand simulations were carried out in which we changed the value of key parameters iteratively. We obtained a set of suitable parameters through this iterative process and chose successful models by visual inspection. As can be seen from Figure 5.2, this set of suitable parameters reproduces the observed data quite successfully. The parameters that have been varied are the following: kinetic luminosity (L_w); inner and outer shell bulk Lorentz factors (BLF : $\Gamma'_{i(0)}$); inner and outer shell widths ($\Delta'_{i(o)}$); electron energy distribution parameter (ε'_e); magnetic field (B'); fraction of accelerated electrons (ζ'_e); electron injection index (q'); zone(/jet) radius (R'_{cyl}). Among all the other parameters listed above, the kinetic luminosity (L_w), width (Δ'_{cyl}) & radius (R'_{cyl}) of the emission region, and the electron injection index (q') have the maximum impact on the values of the magnetic field (B'), γ'_{min}, and γ'_{max}.

We consider the mass of the SMBH to be $M = 2 \times 10^8\ M_\odot$ (Abdo et al. 2011b; $M_\odot$: 1 solar mass) which predicts the Eddington luminosity as 2.6×10^{46} erg/s. The values for the kinetic luminosity obtained from the model fit (see Table 5.4) for all the spectral states are lower than the value mentioned above, implying that the states are sub-Eddington. Figure 5.2 shows the result of our SED modeling for the four states considered here. The low-flux, intermediate, and high-flux states are shown in panels (a), (c) and (d) respectively. In panel (b), we show a comparison of the SED of the low-flux state with the SS of the source. As can be seen from various panels in the figure, the resultant time-averaged SEDs reproduce these spectral states satisfactorily.

The successful model parameters for all spectral states are presented in Table 5.4. As can be seen from Table 5.3, the values of the initial input parameter set do not match the values obtained from successful fits of the four spectral states. However, the pattern of the values of the magnetic field strength, the equipartition parameter, and the particle

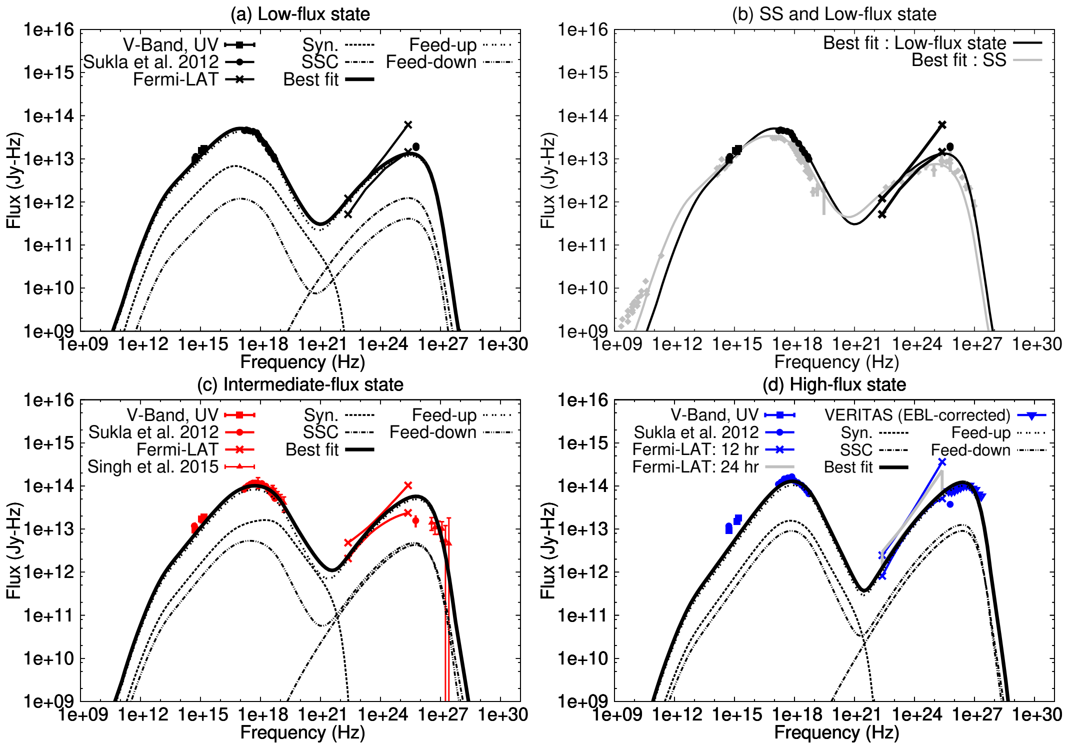

Figure 5.2: The results of the SED modeling for different flux states: (a) low-flux state (2010 February 13-15), (b) steady state (4.5 month average as in Abdo et al. 2011b), (c) intermediate-flux state (2010 February 16), (d) high-flux state (2010 February 17). The black lines represent the successful models for each day. The *broken-line* and the *dash-dot* lines represent the synchrotron and SSC components in each of the successful models in (a), (c) and (d). The feed-up and feed-down components for (a), (c) and (d) are shown in *double dot-blank* and *dash-double dot* lines respectively. The butterfly plots for *Fermi*-LAT data on all the nights are drawn as solid lines with cross at the edges. The optical, X-ray and TeV data taken from Shukla et al. 2012 are shown by filled circles. The optical data from Steward Observatory and *Swift*-UVOT data are shown by square markers. The X-ray data and TeV data on 2010 February 16 (panel (c)) are from Singh et al. 2015 and are shown by regular triangular markers. The TeV data from VERITAS on 2010 February 17 (panel (d)) is shown by inverted triangular markers. For details see text. Figure adapted from Banerjee et al. (2019).

Parameter	Symbol	Steady state	Low-flux state	Intermediate-flux state	High-flux state
Doppler factor	D	40	40	40	40
Slice/Jet Radius(cm)	R'_{cyl}	1.0×10^{17}	1.0×10^{17}	1.0×10^{17}	1.0×10^{17}
Shell Width(cm)	Δ'_{cyl}	1.4×10^{17}	1.4×10^{17}	1.4×10^{17}	1.4×10^{17}
Equipartition parameter (10^3)	e'_B	0.004	0.01	0.045	1.0
Particle Injection Index	q'	2.65	2.6	2.35	2.15
Magnetic field (mG)	B'	13	8	4	2
Minimum energy of an electron	γ'_{min}	2.5×10^5	3.5×10^5	1.5×10^6	2.0×10^6
Maximum energy of an electron	γ'_{max}	1.3×10^7	3.2×10^7	9.0×10^7	1.1×10^8
Variability timescale (s)	t^*_{var}	1-day	1-day	1-day	1-day

Table 5.3: The list of initial input model parameters for different states. Different initial model parameters: Δ'_{cyl}, R'_{cyl}, q', B', γ_{min}, and γ_{max} are estimated from the data for different flux states, using a variability timescale of 1-day and a Doppler factor of 40, based on the prescription described in Böttcher et al. 2003. Here, we have used the optical to X-ray spectral index of Mrk 421 for various spectral states to estimate the injection index for our electron distribution. The magnetic field and electron energy density values have been estimated according to the prescription given in Tavecchio et al. 1998 and Finke et al. 2008, respectively.

Parameter	Symbol	Steady state	Low-flux state	Intermediate-flux state	High-flux State
Kinetic Luminosity (erg/s)	L_w	2.6×10^{45}	4.2×10^{45}	9.5×10^{45}	9.8×10^{45}
Doppler Factor	D	40	40	40	44.0
Bulk Lorentz Factor	Γ'_{sh}	28	28	28	40.0
Magnetic Field (mG)	B'	89	64	60	26
Total shell Width (in cm)	Δ'_{cyl}	1.1×10^{17}	1.1×10^{17}	1.1×10^{17}	1.1×10^{17}
Equipartition parameter (10^3)	e'_B	0.18	0.28	1	5.6
Fraction of accelerated electrons (10^{-3})	ζ'_e	37	4.5	4.5	3.7
Min. energy of an electron	γ'_{min}	4.4×10^{2}	1.2×10^{3}	1.1×10^{3}	1.2×10^{3}
Max. energy of an electron	γ'_{max}	3.1×10^{5}	4.0×10^{5}	7.1×10^{5}	9.5×10^{5}
Particle Injection Index	q'	2.1	2.01	1.86	1.75
Zone(/Jet) Radius (in cm)	R'_{cyl}	1.25×10^{17}	1.25×10^{17}	1.25×10^{17}	1.25×10^{17}
Observing Angle(deg)	θ^*_{obs}	1.3	1.3	1.3	1.3

Table 5.4: The successful model parameters for different days of the flaring episode. A detailed descripton of the comparisons is presented in Section 5.4.

injection does so. The values of these parameters in Table 5.4 hint toward the existence of a general trend in the role of key physical parameters during the evolution of the flare over a period of three days. As the flare sets into the system during the low-flux state and then evolves into the high-flux state, the kinetic luminosity that is injected into the system increases while the magnetic field strength and the fraction of accelerated electrons decrease. This happens because as the flare evolves and higher energy bands become brighter and harder, the corresponding synchrotron component needs to be suppressed sufficiently for the SSC component to rise up and attain its highest flux level in the high-flux state. This is further supported by an increased bulk speed of the emission region for the high-flux state and a more energetic population of particles with a harder distribution.

We note that the values of beaming parameters obtained in Table 5.4 are fully consistent with the results of an independent study, not based on SED modeling, performed on probing the X-ray signature of recollimation shocks in Hervet et al. 2019. The authors found the width of the emitting region (in the plasma frame) to lie within $0.43 - 19 \times 10^{17}$ cm, which is also in agreement with the value of total shell width listed in Table 5.4.

The successful fits for the four spectral states result in a particle injection index value that varies from $q' = 2.2$ to 1.8. In general, relativistic shocks (with their shock normal parallel to the jet axis) are expected to produce a particle distribution with $2.2 < q' < 2.3$ (Achterberg et al. 2001; Gallant & Achterberg 1999) through the Fermi first-order acceleration mechanism. On the other hand, indices with $q' < 2.0$ could be produced from stochastic acceleration in resonance with plasma wave turbulence behind the relativistic shock front (Vainio et al. 2004; Virtanen & Vainio 2005). This implies that typically it is Fermi first order that is prevalent as the dominant acceleration mechanism in Mrk 421. However during the onset of a flare and course of its evolution, the dominant acceleration mechanism, within the shock model, changes from Fermi first to second order or stochastic acceleration. From Table 5.4, one can also see that successful model parameters indicate a departure from equipartition for all spectral states and a matter-dominated jet. This kind of a departure has previously been seen for Mrk 421 (Sinha et al. 2016; Shukla et al. 2012). For our case, this implies that the shocks are mediated by the acceleration of particles and resulting in the energy density of the particles to be much higher than that of the field.

We also note that the parameters obtained from our study closely matched with the general one-zone time-independent models such as Shukla et al. (2012). The magnetic field and hard component in the particle injection index of the broken power-law reported in that paper is around ~20-30 mG and 2.2–2.4 respectively. However, the successful models show a preference for a higher kinetic luminosity and Doppler factor as compared to the other published works. This is because the previously published works on the one zone time-independent models assumes pre-existing particles inside the jets, whereas in case of MUZORF, no foreground or background of particles are assumed. The advantage of MUZORF is that when we allow the shocks to propagate into the system through the merged shell we also calculate the emitted photons at different energies which carries the signature of the dynamics inside the source. These simulated LCs are essential for understanding the interplay of different components of radiation. We find a suitable window with similar length as compared to the variability time-scale (1-day in this case) in such a way that all the flares at different energies can be contained.

In the resultant time-averaged SED (Figure 5.2(a)) for the low-flux state, the synchrotron hump peaks in the soft X-ray at $\nu^*_{syn} = 1 \times 10^{17}$ Hz. The frequency at which we observe the SSC peak is at ν^*_{SSC}= $1.5{\times}10^{25} Hz$. The spectral upturn can be seen at around $\nu^*_{turn} = 3.5 \times 10^{20}$ Hz. This is the frequency above which the spectrum becomes SSC dominated. The position of the spectral upturn indicates that the synchrotron photons extend into hard X-rays. Figure 5.2(a) shows that the optical R-band and 1 keV photons are purely synchrotron dominated while the radiation at 10 keV is mostly produced due to synchrotron emission with small contributions from SSC. On the other hand, photons at energies 1 GeV, 500 GeV, and 2 TeV are purely SSC-dominated. The Compton dominance factor (CD), defined as the ratio of the peak flux of SSC hump ($\nu F_{\nu}^{*SSC,peak}$) to that of the synchrotron hump ($\nu F_{\nu}^{*Syn.,peak}$) for this simulation is ($\nu F_{\nu}^{*SSC,peak}/\nu F_{\nu}^{*Syn.,peak}$=) 0.29. Figure 5.2(b) shows a comparison between the models for SS and the low-flux state. As can be seen from the figure, the synchrotron and SSC peaks for the SS appear at almost the same frequencies as that of the low-flux state. However, the overall flux level is slightly less compared to the low-flux state (see Figure 5.2(b)). In order to reproduce a lower SSC contribution in the SED of SS, a slightly higher value of $B^{'}$ is required in accordance with the general trend of key parameters.

The model parameters (shown in Table 5.4) for the successful SEDs for SS and the low-flux state support our assumption that the low-flux state carries signatures of the initial phase of the flare.

The SED that closely fits the data of the intermediate-flux state is shown in Figure 5.2(c) and the corresponding model parameters are given in Table 5.4. In order to fit the SED corresponding to this spectral state, we decreased the value of B', which increased γ'_{max} and the Compton dominance of the system. In order to correct for this effect on the overall SED, we increased the value of L_w and also decreased the value of q', which resulted in bringing the flux of both synchrotron and SSC components to the right level. We note that our model for the intermediate- and high-flux states overproduce the HAGAR data points located at ~ 250 GeV. In the absence of any data from imaging telescopes, HAGAR data point was used as a guide to approximate the flux level at those gamma-ray energies and was not meant to be used for performing data fitting. This is because HAGAR uses wave-front sampling technique[7] that is known to have systematic uncertainties in the estimation of flux much larger than that of the imaging telescopes operating at TeV energies, such as VERITAS and TACTIC.

The source was observed in the brightest state with highest γ-ray flux on 2010 February 17. The successful model for this SED is shown in Figure 5.2(d) and values of the corresponding key physical parameters are listed in Table 5.4. For this day the SSC component peaked at around 2 TeV. This SSC peak position is at a relatively higher energy as compared to other days and is indicative of spectral hardening of the source in this energy regime. The CD for the high-flux state is 0.85, indicating an increase in the peak of the SSC component as compared to the low-flux state. The magnetic field value has been decreased further to 26 mG in order to obtain a particle population with a slightly higher γ'_{max} in comparison to its low-flux state counterpart. In addition, a higher value of Γ'_{sh} and therefore D shift the SED toward higher energies. An even harder value of $q' = 1.75$ has been used to obtain the successful model for this state as compared to other states under consideration. The recession of q' to lower values, as the source evolves from a low-flux state to the brightest state, imply an interplay of Fermi first- and second-order acceleration mechanisms. Such an interplay along with contribution from shear acceleration has been suggested to energize particles to higher energies (Rieger & Duffy 2004b).

As can be seen from Figure 5.2(d), the overall optical flux for the high-flux state is slightly under-produced. This is mainly because as we go from low- to high-flux state, we need lower magnetic field in order to fit the observed SSC component. A low magnetic field results in low synchrotron output, which is reflected in the optical region of

[7] http://www.tifr.res.in/~hagar/telescopes_details.html

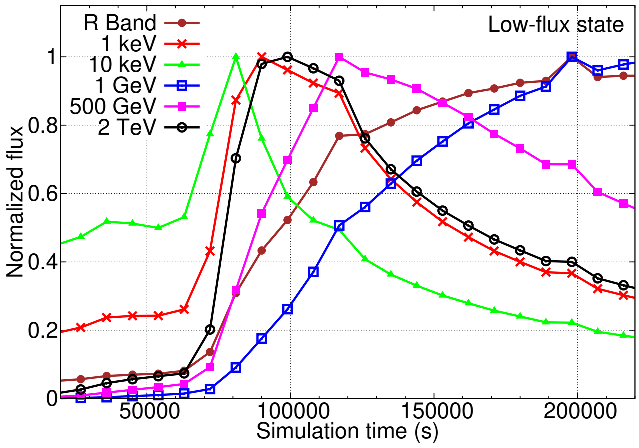

Figure 5.3: The simulated LCs (normalized to the peak flux for each of the LCs) of Mrk 421 at six different energy bands (R-Band [brown-filled circle]; 1 keV [red-cross]; 10 keV [green-filled triangle]; 1 GeV [blue-hollow square]; 500 GeV [pink-filled square]; 2 TeV [black-hollow circle]) corresponding to the successful SED model for the low-flux state. The variation of flux rise time and flux decay time for each energy band can be seen. The selection of time window was made such that both rise and decay of the LCs are considered inside the selected time window for making the time averaged SEDs. The LCs, except for the Optical R-Band, 1 GeV, and 500 GeV, peak around 80 ks. In case of the optical R-Band and 1 GeV, the radiation profiles are produced via relatively low-energy electrons. Hence the optical and GeV components peak outside the selected time window mentioned above. Figure adapted from Banerjee et al. (2019).

the SED. Besides, the high-flux state is mostly devoid of low-energy electrons, as the corresponding particle population is much harder and more energetic compared to the other two states. As a result, it is not possible to reproduce optical emission for that day successfully. In addition, the source did not exhibit any variability in the optical energies over the course of this flaring event. Since the emission at optical and GeV-TeV energies are not correlated at all, it is possible that the optical emission for the high-flux state originates from a slightly larger emitting volume than what has been considered for this day.

Figure 5.3 shows the LC profiles of the low-flux state for six different wavebands corresponding to the successful fit shown in Figure 5.2(a). The LC profiles for all days have been evaluated at frequencies: R-Band [4.68×10^{14} Hz]; 1 keV [2.42×10^{16} Hz]; 10 keV [2.42×10^{17} Hz]; 1 GeV [2.42×10^{23} Hz]; 500 GeV [1.21×10^{26} Hz] and 2 TeV [4.84×10^{26} Hz]. We calculated LCs at these energies because most of the current generation telescopes are most sensitive in these energy bands. These are also the representative LCs for synchrotron (optical and 1 keV LCs) and SSC (2 TeV LC) components for typical HBLs, such as Mrk 421. All the different LCs are characterized by different flux rise times (time scale associated with flux reaching the peak value) and flux decay times (time scale associated with flux decaying from the peak value). In order to calculate time-averaged SEDs for various spectral states appropriately, we used the corresponding simulated LCs and selected the time window of ~ 90 ks in such a way that both the rising and decaying components of the LCs are properly taken into consideration (see Figure 5.4). The fact that the peak of the SSC component appears at ~ 2 TeV for the high-flux state and a harder population of electrons is required to reproduce this feature implies that the pulse at 2 TeV now receives contribution from relatively lower energy electrons as compared to its counterparts for the other three states. As a result, the pulse decays slowly and lasts in the system for a much longer duration. In order to cover the entire flare, we have considered a time-window from 60 ks to 160 ks for the low and intermediate-flux state, whereas, for the high flux state a time-window of 65 ks to 195 ks has been selected. Here, we note that the choice of the time-window depends on the state of the source. In some cases, the time-window is larger than 1-day. Keeping the time-window exactly at 1-day would have given a truncated flare which will reduce the contribution of the emissions in different wavebands. A longer time-window larger than 1-day is necessary for containing the emissions at X-rays and VHE gamma-rays for a low magnetic field.

As shown in the Figure 5.4, the flare at 10 keV is the first to peak because it is a result of synchrotron emission from high-energy electrons. The peak positions of synchrotron-dominated flares (1 keV & R-Band) shift to later times depending on the energy of electrons responsible for producing them. The SSC-dominated flares are expected to lag behind their synchrotron counterparts. Hence, all γ-ray flares peak later. However, depending on the energy of electrons responsible for producing SSC emission at these wavebands, the high-energy SSC flares (2 TeV & 500 GeV) would peak sooner than the low-energy ones (1 GeV). This gradation in peaking times due to the difference in cooling times of high- and low-energy electrons can be easily seen in the LC profiles of the low-flux state in Figure 5.3. The profiles also show a strong correlation between the synchrotron-dominated R-band flare and SSC-dominated 1 GeV flare. The optical flare is a result of synchrotron emission from low-energy electrons compared to those responsible for the synchrotron emission in the X-rays. Hence, the corresponding flare peaks at a later time and lasts in the system for a longer time. In addition, a fraction of these R-band photons is also responsible for producing 1 GeV photons via the SSC mechanism through low-energy electrons. Hence, the corresponding flare is strongly correlated with the optical one. On the other hand, the 500 GeV SSC-dominated flare gets contributions from both X-ray and low-energy photons. As a result, it exhibits a mild correlation with the X-ray flare.

The above-mentioned behavior of flares at various energy bands was present for all days under consideration and is typical of what has been previously seen in Mrk 421. Panels a, b, c, & d of Figure 5.4 show a comparison of the LCs, normalized to their highest flux values, as predicted by successful models for those days at 1 keV, 10 keV, 500 GeV, & 2 TeV, respectively. The LCs at optical and 1 GeV are excluded from the figure, as these bands did not show any significant variation in their profiles during the evolution of the flare. This is also consistent with the Mrk 421 optical LC presented

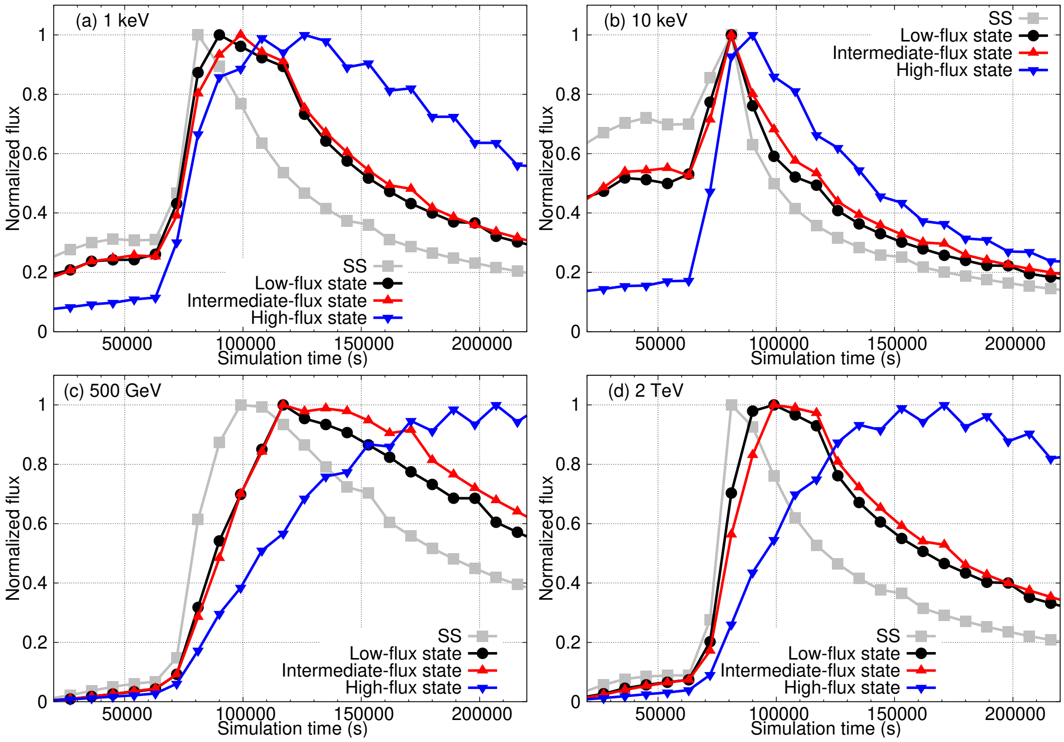

Figure 5.4: The normalized LCs (normalized to the peak flux value for each of the LCs) obtained from the model parameters in Table 5.4. Comparisons of simulated LCs for 1 keV, 10 keV, 500 GeV, and 2 TeV for four different spectral states: i) SS [gray-square], ii) Low-flux state [black-circle], iii) Intermediate-flux state [red-regular triangle], and iv) High-flux state [blue-inverted triangle] are shown in panel (a), (b), (c), and (d) respectively. Figure adapted from Banerjee et al. (2019).

in Shukla et al. 2012 for this time period. Table 5.4 shows that the successful model for intermediate-flux state requires a higher kinetic luminosity, lower magnetic field and harder injection index as compared to that for the low-flux state. This resulted in a larger Larmor radius and a higher γ'_{max} for the electron population, which led to a slightly longer decay time scale for corresponding pulses at all energy bands (see Figure 5.4). For the high-flux state of Mrk 421, the LC profiles are characterized by an even longer rise and decay time for pulses at all energies. In this case, the best fit SED was obtained using a higher value of Γ'_{sh} and a much harder spectral index compared to that of the low- and intermediate-flux states. Hence, the location of synchrotron and SSC peak frequencies shifted to higher values at 1 keV and 2 TeV, respectively. Since a relatively harder population of electrons is involved in producing the emission at 2 TeV compared to the other two days, the flare at 2 TeV lasts for a longer time and decays very gradually, as shown in Figure 5.4(d). Figure 5.5 shows the spectral evolution of the source with flux for various spectral states during the evolution of the flare. As can be seen, for all spectral states the source exhibits a clockwise pattern. This implies a soft lag which results in a higher variability at the higher energies as compared to the lower energies.

It happens because higher energy electrons cool faster than the lower energy ones and the information about particle injection propagates from higher to lower energies through the electron population. This results in a characteristic clockwise loop because the injection is faster than the cooling. The loop depicts the manner in which the information on particle injection travels through the electron population at certain frequencies (Kirk et al. 1998). Such clockwise patterns have previously been observed in Mrk 421 (Tramacere et al. 2009; Takahashi et al. 1996), and other sources, such as OJ 287 (Gear et al. 1986), and PKS 2155-304 (Sembay et al. 1993). This also implies that the evo-

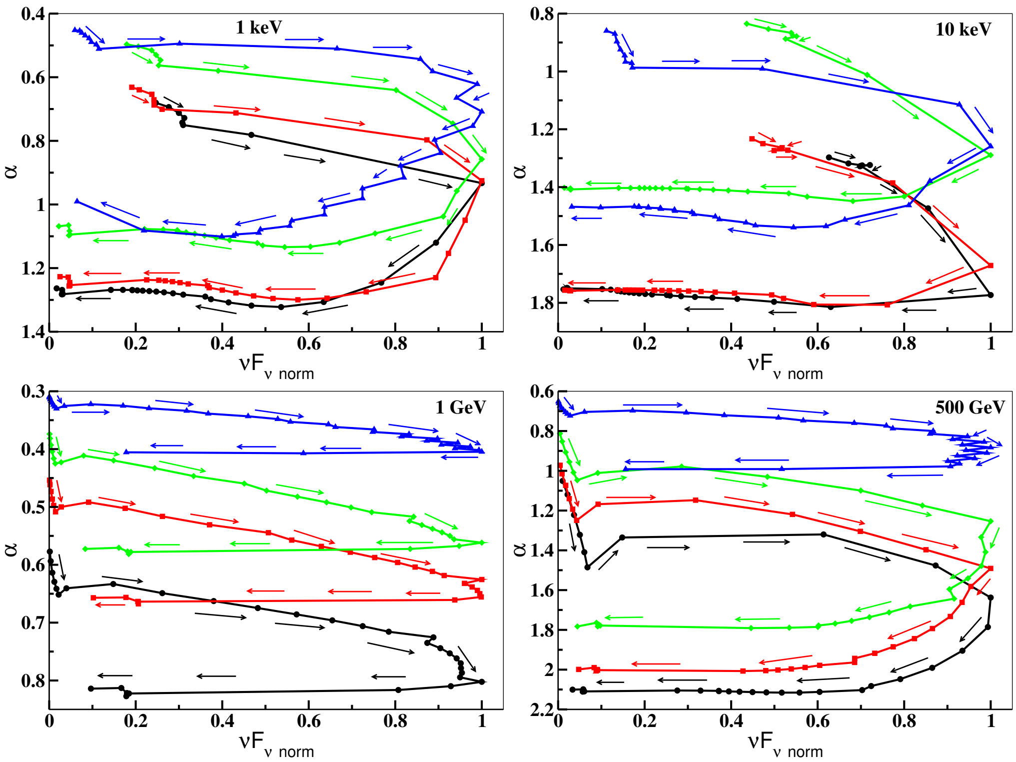

Figure 5.5: Spectral evolution of Mrk 421 as a function of flux calculated at X-ray (1 & 10 keV) and γ-ray (1 & 500 GeV) energies for the four spectral states, SS (solid black line with filled circles), low-flux state (solid red line with filled squares), intermediate-flux state (solid green line with filled diamonds), and high-flux state (solid blue line with filled triangle-up): a) top-left panel shows spectral evolution at 1 keV; (b) top-right panel shows the same for 10 keV; (c) bottom-left shows for 1 GeV; and (d) bottom-right shows the evolution calculated at 500 GeV. The source shows a clockwise pattern in all cases indicating that softer energies lag behind the harder ones. The photon spectral index at each of the energies is denoted by α and follows the relationship, $F_\nu \propto \nu^{-\alpha}$. Figure adapted from Banerjee et al. (2019).

lution of the radiating particles is cooling dominated, as can be seen from the LCs in Figure 5.4 and has been previously reported by Singh et al. 2012, for this time period. However, the spectral evolution at 10 keV for SS, low-flux, and intermediate-flux states exhibits a brief counter-clockwise pattern before returning back to the clockwise pattern. This indicates a brief instant of acceleration and cooling timescales of particles becoming almost equal while producing 10 keV photons. As a result, there is a momentary decrease in the flux at 10 keV accompanied by spectral softening before the pulse at 10 keV returns to its original clockwise behavior.

5.5 Conclusions:

In this work, we carried out extensive simulations to study the spectral energy distributions of Mrk 421 during an outburst in mid-February 2010. During this period the source showed intense flux variations as it underwent a change from the low-flux state (2010 February 13-15) to an intermediate-flux state (observed on 2010 February 16) to a high-flux state (observed on 2010 February 17). In order to perform this study, we analyzed the optical/UV and GeV data and collected X-ray and TeV data from the literature for this period. Neecessary steps have been taken to correct for dereddening and host galaxy contribution for optical-UV data. In addition, we compared the data for the low-flux state with a steady state of the source, which is an average of the emission over a period of 4.5 months. We used a time-dependent leptonic jet model in the internal shock scenario (MUZORF) to reproduce the above mentioned spectral states of Mrk 421. This allowed us to study the origin of variability on a daily basis and the role of intrinsic parameters in shaping the spectral states of the source. We note that the successful models are not unique reproductions of the observed data. Nevertheless, they provide a well-constrained parameter space for the values of key physical parameters, which was extracted using nearly simultaneous data from optical to VHE γ-rays using ground- and space-based facilities. Our findings can be summarized as following:

(i) The key physical parameters that govern the flaring activity in Mrk 421 for the time period under consideration are the kinetic luminosity injected into the system that increases as the flare rises up, magnetic field strength that decreases during this evolution while the source departs progressively from equipartition, energy index of the particle population that becomes harder, and the energy cutoffs of the particle population that increase with the rising of the flare. This type of a trend in the evolution of certain parameters could be taken as the general recipe of driving a multi-waveband flare in SSC-dominated sources. In addition, a change of particle acceleration mechanism, within the shock model scenario, from Fermi first order to stochastic during the evolution of the flare might be required for driving such events in TeV blazars. However, we note that Fermi first-order mechanism under relativistic magnetic reconnection scenario has been suggested to produce flat electron energy spectra (Guo et al. 2014).

(ii) The low-flux state exhibited different spectral features compared to SS and was identified with the onset of the flare. As the source evolved from a low- to a high-flux state it exhibited a "harder when brighter" behavior, which is common for Mrk 421.

(iii) A leptonic time-dependent synchrotron-SSC model with multi-slice scheme successfully reproduces all the above-mentioned spectral states of Mrk 421. As also pointed out in Macomb et al. 1995a, the hadronic model falls short of explaining the variability behavior (strong variability in X-ray & TeV energy regimes but absence of that in the optical and MeV- few-Gev regimes) observed in Mrk 421 during this time period. On the other hand, MUZORF successfully explains this behavior, as also demonstrated in simulated LCs of the source (see Figure 5.4), without invoking high-energy budget requirements associated with accelerating relativistic hadrons. However, it does not carry forward the information of one spectral state to the next and reproduces each of the states individually.

(iv) A simple power-law and an inhomogeneous emission region has been used to reproduce the spectral states during this flaring event. This is in contrast to some previous studies of this source, which mostly used a broken power-law and either a single homogeneous emission region or two disjointed emitting volumes in the jet (Shukla et al. 2012; Singh et al. 2015; Abdo et al. 2011b; Aleksić et al. 2015e; Bartoli et al. 2016b; Carnerero et al. 2017). This could imply that inhomogeneous emission regions give a better agreement with the observed data without invoking complicated distributions of particle population. However, we note that a particle population following a log-parabolic distribution gives an even better agreement with the broadband SED of Mrk 421 for such flaring events. This is because such distributions are a natural consequence of stochastic particle acceleration and reproduce the behavior of particle populations more accurately than a simple power-law distribution (Massaro et al. 2006; Kardashev 1962; Dermer et al. 2014).

(v) The successful model for the high-flux state is characterized by a harder electron energy index with electron population distributed at higher frequencies, higher Doppler factor, and low magnetic field values. A low magnetic field takes care of the required high-flux level of the SSC component observed that day and at the same time suppresses the synchrotron component. The successful model indicates that such "harder when brighter" spectral states are successfully reproduced by a set of parameters instead of a single physical parameter.

(vi) As shown in Figure 5.1, the observed data exhibits no variability in the optical, mild variability in the Fermi-GeV regime, and significant variability at X-rays and TeV energies for this time period. This is supported by the LC realizations of our successful models of different spectral states (see Figure 5.4). The LC profiles of both optical and GeV energies peak later compared to X-ray and TeV flares for all days because relatively low-energy electrons are involved in their production via synchrotron and SSC processes, respectively. Hence, these flares peak later and decay gradually compared to their X-ray and TeV counterparts.

(vii) The flare at 2 TeV is produced via the SSC mechanism. As a result, it peaks later compared to its synchrotron-dominated X-ray flares and decays gradually. However, for the high-flux state the flare exhibits a further spectral hardening and a shifting of the peak of the SSC component to the 2 TeV energy regime. As a result, the flare lasts for a longer time and decays much more gradually compared to 2 TeV flares at other days.

(viii) Due to the fact that the flaring episode could not be observed with high temporal resolution, the simulated LCs can not be validated with the observed LCs. A night-long simultaneous data set (like the campaign described in Baloković et al. 2016b) with variability signatures might provide further scope to validate the model predictions.

Bibliography

Aartsen M. G., Ackermann M., Adams J., et al., 2018, Science, 361, 6398, eaat1378

Abdalla H., Abramowski A., Aharonian F., et al., 2017, A&A, 606, A59

Abdalla H., Abramowski A., Aharonian F., et al., 2018, A&A, 612, A6

Abdo A. A., Ackermann M., Ajello M., et al., 2009, ApJs, 183, 46

Abdo A. A., Ackermann M., Ajello M., et al., 2011a, ApJ, 736, 131

Abdo A. A., Ackermann M., Ajello M., et al., 2011b, ApJ, 736, 131

Abdollahi S., Acero F., Ackermann M., et al., 2020, The Astrophysical Journal Supplement Series, 247, 1, 33

Abeysekara A. U., Albert A., Alfaro R., et al., 2017, ApJ, 841, 2, 100

Abeysekara A. U., Archer A., Benbow W., et al., 2019, ApJ, 885, 2, 150

Abeysekara A. U., Benbow W., Bird R., et al., 2020, ApJ, 890, 2, 97

Acciari V. A., Aliu E., Arlen T., et al., 2011a, ApJ, 738, 25

Acciari V. A., Aliu E., Arlen T., et al., 2011b, ApJ, 738, 1, 25

Acciari V. A., Ansoldi S., Antonelli L. A., et al., 2019, MNRAS, 486, 3, 4233

Acciari V. A., Ansoldi S., Antonelli L. A., et al., 2020, ApJs, 248, 2, 29

Acciari V. A., Arlen T., Aune T., et al., 2014, Astroparticle Physics, 54, 1

Acero F., Ackermann M., Ajello M., et al., 2015a, ApJs, 218, 23

Acero F., Ackermann M., Ajello M., et al., 2015b, VizieR Online Data Catalog, 221

Achterberg A., Gallant Y. A., Kirk J. G., Guthmann A. W., 2001, MNRAS, 328, 393

Ackermann M., Ajello M., Albert A., et al., 2012, ApJs, 203, 4

Ackermann M., Ajello M., Allafort A., et al., 2011, ApJ, 741, 1, 30

Aharonian F., Akhperjanian A., Beilicke M., et al., 2003, A&A, 403, L1

Aharonian F., Akhperjanian A. G., Anton G., et al., 2009, ApJl, 695, 1, L40

Aharonian F., Akhperjanian A. G., Barres de Almeida U., et al., 2008a, A&A, 477, 1, 353

Aharonian F., Akhperjanian A. G., Bazer-Bachi A. R., et al., 2007, ApJl, 664, 2, L71

Aharonian F., Buckley J., Kifune T., Sinnis G., 2008b, Reports on Progress in Physics, 71, 9, 096901

Aharonian F. A., 2000, New Astron., 5, 377

Ahnen M. L., et al., 2017, MNRAS, 472, 3, 2956, [Erratum: Mon. Not. Roy. Astron. Soc.476,no.3,2874(2018)]

Ahnen M. L., Ansoldi S., Antonelli L. A., et al., 2016, A&A, 593, A91

Ahnen M. L., Ansoldi S., Antonelli L. A., et al., 2017a, MNRAS, 472, 3, 2956

Ahnen M. L., Ansoldi S., Antonelli L. A., et al., 2017b, Astroparticle Physics, 94, 29

Albert J., Aliu E., Anderhub H., et al., 2007a, ApJ, 663, 125

Albert J., Aliu E., Anderhub H., et al., 2007b, Nuclear Instruments and Methods in Physics Research A, 583, 2-3, 494

Albert J., Aliu E., Anderhub H., et al., 2008, Nuclear Instruments and Methods in Physics Research A, 588, 3, 424

Aleksić J., Alvarez E. A., Antonelli L. A., et al., 2012a, A&A, 539, L2

Aleksić J., Alvarez E. A., Antonelli L. A., et al., 2012b, A&A, 542, A100

Aleksić J., Alvarez E. A., Antonelli L. A., et al., 2012c, Astroparticle Physics, 35, 7, 435

Aleksić J., Ansoldi S., Antonelli L. A., et al., 2015a, Journal of High Energy Astrophysics, 5, 30

Aleksić J., Ansoldi S., Antonelli L. A., et al., 2015b, A&A, 576, A126

Aleksić J., Ansoldi S., Antonelli L. A., et al., 2015c, A&A, 578, A22

Aleksić J., Ansoldi S., Antonelli L. A., et al., 2015d, A&A, 578, A22

Aleksić J., Ansoldi S., Antonelli L. A., et al., 2015e, A & A, 578, A22

Aleksić J., Ansoldi S., Antonelli L. A., et al., 2016a, Astroparticle Physics, 72, 61

Aleksić J., Ansoldi S., Antonelli L. A., et al., 2016b, Astroparticle Physics, 72, 76

Aleksić J., Antonelli L. A., Antoranz P., et al., 2010a, ApJl, 723, 2, L207

Aleksić J., Antonelli L. A., Antoranz P., et al., 2010b, A&A, 524, A77

Aliu E., Anderhub H., Antonelli L. A., et al., 2008, Science, 322, 5905, 1221

Alves E. P., Zrake J., Fiuza F., 2018, Physical Review Letters, 121, 24, 245101

Anderhub H., Backes M., Biland A., et al., 2013, Journal of Instrumentation, 8, 6, P06008

Ansoldi S., Antonelli L. A., Arcaro C., et al., 2018, ApJl, 863, 1, L10

Antonucci R., 1993, Annual Review of Astron and Astrophys, 31, 473

Antonucci R. R. J., Miller J. S., 1985, ApJ, 297, 621

Assef R. J., Stern D., Noirot G., Jun H. D., Cutri R. M., Eisenhardt P. R. M., 2018, ApJs, 234, 2, 23

Atwood W. B., Abdo A. A., Ackermann M., et al., 2009a, ApJ, 697, 1071

Atwood W. B., Abdo A. A., Ackermann M., et al., 2009b, ApJ, 697, 1071

Bagchi J., Vivek M., Vikram V., et al., 2014, ApJ, 788, 2, 174

Baloković M., Paneque D., Madejski G., et al., 2016a, ApJ, 819, 156

Baloković M., Paneque D., Madejski G., et al., 2016b, ApJ, 819, 156

Banerjee B., Joshi M., Majumdar P., Williamson K. E., Jorstad S. G., Marscher A. P., 2019, MNRAS, 487, 1, 845

Bartoli B., Bernardini P., Bi X. J., et al., 2016a, The Astrophysical Journal Supplement Series, 222, 1, 6

Bartoli B., Bernardini P., Bi X. J., et al., 2016b, ApJs, 222, 6

Beck M., Arbet-Engels A., Baack D., et al., 2019, in 36th International Cosmic Ray Conference (ICRC2019), vol. 36 of International Cosmic Ray Conference, 630

Becker J. K., 2008, Physics Reports, 458, 4-5, 173

Beckmann V., Shrader C. R., 2012, Active Galactic Nuclei

Berezhko E. G., Ellison D. C., 1999, ApJ, 526, 1, 385

Berezhko E. G., Krymskii G. F., 1981, Soviet Astronomy Letters, 7, 352

Bertero M., 1989, vol. 75 of Advances in Electronics and Electron Physics, 1 – 120, Academic Press

Best P. N., Heckman T. M., 2012, MNRAS, 421, 2, 1569

Biland A., Bretz T., Buß J., et al., 2014, Journal of Instrumentation, 9, 10, P10012

Blandford R., Meier D., Readhead A., 2019, Annual Review of Astron and Astrophys, 57, 467

Blandford R. D., Begelman M. C., 1999, MNRAS, 303, 1, L1

Blandford R. D., Königl A., 1979, ApJ, 232, 34

Blandford R. D., Levinson A., 1995, ApJ, 441, 79

Blandford R. D., Payne D. G., 1982, MNRAS, 199, 883

Blandford R. D., Znajek R. L., 1977, MNRAS, 179, 433

Bloom S. D., Marscher A. P., 1996, ApJ, 461, 657

Boettcher M., 2010, arXiv e-prints, arXiv:1006.5048

Boettcher M., 2012, arXiv e-prints, arXiv:1205.0539

Böttcher M., Marscher A. P., Ravasio M., et al., 2003, ApJ, 596, 847

Breeveld A. A., Landsman W., Holland S. T., Roming P., Kuin N. P. M., Page M. J., 2011, in American Institute of Physics Conference Series, edited by J. E. McEnery,

J. L. Racusin, N. Gehrels, vol. 1358 of American Institute of Physics Conference Series, 373–376

Bretz T., Dorner D., 2010, in Astroparticle, Particle and Space Physics, Detectors and Medical Physics Applications, edited by C. Leroy, P.-G. Rancoita, M. Barone, A. Gaddi, L. Price, R. Ruchti, 681–687

Brun R., Rademakers F., 1997, Nuclear Instruments and Methods in Physics Research A, 389, 1, 81

Buckley J. H., Akerlof C. W., Biller S., et al., 1996, ApJl, 472, L9

Burrows D. N., Hill J. E., Nousek J. A., et al., 2005, Space Science Reviews, 120, 3-4, 165

Cao G., Wang J., 2013, PASJ, 65, 109

Carnerero M. I., Raiteri C. M., Villata M., et al., 2017, MNRAS, 472, 3789

Carnerero M. I., Raiteri C. M., Villata M., et al., 2017, Monthly Notices of the Royal Astronomical Society, 472, 4, 3789

Cawthorne T. V., Jorstad S. G., Marscher A. P., 2013, ApJ, 772, 1, 14

Chandra P., Rannot R. C., Yadav K. K., et al., 2012, Journal of Physics G Nuclear Physics, 39, 4, 045201

Chatterjee S., Degraf C., Richardson J., Zheng Z., Nagai D., Di Matteo T., 2012, MNRAS, 419, 3, 2657

Chen L., 2017, ApJ, 842, 2, 129

Chen X., Fossati G., Liang E. P., Böttcher M., 2011a, MNRAS, 416, 2368

Chen X., Fossati G., Liang E. P., Böttcher M., 2011b, MNRAS, 416, 3, 2368

Coto R. L., 2015, Very-high-energy γ-ray observations of pulsar wind nebulae and cataclysmic variable stars with MAGIC and development of trigger systems for IACTs. PhD thesis, Departament de F ısica Universitat Aut‘onoma de Barcelona, Spain

Curtis H. D., 1918, Publications of Lick Observatory, 13, 9

Dazzi F., 2012, A new stereoscopic "Sum-Trigger-II" for the MAGIC Telescopes. PhD thesis, UNIVERSITY OF UDINE

Dazzi F., Herranz Lazaro D., Lopez M., Nakajima D., Rodriguez Garcia J., Schweizer T., 2015, arXiv e-prints, arXiv:1508.05255

Dermer C. D., Cerruti M., Lott B., Boisson C., Zech A., 2014, The Astrophysical Journal, 782, 2, 82

Dermer C. D., Schlickeiser R., 1993a, ApJ, 416, 458

Dermer C. D., Schlickeiser R., 1993b, ApJ, 416, 458

Dermer C. D., Schlickeiser R., Mastichiadis A., 1992, A&A, 256, L27

Domínguez A., Primack J. R., Rosario D. J., et al., 2011, MNRAS, 410, 2556

Dong L., Zhang H., Giannios D., 2020, arXiv e-prints, arXiv:2003.07765

Donnarumma I., AGILE Team, 2012, Mem. Soc. Astron. Italiana, 83, 122

Donnarumma I., Vittorini V., Vercellone S., et al., 2009, ApJl, 691, L13

Dorner D., Adam J., Ahnen L. M., et al., 2017, in 35th International Cosmic Ray Conference (ICRC2017), vol. 301 of International Cosmic Ray Conference, 609

Dorner D., Arbet-Engels A., Baack D., et al., 2019, Galaxies, 7, 2

Drury L. O., 1983, Reports on Progress in Physics, 46, 8, 973

Dyrda M., Wierzcholska A., Moderski R., Ostrowski M., Stawarz L., 2015, in 34th International Cosmic Ray Conference (ICRC2015), vol. 34 of International Cosmic Ray Conference, 801

Edelson R. A., Krolik J. H., 1988, ApJ, 333, 646

Fanaroff B. L., Riley J. M., 1974, Monthly Notices of the Royal Astronomical Society, 167, 1, 31P

Fermi E., 1949, Physical Review, 75, 8, 1169

Finke J. D., Dermer C. D., Böttcher M., 2008, ApJ, 686, 181

Fitzpatrick E. L., 1999, PASP, 111, 755, 63

Fomin V. P., Stepanian A. A., Lamb R. C., Lewis D. A., Punch M., Weekes T. C., 1994, Astroparticle Physics, 2, 2, 137

Foschini L., 2017, Frontiers in Astronomy and Space Sciences, 4, 6

Fossati G., Buckley J. H., Bond I. H., et al., 2008, ApJ, 677, 2, 906

Fox D. B., Frail D. A., Price P. A., et al., 2005, Nature, 437, 7060, 845

Fraija N., Cabrera J. I., Benítez E., Hiriart D., 2015, arXiv e-prints

Gaensler B. M., Slane P. O., 2006, Annual Review of Astron and Astrophys, 44, 1, 17

Gaidos J. A., Akerlof C. W., Biller S., et al., 1996, Nature, 383, 319

Gaisser T. K., 1991, Cosmic Rays and Particle Physics

Galante N., for the VERITAS Collaboration, 2011, arXiv e-prints, arXiv:1109.6059

Gallant Y. A., Achterberg A., 1999, MNRAS, 305, L6

García J. R., Dazzi F., Häfner D., et al., 2014, arXiv e-prints, arXiv:1404.4219

Gaug M., Bartko H., Cortina J., Rico J., 2005, in 29th International Cosmic Ray Conference (ICRC29), Volume 5, vol. 5 of International Cosmic Ray Conference, 375

Gaug M., Fegan S., Mitchell A. M. W., Maccarone M. C., Mineo T., Okumura A., 2019, ApJs, 243, 1, 11

Gear W. K., Brown L. M. J., Robson E. I., et al., 1986, ApJ, 304, 295

Gehrels N., Chincarini G., Giommi P., et al., 2004, ApJ, 611, 1005

Ghisellini G., 2016, Galaxies, 4, 4, 36

Ghisellini G., Celotti A., Fossati G., Maraschi L., Comastri A., 1998, MNRAS, 301, 451

Ghisellini G., Maraschi L., Treves A., 1985, A&A, 146, 204

Ghisellini G., Righi C., Costamante L., Tavecchio F., 2017, MNRAS, 469, 1, 255

Ghisellini G., Tavecchio F., 2008, MNRAS, 387, 4, 1669

Giebels B., Degrange B., 2009, A&A, 503, 3, 797

Giroletti M., Righini S., 2020, MNRAS, 492, 2, 2807

Graff P. B., Georganopoulos M., Perlman E. S., Kazanas D., 2008, ApJ, 689, 1, 68

Grandi S. A., Osterbrock D. E., 1978, ApJ, 220, 783

Guberman D. A., 2018, MAGIC observations with bright Moon and their application to measuring the VHE gamma-ray spectral cut-off of the PeVatron candidate Cassiopeia A, Ph.D. thesis, Barcelona, Autonoma U.

Guo F., Li H., Daughton W., Liu Y.-H., 2014, Physical Review Letters, 113, 15, 155005

H. E. S. S. S., Fermi, NuSTAR collaborations, 2019, arXiv e-prints, arXiv:1912.07273

H. E. S. S. Collaboration, Abdalla H., Aharonian F., et al., 2018, , 620, A66

Hervet O., Williams D. A., Falcone A. D., Kaur A., 2019, arXiv e-prints, arXiv:1904.06802

Hillas A. M., 1985, in 19th International Cosmic Ray Conference (ICRC19), Volume 3, vol. 3 of International Cosmic Ray Conference, 445

Horan D., Acciari V. A., Bradbury S. M., et al., 2009, ApJ, 695, 1, 596

Hovatta T., Petropoulou M., Richards J. L., et al., 2015, MNRAS, 448, 4, 3121

Hrupec D., 2008, Extragalactic sources of rapidly variable high energy gamma radiation. PhD thesis, University of Zagreb, Croatia

Isobe N., Sato R., Ueda Y., et al., 2015, ApJ, 798, 27

Isobe N., Sugimori K., Kawai N., et al., 2010, PASJ, 62, L55

Jester S., Röser H. J., Meisenheimer K., Perley R., 2005, A&A, 431, 477

Jester S., Röser H. J., Meisenheimer K., Perley R., Conway R., 2001, A&A, 373, 447

Jokipii J. R., Morfill G. E., 1990, ApJ, 356, 255

Jones T. W., O'dell S. L., Stein W. A., 1974, ApJ, 188, 353

Jorstad S. G., Marscher A. P., Mattox J. R., Wehrle A. E., Bloom S. D., Yurchenko A. V., 2001, ApJs, 134, 2, 181

Jorstad S. G., Marscher A. P., Morozova D. A., et al., 2017, ApJ, 846, 2, 98

Jorstad S. G., Marscher A. P., Stevens J. A., et al., 2007, AJ, 134, 2, 799

Joshi M., Böttcher M., 2011, ApJ, 727, 21

Joshi M., Böttcher M., 2010, The Astrophysical Journal, 727, 1, 21

Joshi M., Marscher A. P., Böttcher M., 2014, ApJ, 785, 132

Kalberla P. M. W., Burton W. B., Hartmann D., et al., 2005, A&A, 440, 2, 775

Kapanadze B., Dorner D., Romano P., Vercellone S., Kapanadze S., Tabagari L., 2017, ApJ, 848, 103

Kardashev N. S., 1962, Soviet Ast., 6, 317

Kataoka J., 1999, X-Ray Study of Rapid Variability in TeV Blazars and Implications on Particle Acceleration in Jets, Ph.D. thesis, Tokyo U.

Kataoka J., Stawarz Ł., 2016, ApJ, 827, 1, 55

Katarzyński K., Sol H., Kus A., 2003, A&A, 410, 101

Keenan M., Meyer E. T., Georganopoulos M., Reddy K., French O. J., 2020, arXiv e-prints, arXiv:2007.12661

Kirk J. G., Duffy P., Gallant Y. A., 1996, A&A, 314, 1010

Kirk J. G., Rieger F. M., Mastichiadis A., 1998, A&A, 333, 452

Kirk J. G., Rieger F. M., Mastichiadis A., 1998, Astron. Astrophys., 333, 452

Konigl A., 1981, ApJ, 243, 700

Krennrich F., Bond I. H., Bradbury S. M., et al., 2002, The Astrophysical Journal Letters, 575, 1, L9

Krimm H. A., Holland S. T., Corbet R. H. D., et al., 2013, ApJs, 209, 1, 14

Krolik J. H., 1999, Active galactic nuclei : from the central black hole to the galactic environment

Kronberg P. P., Dufton Q. W., Li H., Colgate S. A., 2001, ApJ, 560, 1, 178

Lähteenmäki A., Valtaoja E., 2003, ApJ, 590, 1, 95

León-Tavares J., Valtaoja E., Tornikoski M., Lähteenmäki A., Nieppola E., 2011, A&A, 532, A146

Li T. P., Ma Y. Q., 1983, ApJ, 272, 317

Li W., Jha S., Filippenko A. V., et al., 2006, PASP, 118, 839, 37

Lico R., Giroletti M., Orienti M., et al., 2014, A&A, 571, A54

Longair M. S., 2011, High Energy Astrophysics

Lyubarskii Y. E., 1997, MNRAS, 292, 3, 679

Macomb D. J., Akerlof C. W., Aller H. D., et al., 1995a, ApJl, 449, L99

Macomb D. J., Akerlof C. W., Aller H. D., et al., 1995b, ApJl, 449, L99

Madejski G. M., Nalewajko K., Madsen K. K., et al., 2016, ApJ, 831, 2, 142

MAGIC Collaboration, Acciari V. A., Ansoldi S., et al., 2020a, A&A, 637, A86

MAGIC Collaboration, Acciari, V. A., Ansoldi, S., et al., 2020b, A&A, 643, L14

Mannheim K., 1993, A&A, 269, 67

Maraschi L., Ghisellini G., Celotti A., 1992, ApJl, 397, L5

Marscher A., 2016, Galaxies, 4, 4, 37

Marscher A. P., 1980, Nature, 288, 12

Marscher A. P., 2014, ApJ, 780, 1, 87

Marscher A. P., Gear W. K., 1985, ApJ, 298, 114

Marscher A. P., Jorstad S. G., Mattox J. R., Wehrle A. E., 2002, ApJ, 577, 1, 85

Massaro E., Tramacere A., Perri M., Giommi P., Tosti G., 2006, A&A, 448, 861

Mastichiadis A., Kirk J. G., 1997, A&A, 320, 19

Mattox J. R., Bertsch D. L., Chiang J., et al., 1996, ApJ, 461, 396

Max-Moerbeck W., Hovatta T., Richards J. L., et al., 2014, MNRAS, 445, 1, 428

McEnery J., Bond I. H., Boyle P. J., et al., 1997, International Cosmic Ray Conference, 3, 257

McHardy I., 2010, X-Ray Variability of AGN and Relationship to Galactic Black Hole Binary Systems, vol. 794, 203

McHardy I. M., Koerding E., Knigge C., Uttley P., Fender R. P., 2006, Nature, 444, 7120, 730

Mikhailova M. S., Bannikova E. Y., Kontorovich V. M., 2010, Astronomy Reports, 54, 6, 481

Mirzoyan R., 1997, in International Cosmic Ray Conference, vol. 7 of International Cosmic Ray Conference, 265

Mücke A., Protheroe R. J., 2001, Astroparticle Physics, 15, 121

Mücke A., Protheroe R. J., Engel R., Rachen J. P., Stanev T., 2003a, Astroparticle Physics, 18, 593

Mücke A., Protheroe R. J., Engel R., Rachen J. P., Stanev T., 2003b, Astroparticle Physics, 18, 593

Nakagawa K., Mori M., 2013, ApJ, 773, 2, 177

Nalewajko K., 2017, Galaxies, 5, 4, 64

Narayan R., Piran T., 2012, MNRAS, 420, 1, 604

Narayan R., Yi I., 1994, ApJl, 428, L13

Narayan R., Yi I., 1995, ApJ, 452, 710

Nieppola E., Tornikoski M., Valtaoja E., 2006, A&A, 445, 2, 441

Niinuma K., Kino M., Nagai H., et al., 2012, The Astrophysical Journal, 759, 2, 84

Nilsson K., Pasanen M., Takalo L. O., et al., 2007, A&A, 475, 1, 199

Owen F. N., Eilek J. A., Kassim N. E., 2000, ApJ, 543, 2, 611

Pacholczyk A. G., 1970, Radio astrophysics. Nonthermal processes in galactic and extragalactic sources

Paczyński B., 1998, , 494, 1, L45

Padovani P., Giommi P., 1995, MNRAS, 277, 1477

Padovani P., Urry C. M., 1990, ApJ, 356, 75

Padovani P., Urry C. M., 1992, ApJ, 387, 449

Peterson B. M., Ferrarese L., Gilbert K. M., et al., 2004, ApJ, 613, 2, 682

Peterson B. M., Wanders I., Horne K., et al., 1998, PASP, 110, 748, 660

Piner B. G., Pant N., Edwards P. G., 2010, ApJ, 723, 2, 1150

Piro L., 2005, Nature, 437, 7060, 822

Pittori C., Cutini S., Gasparrini D., et al., 2008, The Astronomer's Telegram, 1583

Poutanen J., Zdziarski A. A., Ibragimov A., 2008, MNRAS, 389, 1427

Press W. H., Teukolsky S. A., Vetterling W. T., Flannery B. P., 2002, Numerical recipes in C++ : the art of scientific computing

Punch M., Akerlof C. W., Cawley M. F., et al., 1992, Nature, 358, 477

Ramakrishnan V., Hovatta T., Nieppola E., Tornikoski M., Lähteenmäki A., Valtaoja E., 2015, MNRAS, 452, 2, 1280

Richards J. L., Max-Moerbeck W., Pavlidou V., et al., 2011, ApJs, 194, 2, 29

Rieger F., Levinson A., 2018, Galaxies, 6, 4, 116

Rieger F. M., Bosch-Ramon V., Duffy P., 2007, Ap&SS, 309, 1-4, 119

Rieger F. M., Duffy P., 2004a, ApJ, 617, 1, 155

Rieger F. M., Duffy P., 2004b, ApJ, 617, 155

Ritt S., 2004, Nuclear Instruments and Methods in Physics Research A, 518, 1-2, 470

Roming P. W. A., Kennedy T. E., Mason K. O., et al., 2005a, Space Sci. Rev., 120, 3-4, 95

Roming P. W. A., Kennedy T. E., Mason K. O., et al., 2005b, Space Sci. Rev., 120, 95

Romoli C., Chakraborty N., Dorner D., Taylor A., Blank M., 2018, Galaxies, 6, 4, 135

Sambruna R. M., Maraschi L., Urry C. M., 1996, ApJ, 463, 444

Schlafly E. F., Finkbeiner D. P., 2011, ApJ, 737, 2, 103

Schmelling M., 1994, Nuclear Instruments and Methods in Physics Research A, 340, 2, 400

Schmidt M., 1963, Nature, 197, 4872, 1040

Sembay S., Warwick R. S., Urry C. M., et al., 1993, ApJ, 404, 112

Seyfert C. K., 1943, ApJ, 97, 28

Shakura N. I., Sunyaev R. A., 1973, A&A, 500, 33

Shukla A., Chitnis V. R., Vishwanath P. R., et al., 2012, A&A, 541, A140

Sikora M., Begelman M. C., Rees M. J., 1994a, ApJ, 421, 153

Sikora M., Begelman M. C., Rees M. J., 1994b, ApJ, 421, 153

Singh K., Bhattacharyya S., Bhatt N., Tickoo A., 2012, New Astronomy, 17, 679

Singh K. K., Yadav K. K., Chandra P., et al., 2015, Astroparticle Physics, 61, 32

Sinha A., et al., 2016, Astron. Astrophys., 591, A83

Sinha A., Sahayanathan S., Acharya B. S., Anupama G. C., Chitnis V. R., Singh B. B., 2017, ApJ, 836, 1, 83

Sinha A., Shukla A., Saha L., et al., 2016, A&A, 591, A83

Sitarek J., Gaug M., Mazin D., Paoletti R., Tescaro D., 2013, Nuclear Instruments and Methods in Physics Research A, 723, 109

Smith A. J., 2005, in 29th International Cosmic Ray Conference (ICRC29), Volume 10, vol. 10 of International Cosmic Ray Conference, 227

Smith P. S., Montiel E., Rightley S., Turner J., Schmidt G. D., Jannuzi B. T., 2009, arXiv e-prints, arXiv:0912.3621

Sobolewska M. A., Siemiginowska A., Kelly B. C., Nalewajko K., 2014, ApJ, 786, 2, 143

Stawarz Ł., 2004, ApJ, 613, 1, 119

Steinke B., 2012, First study of fast variability in Markarian 421 with the MAGIC stereoscopic system. PhD thesis, Max-Planck-Institut für Physik (Werner-Heisenberg-Institut), Germany

Swordy S., 2008, The Astronomer's Telegram, 1506

Takahashi T., Tashiro M., Madejski G., et al., 1996, ApJl, 470, L89

Tanihata C., Kataoka J., Takahashi T., Madejski G. M., 2004, ApJ, 601, 759

Tavecchio F., Maraschi L., Ghisellini G., 1998, ApJ, 509, 608

Teraesranta H., Tornikoski M., Mujunen A., et al., 1998, A&As, 132, 305

Tescaro D., 2010, TeV gamma-ray observations of nearby Active Galactic Nuclei with the MAGIC telescope: exploring the high energy region of the multiwavelength picture. PhD thesis, IFAE Barcelona, July 2010, Spain

Tikhonov A. N., Arsenin V. Y., 1977, Solutions of ill-posed problems, V. H. Winston & Sons, Washington, D.C.: John Wiley & Sons, New York, Translated from the Russian, Preface by translation editor Fritz John, Scripta Series in Mathematics

Tluczykont M., 2011, arXiv e-prints, arXiv:1106.1035

Tluczykont M., Bernardini E., Satalecka K., Clavero R., Shayduk M., Kalekin O., 2010, A&A, 524, A48

Tramacere A., 2010, arXiv e-prints, arXiv:1003.5001

Tramacere A., Giommi P., Perri M., Verrecchia F., Tosti G., 2009, A&A, 501, 879

Uchiyama Y., Urry C. M., Cheung C. C., et al., 2006, ApJ, 648, 2, 910

Ulrich M.-H., Kinman T. D., Lynds C. R., Rieke G. H., Ekers R. D., 1975, ApJ, 198, 261

Urry C., 2004, in AGN Physics with the Sloan Digital Sky Survey, edited by G. T. Richards, P. B. Hall, vol. 311 of Astronomical Society of the Pacific Conference Series, 49

Urry C. M., Padovani P., 1995, PASP, 107, 803

Ushio M., Tanaka T., Madejski G., et al., 2009, ApJ, 699, 1964

Uttley P., McHardy I. M., 2001, MNRAS, 323, 2, L26

Uttley P., McHardy I. M., Vaughan S., 2005, MNRAS, 359, 1, 345

Vacanti G., Fleury P., Jiang Y., et al., 1994, Astroparticle Physics, 2, 1, 1

Vainio R., Pohl M., Schlickeiser R., 2004, A&A, 414, 463

Valverde J., Horan D., Bernard D., et al., 2020, ApJ, 891, 2, 170

Vaughan S., Edelson R., Warwick R. S., Uttley P., 2003, MNRAS, 345, 1271

Villata M., Raiteri C. M., Lanteri L., Sobrito G., Cavallone M., 1998, A&As, 130, 305

Virtanen J. J. P., Vainio R., 2005, ApJ, 621, 1, 313

Virtanen J. J. P., Vainio R., 2005, The Astrophysical Journal, 621, 1, 313

Webb G. M., 1987, ApJ, 319, 215

Weekes T. C., 2003, Very high energy gamma-ray astronomy

Will M., Mirzoyan R., van Scherpenberg J., Garczarczyk M., 2019, in 36th International Cosmic Ray Conference (ICRC2019), vol. 36 of International Cosmic Ray Conference, 823

Williamson K. E., Jorstad S. G., Marscher A. P., et al., 2014, ApJ, 789, 135

Yao W. M., Amsler C., Asner D., et al., 2006, Journal of Physics G Nuclear Physics, 33, 1, 1

Zanin R., Carmona E., Sitarek J., et al., 2013, in International Cosmic Ray Conference, vol. 33 of International Cosmic Ray Conference, 2937

Zanin R., Carmona E., Sitarek J., et al., 2013, in Proceedings of the 33rd International Cosmic Ray Conference (ICRC2013): Rio de Janeiro, Brazil, July 2-9, 2013, 0773

Zhang H., Li H., Guo F., Taylor G., 2017, ApJ, 835, 2, 125

Zweerink J. A., Akerlof C. W., Biller S. D., et al., 1997, ApJl, 490, L141

Thesis Highlight

Name of the Student: Biswajit Banerjee

Name of the CI/OCC: Saha Institute of Nuclear Physics, Kolkata

Enrolment No.: PHYS05201304005

Thesis Title: MULTIWAVELENGTH LONG TERM MONITORING AND SPECTRAL ENERGY DISTRIBUTION MODELING OF BRIGHT ACTIVE GALACTIC NUCLEI MARKARIAN 421

Discipline: **Physical Sciences**

Sub-Area of Discipline: **Astro-particle Physics and Cosmology**

Date of viva voce: 23rd November 2020

The blazar, Markarian 421 (Mrk 421) has been studied vastly over many years with a huge amount of simultaneous radio to very-high-energy (VHE) gamma-ray (γ-ray) data. However, previous multiwavelength (MWL) studies are mostly biased towards the high flux states. Besides, the studies on modeling the spectral energy distributions are performed with time independent spherical one zone models. One of the works described in this thesis presents deep investigation the correlations between the light curves (LC) and the variability of the signal in energy bands, sampled with 15 different instruments from radio to VHE γ-ray band. During the period, 2015-2016, Mrk 421 is found in a state of low activity in the X-ray and VHE γ-ray which are the energy bands where the emitted power is the largest, and has shown correlated behavior in X-rays and VHE γ-rays. Apart from the non-zero correlation around a time-lag of ~45 days between optical (and high-energy γ-ray band) vs. radio bands, the emergence of a new spectral component in the hard X-ray band has been observed by the Swift-BAT telescope. Two new methods, namely, Unbinned Likelihood method and flux profile method (similar to Kernel Density Estimator) for understanding the MWL flux distribution have been devised, which includes the flux uncertainties. This above mentioned study has been complemented by spectral modeling of Mrk 421 is carried out with a time-dependent multi-zone radiation feedback model during a very high flux state in X-ray and VHE γ-rays in 2010. For the first time, with the help of the time-dependent leptonic model, all the three states during the outburst has been explained and realization of MWL radiation profiles are derived. These simulated light curves highlight the main differences between the role of different model parameters in shaping the MWL emission profiles. In this study, a general trend can be established which shows that as the flare evolves from a low- to a high-flux state, higher bulk kinetic energy is injected into the system with a harder particle population and a lower magnetic field strength. The study on the performance of MAGIC telescopes below 100 GeV focuses on recovering the low energy gamma-ray events from soft spectrum sources such as GRB, high redshift AGNs and pulsars. The New Cleaning algorithm showed that an improvement in the sensitivity of the MAGIC telescopes down to 40-50 GeV is possible with the standard triggered data. The new algorithm is a very promising tool which can be used in regular analysis of the data for sources with steep spectra expected from high redshift AGNs, GRBs, pulsars etc.